THE QUANTUM SPIN ICE CANDIDATE $Ce_2Zr_2O_7$

THE DIPOLE-OCTUPOLE
QUANTUM SPIN ICE CANDIDATE $Ce_2Zr_2O_7$

EVAN M. SMITH, B.Sc.

A Thesis Submitted to the School of Graduate Studies
in Partial Fulfilment of the Requirements
for the Degree Doctor of Philosophy

McMaster University

DOCTOR OF PHILOSOPHY (2023)

(Physics)

McMaster University
Hamilton, Ontario

TITLE: The Dipole-Octupole Quantum Spin Ice Candidate $Ce_2Zr_2O_7$

AUTHOR: Evan M. Smith, B.Sc.

SUPERVISOR: Professor Bruce Gaulin

NUMBER OF PAGES: viii, 139

Lay Abstract

This thesis contains an experimental study of the quantum spin ice candidate $Ce_2Zr_2O_7$. Quantum spin *liquids* are a highly sought-after type of collective magnetic phase in which the magnetic spins remain disordered and fluctuate in a quantum-entangled manner down to absolute zero temperature, and quantum spin *ices* are a particular class of quantum spin liquids in which the spin disorder resembles the proton disorder in water ice. These phases have been studied across a large amount of theoretical works due to the fact that they provide unique playgrounds for interesting physics. However, quantum spin liquids are rarely realized in real materials. We have used neutron scattering and other complementary experimental techniques to provide strong evidence for a novel quantum spin ice phase at low temperature in $Ce_2Zr_2O_7$. The low-temperature magnetic behavior of this quantum spin ice candidate is further investigated through a series of experiments in both zero and nonzero magnetic field.

Abstract

This thesis focuses on the cerium-based, insulating pyrochlore magnet $Ce_2Zr_2O_7$. Of particular popularity in the condensed matter community are insulating rare-earth pyrochlores with chemical formula $R_2B_2O_7$, with magnetism based on trivalent rare-earth ions, R^{3+}, and where B^{4+} is a tetravalent transition metal ion. The magnetic R^{3+} ions occupy a sublattice of corner-sharing tetrahedra, which is one of the archetypes for geometric frustration and aids in the promotion of exotic magnetic phases at low temperature. In these rare-earth pyrochlores, the crystal electric field plays an important role in the description of the magnetic behavior. Our high-energy inelastic neutron scattering measurements of the crystal electric field excitations in $Ce_2Zr_2O_7$ reveal a crystal electric field ground state with dipole-octupole symmetry. This dipole-octupole symmetry is particularly intriguing as it allows for novel types of quantum spin ice phases, including some which are based off of quantum-correlated magnetic octupoles rather than magnetic dipoles. Our low-energy neutron scattering measurements provide strong experimental evidence for a quantum spin ice phase at low temperature in $Ce_2Zr_2O_7$. We fit the measured heat capacity, magnetic susceptibility, and neutron scattering signal from $Ce_2Zr_2O_7$ to yield experimental estimates of the exchange parameters describing the magnetic interactions between Ce^{3+} ions in $Ce_2Zr_2O_7$. The resulting parameter values, in accordance with the existing theory, provide evidence for a novel octupole-based quantum spin ice ground state in $Ce_2Zr_2O_7$. Polarized neutron diffraction measurements were also performed on $Ce_2Zr_2O_7$ and provide evidence for the significance of further-than-nearest neighbor interactions. This thesis concludes with an investigation of $Ce_2Zr_2O_7$ in magnetic fields along the $[1, \bar{1}, 0]$ and $[0, 0, 1]$ crystallographic axes, using neutron scattering and heat capacity measurements, with results revealing a different polarized spin ice phase for each of these field directions.

Acknowledgements

I am beyond grateful to my PhD supervisor Bruce Gaulin, who has been an excellent supervisor and mentor to me throughout the entirety of my time in his group. I truly can't thank you enough for all that you have taught me over the years in physics and in general, and for the time that you have spent, and the positive attitude that you always kept, while doing so. I consider myself extremely fortunate to have had the opportunity to research under Bruce's supervision and I will forever cherish my time spent in Bruce's group.

I would like to thank Pat Clancy and Jonathan Gaudet for being outstanding mentors and role models to me. I am extremely appreciative of all of the guidance and teaching you have provided me. I am very grateful to Casey Marjerrison, James Beare, and Jim Garrett for their help with materials synthesis and crystal growth at McMaster University, and for all that they have taught me in this area.

I would also like to thank Marek Kiela for all of the great technical support in the crystal growth lab and x-ray lab over the years. I am also very grateful for the administrative support that I have received from Rosemary McNeice, Tina Stewart, Jennifer Ayres, Mara Esposto, and John Benton. I would like to thank Maikel Rheinstadter and John Greedan for all of the time they donated and all of the insight they gave while acting as committee members for the entirety of my graduate studies.

I am deeply grateful to Owen Benton, Benedikt Placke, and Robin Schäfer for being the driving force behind the theoretical portion of this research, and for all their time and effort spent performing calculations and helping make sense of those calculations with respect to measured data. This work would not have been possible without the single crystal samples prepared by Jeremi Dudemaine and Avner Fitterman in Andrea Bianchi's group at Université de Montreal. Thank you each very much for all of the time and effort that went into making these samples. I would also like to thank Kate Ross, Danielle Yahne, and Timothy DeLazzer for their collaboration on heat capacity measurements performed at Colorodo State University, and Roman Movshovich, Sangyun Lee, and Andrew Woods for their collaboration on heat capacity measurements performed at Los Alamos National Laboratory. I am grateful to Sudarshan Sharma, James Beare, and Graeme Luke for their collaboration on magnetic susceptibility measurements performed at McMaster University, and to Edwin Kermarrec, Suvam Bhattacharya, and Dipranjan Chatterjee for their collaboration on neutron scattering measurements performed at the Institut Laue-Langevin.

I would also like to sincerely thank the many instrument scientists that I've worked with on neutron scattering experiments over the years: Andrew Wildes, Jacques Ollivier, Wolfgang Schmidt, and Karin Schmalzl at the Institut Laue-Langevin, Pascal Manuel, Dmitry Khalyavin, Christian Balz at the ISIS Neutron and Muon Source, Nick Butch, Guangyong Xu, Yang Zhao at the NIST Center for Neutron Research, and Andrey Podlesnyak, Matt Stone, Aleksander Kolsenikov, Adam Aczel, Feng Ye, Keith Taddei, and Stuart Calder at Oak Ridge National Laboratory. Thank you each for contributing to my research and learning, and for creating such a welcoming environment and positive atmosphere for experiments.

I also want to thank the groupmates, officemates, and labmates that I have worked with closely over the years at McMaster University: Connor Buhariwalla, Zach Cronkwright, Kyle Ma, Symphony Huang, Qiang Chen, Bo Yuan, Zan Yang, Jerry Wang, James Beare, Sudarshan Sharma, Jonah Gautreau, Mat Pula, Melissa Henderson, Matthew Nugent, and Megan Rutherford. I have very much enjoyed collaborating with you on various projects, traveling to experiments and conferences with you, and of course, building friendships with you along the way.

I dedicate my thesis to my parents, Gayle and Greg, whose continuous support, guidance, and encouragement made this possible.

Contents

1 Introduction **1**

1.1 Magnetic Frustration and Rare-Earth Pyrochlore Magnets . . . 2

1.2 The Crystal Electric Field in Rare-Earth Pyrochlores . . . 6

1.2.1 The Crystal Electric Field Hamiltonian and Eigenstates . . . 6

1.2.2 The Pseudospin-1/2 Formalism and Single-ion Anisotropy . . . 9

1.3 Magnetic Interactions in Rare-Earth Pyrochlores . . . 11

1.3.1 Exchange Interactions . . . 11

1.3.2 The Dipole-Dipole Interaction . . . 14

1.4 The Basics of Ising Rare-Earth Pyrochlores and Spin Ices . . . 17

1.5 Dipole-Octupole Rare-Earth Pyrochlores . . . 20

1.5.1 Single-ion Properties in Dipole-Octupole Rare-Earth Pyrochlores . . . 20

1.5.2 Interactions and Phases in Dipole-Octupole Rare-Earth Pyrochlores . . . 21

1.5.3 The Distinction Between 0-flux and π-flux Quantum Spin Ice Phases . . . 25

1.5.4 The Reduced Ground State Phase Diagram for Dipole-Octupole Pyrochlores . . . 27

1.6 Neutron Scattering . . . 28

1.6.1 The Basics of Neutron Scattering . . . 28

1.6.2 Nuclear Scattering . . . 32

1.6.3 Magnetic Scattering . . . 35

1.6.4 Neutron Sources and Neutron Scattering Instrumentation . . . 38

1.7 Overview of Thesis . . . 40

2 $Ce_2Zr_2O_7$ in Zero Magnetic Field **42**

2.1 Preface to Publication I: Evidence for a Dipole-Octupole Crystal Electric Field Ground State and Quantum Spin Ice Correlations in the Cerium-Based Pyrochlore Magnet $Ce_2Zr_2O_7$ . . . 43

2.2 Preface to Publication II: Estimating the Nearest-Neighbor Exchange Parameters and Further Evidence for a Quantum Spin Ice Ground State in the Dipole-Octupole Pyrochlore $Ce_2Zr_2O_7$ . . . 60

3 $Ce_2Zr_2O_7$ in a Magnetic Field **83**

3.1 Preface to Publication III: Polarized Spin Ice Phases and Quasi-1D Quantum Spin Chains in the Dipole-Octupole Pyrochlore $Ce_2Zr_2O_7$ at Low Temperature in a Magnetic Field . . . 83

4 Summary and Closing Remarks **121**

4.1 Summary, Conclusions, and Closing Discussions . . . 121

4.2 Future Directions . . . 123

Bibliography **125**

Preface

This is a stapled paper thesis containing three published or submitted articles. The surrounding material aims to provide background and place the work into a broader context. All of the original research is found in the three articles.

Publication I:
"*Quantum Spin Ice Dynamics in the Dipole-Octupole Pyrochlore Magnet* $Ce_2Zr_2O_7$",
J. Gaudet, E. M. Smith, J. Dudemaine, J. Beare, C. R. C. Buhariwalla, N. P. Butch, M. B. Stone, A. I. Kolesnikov, G. Xu, D. R. Yahne, K. A. Ross, C. A. Marjerrison, J. D. Garrett, G. M. Luke, A. D. Bianchi, and B. D. Gaulin,
Physical Review Letters **122**, 187201 (2019).
Reproduced from Reference [1] with permission, copyrighted by the American Physical Society.

Publication II:
"*Case for a* $U(1)_\pi$ *Quantum Spin Liquid Ground State in the Dipole-Octupole Pyrochlore* $Ce_2Zr_2O_7$",
E. M. Smith, O. Benton, D. R. Yahne, B. Placke, R. Schäfer, J. Gaudet, J. Dudemaine, A Fitterman, J. Beare, A. R. Wildes, S. Bhattacharya, T. DeLazzer, C. R. C. Buhariwalla, N. P. Butch, R. Movshovich, J. D. Garrett, C. A. Marjerrison, J. P. Clancy, E. Kermarrec, G. M. Luke, A. D. Bianchi, K. A. Ross, and B. D. Gaulin,
Physical Review X **12**, 021015 (2022).
Reproduced from Reference [2] with permission, copyrighted by the American Physical Society.

Publication III:
"*Quantum Spin Ice Response to a Magnetic Field in the Dipole-Octupole Pyrochlore* $Ce_2Zr_2O_7$",
E. M. Smith, J. Dudemaine, B. Placke, R. Schäfer, D. R Yahne, T. DeLazzer, A. Fitterman, J. Beare, J. Gaudet, C. R. C. Buhariwalla, A. Podlesnyak, Guangyong Xu, J. P. Clancy, R. Movshovich, G. M. Luke, K. A. Ross, R. Moessner, O. Benton, A. D. Bianchi, and B. D. Gaulin.
Reproduced from Reference [3] with permission, copyrighted by the American Physical Society.

Chapter 1

Introduction

Rare-earth pyrochlore magnets have attracted a large amount of attention and notability over the years in the condensed matter physics community. This popularity is due in large part to the fact that the magnetic ions in these pyrochlore-structured materials decorate a network of corner-sharing tetrahedra that is vulnerable to magnetic frustration, together with the fact that magnetic frustration often leads to the promotion of exotic, disordered magnetic phases over more-ordinary ordered phases. In this chapter, we begin with an introduction to magnetic frustration and outline the rudiments of insulating rare-earth pyrochlore magnets (Section 1.1) before going into further detail about the crystal electric field (Section 1.2) and magnetic interactions (Section 1.3) in insulating rare-earth pyrochlore materials. In Section 1.4, we discuss some of the magnetic phases that can occur in pyrochlores that have a crystal electric field ground state corresponding to Ising single-ion anisotropy. There we include an introduction to the concept of spin ice, which is a type of exotic magnetic phase that can exist in many different flavors in the rare-earth pyrochlores. In Section 1.5, we discuss rare-earth pyrochlores that have a crystal electric ground state corresponding to dipole-octupole symmetry. These dipole-octupole pyrochlores have Ising single-ion anisotropy but also have a peculiar mixing of dipolar and octupolar degrees of freedom that leads to the possibility for additional, novel quantum spin ice ground states distinct from those that arise through pure-dipolar degrees of freedom with Ising anisotropy. Section 1.6 provides an overview of neutron scattering: The primary experimental method used for investigating the magnetic properties and quantum spin ice behavior of the dipole-octupole pyrochlore $Ce_2Zr_2O_7$ throughout this thesis. To conclude this chapter, we provide an overview of the following chapters in Section 1.7.

1.1 Magnetic Frustration and Rare-Earth Pyrochlore Magnets

Magnetic frustration is the inability of a system to satisfy all of its pairwise magnetic interactions simultaneously [5–8]. In some systems, this happens due to the geometry of the lattice resulting in an unsatisfiable competition of interactions, and such systems are often referred to as geometrically frustrated (as well as magnetically frustrated). We illustrate the concept of geometric magnetic frustration in Fig. 1.1 using square, triangular, and tetrahedral arrangements of atoms; The square is not geometrically frustrated while the triangle and tetrahedron are both shapes that are prone to magnetic frustration [5–8]. While not relevant hereafter in this thesis, it is worth briefly mentioning that magnetic frustration is also possible due to non-geometric reasons. For example, for a square lattice with antiferromagnetic nearest-neighbor interactions, ideal magnetic frustration can be generated by introducing an antiferromagnetic next-nearest-neighbor interaction with strength equal to the nearest-neighbor interaction.

The magnetic rare-earth pyrochlores are a family of materials in which the magnetic ions occupy a network of corner-sharing tetrahedra and these materials have attracted a large amount of attention over the years, due in large-part to the likelihood and realization of exotic magnetic phases accompanying frustration in these materials [5–12]. Of high popularity among the magnetic rare-earth pyrochlores are insulators with the chemical formula $R_2B_2O_7$,

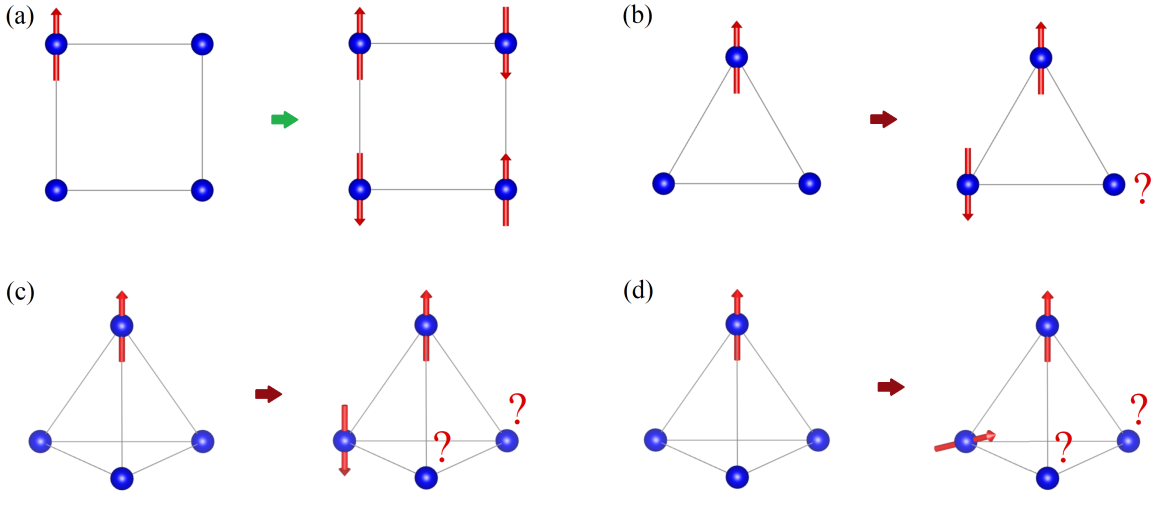

Figure 1.1: A schematic diagram illustrating magnetic frustration using the non-frustrated square lattice and the frustrated triangular and tetrahedral lattices. (a) For a square lattice of ions with antiferromagnetic interactions between nearest neighbors, the direction of all spins in the lattice can be determined from the direction of any single spin. (b) For an equilateral triangle of ions with antiferromagnetic interactions between nearest neighbors, placing one spin on the triangle gives the direction of the next spin placed on the triangle but does not determine the direction of the third spin placed on the triangle as both configurations for this third spin have equal energies. Hand-in-hand with this undetermined spin configuration is the fact that it is not possible to satisfy all interactions between pairs of spins for any possible arrangement of the spins, which defines magnetic frustration. (c) Magnetic frustration occurs in three-dimensions for tetrahedral lattices with isotropic antiferromagnetic interactions between nearest neighbors, such that placing one spin on a tetrahedron gives the direction of second spin placed on the same tetrahedron but does not determine the directions of the third and fourth spins. (d) When each spin is confined along the three-fold rotation axis of the corresponding site (towards or away from the center of the tetrahedron), magnetic frustration occurs for *ferromagnetic* nearest-neighbor interactions, rather than *antiferromagnetic* nearest-neighbor interactions as is the case for the isotropic system of spins in (c). The antiferromagnetic, isotropic case in (c) maps to the ferromagnetic, anisotropic case in (d) with a down or up spin in (c) mapping to an in or out spin in (d), respectively. This figure was created using the VESTA visualization software [4].

where R^{3+} is a magnetic rare-earth ion and B^{4+} is a nonmagnetic transition metal ion [9]. The conventional cubic unit cell of the $R_2B_2O_7$ pyrochlore structure is shown in Fig. 1.2(a) and in Fig. 1.2(b), we show the magnetic sublattice of corner-sharing tetrahedra formed by the R^{3+} ions. The B^{4+} ions also occupy a sublattice of corner-sharing tetrahedra which can be obtained by shifting the R^{3+} sublattice by $a/2$ along any unit-cell edge direction, where a is the cubic lattice constant. The local environment of the rare-earth site, which has D_{3d} point-group symmetry, is shown in Fig. 1.2(c).

The magnetic rare-earth pyrochlores are convenient to work with from a theoretical standpoint in the sense that there typically exists a clear energy hierarchy for the interactions governing the electronic degrees of freedom in the rare-earth ions, with the Coulomb interactions of the electrons dominating over the spin-orbit coupling interaction which subsequently dominates over the crystal electric field (CEF) [9–12]. The resulting electronic configurations can be described using the eigenvalues associated with the vector operators $\hat{\mathbf{J}}$, $\hat{\mathbf{L}}$, and $\hat{\mathbf{S}}$, which are the angular momentum operators for the total, orbital, and spin angular momentum, respectively, in units of $\hbar$. Specifically, $\hat{\mathbf{J}}^2$, $\hat{\mathbf{L}}^2$, $\hat{\mathbf{S}}^2$, and $\hat{J}_z$ are eigenvectors for states of definite total angular momentum (J), orbital angular moment (L), spin angular momentum (S), and total angular momentum projection (m_J), with corresponding eigenvalues of $J(J+1)$, $L(L+1)$, $S(S+1)$, and m_J [13–15]. For a given filling of electron orbitals, the values of S and L are determined from the sums of the spin and orbital angular momentum projection quantum numbers of the electrons, $S = |\sum s_z|$ and $L = |\sum l_z|$, respectively.

The filling of electron orbitals that minimizes the Coulomb interactions experienced by the electrons is conveniently summarized using two rules that are commonly referred to as Hund's rules [13, 14]. Hund's first rule is used to minimize the dominant Coulomb interaction and this rule states that the lowest energy states of an ion are those with

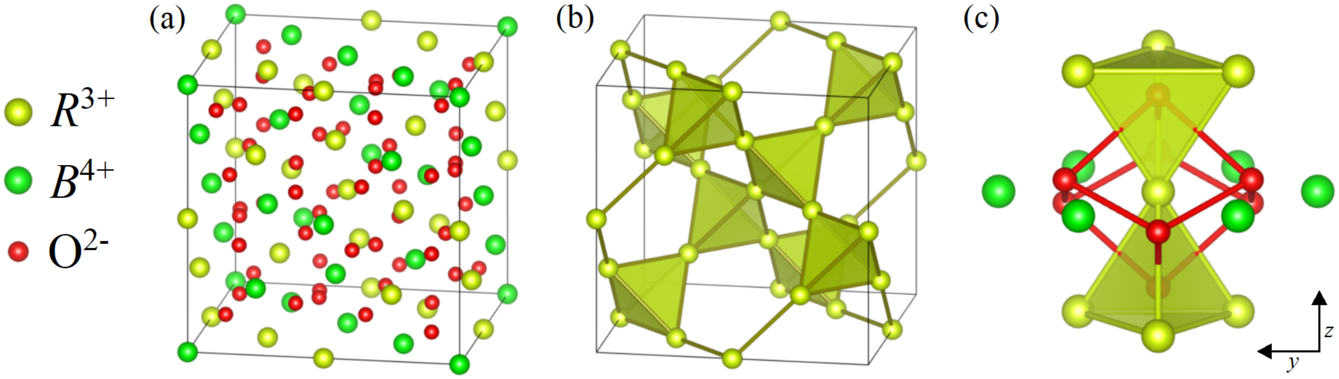

Figure 1.2: (a) The conventional cubic unit cell for the $R_2B_2O_7$ pyrochlore crystal structure. (b) The network of corner-sharing tetrahedra formed by the magnetic sublattice of R^{3+} ions in the $R_2B_2O_7$ pyrochlore crystal structure. Each R^{3+} ion is at the corners of two connected tetrahedrons; The outermost ions in this cubic unit cell, which are not shown as part of two tetrahedra, connect with neighboring unit cells and continue the corner-sharing tetrahedral network. (c) A pair of corner-sharing R^{3+}-tetrahedra in the $R_2B_2O_7$ pyrochlore crystal structure. Here we show the local environment around an R^{3+} ion in the $R_2B_2O_7$ pyrochlores and we show this for the center-most R^{3+} ion in the figure, including the hexagon formed by the neighboring B^{4+} ions as well as the distorted cube of neighboring O^{2-} ions, both centered on the R^{3+} ion. The arrows in (c) show the local y and z axes for the center-most R^{3+} ion in the figure, along one-of-three $\mathcal{C}_2$ axes and along the only $\mathcal{C}_3$ axis of the corresponding R^{3+} site, respectively; We discuss the relevance of these directions in further detail in Section 1.2. This figure was created using the VESTA visualization software [4].

the largest S allowable by the Pauli exclusion principle. Hund's second rule is used to minimize more of the Coulomb interactions and this rule states that the lowest energy states of an ion are those with the largest L allowable by the Pauli exclusion principle. In Fig. 1.3 we show the filling of electronic orbitals that results from following Hund's rules for the rare-earth ions Ce^{3+}, Nd^{3+}, Dy^{3+}, and Ho^{3+}.

Hund's first rule is always obeyed while that is not the case for Hund's second rule, specifically when the crystal electric field competes with the strength of the Coulomb interaction behind Hund's second rule, as is common for transition-metals ions in insulators for example [13]. For rare-earth ions, Hund's second rule is indeed obeyed as the screening of the partially-filled $4f$ shell from the filled $5s$ and $5p$ shells renders the strength of the crystal electric field on $4f$ shell as much weaker than the Coulomb interactions behind Hund's rules [13, 14]. This excludes neutral atoms and cations of the lighter rare-earth elements, scandium, yttrium, and lanthanum, which lack electrons in their $4f$ shells; These atoms are naturally excluded from being the magnetic R^{3+} atoms in rare-earth pyrochlore insulators anyway as they are nonmagnetic in their 3+ oxidation states.

For rare-earth ions, typically the spin-orbit coupling interaction is the next-strongest electronic interaction governing the behavior of the magnetism for the ion, second only to the Coulomb interactions behind Hund's rules, as is the case in the $R_2B_2O_7$ pyrochlores. Put simply, the spin-orbit coupling interaction is due to the sum of interactions between the electronic spins and the magnetic field that results from the charged nucleus due to the fact that the nucleus is rotating in the inertial reference frame of the electron [14]. The Hamiltonian describing the spin-orbit

$l_z =$	-3	-2	-1	0	1	2	3	S	L	J	g_J	μ_{free}
Ce^{3+} ($4f^1$)	↑							1/2	3	5/2	6/7	2.54 μ_B
Nd^{3+} ($4f^3$)	↑	↑	↑					3/2	6	9/2	8/11	3.62 μ_B
Dy^{3+} ($4f^9$)	↑↓	↑↓	↑	↑	↑	↑	↑	5/2	5	15/2	4/3	10.65 μ_B
Ho^{3+} ($4f^{10}$)	↑↓	↑↓	↑↓	↑	↑	↑	↑	2	6	8	5/4	10.61 μ_B

Figure 1.3: A schematic diagram showing the filling of electronic orbitals according to Hund's rules for the rare-earth ions Ce^{3+}, Nd^{3+}, Dy^{3+}, and Ho^{3+}. In each case, the electron levels are filled as to maximize the total spin $S = |\sum s_z|$, satisfying Hund's first rule, as well as maximize is the total orbital angular momentum $L = |\sum l_z|$, which satisfies Hund's second rule, where s_z and l_z denote the spin and orbital angular momentum projection quantum numbers, respectively, for the individual electrons. Here, $s_z = \pm 1/2$ and $l_z = -l, -l+1, \ldots, l-1, l$, with $l = 3$ for the $4f$ shell. Using this diagram, Hund's rules amount to placing electrons in electronic orbitals one at a time from left-to-right with spins in the same direction, before filling orbitals with spins of the opposite direction as necessary, again going from left-to-right, until all spins are placed. This table also shows the value of J and g_J in the spin-orbit ground state multiplet for each ion, as well as the corresponding size of the free-ion magnetic dipole moment, μ_{free} (see main text).

coupling interaction is given by [14]:

$$\mathcal{H}_{\mathrm{SO}} = \lambda\hat{\mathbf{L}}\cdot\hat{\mathbf{S}} = \frac{\lambda}{2}[\hat{\mathbf{J}}^2 - \hat{\mathbf{L}}^2 - \hat{\mathbf{S}}^2] = \frac{\lambda}{2}[J(J+1) - L(L+1) - S(S+1)] \ , \tag{1.1}$$

where the second equality in Eq. (1.1) employs the definition $\hat{\mathbf{J}} = \hat{\mathbf{L}} + \hat{\mathbf{S}}$, and the eigenvalues S and L are given by Hund's rules. The parameter λ is called the spin-orbit coupling parameter and is constant in absolute value for each ion. The spin-orbit coupling parameter is positive for ions that have their partially-filled shell less than half-filled, and negative for ions that have their partially-filled shell more than half-filled [13, 14]. Accordingly, for ions with magnetic shells that are less than half-filled ($\lambda < 0$), the spin-orbit coupling Hamiltonian [Eq. (1.1)] is minimal in the states of lowest possible J (with $J = |L - S|$), with the value of J increasing in steps of one with each further-excited multiplet up to the highest-energy spin-orbit multiplet of maximum J (with $J = L + S$). On the other hand, for ions with their magnetic shell more than half-filled ($\lambda > 0$), the opposite situation occurs and the spin-orbit coupling Hamiltonian [Eq. (1.1)] is minimal in the states of highest possible J (with $J = L + S$), with the value of J decreasing in steps of one with each further-excited multiplet up to the highest-energy spin-orbit multiplet of minimal J (with $J = |L - S|$). The values of J in the spin-orbit ground state manifold are shown for Ce^{3+}, Nd^{3+}, Dy^{3+}, and Ho^{3+} in Fig. 1.3, given by $J = |L - S|$ for the ions with less than 7 electrons in their magnetic $4f$ shell (Ce^{3+} and Nd^{3+}) and by $J = L + S$ for the ions with more than 7 electrons in their $4f$ shell (Dy^{3+} and Ho^{3+}).

The magnetic dipole moment is related to the total angular momentum within any single spin-orbit multiplet through the Landé g-factor, g_J, and the equation [13, 14]:

$$\hat{\boldsymbol{\mu}} = -g_J\mu_{\mathrm{B}}\hat{\boldsymbol{J}} \ , \tag{1.2}$$

where $\hat{\boldsymbol{\mu}}$ and $\hat{\boldsymbol{J}}$ are the magnetic dipole moment and total angular momentum operators, respectively, and $\mu_{\mathrm{B}} = e\hbar/(2m_{\mathrm{e}}) = 9.274 \times 10^{-24}\,\mathrm{J\,T^{-1}}$ is the Bohr magneton [13, 14]. The Landé g-factor is given by [13, 14]:

$$g_J = \frac{3}{2} + \frac{1}{2}\frac{S(S+1) - L(L+1)}{J(J+1)} \ , \tag{1.3}$$

where S and L are given by Hund's rules and J is determined by its value in the respective spin-orbit manifold. Equations (1.2) and (1.3) are valid within any single spin-orbit multiplet but they are most commonly used for the ground state spin orbit multiplet. Throughout this thesis, all values of g_J that we discuss are for the spin-orbit ground state multiplet of the corresponding ion and as is common in the literature, this is implied when the J value is not specifically mentioned. Using the fact the eigenvalue of $\hat{\boldsymbol{J}}^2$ is $J(J+1)$, squaring Eq. (1.2) and taking the expectation value of both sides gives the size of the free-ion magnetic dipole moment, μ_{free}, via the equation: $\mu_{free}^2 = (g_J\mu_{\mathrm{B}})^2 J(J+1)$, where J and g_J are given by their values in the spin-orbit ground state. The values of g_J and μ_{free} for Ce^{3+}, Nd^{3+}, Dy^{3+}, and Ho^{3+} are shown in Fig. 1.3.

The energy gaps between successive spin-orbit manifolds can also be determined via Eq. (1.1): For ions with partially-filled shells that are less (more) than half-filled, the gap between the successive spin-orbit manifolds is $|\lambda|J$ where J is eigenvalue in manifold of higher (lower) energy. The spin-orbit coupling parameter scales with the atomic number of the ion as $\lambda \propto Z^4$ such that spin-orbit coupling is significantly stronger for heavier ions [14]. For rare-earth ions, the strength of the spin-orbit coupling interaction typically dominates heavily over the crystal electric field, due in part to the relatively large values of Z for the rare-earth ions and also in part to the screening of the crystal electric field by the outermost, nonmagnetic $5s$ and $5p$ shells [13, 14]. This is often the case in the $R_2B_2O_7$ pyrochlores and in such cases the crystal electric field can be treated as a perturbation to the spin-orbit coupling [9–12]. This clear energy hierarchy is less likely for ions that are lighter than the rare-earth ions, where closer energy scales of the crystal electric field and spin-orbit coupling can lead to a large amount of mixing of the spin-orbit manifolds by the crystal electric field. In fact, for some light ions, the energy hierarchy is reversed in comparison to the rare-earth ions, such that the spin-orbit coupling can be treated as a perturbation to the crystal electric field. Importantly, Equation (1.2) and the corresponding equation for μ_{free} describe the magnetic dipole moment in the spin-orbit manifold *without* any effects from the crystal electric field. We discuss the crystal electric field in the following section, along with its effect on the description of the magnetism at low-temperature in $R_2B_2O_7$ pyrochlores.

1.2 The Crystal Electric Field in Rare-Earth Pyrochlores

1.2.1 The Crystal Electric Field Hamiltonian and Eigenstates

The crystal electric field on the individual electrons in the magnetic, $4f$ shell of the R^{3+} ions, resulting from the charges on the surrounding ions, further splits the degenerate levels in the spin-orbit manifolds in $R_2B_2O_7$ pyrochlores. For the magnetic $R_2B_2O_7$ pyrochlores, the typical splitting between any two CEF manifolds that are adjacent in energy ($\delta_{\mathrm{CEF}} \lesssim 100$ meV [1, 11, 16–20]) is significantly smaller than the typical splitting between any two spin-orbit manifolds that are adjacent in energy, $|\lambda|J \gtrsim 250$ meV, especially for heavier rare-earth ions where $|\lambda|J \gg 250$ meV [21]. This is important as it allows for the treatment of the CEF as a perturbation to the spin-orbit coupling, such that the resultant CEF states can be described with reasonable accuracy as linear combinations of states with constant J and m_J, denoted as $|J, m_J\rangle$. Additionally, the typical CEF level splitting ($\delta_{\mathrm{CEF}} \lesssim 100$ meV [1, 11, 16–20]) is small enough to only induce minor mixing of degenerate spin-orbit manifolds, which is often ignored. The accuracy of these approximations for R^{3+} ions generally increases from left to right across the $4f$ row of the periodic table, with the weight of the R^{3+} ions, due to the fact that $\lambda \propto Z^4$ (see Section 1.1).

The energy gap, Δ_{CEF}, between the CEF ground state manifold and the first excited-state manifold in the $R_2B_2O_7$ pyrochlores, is typically within the approximate range 10 meV $\lesssim \Delta_{\mathrm{CEF}} \lesssim 100$ meV [1, 11, 16–20]. Importantly, this is large enough to provide accuracy to the approximation that the CEF ground state is the only CEF level occupied at low temperature. To provide some examples, the energy gap between the CEF ground state and the first excited state is $\Delta_{CEF} \sim 55$ meV for $Ce_2Zr_2O_7$ [1, 22], $\Delta_{CEF} \sim 25$ meV for $Nd_2Zr_2O_7$ [23], $\Delta_{CEF} \sim 20$ meV for $Dy_2Ti_2O_7$ [18], and $\Delta_{CEF} \sim 20$ meV for $Ho_2Ti_2O_7$ [16, 18, 24].

Ignoring any mixing of the spin-orbit ground state manifold with excited spin-orbit manifolds, induced by the CEF, the lowest-lying CEF states are linear combinations of $|J, m_J\rangle$ states with J fixed at the value it takes in the spin-orbit ground state manifold. We use this approximation in Fig. 1.4 to illustrate the energy hierarchy and splitting of CEF levels for R^{3+} ions in the $R_2B_2O_7$ pyrochlores. Under this approximation, the Hamiltonian can be simplified using the Stevens operator method, in which the CEF Hamiltonian is approximated using the form $\sum_{nm} B_n^m \hat{O}_n^m$, where the operators, $\hat{O}_n^m$, are called Stevens operators and are polynomials of order n in $\hat{J}_z$, $\hat{J}_+$, and $\hat{J}_-$, where $\hat{J}_\pm = \hat{J}_x \pm \mathrm{i}\hat{J}_y$. Of course, these can also be written as polynomials of $\hat{J}_x$, $\hat{J}_y$, and $\hat{J}_z$ but the convention is to use $\hat{J}_z$ and $\hat{J}_\pm$. The matrix elements of the Stevens operators between different $|J, m_J\rangle$ states with the same J are tabulated for $-J \leq m_J \leq J$ in Refs. [25, 26], for the various values of J relevant to magnetic rare-earth ions. Here, n and m are integers which satisfy $m, n \geq 0$ with $m \leq n$. Additionally, all terms with $n > 2l$ vanish [25–27], where l is the orbital

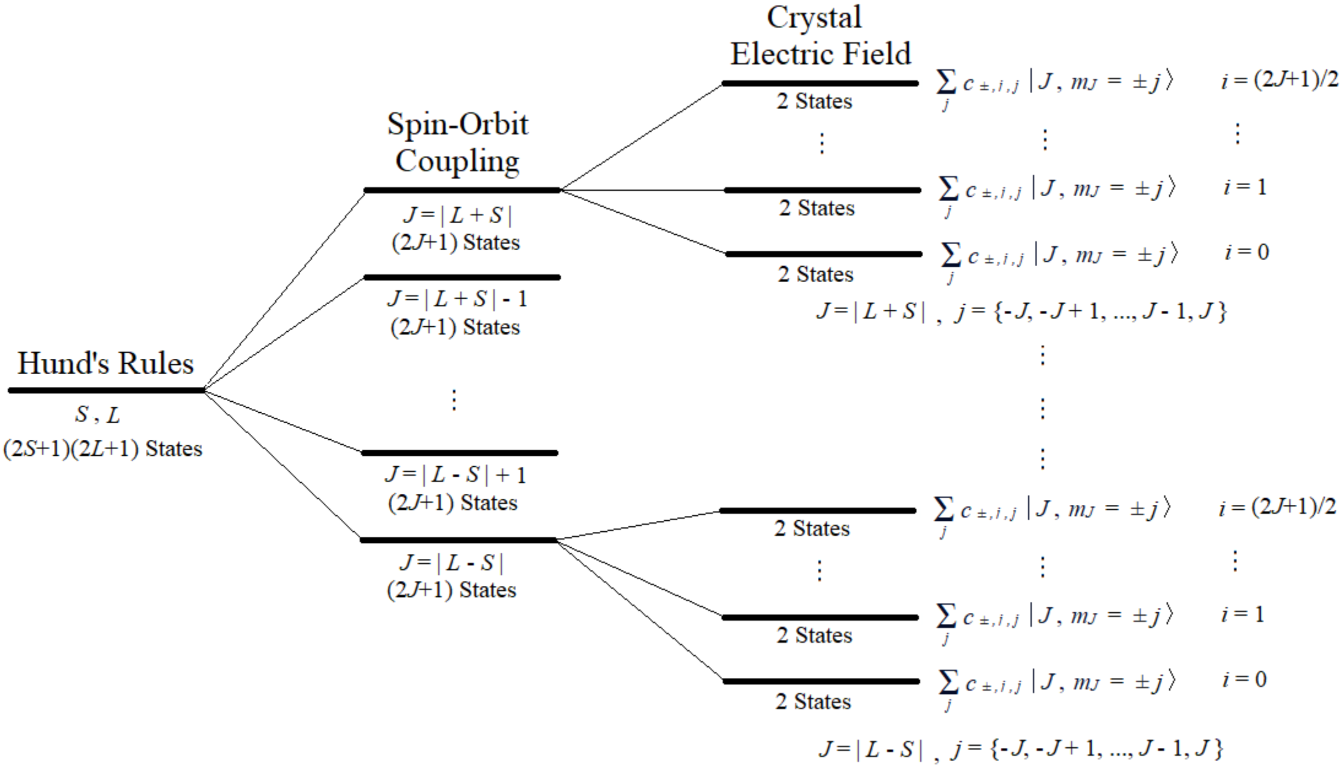

Figure 1.4: A schematic illustration of the energy hierarchy and corresponding level-splitting associated with Hund's rules, spin orbit coupling, and the crystal electric field, for the R^{3+} single-ion energy levels in $R_2B_2O_7$ pyrochlores. The leftmost line represents the $(2S+1)(2L+1)$ degenerate ground states of the coulomb interactions behind Hund's rules, with S and L given by Hund's rules in these states. The center collection of lines represents the spin-orbit coupling manifolds, with each individual line representing a set of $(2J+1)$ degenerate eigenstates of the spin-orbit coupling interaction, with total angular momentum eigenvalue of J in each of these states. We show this for the case of a rare-earth ion with less than 7 electrons, where the spin-orbit ground state manifold has $J = |L-S|$ and the manifold of highest energy has $J = L+S$, rather than vise versa as would be the case for a rare-earth ion with more than 7 electrons. The rightmost collection of lines represents the different eigenstates of the crystal electric field interaction with each state given as a linear combination of $|J, m_J\rangle$ states where $-J \leq m_J \leq J$ for each J. We show this for the case of negligible mixing, of different spin orbit manifolds, induced by the crystal electric field. We also show this for the case in which the CEF eigenstates are all doublets, which would be relevant for a Kramer's ion with maximal CEF level-splitting for example. In this approximation, each spin-orbit coupling manifold is split into a collection of $(2J+1)/2$ doublets which are each linear combinations of $|J, m_J\rangle$ states, where J is given by the eigenvalue of the spin-orbit manifold and $-J \leq m_J \leq J$ for each J.

quantum number of the magnetic electrons, which gives nonzero terms for $n \leq 6$ for the rare-earth ions ($l = 3$).

The number of nonzero B_n^m parameters in the CEF Hamiltonian for $R_2B_2O_7$ pyrochlores is further governed by the symmetry of the R^{3+} site. Specifically, for the D_{3d} point group symmetry appropriate to the R^{3+} site, the description of the CEF Hamiltonian and its eigenstates are simplified by setting the z-axis along the three-fold rotation ($\mathcal{C}_3$) axis of the R^{3+} site, the y-axes along one of the three two-fold rotation ($\mathcal{C}_2$) axes of the R^{3+} site, and setting the x-axis via $\mathbf{x} = \mathbf{y} \times \mathbf{z}$ [26, 27]. An example of these local axes (one of three options) is shown in Fig. 1.2(c) and listed in Table 1.1; Because these axes are defined according to the symmetry of the R^{3+} site, they are defined *locally* such that they are different for each of the four ions on a tetrahedron, as shown in Table 1.1. With this choice of local axes, the CEF Hamiltonian in the Stevens operator approximation is reduced to one with only six nonzero B_n^m parameters [26, 27]:

$$\mathcal{H}_{\mathrm{CEF}} = B_2^0\hat{O}_2^0 + B_4^0\hat{O}_4^0 + B_4^3\hat{O}_4^3 + B_6^0\hat{O}_6^0 + B_6^3\hat{O}_6^3 + B_6^6\hat{O}_6^6. \tag{1.4}$$

In fact, terms with $n > 2J$ vanish as well [25–27], meaning that for $R_2B_2O_7$ pyrochlores with R^{3+} as Ce^{3+} or Sm^{3+}, which have $J = 5/2$ in the spin-orbit ground state manifold, Eq. (1.4) contains only three nonzero coefficients: B_2^0, B_4^0, and B_4^3. This latter restriction provides an additional simplification for the CEF Hamiltonian in the Stevens operator approximation for the main material of interest in this thesis, $\mathrm{Ce_2Zr_2O_7}$.

In principle, the B_n^m coefficients can be approximated using a simple point charge model [24, 26]. However, these calculations are not reliable due to the need to account for effects which are not included in a simple point charge model, such as shielding effects, as well as wavefunction-overlap between neighboring ions, to provide a couple examples [26, 28, 29]. Instead, the B_n^m parameters are most-often estimated by performing fits to the CEF transitions measured in inelastic neutron scattering experiments [1, 16–20, 22, 24, 30–34], as we do in Publication I of this thesis

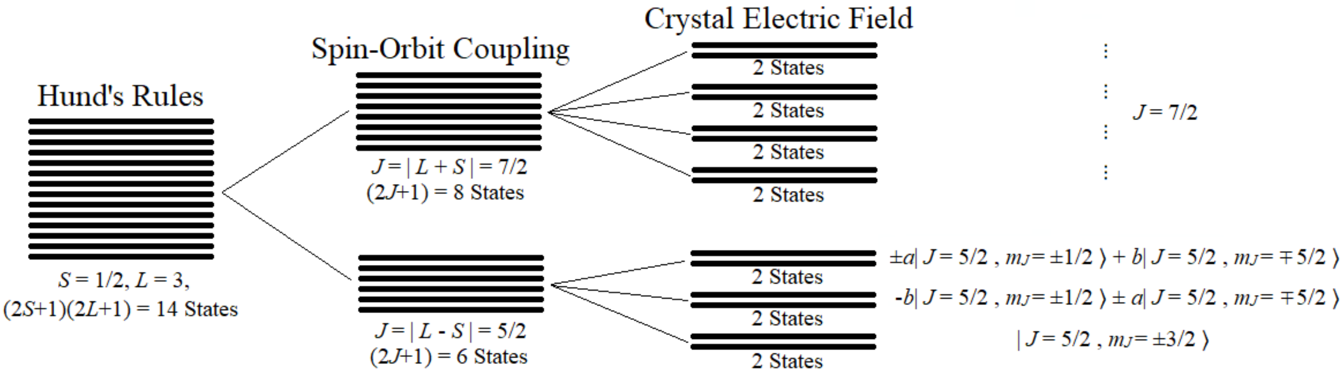

Figure 1.5: A schematic illustration of the energy hierarchy and corresponding level-splitting associated with Hund's rules, spin orbit coupling, and the crystal electric field, for the single-ion energy levels of the $4f^1$ Ce^{3+}, Kramers ions in $\mathrm{Ce_2Zr_2O_7}$. The leftmost collection of lines represents the $(2S + 1)(2L + 1) = 14$ degenerate ground states of the coulomb interactions behind Hund's rules, with $S = 1/2$ and $L = 3$ in these states as given by Hund's rules. The center collection of lines represents the two spin-orbit coupling manifolds, with $J = |L - S| = 5/2$ in the spin-orbit ground state manifold, which contains $(2J + 1) = 6$ states, and with $J = L + S = 7/2$ in the excited spin-orbit manifold, which contains $(2J + 1) = 8$ states. The rightmost collection of lines represents the different eigenstates of the crystal electric field interaction, as determined in Ref. [1], ignoring any mixing of different spin orbit manifolds induced by the crystal electric field and showing only the three doublets arising from the spin-orbit ground-state manifold. Under this approximation, the ground state is a pure $|J = 5/2,\ m_J = \pm 3/2\rangle$ doublet with Ising single-ion anisotropy and dipole-octupole symmetry (see main text).

for $Ce_2Zr_2O_7$, and as we explain further in Section 1.6.3.

Importantly, the CEF splitting often results in a doublet ground state, which allows for a convenient description of the magnetic interactions at low temperature using pseudospin-1/2 degrees of freedom as we further introduce in the following subsection. In fact, for Kramers ions, the states are at least doubly-generate, meaning that doublet ground states are particularly likely for Kramers ions considering that maximal CEF splitting is often the case. The material of main interest for this thesis, $Ce_2Zr_2O_7$, has a CEF ground state doublet that is estimated to be a pure $|J = 5/2,\ m_J = \pm 3/2\rangle$ doublet [1, 22], as shown in Fig. 1.5. Similarly, $Ho_2Ti_2O_7$, $Dy_2Ti_2O_7$, and $Nd_2Zr_2O_7$, have CEF ground state doublets [16, 18, 24, 33], and so a description via pseudospin-1/2 operators is possible for each of those materials. The two states in the CEF ground state doublet for each material are commonly denoted by $|\pm\rangle$; Of course, this leaves two options, based on which of the CEF ground states is denoted as $|+\rangle$ and which is denoted as $|-\rangle$, and this is settled using the convention that $|+\rangle$ is chosen as the state satisfying $\langle +| \hat{J}_z |+\rangle > 0$ and $|-\rangle$ is chosen as the state satisfying $\langle -| \hat{J}_z |-\rangle < 0$, where $\langle -| \hat{J}_z |-\rangle = -\langle +| \hat{J}_z |+\rangle$.

α	1	2	3	4
$\mathbf{x}_\alpha$	$\frac{1}{\sqrt{6}}[\bar{2},1,1]$	$\frac{1}{\sqrt{6}}[\bar{2},\bar{1},\bar{1}]$	$\frac{1}{\sqrt{6}}[2,1,\bar{1}]$	$\frac{1}{\sqrt{6}}[2,\bar{1},1]$
$\mathbf{y}_\alpha$	$\frac{1}{\sqrt{2}}[0,\bar{1},1]$	$\frac{1}{\sqrt{2}}[0,1,\bar{1}]$	$\frac{1}{\sqrt{2}}[0,\bar{1},\bar{1}]$	$\frac{1}{\sqrt{2}}[0,1,1]$
$\mathbf{z}_\alpha$	$\frac{1}{\sqrt{3}}[1,1,1]$	$\frac{1}{\sqrt{3}}[1,\bar{1},\bar{1}]$	$\frac{1}{\sqrt{3}}[\bar{1},1,\bar{1}]$	$\frac{1}{\sqrt{3}}[\bar{1},\bar{1},1]$

Table 1.1: The local x, y, and z directions for the four different sublattices ($\alpha = 1, 2, 3, 4$) composing the tetrahedral network of rare-earth ions in the $R_2B_2O_7$ pyrochlores [12, 35]. In this sublattice description, the location of each R^{3+} ion with respect to the center of its tetrahedron is given by $\mathbf{b}_\alpha = -\frac{\sqrt{3}}{8}\mathbf{z}_\alpha$, and these tetrahedra form a face-centered cubic lattice with tetrahedra centered on the primitive lattice locations, $R = n_1\mathbf{a}_1 + n_2\mathbf{a}_2 + n_3\mathbf{a}_3$ for $n_1, n_2, n_3 \in \mathbb{Z}$, where $\mathbf{a}_1 = \frac{a}{2}[1/2, 1/2, 0]$, $\mathbf{a}_2 = \frac{a}{2}[1/2, 0, 1/2]$, and $\mathbf{a}_3 = \frac{a}{2}[0, 1/2, 1/2]$.

1.2.2 The Pseudospin-1/2 Formalism and Single-ion Anisotropy

Magnetic interactions within the CEF ground state doublet, $|\pm\rangle$, can accurately be described using pseudospin-1/2 degrees of freedom, as is standard in the literature on rare-earth pyrochlores and frustrated rare-earth magnets in general [2, 3, 12, 30, 35–43]. Specifically, this is an accurate approximation at temperatures low enough as to not significantly populate any excited CEF states. These pseudospin-1/2 operators are represented in terms of outer products of the $|\pm\rangle$ states [12, 39]:

$$\hat{S}^z = \frac{|+\rangle\langle+| \; - \; |-\rangle\langle-|}{2}, \tag{1.5}$$

and

$$\hat{S}^\pm = |\pm\rangle\langle\mp| \ , \tag{1.6}$$

where,

$$\hat{S}^x = \frac{\hat{S}^+ + \hat{S}^-}{2}, \quad \hat{S}^y = \frac{\hat{S}^+ - \hat{S}^-}{2\mathrm{i}} \ . \tag{1.7}$$

.

These pseudospin-1/2 operators, $\hat{S}^x$, $\hat{S}^y$, and $\hat{S}^z$, act like normal spin-1/2 operators within the CEF ground state manifold in that their eigenvalues are $\pm 1/2$ with corresponding eigenstates $|+\rangle \pm |-\rangle$, $|+\rangle \pm \mathrm{i}|-\rangle$, and $|\pm\rangle$, respectively, mimicking the typical spin-1/2 algebra [15]. Similarly, the pseudospin-1/2 ladder operators, $\hat{S}^+$ and $\hat{S}^-$, act like normal spin-1/2 operators within the CEF ground state manifold in that $\hat{S}^{\pm}|\pm\rangle = 0$ and $\hat{S}^{\pm}|\mp\rangle = |\pm\rangle$. As we will show in the next section, these pseudospin operators are useful for describing magnetic interactions at low temperature in pyrochlores with CEF ground states that are doublets. Their relation to the magnetic dipole moment is also particularly useful, with any CEF-induced single-ion anisotropy for the dipole moments represented in a simple way through the equation [12, 44]:

$$\hat{\boldsymbol{\mu}}_i = -\mu_{\mathrm{B}}[g_{xy}(\mathbf{x}_i\hat{S}_i^x + \mathbf{y}_i\hat{S}_i^y) + g_z\mathbf{z}_i\hat{S}_i^z] \ , \tag{1.8}$$

where $\hat{\boldsymbol{\mu}}_i$ is the magnetic dipole moment operator and $\mathbf{x}_i$, $\mathbf{y}_i$, and $\mathbf{z}_i$ are unit vectors along the x, y, and z directions in the local coordinate system relevant for atom i (see Table 1.1). The anisotropic g-factors, g_z and g_{xy}, relating the relating the magnetic dipole moment to the pseudospin components, are given by [17, 19, 20, 45, 46]:

$$g_z = 2g_J \left|\langle\pm|\, \hat{J}_z \,|\pm\rangle\right| \ , \tag{1.9}$$

and,

$$g_{xy} = g_J \left|\langle\pm|\, \hat{J}_\pm \,|\mp\rangle\right| \ , \tag{1.10}$$

where $\hat{J}_\pm = \hat{J}_x \pm \mathrm{i}\hat{J}_y$ (see Section 1.1) and g_J is given by Eq. (1.3). The factor of 2 in g_z accounts for the fact that the expectation values of $\hat{S}^z$ are $\pm 1/2$ in the CEF ground state doublet, and this factor is missing from g_{xy} as $\hat{J}_\pm$ already includes both $\hat{J}_x$ and $\hat{J}_y$. The anisotropic g-factors contain the information on the single-ion anisotropy of the magnetic dipole moment, with three limiting scenarios arising: 1) When $g_{xy} = 0$ and $g_z \neq 0$, each magnetic dipole moment is entirely along its local z-direction and the anisotropy is referred to as *Ising single-ion anisotropy*, 2) When $g_{xy} \neq 0$ and $g_z = 0$, each magnetic dipole moment lies entirely in the local xy-plane and the anisotropy is referred to as *XY single-ion anisotropy*, and 3) When $g_z = g_{xy} \neq 0$, the magnetic dipole moments are isotropic and are free to align in whatever directions best-satisfy the interactions in the system. This latter case is referred to as *Heisenberg isotropy*.

In fact, these terms for the different anisotropies are used more loosely than in the aforementioned limiting cases where Ising, XY, and Heisenberg single-ion anisotropy was ideal. While Ising single-ion anisotropy *does* most often refer to perfect single-ion anisotropy ($g_{xy} = 0$ and $g_z \neq 0$), as will be the case throughout this thesis, the term XY single-ion anisotropy is often used to describe anisotropies where $g_{xy} \gg g_z$ but $g_z \neq 0$, and the term Heisenberg single-ion anisotropy is often used to describe anisotropies where $g_{xy} \approx g_z$ but $g_{xy} \neq g_z$ [11, 19, 24, 47]. The rare-earth pyrochlore of primary interest for this thesis, $\mathrm{Ce_2Zr_2O_7}$, has a CEF ground state with Ising single-ion anisotropy, $g_{xy} = 0$ and $g_z \neq 0$ [1, 22]. Similarly, $\mathrm{Ho_2Ti_2O_7}$, $\mathrm{Dy_2Ti_2O_7}$, and $\mathrm{Nd_2Zr_2O_7}$, also have CEF ground states with

Ising single-ion anisotropy, $g_{xy} = 0$ and $g_z \neq 0$ [16, 18, 24, 33, 48]; We use $Ho_2Ti_2O_7$, $Dy_2Ti_2O_7$, and $Nd_2Zr_2O_7$ as alternative examples of $R_2B_2O_7$ pyrochlores throughout this thesis, to complement our discussions on $Ce_2Zr_2O_7$, and in line with the fact that we compare $Ce_2Zr_2O_7$ to these materials in further detail in Publication III of this thesis.

We end this section by noting that the symmetry properties of the CEF ground state and corresponding pseudospins play an important role in governing the form of the magnetic interaction Hamiltonian, as we discuss further in the following section. Importantly, there are three possible symmetry classifications that arise in the rare-earth pyrochlores, based on how the pseudospin-1/2 degrees of freedom transform under the D_{3d} symmetry operations and time-reversal symmetry [12, 49–53]. The z-component of pseudospin, $\hat{S}^z$, transforms like a magnetic dipole in each case and the classifications are drawn according to the differing behavior of $\hat{S}^x$ and $\hat{S}^y$. The *non-Kramers* ground state doublet occurs for all magnetic rare-earth ions with an even number of electrons, and for these doublets, $\hat{S}^x$ and $\hat{S}^y$ both transform like electric quadrupoles. The *effective spin-1/2* ground state doublet is one of two possibilities for rare-earth ions with an odd number of electrons and is characterized by x- and y-components of pseudospin that both transform like magnetic dipoles. The other possibility for Kramers ions is the *dipole-octupole* doublet for which $\hat{S}^x$ transforms under the site symmetries and time-reversal symmetry as a magnetic dipole would while $\hat{S}^y$ transforms like the component of a magnetic octupole tensor. This latter case is the one of most relevance to Ce^{3+} in $Ce_2Zr_2O_7$, which has a CEF ground state doublet that is estimated to be a pure $|J = 5/2,\ m_J = \pm 3/2\rangle$ doublet (Refs [1, 22]) with dipole-octupole symmetry [51, 52]. Figure 1.5 illustrates the energy hierarchy and splitting of CEF levels for Ce^{3+} in $Ce_2Zr_2O_7$, as estimated from the work in Publication I of this thesis. This shows the $|J = 5/2,\ m_J = \pm 3/2\rangle$, dipole-octupole, CEF ground state doublet for Ce^{3+} in $Ce_2Zr_2O_7$, which is separated from the first excited CEF state by ~55 meV [1, 22]. The rare-earth pyrochlores $Ho_2Ti_2O_7$, $Dy_2Ti_2O_7$, and $Nd_2Zr_2O_7$ have CEF ground state doublets with non-Kramers, dipole-octupole, and dipole-octupole, symmetry, respectively [12, 16, 18, 24, 33].

1.3 Magnetic Interactions in Rare-Earth Pyrochlores

1.3.1 Exchange Interactions

In this section, we discuss magnetic interactions in the $R_2B_2O_7$ pyrochlores and specifically, how they are described within the CEF ground state at low temperature for pyrochlores with a CEF ground state doublet that is well-separated in energy from the excited CEF states. Foremost, it is almost always required that exchange interactions be included in providing an accurate description of the magnetic interactions in rare-earth pyrochlores, such as the oxygen-mediated superexchange between rare-earth ions [39, 50]. The most general form of the exchange Hamiltonian, describing all exchange interactions projected into the CEF ground state doublet, is given by [11, 12, 54, 55]:

$$\mathcal{H}_{\text{Exchange}} = \sum_{ij} \sum_{u} \sum_{v} J_{uv}^{ij} \hat{S}_i^u \hat{S}_j^v \ , \tag{1.11}$$

where u and v denote the local directions, $\{x, y, z\}$, for ions i and j, respectively, and the pseudospins $\hat{S}_k^x$, $\hat{S}_k^y$, and $\hat{S}_k^z$ $(k = i, j)$ are given by Eqs. (1.5)-(1.7). The first sum in Eq. (1.11) is over all pairs of magnetic atoms in the lattice, denoted as i and j. In fact, within the CEF ground state doublet, it is possible to write *any* pairwise interactions between the total angular momenta of R^{3+} ions in the pyrochlore lattice using a form similar to Eq. (1.11), $\mathcal{H}_{\text{Pairwise,General}} = \sum_{ij} \sum_u \sum_v M_{uv}^{ij} \hat{S}_i^u \hat{S}_j^v$ [12]. This includes non-exchange-based interactions such as the dipole-dipole, dipole-octupole, and octupole-octupole interactions [12], to name a few that are particularly relevant to this thesis. Due to the similarity in the form for the exchange interaction Hamiltonian in Eq. (1.11) and the form for $\mathcal{H}_{\text{Pairwise,General}}$, all pairwise magnetic interactions can be absorbed into the definition of the "exchange" parameters in Eq. (1.11), as is done throughout this thesis, and as is shown in further detail for the dipole-dipole interaction in the following subsection.

For a given local direction, $\alpha = x$, y, or z, an exchange constant, $J_{\alpha\alpha}^{ij}$, that is less (greater) than zero gives a ferromagnetic (an antiferromagnetic) interaction with respect to the local α directions for ions i and j, such that, apart from any competition from other terms in the Hamiltonian, the pseudospin-components $\hat{S}_i^\alpha$ and $\hat{S}_j^\alpha$ perfer to have their expectation values of the same (opposite) sign to satisfy the $J_{\alpha\alpha}^{ij} \hat{S}_i^\alpha \hat{S}_j^\alpha$ term in the Hamiltonian. Of course, given local directions, α, $\beta = x$, y, or z with $\alpha \neq \beta$, an exchange constant, $J_{\alpha\beta}^{ij}$, that is less (greater) also dictates that, apart from any competition from other terms in the Hamiltonian, the pseudospin-components $\hat{S}_i^\alpha$ and $\hat{S}_j^\beta$ perfer to have their expectation values of the same (opposite) sign to satisfy the $J_{\alpha\beta}^{ij} \hat{S}_i^\alpha \hat{S}_j^\beta$ term in the Hamiltonian, although such off-diagonal interactions are not typically referred to as ferromagnetic or antiferromagnetic.

Importantly, a ferromagnetic (an antiferromagnetic) interaction with respect to two local z directions, with corresponding exchange constant, $J_{zz}^{ij} < 0$ $(\, J_{zz}^{ij} > 0\,)$, actually corresponds to an antiferromagnetic (a ferromagnetic) interaction, with preferred alignment that is non-colinear, with respect to the crystallographic coordinates, due to how the local z-directions are defined with respect to the crystallographic axes for each rare-earth site, and the fact that positive z-directions for different sites have negative dot products with each other (see Table 1.1). This interesting subtlety is the underlying reason that the frustrated tetrahedra with *isotropic antiferromagnetic* interactions in Fig. 1.1(c) maps directly onto the frustrated tetrahedra with *Ising single-ion anisotropy and ferromagnetic interactions* in Fig. 1.1(d), for example. This subtlety has resulted in conflicting uses of the terms ferromagnetic and antiferromagnetic throughout the literature on rare-earth pyrochlores (see Refs. [56, 57] for example). Here we adopt the convention implied by our previous example for the z-direction, and refer to interactions with positive (negative) exchange constant, $J_{\alpha\alpha}^{ij}$, as ferromagnetic (antiferromagnetic) interactions. We do this despite the fact that the interpretation of a positive or negative exchange constant with respect to the crystallographic axes is more complicated for the local x and y directions where the sign of the dot product between two positive local x directions varies in sign depending on which two sites are chosen, and the dot product between two positive local y directions is zero for some combinations of sites. Nonetheless, our aim is that this choice in nomenclature reduces potential confusion in discussions of the magnetism with respect to the crystallographic coordinate system for the magnetic dipole moments in $\mathrm{Ce_2Zr_2O_7}$, which are confined to the *z-axes* due to the Ising single-ion anisotropy [1, 22]; This choice in nomenclature is motivated in part by Publication III of this thesis, where we investigate the field-induced behavior of the magnetic dipole moments in $Ce_2Zr_2O_7$ and discuss the results with respect to the crystallographic coordinate system.

Fortunately, the symmetry of the R^{3+} site in the pyrochlore lattice reduces the number of nonzero exchange parameters that are permitted [12, 35, 49, 55]. For example, the symmetry of the rare-earth site reduces the nine anisotropic nearest-neighbor parameters to only four distinct parameters which are capable of describing the interactions at the nearest-neighbor level [12, 35, 49, 55]. In the global crystallographic coordinate system, these four exchange parameters describe the Heisenberg, Kitaev, pseudo-dipolar and Dzyaloshinskii-Moriya exchange [12, 55], as well as any other pairwise magnetic interactions which contribute to the nearest-neighbor parameters, such as magnetic multipole-multipole interactions. In the local coordinate system for the $R_2B_2O_7$ pyrochlores (Table 1.1), the physical interpretation of the underlying exchange interactions for each of the parameters is more complicated due to the fact that, in general, each exchange parameter in the local coordinate system has contributions from all four of the aforementioned exchanges [35, 55]. Nonetheless, the Hamiltonian itself takes a simpler form in the local coordinate system compared to the crystallographic coordinate system [35, 55]. Specifically, in the local coordinate system for the $R_2B_2O_7$ pyrochlores, the pseudospin interaction Hamiltonian at the nearest-neighbor level is given by [12, 35, 55]:

$$\begin{aligned}\mathcal{H}_{\mathrm{NN}} = \sum_{<ij>} \Big[& J_z \hat{S}_i^z \hat{S}_j^z - J_\pm (\hat{S}_i^+ \hat{S}_j^- + \hat{S}_i^- \hat{S}_j^+) + J_{\pm\pm}(\gamma_{ij} \hat{S}_i^+ \hat{S}_j^+ + \gamma_{ij}^* \hat{S}_i^- \hat{S}_j^-) \\ & + J_{z\pm}\left[\zeta_{ij}(\hat{S}_i^z \hat{S}_j^+ + \hat{S}_i^+ \hat{S}_j^z) + \zeta_{ij}^*(\hat{S}_i^z \hat{S}_j^- + \hat{S}_i^- \hat{S}_j^z)\right] \Big] ,\end{aligned} \tag{1.12}$$

where the sum is over all nearest-neighbor pairs of R^{3+} ions in the pyrochlore lattice, denoted as i and j, and the pseudospin operators are as defined in Eqs. (1.5)-(1.7). The exchange parameters J_z, $J_\pm$, $J_{\pm\pm}$, and $J_{z\pm}$ are material-dependent parameters that depend on the details of the magnetic interactions at a microscopic level [12, 35, 39, 55], which are often estimated for a material via fits to experimental data [2, 3, 35, 37, 38, 58–67], as we do for $Ce_2Zr_2O_7$ in Publications II and III of thesis. The bond-dependent factors, γ_{ij} and ζ_{ij}, are material-dependent as well but depend only on the symmetry of the CEF ground state doublet and have been determined previously for each of the three possible symmetry classifications of CEF ground state doublet possible for the $R_2B_2O_7$ pyrochlores, as we now discuss.

The symmetry of the CEF ground state doublet puts restrictions γ_{ij} and ζ_{ij}, and can even further reduce the number of distinct exchange parameters. For the effective spin-1/2 ground state doublet, all terms are present with $\gamma_{ij} = -\zeta_{ij}^*$; The values of ζ_{ij} for each distinct bond are given in Refs. [35, 55]. This Hamiltonian is appropriate to the effective spin-1/2 pyrochlore $Yb_2Ti_2O_7$ [12, 35, 68], for example. In contrast to this, for the case of a non-Kramers CEF ground state doublet, the lack of time-reversal symmetry for the CEF ground state doublet and corresponding pseudospins dictates that $J_{z\pm} = 0$ [12, 44, 49]. This Hamiltonian is appropriate to the non-Kramers pyrochlore $Ho_2Ti_2O_7$ [12, 16, 18, 24, 44, 49], for example. Finally, in the case of a dipole-octupole CEF ground state doublet, each the pseudospin operators transform trivially under $\mathcal{C}_3$ rotation about the local z-axis and this dictates that there can be no bond-dependence at the nearest-neighbor level, such that it suffices to take $\gamma_{ij} = \zeta_{ij} = 1$ [12, 51]. This latter Hamiltonian is appropriate to the dipole-octupole pyrochlores $Ce_2Zr_2O_7$, $Nd_2Zr_2O_7$, and $Dy_2Ti_2O_7$ [12, 16, 24, 44], to name a few examples which are particularly relevant to this thesis.

While the general form of the Hamiltonian differs between the non-Kramers pyrochlore $Ho_2Ti_2O_7$ and the dipole-octupole pyrochlore $Dy_2Ti_2O_7$, the lack of significant quantum terms, $J_{\pm}$, $J_{\pm\pm}$, and $J_{z\pm}$, for each of these materials leads to the same, commonly-used approximation for both $Ho_2Ti_2O_7$ and $Dy_2Ti_2O_7$ [39, 69–71], which consists of including only the $\hat{S}_i^z\hat{S}_j^z$ terms, but past the nearest-neighbor level due to the significance of the dipolar interaction well beyond nearest neighbors in these materials (as shown in the following subsection).

We discuss the dipole-octupole pseudospin Hamiltonian at the nearest-neighbor level in Section 1.5, with a recasting of the nearest-neighbor Hamiltonian in terms of $\hat{S}^x$, $\hat{S}^y$, and $\hat{S}^z$, instead of $\hat{S}^-$, $\hat{S}^+$, and $\hat{S}^z$, which leads to a particularly simple form for the Hamiltonian.

1.3.2 The Dipole-Dipole Interaction

Along with exchange interactions, it is most often required that the magnetic dipole-dipole interaction be included in providing an accurate description of the magnetic interactions in rare-earth pyrochlores. The Hamiltonian describing magnetic dipole-dipole interactions is given by [14]:

$$\mathcal{H}_{\text{Dipolar}} = \frac{\mu_0}{4\pi}\sum_{i>j}\frac{1}{R_{ij}^3}\left[(\hat{\boldsymbol{\mu}}_i\cdot\hat{\boldsymbol{\mu}}_j) - \frac{3}{R_{ij}^2}(\hat{\boldsymbol{\mu}}_i\cdot\mathbf{R}_{ij})(\hat{\boldsymbol{\mu}}_j\cdot\mathbf{R}_{ij})\right], \tag{1.13}$$

where $\hat{\boldsymbol{\mu}}_i$ is given by Equation (1.8), $\mathbf{R}_{ij}$ is the displacement vector connecting the locations of ions i and j, with magnitude R_{ij}, and the constant $\mu_0 = 1.2566\times10^{-6}\,\mathrm{kg\,m\,s^{-2}\,A^{-2}}$ is the permeability of free space. The sum is over all pairs of magnetic atoms i and j, with $i > j$ to avoid double-counting interactions, as is conventional in defining the dipolar interaction. Notice this is different than the convention used to define the exchange Hamiltonian, where the sum is instead over *all* pairs and the definition of the exchange constants accounts for any double counting of pairs. The $1/R^3$ dependence of the dipole-dipole interaction dictates that it acts at a long range compared to exchange interactions. The dipole-dipole interaction between two magnetic dipole moments scales linearly with *each* of the moment sizes.

For ions with the same magnetic dipole moment, the strength of the dipole-dipole interaction scales with square of the magnetic dipole moment, which varies by a large amount across the $R_2B_2O_7$ pyrochlores. For example, the long-ranged dipole interaction is significantly reduced in both the Ising pyrochlores $Ce_2Zr_2O_7$ and $Nd_2Zr_2O_7$ compared to other Ising pyrochlores $Ho_2Ti_2O_7$ and $Dy_2Ti_2O_7$, as the dipole moments within the CEF ground states doublets in $Ce_2Zr_2O_7$ ($\sim$1.29 μ_B [1, 22]) and $Nd_2Zr_2O_7$ ($\sim$2.65 μ_B [33]) are much smaller than those in $Ho_2Ti_2O_7$ ($\sim$9.85 μ_B [16, 18, 72]) and $Dy_2Ti_2O_7$ ($\sim$9.77 μ_B [18, 48]). Accordingly, the dipole-dipole interaction is $\sim$58 ($\sim$14) times weaker in $Ce_2Zr_2O_7$ ($Nd_2Zr_2O_7$) compared to $Ho_2Ti_2O_7$ and $Dy_2Ti_2O_7$. Of course, the exact numbers here also depend on the different cubic lattice constants in each material, but the lattice constant varies far less than the moment size across these materials (and in the rare-earth pyrochlore in general); We return to a more detailed calculation shortly, using these materials as examples again, and include such finer details as the change in lattice constant between the materials. In general, the relatively small magnetic dipole moment of $Ce_2Zr_2O_7$ results in a particularly weak dipole-dipole interaction strength in $Ce_2Zr_2O_7$ compared to other $R_2B_2O_7$ pyrochlores [11, 16, 24, 33, 48, 72].

The sign of the dipole-dipole interaction between two dipole moments depends on the direction of each dipole moment and the direction of the vector connecting their locations. The strength of the dipole-dipole interaction depends on these vector directions as well, but also depends on the distance between the magnetic moments and the moment sizes, as previously mentioned. For the case of Ising single-ion anisotropy, the vector connecting any two R^{3+} ions can be used to determine sign of the dipole-dipole interaction between the two R^{3+} ions, and the strength of this interaction in terms of the magnetic moment size. In further detail, for the case of Ising single-ion anisotropy, Eq. (1.8) gives $\hat{\boldsymbol{\mu}}_i = -g_z \mu_\mathrm{B} \hat{S}_i^z \mathbf{z}_i$ for each ion i, within the CEF ground state doublet, and the dipole-dipole interaction can be reduced to the effective form [39, 58, 69, 73, 74]:

$$\mathcal{H}_\mathrm{Dipolar,Ising} = \sum_{ij} D_{ij} \hat{S}_i^z \hat{S}_j^z \,, \tag{1.14}$$

which acts within the CEF ground state doublet. The sum is now over *all* pairs of atoms for better comparison with the form of the exchange interactions, and the dipole-dipole interaction parameters are given by [58, 69, 73, 74]:

$$\begin{aligned} D_{ij} &= \frac{\mu_0 (g_z \mu_\mathrm{B})^2}{8\pi R_{ij}^3} \left[(\hat{\mathbf{z}}_i \cdot \hat{\mathbf{z}}_j) - 3(\hat{\mathbf{z}}_i \cdot \hat{\mathbf{R}}_{ij})(\hat{\mathbf{z}}_j \cdot \hat{\mathbf{R}}_{ij}) \right] \\ &= \frac{\mu_0 \mu^2}{2\pi R_{ij}^3} \left[(\hat{\mathbf{z}}_i \cdot \hat{\mathbf{z}}_j) - 3(\hat{\mathbf{z}}_i \cdot \hat{\mathbf{R}}_{ij})(\hat{\mathbf{z}}_j \cdot \hat{\mathbf{R}}_{ij}) \right] , \end{aligned} \tag{1.15}$$

where μ is the magnitude of the magnetic dipole moment within the CEF ground doublet for each ion i, with $\mu = \langle\, ||\hat{\boldsymbol{\mu}}_i||\, \rangle = (g_z/2)\, \mu_\mathrm{B}$ giving the expectation value of the magnetic moment size in the CEF ground state. Here the "hat" symbols on the classical vectors, $\hat{\mathbf{R}}_{ij}$, $\hat{\mathbf{z}}_i$, and $\hat{\mathbf{z}}_j$, are used to denote the fact that these vectors are unit-length.

We calculate D_{ij} for first-, second-, and third-nearest neighbor R^{3+} ions in the pyrochlore lattice and this process shows that, for the case of Ising single-ion anisotropy, the dipole-dipole interaction is ferromagnetic for first-nearest neighbors, antiferromagnetic for second-nearest neighbors, and multi-valued for third-nearest neighbors. Table 1.2

	1^st NN	2^nd NN	3^rd NN
D_{ij}	$+\frac{5\mu_0\mu^2}{6\pi R_\mathrm{NN}^3}$	$-\frac{\mu_0\mu^2}{2\pi R_\mathrm{NN}^3}(\frac{R_\mathrm{NN}}{R_{ij}})^3$	$\pm\frac{\mu_0\mu^2}{2\pi R_\mathrm{NN}^3}(\frac{R_\mathrm{NN}}{R_{ij}})^3$
R_{ij}	R_NN	$\sqrt{3}R_\mathrm{NN}$	$2R_\mathrm{NN}$

Table 1.2: The first row of this table shows our calculated expressions for D_{ij} [Eq. (1.15)] for first-, second-, and third-nearest-neighbor R^{3+} ions in the pyrochlore lattice, in terms of the magnetic moment size for the ions, μ, and the distance between ions, R_{ij}, which is shown in the second row of this table in terms of $R_\mathrm{NN} = a/\sqrt{8}$. Note that the D_{ij} is equal for all six nearest neighbors, and equal for all twelve second-nearest neighbors, but varies in sign across the twelve third-nearest neighbors. As pointed out in Ref. [58], this differing trend for the third-nearest neighbors is due to the fact that for a given ion, i, six of its third-nearest neighbors (denoted at j) have their displacement vector, $\mathbf{R}_{ij}$, perpendicular to both $\hat{\mathbf{z}}_i$ and $\hat{\mathbf{z}}_j$, while the other six of the third-nearest neighbors have $\mathbf{R}_{ij}$ perpendicular to neither $\hat{\mathbf{z}}_i$ or $\hat{\mathbf{z}}_j$.

	D_{ij} for 1st NN	D_{ij} for 2nd NN	D_{ij} for 3rd NN
$Ce_2Zr_2O_7$	5.41 μeV 0.063 K	-0.63 μeV -0.007 K	±0.41μeV ±0.005 K
$Nd_2Zr_2O_7$	0.273 K	0.032 K	±0.020 K
$Dy_2Ti_2O_7$	4.328 K	-0.499 K	±0.325 K
$Ho_2Ti_2O_7$	4.425 K	-0.511 K	±0.332 K

Table 1.3: The calculated values of D_{ij} [Eq. (1.15)] for the first-, second-, and third-nearest neighbors in the Ising pyrochlores $Ce_2Zr_2O_7$, $Nd_2Zr_2O_7$, $Dy_2Ti_2O_7$, and $Ho_2Ti_2O_7$ using the expressions for D_{ij} listed in Table 1.2, in units of temperature (K). Here we use the value of the magnetic dipole moment size in the CEF ground state for each material, from Refs. [1, 16, 18, 22, 33, 48, 72] as outlined in the main text, and the lattice constant $a = 10.73$ Å for $Ce_2Zr_2O_7$ [1], $a = 10.65$ Å for $Nd_2Zr_2O_7$ [1], $a = 10.12$ Å for $Dy_2Ti_2O_7$ [75, 76], and $a = 10.10$ Å for $Ho_2Ti_2O_7$ [76]. For $Ce_2Zr_2O_7$, we also show the calculated values in μeV to ease the comparison with the $Ce_2Zr_2O_7$ interaction parameters elsewhere in this thesis.

shows the calculated expression for D_{ij} for first-, second-, and third-nearest neighbor R^{3+} ions in the pyrochlore lattice. Table 1.3 shows the calculated values of D_{ij} for the first-, second-, and third-nearest neighbors in $Ce_2Zr_2O_7$, $Nd_2Zr_2O_7$, $Dy_2Ti_2O_7$, and $Ho_2Ti_2O_7$. We use this latter table to reiterate that the strength of the dipole-dipole interaction in $Ce_2Zr_2O_7$ is weak, particularly in comparison to other rare-earth pyrochlores such as $Nd_2Zr_2O_7$, $Dy_2Ti_2O_7$, and $Ho_2Ti_2O_7$. Table 1.3 also shows that dipole-dipole interactions beyond nearest neighbor in $Ce_2Zr_2O_7$ are unlikely to have any significant impact on the magnetic behavior at typical experimentally-accessible temperatures, and certainly those include in this thesis (above 0.02 K), while that is not the case for $Nd_2Zr_2O_7$, $Dy_2Ti_2O_7$, and $Ho_2Ti_2O_7$.

Due to the similarity in the form for the exchange interaction Hamiltonian in Eq. (1.11) and the form for the dipole-dipole interaction Hamiltonian for Ising pyrochlores in Eq. (1.14), the dipole-dipole interaction can be absorbed into the definition of the "exchange" parameters for Eq. (1.11), for the case of Ising single-ion anisotropy, as is done throughout this thesis. In fact, it is possible to use Eq. (1.8) to write the dipole-dipole interaction Hamiltonian in terms of the pseudospin operators for any single-ion anisotropy, giving an effective Hamiltonian of the form $\mathcal{H}_{\text{Dipolar}} = \sum_{ij} \sum_u \sum_v D^{ij}_{uv} \hat{S}^u_i \hat{S}^v_j$, where u and v each denote the local directions, $\{x, y, z\}$, for atoms i and j, respectively, similar to the form in Eq. (1.11) for the exchange Hamiltonian and again the dipole-dipole interaction parameters, now written as D^{ij}_{uv}, can be absorbed into the definition of the "exchange" parameters (as was mentioned for general magnetic multipole-multipole interactions, and all other pairwise magnetic interactions, in the previous subsection). Returning to the case of Ising single-ion anisotropy as is relevant for $Ce_2Zr_2O_7$, and comparing the calculated value of D_{ij} for first-nearest neighbors in $Ce_2Zr_2O_7$ (Table 1.3) to the estimated value of the z-component interaction parameter for nearest neighbors in $Ce_2Zr_2O_7$, J_z (from the work in Publication III of this thesis), gives the estimate $J^\star_z = J_z - D_{ij} = 11.3$ μeV $- 5.4$ μeV $= 5.9$ μeV, where $J^\star_z$ is the real exchange parameter for nearest-neighbor z-component interactions (without contribution from the dipole-dipole interaction). Notably, the exchange interaction ($J^\star_z \approx 5.9$ μeV) and dipole-dipole interaction ($D_{ij} \approx 5.4$ μeV) are near equal for the z-components of nearest-neighbors in $Ce_2Zr_2O_7$, with the z-component exchange interaction slightly stronger than the dipole-dipole interaction, according to this analysis.

In fact, the work in Publication III of this thesis also shows evidence for a low-temperature moment-size in $Ce_2Zr_2O_7$ which is $1.12\,\mu_B$ and is slightly reduced from the value of $1.285\,\mu_B$ used in calculating D_{ij} in Table 1.3. Re-evaluation of the previous energies using a moment size of $1.12\,\mu_B$ instead yields: $J_z^\star = 11.3$ μeV − 4.1 μeV = 7.1 μeV, with the z-component exchange interaction ($J_z^\star \approx 7.1$ μeV) dominating more heavily over the dipole-dipole interaction ($D_{ij} \approx 4.1$ μeV) than for the first analysis. This is in contrast to $Ho_2Ti_2O_7$ and $Dy_2Ti_2O_7$ for example, where the dipole-dipole interactions are responsible for the majority of the magnetic interaction between nearest neighbors [70], which is not so surprising considering the relatively large magnetic dipole moments at the Ho^{3+} and Dy^{3+} sites, ∼10 μ_B [16, 18, 48, 72]. In fact, for the case of $Ce_2Zr_2O_7$, the J_z parameter is heavily-dominated by the parameters J_x and J_y, which are each ∼60 μeV and have no contribution from the dipole-dipole interaction [2, 3, 37], as we discuss further in Section 1.5 as well as Publications II and III of this thesis. Similarly, the nearest-neighbor exchange parameters for $Nd_2Zr_2O_7$ have energy scale on the order of 100 μeV [42, 67, 77], which is much larger than the ∼25 μeV (∼0.3 K) calculated for the nearest-neighbor dipole-dipole interaction in $Nd_2Zr_2O_7$ in Table 1.3.

1.4 The Basics of Ising Rare-Earth Pyrochlores and Spin Ices

The purpose of this section is to provide a short introduction to the some of the zero-field magnetic phases that occur in pyrochlores with Ising single-ion anisotropy, before these concepts arise again with added complications in our discussion of the dipole-octupole pyrochlores in the following section. In this section, we will consider only the magnetic dipole moments of the system and ignore the possibility that significant higher-order multipoles may be present and may even have stronger coupling to each other than the dipoles do, and we will consider a case with significant multipole moments in the following section. As discussed in Section 1.2.2, Ising single-ion anisotropy occurs for pyrochlores with a CEF ground state that yields $g_{xy} = 0$ and $g_z \neq 0$ [11, 19, 24, 72], such that the magnetic dipole moments [see Eq. (1.8)] are parallel or anti-parallel to the local z-directions.

For dominant antiferromagnetic nearest-neighbor interactions between dipole moments with Ising single-ion anisotropy, the ground state spin configurations for a single tetrahedron are those in which all of the ions on the tetrahedron have their magnetic dipole moments pointing directly towards the center of the tetrahedron or all of the ions on the tetrahedron have their magnetic dipole moments pointing directly away from the center of the tetrahedron [78, 79]. Fig. 1.6(a) illustrates these all-in, all-out configurations on a pair of corner-sharing tetrahedra. The degeneracy of the all-in state and all-out state for a single tetrahedron does not propagate to a macroscopic degeneracy when considering the full pyrochlore lattice, due to the fact that the corner-sharing nature of the tetrahedral network dictates that neighboring tetrahedra cannot both have all-in configurations or both have all-out configurations, simultaneously. Accordingly, the configuration of magnetic moments alternates from all-in to all-out or vise versa with each pair of neighboring tetrahedra in the pyrochlore lattice (except for domain walls), giving magnetic order. $Sm_2Ti_2O_7$, $Nd_2Hf_2O_7$, and $Nd_2Zr_2O_7$ are each $R_2B_2O_7$ pyrochlores (as defined in Section 1.1) with Ising single-ion anisotropy, $g_{xy} = 0$, in their CEF ground states, and which each display all-in, all-out magnetic dipole order at low

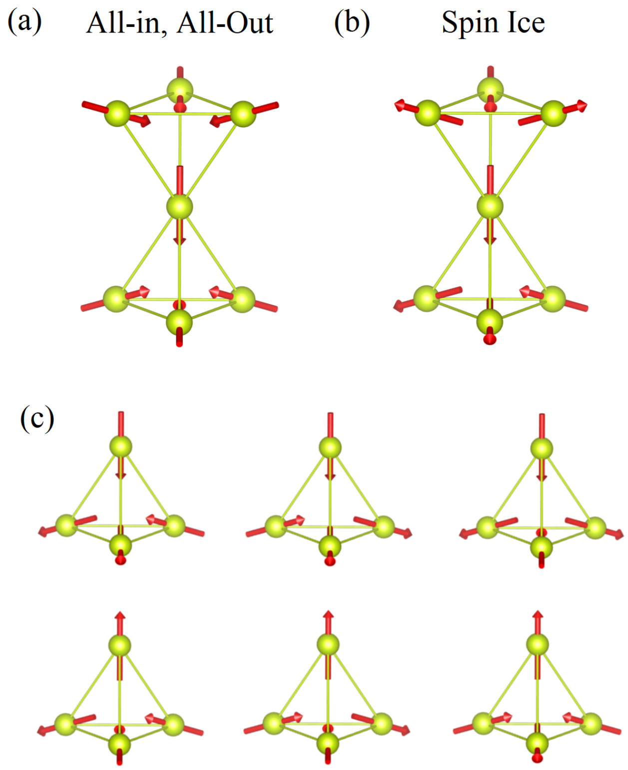

Figure 1.6: Illustrating the different orientations of magnetic dipole moments that are possible in the Ising pyrochlores. (a) A pair of corner-sharing tetrahedra with magnetic dipole moments (red) corresponding to the all-in, all-out magnetic structure. (b) A pair of corner-sharing R^{3+}-tetrahedra with R^{3+} magnetic dipole moments that satisfy the two-in, two-out rule for spin ices. (c) The six different ways to satisfy the two-in, two-out rule for a single tetrahedron. This figure was created using the VESTA visualization software [4].

temperature due to antiferromagnetic coupling between nearest-neighbor dipole moments [23, 33, 34, 80–84].

For heavily-dominant ferromagnetic nearest-neighbor interactions between dipole moments with Ising single-ion anisotropy, the ground state spin configurations for a single tetrahedron are those in which two of the ions on the tetrahedron have their magnetic dipole moments pointing directly towards the center of the tetrahedron and the other two ions on the tetrahedron have their magnetic moments pointing directly away from the center of the tetrahedron [78, 79]. Fig. 1.6(b) shows a pair of two corner-sharing tetrahedra in the pyrochlore lattice with magnetic moments satisfying the two-in, two-out configurations on each tetrahedron. This rule for the energy-minimizing spin configurations is called the *two-in, two-out rule* [69, 79, 85]. Materials governed by this rule are magnetically frustrated (see Fig. 1.1) and the six ways to satisfy the two-in, two-out rule for a single isolated tetrahedron are shown in Fig. 1.6(c). This single-tetrahedron degeneracy leads to a macroscopic degeneracy when considering the full pyrochlore lattice and the number of degenerate states in this two-in, two-out manifold is $(\frac{3}{2})^{\frac{N}{2}}$, where N is the number of R^{3+} ions in the lattice [69, 78, 79, 85, 86]. The corner-sharing nature of the lattice causes this number of degenerate states, $(\frac{3}{2})^{\frac{N}{2}}$, to be less than six states per tetrahedron, but nonetheless, this degeneracy is macroscopic due to its exponential dependence on the number of ions in the lattice.

The two-in, two-out rule maps directly onto the rule describing proton disorder in water ice [69, 78, 79, 85–87], and due to this similarity, materials that obey the two-in, two-out rule are called *spin ices*. $Ho_2Ti_2O_7$ and $Dy_2Ti_2O_7$

are each $R_2B_2O_7$ pyrochlores with Ising single-ion anisotropy ($g_{xy} = 0$ [16, 18, 24, 48]) in their CEF ground states, and which each display disordered spin ice phases at low temperature due to ferromagnetic coupling between nearest-neighbor dipole moments in these materials. $\mathrm{Ho_2Ti_2O_7}$ and $\mathrm{Dy_2Ti_2O_7}$ were the first spin ices to be discovered and are examples of classical spin ices due to the lack of significant quantum fluctuations in these materials [39, 69, 70, 79, 85, 88, 89]. The lack of significant quantum fluctuations and the corresponding, approximately-classical nature of these spin ices results from the small magnitude of coupling between x- and y- components of pseudospin compared the coupling between z-components of pseudospin, as mentioned in Section 1.3.1, and we further discuss quantum fluctuations in spin ice materials in the following section. The classical ground state degeneracy with $(\frac{3}{2})^{\frac{N}{2}}$ degenerate two-in, two-out states leads to a prediction for the entropy and gives $S_0 = \frac{R}{2}\ln\frac{3}{2}$ for the residual entropy in the low-temperature classical spin ice phase, where $R = 8.314\ \mathrm{J\cdot K^{-1}\cdot mol}^{-1}_{R^{3+}}$ is the molar gas constant with respect to the R^{3+} ions. This residual entropy has been detected experimentally, via heat capacity measurements, to within a few percent for both $\mathrm{Dy_2Ti_2O_7}$ and $\mathrm{Ho_2Ti_2O_7}$ [85, 90], as well as in the analogous case of water ice where the expected entropy is again $\frac{R}{2}\ln\frac{3}{2}$ but with $R = 8.314\ \mathrm{J\cdot K^{-1}\cdot mol}^{-1}_{\mathrm{H}}$ as the appropriate molar gas constant in that case.

In general, spin ices have become a very popular topic due to the wealth of interesting physics that accompanies these disordered phases; Reviews on spin ice are available in Refs. [10, 69, 71] to provide a few examples. In further detail, the classical spin ices have gained a large amount of acclaim due to the fact that spin-flip excitations resulting in three-in, one-out, or one-in, three-out, tetrahedra can be described as magnetic monopoles at the center of the excited tetrahedra [88, 89, 91, 92]. In this emergent electrodynamics description, these monopoles interact via a magnetic coulomb law with interaction energy $\propto Q_1Q_2/r$ where r is the distance between monopoles and Q_1 and Q_2 are their "charges" [88, 89, 91, 92]. These monopoles arise as pairs of monopoles with opposite emergent charge, corresponding to the fact that flipping a spin to generate a three-in, one-out tetrahedra also generates a one-in, three-out tetrahedra for the second tetrahedron that the spin is a part of, or vise-versa. In the case of *quantum* spin ices, the significance of x- and y-based terms in the Hamiltonian leads to a similar, again rare, emergent quantum electrodynamics description in which the "electric field" associated with the z-component of pseudospin is accompanied by a "magnetic field" associated with the x- and y-components of pseudospin [10, 47, 51, 93–95], as we discuss in further detail in the following section.

In terms of the local z-directions, the two-in, two-out rule corresponds to two magnetic dipole moments along their local $+z$-directions and two magnetic moments along their local $-z$-directions for each tetrahedron (see Table 1.1). Similarly, all-in, all-out magnetic order corresponds to tetrahedra that have all magnetic moments along their local $+z$-directions or all magnetic moments along their local $-z$-directions [52].

The dipole-octupole pyrochlores, which we discuss in the following section, have Ising single-ion anisotropy in their CEF ground states, but in general, also have significant interactions between higher-order multipoles, beyond dipoles, such that the phases and concepts discussed in this section also arise in the context of dipole-octupole pyrochlores but with adjusted and expanded forms.

‘

1.5 Dipole-Octupole Rare-Earth Pyrochlores

1.5.1 Single-ion Properties in Dipole-Octupole Rare-Earth Pyrochlores

As discussed in Section 1.2.2, when the CEF ground state is a doublet that is well-separated in energy from the first excited CEF state, the low-temperature magnetism can be accurately-described using the pseudospin-1/2 formalism which approximates the magnetic degrees of freedom of each ion using pseudospin-1/2 operators given by Eqs. (1.5)-(1.7) [11, 12]. In such cases, the rare-earth pseudospins inherit their symmetry properties from the CEF ground state doublet and these properties govern the allowed nonzero terms in the Hamiltonian that describes the interactions between the pseudospins (see Section 1.3.1). As mentioned in Sections 1.2.2 and 1.3.1, there are three possible symmetry classifications that arise in the rare-earth pyrochlores, based on how the pseudospin-1/2 degrees of freedom transform under the D_{3d} symmetry operations and time-reversal symmetry [12, 49–53].

The main focus of this thesis is the dipole-octupole pyrochlore $Ce_2Zr_2O_7$, where the $|J = 5/2,\ m_J = \pm 3/2\rangle$ CEF ground state doublet estimated for Ce^{3+} in $Ce_2Zr_2O_7$ (Refs. [1, 22]) has dipole-octupole symmetry [51, 52]. Dipole-octupole symmetry corresponds to x- and z-components of pseudospin, $\hat{S}^x$ and $\hat{S}^z$, that transform like magnetic dipoles under the R^{3+} site symmetries and time-reversal symmetry, and a y-component of pseudospin, $\hat{S}^y$, that transforms like a magnetic octupole. This difference in symmetry for the pseudospin components in the dipole-octupole pyrochlores is illustrated in Fig. 1.7(a) using the magnetic charge distributions associated with different directions of pseudospin in the in yz-plane. More generally, a pseudospin in the xz-plane ($\pm y$-direction) of pseudospin-space has

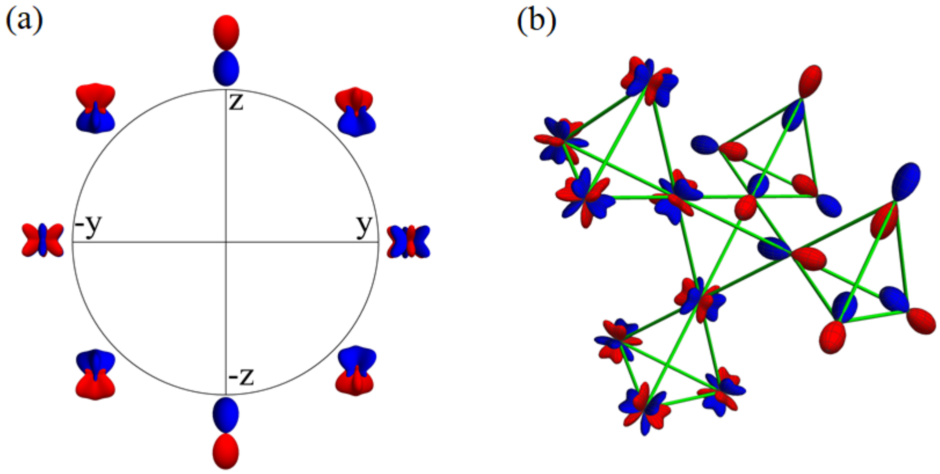

Figure 1.7: A representation of the symmetry of the dipolar and octupolar pseudospin-components in the pyrochlore lattice using their associated magnetic charge distributions. (a) The magnetic charge distributions associated with different pseudospin directions in the local yz plane. For pseudospins in the yz-plane, a pseudospin along the $\pm z$ ($\pm y$) direction has pure dipolar (octupolar) symmetry and pseudospins that are not directly along $\pm y$ or $\pm z$ have mixed dipolar and octupolar symmetry. (b) The magnetic charge distributions for an assortment of dipoles (right) and octupoles (left) located at R^{3+} sites of the pyrochlore lattice. This figure has been reproduced from Ref. [2] with permission copyrighted by the American Physical Society.

Component	Symmetry	Magnetic Moment
$\hat{S}^x$	Dipolar $\mathcal{T}$: $-\hat{S}^x$, $\mathcal{C}_3$: $\hat{S}^x$, $\mathcal{I}$: $\hat{S}^x$, $\mathcal{M}$: $-\hat{S}^x$	Octupolar $\hat{\mu}^x_{\text{Oct}} \propto \mathcal{P}\left(\hat{J}_x^3 - \frac{1}{3}(\hat{J}_x\hat{J}_y^2 + \hat{J}_y\hat{J}_x\hat{J}_y + \hat{J}_y^2\hat{J}_x)\right)\mathcal{P} = C_x\hat{S}^x$
$\hat{S}^y$	Octupolar $\mathcal{T}$: $-\hat{S}^y$, $\mathcal{C}_3$: $\hat{S}^y$, $\mathcal{I}$: $\hat{S}^y$, $\mathcal{M}$: $\hat{S}^y$	Octupolar $\hat{\mu}^y_{\text{Oct}} \propto \mathcal{P}\left(\hat{J}_y^3 - \frac{1}{3}(\hat{J}_y\hat{J}_x^2 + \hat{J}_x\hat{J}_y\hat{J}_x + \hat{J}_x^2\hat{J}_y)\right)\mathcal{P} = C_y\hat{S}^y$
$\hat{S}^z$	Dipolar $\mathcal{T}$: $-\hat{S}^z$, $\mathcal{C}_3$: $\hat{S}^z$, $\mathcal{I}$: $\hat{S}^z$, $\mathcal{M}$: $-\hat{S}^z$	Dipolar $\hat{\mu}^z_{\text{Dip}} \propto \mathcal{P}\hat{J}_z\mathcal{P} = C_z\hat{S}^z$

Table 1.4: The symmetry and multipolar magnetic moment associated with each of the three pseudospin components, $\hat{S}^x$, $\hat{S}^y$, and $\hat{S}^z$, for the dipole-octupole pyrochlores [12, 51, 52, 96, 97]. Each pseudospin component transforms identically under the time-reversal symmetry operation, $\mathcal{T}$. The symmetry elements corresponding to the D_{3d} point group can be generated by the operations, $\mathcal{C}_3$, $\mathcal{I}$, and $\mathcal{M}$, where $\mathcal{C}_3$ is a three-fold rotation along the z-direction, $\mathcal{I}$ is the inversion operation, and $\mathcal{M}$ is the mirror-plane that takes the $+x$ and $+y$ directions to the $-y$ and $-x$ directions respectively [51]. Each pseudospin component transforms identically under $\mathcal{C}_3$ and $\mathcal{I}$ and the transformation under $\mathcal{M}$ is what distinguishes the symmetry of the pseudospin components in this basis for the D_{3d} point group, with $\hat{S}^x$ and $\hat{S}^z$ transforming like the z-component of a magnetic dipole and $\hat{S}^y$ transforming the component of a magnetic octupole tensor [51]. The rightmost column in the table shows the multipolar magnetic moments carried by each pseudospin component, where $\mathcal{P} = |-\rangle\langle-| + |+\rangle\langle+|$ is the projection operator that projects into the basis of the CEF ground state doublet [15, 31, 53, 97], and C_x, C_y, and C_z are constants with values that depend on the composition of the CEF ground state doublet, $|\pm\rangle$, in terms of the $|J, m_J\rangle$ eigenstates of $\hat{J}^2$ and $\hat{J}_z$. The expression for the dipole moment carried by $\hat{S}^z$ also follows from Eq. (1.8) with $g_{xy} = 0$.

pure dipolar (octupolar) symmetry, and pseudospins that are not directly along the $\pm y$ direction or in the xz-plane have mixed dipolar and octupolar symmetry. We also use the representation of the symmetry via magnetic charge distributions to provide an example of pure-dipoles and pure-octupoles on the pyrochlore lattice in Fig. 1.7(b). In reality, pseudospins do not point along actual directions in real space as the previous phrasing may suggest [see Eqs. (1.5)-(1.7)], but a visualization as such is permitted if one keeps in mind that, for example, a pseudospin along the $+z$ direction should be taken to mean that $\langle\hat{S}^z\rangle > 0$ and $\langle\hat{S}^x\rangle$, $\langle\hat{S}^y\rangle = 0$ for that pseudospin.

An interesting and important feature to mention about the dipole-octupole pyrochlores is that, while $\hat{S}^x$ has dipolar symmetry, it carries an octupolar magnetic moment in the x-direction. This is different from both $\hat{S}^y$ and $\hat{S}^z$ where the multipolar nature of the magnetic moment is the same as the symmetry in each case. That is, $\hat{S}^y$ carries an octupolar magnetic moment and $\hat{S}^z$ carries a dipolar magnetic moment. The different symmetries and multipolar magnetic moments for the pseudospin-1/2 components in the dipole-octupole pyrochlores are summarized in Table 1.4. All dipole-octupole doublets yield an Ising single-ion anisotropy ($g_{xy} = 0$, $g_z \neq 0$) with the magnetic dipole moment along the local $\pm z$-direction, simply due to the fact that only the z-component of pseudospin carries a dipole moment.

1.5.2 Interactions and Phases in Dipole-Octupole Rare-Earth Pyrochlores

Along with the symmetry of the CEF ground state imprinting itself on pseudospin-1/2 degrees of freedom, this symmetry is also represented in the general form of the microscopic spin Hamiltonian that describes the interactions between these pseudospin-1/2 degrees of freedom [12]. In other words, the symmetry of the pseudospins and underlying CEF ground state doublet governs the allowed nonzero terms in the exchange Hamiltonian, as outlined in Section 1.3.1. The general form of the exchange Hamiltonian for dipole-octupole pyrochlores at the nearest-neighbor level is given by [51]:

$$\mathcal{H}_{\rm DO} = \sum_{<ij>} [(J_x \hat{S}_i^x \hat{S}_j^x + J_y \hat{S}_i^y \hat{S}_j^y + J_z \hat{S}_i^z \hat{S}_j^z) + J_{xz}(\hat{S}_i^x \hat{S}_j^z + \hat{S}_i^z \hat{S}_j^x)] - \sum_i g_z \mu_{\rm B} (\mathbf{h} \cdot \hat{\mathbf{z}}_i) \hat{S}_i^z \ , \tag{1.16}$$

where $\hat{S}_i^\alpha$ ($\alpha = x,\ y,\ z$) are the pseudospin-1/2 components of rare-earth atom i in the local $\{x, y, z\}$ coordinate frame as given by Eq. (1.5)-(1.7). The second sum in Eq. (1.16) represents the Zeeman interactions between the magnetic dipole moments of the R^{3+} ions and the magnetic field, where the magnetic field is denoted as $\mathbf{h}$ and $\hat{\mathbf{z}}_i$ is the local z axis for ion i (see Table 1.1). The constant g_z is determined via Eq. (1.9) which gives $g_z = 2.57$ for the pure $|J = 5/2,\ m_J = \pm 3/2\rangle$ ground state doublet estimated for Ce^{3+} in Ce$_2$Zr$_2$O$_7$ [1, 22].

Another form of this dipole-octupole Hamiltonian [Eq. (1.16)] can be arrived at by applying the specific rotation of local axes that removes the J_{xz} coupling term, yielding the XYZ Hamiltonian [51, 52]. Specifically, this requires a rotation of the local frame about the y-axis by an amount θ, where θ is given by [42, 51, 52]:

$$\theta = \frac{1}{2} \tan^{-1} \left(\frac{2J_{xz}}{J_x - J_z} \right), \tag{1.17}$$

Rotating the local $\{x, y, z\}$ coordinate frame by θ about the y-axis yields a new coordinate frame which is commonly denoted as $\{\tilde{x}, \tilde{y}, \tilde{z}\}$. This transformation yields the pseudospin relations [51, 52]:

$$\hat{S}_i^{\tilde{x}} = \hat{S}_i^x \cos\theta + \hat{S}_i^z \sin\theta, \tag{1.18}$$

$$\hat{S}_i^{\tilde{y}} = \hat{S}_i^y, \tag{1.19}$$

$$\hat{S}_i^{\tilde{z}} = -\hat{S}_i^x \sin\theta + \hat{S}_i^z \cos\theta, \tag{1.20}$$

The new Hamiltonian in the $\{\tilde{x}, \tilde{y}, \tilde{z}\}$ coordinate frame, the XYZ Hamiltonian, is given by [51, 52]:

$$\mathcal{H}_{\rm XYZ} = \sum_{<ij>} [J_{\tilde{x}} \hat{S}_i^{\tilde{x}} \hat{S}_j^{\tilde{x}} + J_{\tilde{y}} \hat{S}_i^{\tilde{y}} \hat{S}_j^{\tilde{y}} + J_{\tilde{z}} \hat{S}_i^{\tilde{z}} \hat{S}_j^{\tilde{z}}] - g_z \mu_{\rm B} \sum_i (\mathbf{h} \cdot \hat{\mathbf{z}}_i)(\hat{S}_i^{\tilde{z}} \cos\theta + \hat{S}_i^{\tilde{x}} \sin\theta) \ , \tag{1.21}$$

where the nearest-neighbor exchange constants in $\mathcal{H}_{\rm XYZ}$ are related to those in $\mathcal{H}_{\rm DO}$ through the equations,

$$J_{\tilde{x}} = \frac{1}{2}\Big(J_x + J_z + \sqrt{4J_{xz}^2 + (J_x - J_z)^2} \Big), \tag{1.22}$$

$$J_{\tilde{y}} = J_y, \tag{1.23}$$

$$J_{\tilde{z}} = \frac{1}{2}\Big(J_x + J_z - \sqrt{4J_{xz}^2 + (J_x - J_z)^2} \Big). \tag{1.24}$$

The XYZ Hamiltonian in Eq. (1.21) is used throughout this thesis due to the fact that the lack of J_{xz}-coupling compared to Eq. (1.16) results in a simpler expression for the Hamiltonian in zero-field. However, the field-dependent term in the Hamiltonian becomes more complicated in the transformed coordinate system due to the fact that neither the $\tilde{x}$ or $\tilde{z}$ direction is necessarily along the direction of the magnetic dipole-moment of the ion, whereas the local z direction is along the direction of the magnetic dipole at that site, making the field-dipole coupling term simpler in Eq. (1.16) compared to Eq. (1.21).

Transformation to the XYZ Hamiltonian is particularly useful for investigating the zero-field magnetic ground state phase diagram. The zero-field magnetic ground state phase diagram for the XYZ Hamiltonian is known to contain six distinct phases with two of which being ordered phases and four of which being U(1) quantum spin liquid phases with low-energy physics that mimics the theory of quantum electrodynamics [56, 57, 96–98]. The two ordered phases are distinguishable by the dipolar or octupolar symmetry of their order parameter, and the four quantum spin liquid phases are distinguishable by the dipolar or octupolar symmetry of their emergent electric field as well as by their emergent flux on a hexagonal plaquette of the lattice, which can be 0 or π.

The quantum spin liquid ground states occur when the dominant exchange parameter is positive (ferromagnetic) and much stronger than the largest negative exchange parameter; In the classical phase diagram, the spin liquid states occur when the dominant exchange parameter is positive and is more than three times the size (in absolute value) of the largest negative exchange parameter [96, 99]. A spin liquid ground state of the XYZ Hamiltonian has octupolar nature if $|J_{\tilde{y}}| > |J_{\tilde{x}}|, |J_{\tilde{z}}|$ and dipolar nature if $|J_{\tilde{z}}| > |J_{\tilde{y}}|$ or $|J_{\tilde{x}}| > |J_{\tilde{y}}|$ [2]. A dipolar (octupolar) spin liquid has the $\tilde{x}$ or $\tilde{z}$ (the $\tilde{y}$) components of pseudospin, with dipolar (octupolar) symmetry, associated with the emergent electric field in the emergent quantum electrodynamics description that is often used for quantum spin ices [56, 96, 98]. These quantum spin liquids are each governed by a "two-plus, two-minus rule" rule for the component of pseudospin associated with the most dominant exchange parameter and the emergent electric field [56, 96, 98], analogous to the conventional two-in, two-out rule [Fig. 1.6(b,c)] for the dipole moments associated with the z components of pseudospin in conventional spin ices [39, 69, 70, 79, 85, 88, 89]. Specifically, the two-plus, two-minus rule governs the behavior of $\hat{S}^{\alpha}$, where $\alpha = \tilde{x}$, $\tilde{y}$, or $\tilde{z}$ and J_{α} is positive and is the dominant exchange parameter; The two-plus, two-minus dictates that $\langle \hat{S}^{\alpha} \rangle$ is positive for two rare-earth ions in each tetrahedron and negative for the other two rare-earth ions in each tetrahedron. In further detail, each of these quantum spin liquids can be obtained by adding quantum fluctuations to a classical phase adhering to the two-plus, two-minus rule for the component of pseudospin associated with the dominant exchange parameter [51, 52, 56, 57, 96–98], similar to the addition of quantum fluctuations to the two-in, two-out rule for the z components of pseudospin in conventional spin ices [10, 47, 51, 93–95]. Because of these similarities, we refer to these U(1) quantum spin liquids as quantum spin ice (QSI) phases. In fact, in the special case of a spin ice with $\theta = 0$ and $J_{\tilde{z}}$ as the dominant exchange parameter, the relevant two-plus, two-minus rule *is* the conventional two-in, two-out rule.

The ordered ground states occur when there exists a negative (antiferromagnetic) exchange parameter that it is not strongly dominated by some positive exchange parameter; In the classical phase diagram, the ordered states occur when the most-dominant negative exchange parameter is more than a third of the size (in absolute value) of the largest positive exchange parameter [96, 99]. An ordered phase has octupolar nature if $J_{\tilde{y}} < J_{\tilde{x}}, J_{\tilde{z}}$ and dipolar nature if $J_{\tilde{z}} < J_{\tilde{y}}$ or $J_{\tilde{x}} < J_{\tilde{y}}$ [2]. A dipolar (octupolar) ordered phase has the $\tilde{x}$ or $\tilde{z}$ (the $\tilde{y}$) components of pseudospin, with dipolar (octupolar) symmetry, associated with the order parameter [56, 96, 98]. These ordered phases display an "all-plus, all-minus" ordering of the pseudospin-component associated with the most dominant negative exchange parameter, analogous to conventional all-in, all-out magnetic order [Fig. 1.6(a)] for the dipole moments associated with the z components of pseudospin in a conventional all-in, all-out ordered phase. Specifically, in these all-plus, all-minus ordered phases, the ordered component of the pseudospin is $\hat{S}^{\alpha}$, where $\alpha = \tilde{x}$, $\tilde{y}$, or $\tilde{z}$ and J_{α} is the largest negative exchange parameter in terms of absolute value; $\hat{S}^{\alpha}$ exhibits a magnetic order with $\langle \hat{S}^{\alpha} \rangle$ either positive for all four rare-earth ions in each tetrahedron or negative for all four rare-earth ions in each tetrahedron, with alternation between positive and negative for neighboring tetrahedra due to the corner-sharing nature of the lattice.

For both the ordered phases and the spin ice phases, the $J_{\tilde{x}}$- and $J_{\tilde{z}}$-dominated ground states are smoothly-connected to one another by the parameter θ and so they do not represent distinct phases. Accordingly, we do not distinguish between the spin ice phases appearing for large, positive $J_{\tilde{x}}$ and the spin ice phases appearing for large, positive $J_{\tilde{z}}$, or between the ordered phases appearing for large, negative $J_{\tilde{x}}$ and the ordered phases appearing for

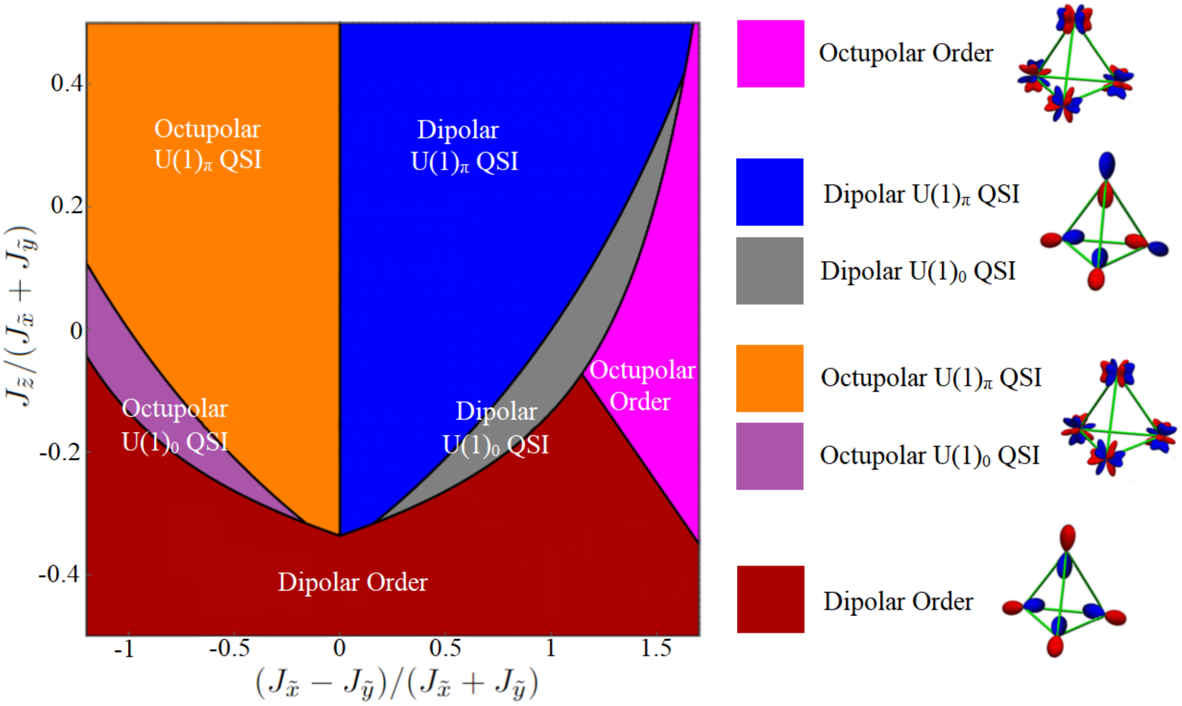

Figure 1.8: The zero-field magnetic ground state phase diagram for the XYZ Hamiltonian [Eq. (1.21)] which is relevant to dipole-octupole pyrochlores at the nearest-neighbor level, along with illustrations of the different phases present in the diagram using magnetic charge distributions to represent the symmetry of the pseudospins (see Fig. 1.7). Six phases in total are present in this ground state phase diagram: two ordered phases which are distinguishable by the dipolar or octupolar symmetry of their corresponding order parameter, and four QSI phases which are distinguishable by the dipolar or octupolar symmetry of their corresponding emergent electric field, and by the emergent flux that is generated when a spinon travels around hexagonal loop in the pyrochlore lattice, which can be 0 or π. The emergent flux of a spinon around a hexagon is not considered in the phase representations shown in this figure (see Section 1.5.3). The phase diagram in this figure uses calculations from Ref. [56] and has been adapted from Ref. [3] with permission copyrighted by the American Physical Society.

large, negative $J_{\tilde{z}}$.

The magnetic ground state phase diagram for the XYZ Hamiltonian, as determined from Ref. [56], is shown in Fig. 1.8, which shows the large amount of phase space inhabited by the quantum spin ice ground states. We show this phase diagram alongside a representation of the ground-state phases using magnetic charge distributions to illustrate the dipolar and octupolar symmetries of the pseudospin components. The representation using magnetic charge distributions on a single tetrahedron gives no distinction between 0-flux and π-flux quantum spin ices of the same symmetry and we instead discuss the distinction between 0-flux and π-flux quantum spin ices further in the following subsection. We defer our discussion of magnetic phases in dipole-octupole pyrochlores in nonzero magnetic field until Chapter 3, where we discuss some of the magnetic phases that can exist in magnetic fields along the $[1, \bar{1}, 0]$ and $[1, 0, 0]$ crystallographic axes.

1.5.3 The Distinction Between 0-flux and π-flux Quantum Spin Ice Phases

The distinction between the 0-flux and π-flux quantum spin ice phases arises through details of the quantum fluctuations in these phases. Specifically, the lowest order quantum effects originate through a ring-exchange term which flips pseudospins on specific hexagons in the pyrochlore lattice and the two possibilities of sign for the effective exchange constant of this term, g_{eff}, ultimately lead to the distinction between the 0-flux and π-flux quantum spin ice phases [37, 44, 52, 57, 93, 100, 101]. This ring exchange term acts on specific hexagons where the component of pseudospin associated with the two-plus, two-minus rule has an expectation value with alternating sign around the hexagon. For these specific hexagons, the ring exchange takes the collection of tetrahedra forming the hexagon from one state to another within the macroscopically degenerate two-plus, two-minus manifold. In further detail, if the system is in a spin ice phase and the dominant exchange parameter is J_α, where $\alpha = \tilde{x}$, $\tilde{y}$, or $\tilde{z}$, then the role of J_α is to enforce the two-plus, two-minus rule for the $\hat{S}^\alpha$ components of pseudospin and quantum fluctuations enter in through J_β and J_γ where β and γ denote the local-axes of $\tilde{x}$, $\tilde{y}$, and $\tilde{z}$ that are perpendicular to the local α direction. The spin Hamiltonian can be separated into a classical spin ice term $\mathcal{H}_{\mathrm{CSI}} = \sum_{<ij>} J_\alpha \hat{S}_i^\alpha \hat{S}_j^\alpha$, with ground states that correspond to the degenerate, classical manifold of two-plus, two-minus states, and a quantum term $\mathcal{H}_{\beta\gamma} = \sum_{<ij>} (J_\beta \hat{S}_i^\beta \hat{S}_j^\beta + J_\gamma \hat{S}_i^\gamma \hat{S}_j^\gamma)$. Degenerate perturbation theory (see Ref. [15] for example) can be applied on the quantum term to yield an effective Hamiltonian which acts within the ground-state manifold of two-plus, two-minus states [35, 37, 44, 52, 57, 93, 100, 101]:

$$\mathcal{H}_{\mathrm{ring}} = g_{\mathrm{eff}} \sum_{\hexagon} \left(\hat{S}_1^{\tilde{+}} \hat{S}_2^{\tilde{-}} \hat{S}_3^{\tilde{+}} \hat{S}_4^{\tilde{-}} \hat{S}_5^{\tilde{+}} \hat{S}_6^{\tilde{-}} + \hat{S}_6^{\tilde{+}} \hat{S}_5^{\tilde{-}} \hat{S}_4^{\tilde{+}} \hat{S}_3^{\tilde{-}} \hat{S}_2^{\tilde{+}} \hat{S}_1^{\tilde{-}} \right) \quad , \tag{1.25}$$

where the sum is over the different hexagonal plaquettes in the pyrochlore lattice with $j = \{1, 2, 3, 4, 5, 6\}$ denoting the six ions forming a hexagon. The pseudospin ladder operators here are redefined as $\hat{S}_{\mathrm{j}}^{\tilde{\pm}} = \hat{S}_{\mathrm{j}}^\beta \pm \hat{S}_{\mathrm{j}}^\gamma$ in Eq. (1.25) and for the discussions in this section due to the convenient form that results for $\mathcal{H}_{\mathrm{ring}}$, and in accordance with the fact that the quantum fluctuations arise through J_β and J_γ when J_α is dominant. The ring exchange Hamiltonian, $\mathcal{H}_{\mathrm{ring}}$, flips spins on hexagons where $\langle \hat{S}^\alpha \rangle$ alternates in sign around the hexagon [Fig. 1.9] and yields zero otherwise.

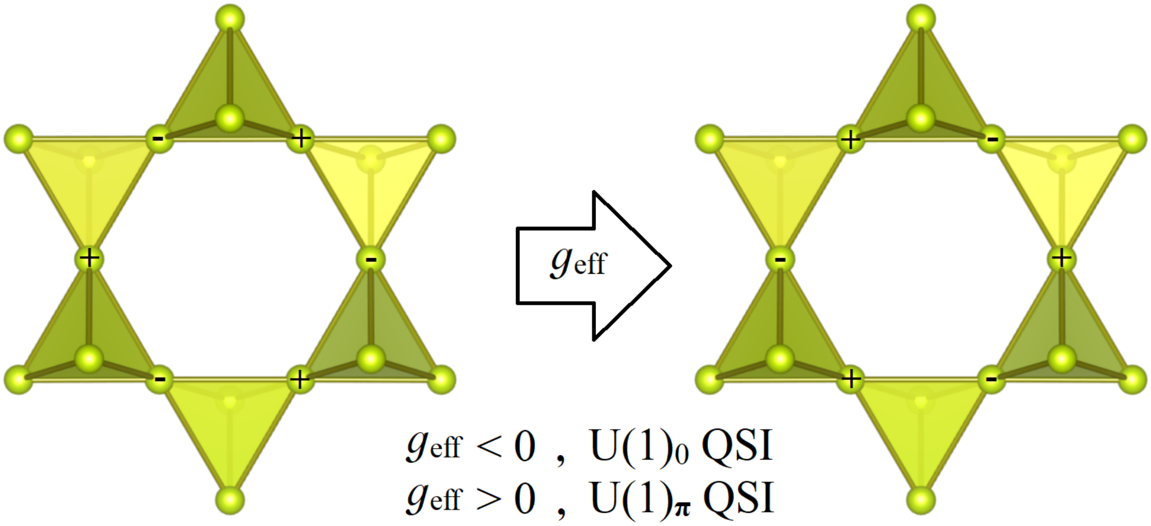

Figure 1.9: A loop of six corner-sharing tetrahedra in the pyrochlore lattice, shown in a plane perpendicular to the $[1,1,1]$ direction. This is the shortest loop of tetrahedra possible for the pyrochlore lattice. The R^{3+} triangles perpendicular to the $[1,1,1]$ direction form a Kagome lattice with corner-sharing-triangular geometry that is highly susceptible to magnetic frustration [7, 8]. The inner-most R^{3+} ions form a hexagon which supports quantum fluctuations between different two-plus, two-minus configurations for the dipolar and octupolar U(1) QSIs present in the phase space of the dipole-octupole pyrochlores, and between different two-in, two-out configurations for conventional QSIs in non-DO pyrochlores. The positive and negative signs denote the sign of the expectation value of pseudospin component associated with the two-plus, two-minus rule and we show this for a collection of tetrahedra for which this pseudospin component has expectation value that is alternating in sign around the inner hexagon, which permits pseudospin-flipping by the ring exchange Hamiltonian (see main text). The sign of the effective exchange constant for this ring exchange, g_{eff}, governs the flux of the gauge field through this hexagon in the emergent quantum electrodynamics description used for quantum spin ices, yielding a 0-flux quantum spin ice for $g_{\mathrm{eff}} < 0$ and a π-flux quantum spin ice for $g_{\mathrm{eff}} > 0$. This figure was created using the VESTA visualization software [4].

In the emergent quantum electrodynamics description that is often used to describe quantum spin ices, the component of pseudospin governed by the two-plus, two-minus rule is associated with the emergent electric field such that $\mathcal{H}_{\mathrm{CSI}} \propto J_\alpha \sum_{<ij>} \hat{E}_i \hat{E}_j$, where $\hat{E}_i$ denotes the emergent electric field of the rare-earth ion at site i in the pyrochlore lattice [44, 51, 52, 56, 102]. Similarly, in this description, the effective Hamiltonian describing the ring exchange can be written as [37, 44, 51, 52, 93, 102]:

$$\mathcal{H}_{\mathrm{ring}} = 2 g_{\mathrm{eff}} \sum_{\varhexagon} \cos(\nabla_{\varhexagon} \times \mathbf{A}) \quad , \tag{1.26}$$

where $\nabla_{\varhexagon} \times \mathbf{A}$ represents the emergent gauge flux through a hexagonal loop in the pyrochlore lattice. For $g_{\mathrm{eff}} < 0$ ($g_{\mathrm{eff}} > 0$), $\mathcal{H}_{\mathrm{ring}}$ is minimized when $\nabla_{\varhexagon} \times \mathbf{A}$ has the expectation value of 0 (π) for each hexagon where $\langle \hat{S}^\alpha \rangle$ alternates in sign around the hexagon, giving the distinction between 0- and π-flux quantum spin ices based on the value of the emergent gauge flux through each flippable hexagonal loop and on the underlying sign of g_{eff}, which governs the value of that flux.

Evaluation of $\mathcal{H}_{\mathrm{ring}}$ to the lowest non-vanishing order via degenerate perturbation theory results in the approximation: $g_{\mathrm{eff}} = -12 J_{\pm}^3 / J_\alpha^2$, where $J_{\pm} = -\frac{1}{4}(J_\beta + J_\gamma)$ [100]. In this limit, $J_\beta + J_\gamma < 0$ results in a U(1)$_0$ QSI, and $J_\beta + J_\gamma > 0$ gives a U(1)$_\pi$ QSI. This approximation can be improved using a variational extension to cluster mean-field theory [56], which leads to the 0- and π-flux phase boundaries shown in Fig. 1.8. This boundary is indeed near the $J_\beta + J_\gamma = 0$ boundary that exists in the aforementioned perturbative limit, although this is easier to see from the reduced ground state phase diagram that we introduce in the following section. The reader is encouraged to find further details on this phase boundary, and calculations used to investigate it, in Refs. [51, 56, 57, 96–98, 100]. In fact, this distinction between 0- and π-flux phases exists for effective spin-1/2 (see Ref. [35]) and non-Kramers (see Ref. [44]) quantum spin ices as well, where degenerate perturbation theory gives analogous results to those for the dipole-octupole pyrochlores and again, a clear distinction between 0- and π-flux phases exists based on the sign of the effective ring-exchange constant.

1.5.4 The Reduced Ground State Phase Diagram for Dipole-Octupole Pyrochlores

Since some physical quantities have no directional dependence, such as the heat capacity in zero magnetic field for example, it can be convenient to introduce a reduced form the XYZ Hamiltonian and a corresponding reduced ground state phase diagram to be used for fitting directional-independent quantities and interpreting the results. Put simply, directional-independent quantities depend only on the values of the exchange parameters and not on which parameters describe which directions. Therefore, the size of the phase space can be reduced by defining axes $\{a, b, c\}$ to be the permutation of $\{\tilde{x},\ \tilde{y},\ \tilde{z}\}$ such that $|J_a| \geq |J_b|, |J_c|$ and $J_b \geq J_c$. For the resulting Hamiltonian, the ABC Hamiltonian,

$$\mathcal{H}_{\mathrm{ABC}} = \sum_{<ij>} [J_a \hat{S}_i^a \hat{S}_j^a + J_b \hat{S}_i^b \hat{S}_j^b + J_c \hat{S}_i^c \hat{S}_j^c] \ , \tag{1.27}$$

it is assumed that the permutation relating $\{a, b, c\}$ and $\{\tilde{x},\ \tilde{y},\ \tilde{z}\}$ is unknown as would be the case without prior knowledge of the exchange parameters. Accordingly, the values of J_a, J_b, and J_c provide no information on the dipolar or octupolar symmetry of the corresponding ground state. The result of the transformation is a ground state phase diagram for the ABC Hamiltonian that is more vague than that of the XYZ Hamiltonian, but over a smaller phase space in comparison to the XYZ Hamiltonian, as shown in Fig. 1.10. The typical approach in using the ABC Hamiltonian is to fit directional-independent data to determine values of J_a, J_b, and J_c before fitting directional-*dependent* data using the XYZ Hamiltonian with $J_{\tilde{x}}$, $J_{\tilde{y}}$, and $J_{\tilde{z}}$ equal to different permutations of the best-fit J_a, J_b, and J_c [2, 3, 60].

The fitting of J_a, J_b, and J_c is often done using the magnetic heat capacity [2, 3, 60], as it has significant sensitive to all pseudospin components such that in general it is not strongly-dominated by the signal from the single component of pseudospin carrying a magnetic dipole moment, $\hat{S}^z$, as is the case for many experimental techniques and probes [52, 103]. In further detail, the type of multipolar magnetic moment carried by each pseudospin component dictates how that component couples to a magnetic field and to experimental probes [52, 103]. This is particularly relevant for probes with an underlying reliance on the coupling to the magnetic field or on the dipole-dipole interaction, such as magnetic susceptibility measurements and magnetic neutron scattering respectively, and those with an underlying reliance on measurement of the magnetic field from the sample (due to the exceedingly short-ranged

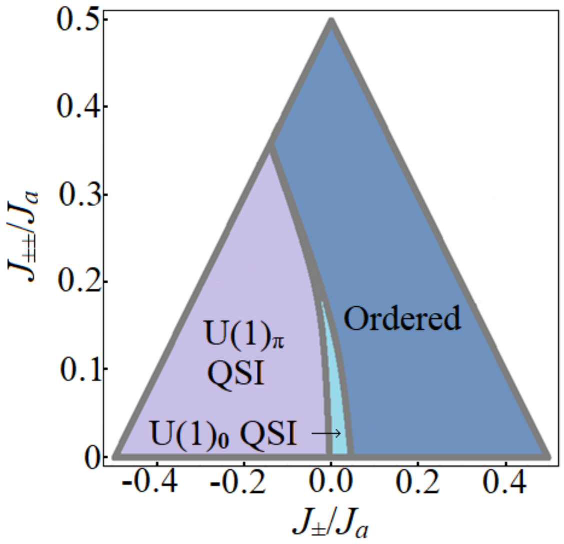

Figure 1.10: The magnetic ground state phase diagram for the ABC Hamiltonian [Eq. (1.27)], which is equivalent to the XYZ Hamiltonian [Eq. (1.21)] in zero field except that $\{a, b, c\}$ is the permutation of $\{\tilde{x},\ \tilde{y},\ \tilde{z}\}$ such that $|J_a| \geq |J_b|, |J_c|$ and $J_b \geq J_c$. We show this phase diagram as a function of the exchange parameters, J_a, $J_\pm = -\frac{1}{4}(J_b + J_c)$, and $J_{\pm\pm} = \frac{1}{4}(J_b - J_c)$. The redefinition of axes for the ABC Hamiltonian still allows for quantities with no directional-dependence to be described by the ABC Hamiltonian and the reduction of parameter space compared to XYZ Hamiltonian typically makes the ABC Hamiltonian and its corresponding phase diagram more convenient to use in such cases. We show the phase diagram for the general case when the permutation relating $\{a, b, c\}$ and $\{\tilde{x},\ \tilde{y},\ \tilde{z}\}$ is unknown. In this case, the ground-state phase diagram for the ABC Hamiltonian contains three regions: a region with magnetic order and regions with $\mathrm{U}(1)_0$ and $\mathrm{U}(1)_\pi$ QSIs. The dipolar or octupolar nature of each region is undetermined; The dipolar or octupolar nature of the corresponding ground-state phase would be determined from the permutation giving $\{\tilde{x},\ \tilde{y},\ \tilde{z}\}$ from $\{a, b, c\}$. The phase diagram in this figure uses calculations from Ref. [56] and has been adapted from Ref. [2] with permission copyrighted by the American Physical Society.

nature of the magnetic field of an octupole moment compared to that of a magnetic dipole [104]), such as muon spin relaxation and rotation measurements, or again magnetic susceptibility measurements, to provide some examples. For such measurements, it is common for the signal from magnetic dipoles, associated with the z-components of pseudospin, to completely dominate over the signal from magnetic octupole moments, associated with the x- and z-components of pseudospin [2, 3, 103]. Another notable exception to this, along with heat capacity measurements, is neutron scattering measurements focused on probing weak scattering from magnetic octupoles at high-$||\mathbf{Q}||$ where the octupolar scattering is near its highest and the dipolar scattering is near zero [30, 105]. We discuss neutron scattering as an experimental technique for probing hard condensed matter systems in the upcoming section, although detailed discussion of high-$||\mathbf{Q}||$ magnetic scattering from octupoles is beyond the scope of this thesis.

1.6 Neutron Scattering

1.6.1 The Basics of Neutron Scattering

The quark-structure of a neutron, with one up quark and two down quarks, results in a lack of total electric charge for a neutron and a total neutron mass of $m_n = 1.6749 \times 10^{-27}$ kg for the bound pair of three quarks [106–109]. Additionally, the up quark and two down quarks combine to give a neutron spin of 1/2 and a magnetic dipole moment of $-1.913\ \mu_\mathrm{N}$ [106–109]. The negative value of the neutron magnetic moment indicates that the moment is in the opposite direction as the spin, and μ_N is the nuclear magneton given by $\mu_\mathrm{N} = \frac{e\hbar}{2m_P} = 5.0508 \times 10^{-27}\,\mathrm{J\,T^{-1}}$. In fact, the quark content of the neutron does also allow for a resulting spin of 3/2 but experiments have shown that the neutron has spin of 1/2 [110].

To understand the topic of neutron scattering, it is important to first consider how a neutron interacts with an atom: Neutrons primarily interact with the atomic nuclei through short-ranged nuclear forces and with unpaired (magnetic) electrons through magnetic dipole-dipole interactions [106, 107, 109]. This is different than x-rays for example, which interact with all electrons via electromagnetic interactions [106, 107, 109]. Some of the advantages and disadvantages of neutron scattering are conveniently tabulated in Ref. [106]. To highlight some of these, we begin by mentioning that neutron energies and wavelengths are generally around the same order of magnitude as inter-atomic distances and excitation-energies in materials, respectively, which is important as this permits for the measurement of these properties with appropriate resolutions, using neutrons. Additionally, the lack of charge, and the fact that neutrons are not a form of electromagnetic radiation (like x-rays are for example), allows neutrons to penetrate into the bulk of samples rather simply probing a small volume of sample near its surface (like x-rays typically do). One disadvantage of neutron scattering is that large-scale neutron sources (fission reactors and spallation neutron sources) operate with a much lower flux than synchrotron x-ray sources, for example, such that neutron scattering investigations generally require larger sample-sizes and longer counting times compared to x-ray scattering investigations. Nonetheless, neutron scattering from magnetic electrons is a powerful and valuable probe of magnetism in materials; A point which we hope to make evident to the reader through our work on $\mathrm{Ce_2Zr_2O_7}$ in the following chapters.

For each neutron scattering event, the initial and final momenta of the neutron are denoted by $\hbar\mathbf{k}_0$ and $\hbar\mathbf{k}_\mathrm{f}$, respectively, where $\hbar\mathbf{k}_0$ and $\hbar\mathbf{k}_\mathrm{f}$ are called the neutron wave vector and $\mathbf{Q}$ is called the scattering vector. The incident and final neutron energy, E_0 and E_f, are then given in terms of the corresponding wavevectors by [106, 107, 109]:

$$E_0 = \frac{\hbar^2 k_0^2}{2m_n}\ , \quad E_\mathrm{f} = \frac{\hbar^2 k_\mathrm{f}^2}{2m_n}\ . \tag{1.28}$$

It is convenient to define the scattering vector Q and the neutron energy transfer E as [106, 107, 109]:

$$\mathbf{Q} = \mathbf{k}_0 - \mathbf{k}_\mathrm{f}, \tag{1.29}$$

and,

$$E = E_0 - E_\mathrm{f}, \tag{1.30}$$

where $\hbar Q$ and E are the momentum and energy transferred to the sample from the neutron. For elastic neutron scattering events, the energy transfer E is zero while for inelastic scattering, $E \neq 0$. Diffraction is another popular form of neutron measurement and involves both elastic and inelastic scattering but with no measurement of the energy of the scattered neutrons; It is typically a good approximation to ignore the inelastic scattering for diffraction measurements due to the fact that the large majority of scattering is elastic (there is typically ∼100 times more elastic scattering then inelastic scattering).

Neutron scattering is an experimental technique focused on measuring the neutron scattering cross section and derivatives of the neutron scattering cross sections in various forms including the *differential cross section* and *partial differential cross section* (also known as the *double differential cross section*). The cross section is proportional to the probability of occurrence for a certain collision process, and the total neutron collision cross section includes both scattering and absorption processes. The scattering cross section and its derivatives depend on both the single-ion physics through the incoherent scattering and the collective atomic-behavior through the coherent scattering, and accordingly, measuring such cross sections and identifying the different contributors to the measured signal is a powerful technique for investigating the properties of different materials. The differential cross section $\frac{\mathrm{d}\sigma}{\mathrm{d}\Omega}$ is defined as the number of neutrons scattered per second into a specific infinitesimal solid angle $d\Omega$, divided by both the neutron flux Φ and the solid angle $d\Omega$; The flux Φ is equal to the number of neutrons that pass through a unit area in one second and has units of $\mathrm{m}^{-2}\mathrm{s}^{-1}$. The partial differential cross section $\frac{\mathrm{d}^2\sigma}{\mathrm{d}\Omega\mathrm{d}E_\mathrm{f}}$ is defined as the number of neutrons scattered per second into a specific infinitesimal solid angle $d\Omega$ and between energy E_f and $E_\mathrm{f} + dE_\mathrm{f}$, divided by both the neutron flux Φ and the solid angle $d\Omega$.

The three commonly-used derivatives of the cross section are related by $\frac{\mathrm{d}\sigma}{\mathrm{d}\Omega} = \int_0^\infty \frac{\mathrm{d}^2\sigma}{\mathrm{d}\Omega\mathrm{d}E_\mathrm{f}}\,\mathrm{d}E_\mathrm{f} = \int_{-\infty}^{E_0} \frac{\mathrm{d}^2\sigma}{\mathrm{d}\Omega\mathrm{d}E}\,\mathrm{d}E$ (where the final equality holds for constant incident energy) and $\sigma = \int_{4\pi} \frac{\mathrm{d}\sigma}{\mathrm{d}\Omega}\,\mathrm{d}\Omega$. Neutron diffraction experiments measure $\frac{\mathrm{d}\sigma}{\mathrm{d}\Omega}$ due to the fact that scattered neutrons of all energies are measured in diffraction measurements, as opposed to inelastic neutron scattering experiments which measure $\frac{\mathrm{d}^2\sigma}{\mathrm{d}\Omega\mathrm{d}E_\mathrm{f}}$ for some energy or range of energies, or elastic experiments, which have $E_0 = E_\mathrm{f}$ and measure $\left(\frac{\mathrm{d}^2\sigma}{\mathrm{d}\Omega\mathrm{d}E_\mathrm{f}}\right)_{E=0}$.

It is convenient to further define the differential cross section for a particular transition of the combined neutron and sample system, $(\frac{\mathrm{d}\sigma}{\mathrm{d}\Omega})_{\mathbf{k}_0,\mathbf{S}_0,\Psi_0\rightarrow\mathbf{k}_\mathrm{f},\mathbf{S}_\mathrm{f},\Psi_\mathrm{f}}$, using the normal definition of the differential cross section, $\frac{\mathrm{d}\sigma}{\mathrm{d}\Omega}$, but including only scattering events in which the combined system of the neutron and sample transitions from the state $|\mathbf{k}_0, \mathbf{S}_0, \Psi_0\rangle$ to the state $|\mathbf{k}_\mathrm{f}, \mathbf{S}_\mathrm{f}, \Psi_\mathrm{f}\rangle$, where Ψ corresponds to the state of the sample, $\mathbf{S}$ and $\hbar\mathbf{k}$ correspond to the polarization (spin) and momentum states of the neutron, respectively, and the subscripts 0 and f are used to denote the states before and after the scattering event, respectively. In other words, $(\frac{\mathrm{d}\sigma}{\mathrm{d}\Omega})_{\mathbf{k}_0,\mathbf{S}_0,\Psi_0\rightarrow\mathbf{k}_\mathrm{f},\mathbf{S}_\mathrm{f},\Psi_\mathrm{f}}$ is defined as the number of neutrons scattered per second into a specific infinitesimal solid angle $d\Omega$ for scattering events in which the combined system of the neutron and sample begins in the state $|\mathbf{k}_0, \mathbf{S}_0, \Psi_0\rangle$ and ends in the state $|\mathbf{k}_\mathrm{f}, \mathbf{S}_\mathrm{f}, \Psi_\mathrm{f}\rangle$, divided by both the neutron flux Φ and the solid angle $d\Omega$. According to this definition of $(\frac{\mathrm{d}\sigma}{\mathrm{d}\Omega})_{\mathbf{k}_0,\mathbf{S}_0,\Psi_0\rightarrow\mathbf{k}_\mathrm{f},\mathbf{S}_\mathrm{f},\Psi_\mathrm{f}}$, we then have [106, 107, 109],

$$\left(\frac{\mathrm{d}\sigma}{\mathrm{d}\Omega}\right)_{\mathbf{k}_0,\mathbf{S}_0,\Psi_0\rightarrow\mathbf{k}_\mathrm{f},\mathbf{S}_\mathrm{f},\Psi_\mathrm{f}} = \frac{1}{\Phi\mathrm{d}\Omega}\mathcal{W}_{\mathbf{k}_0,\mathbf{S}_0,\Psi_0\rightarrow\mathbf{k}_\mathrm{f},\mathbf{S}_\mathrm{f},\Psi_\mathrm{f}}\ , \tag{1.31}$$

where the transition rate $\mathcal{W}_{\mathbf{k}_0,\mathbf{S}_0,\Psi_0\rightarrow\mathbf{k}_\mathrm{f},\mathbf{S}_\mathrm{f},\Psi_\mathrm{f}}$ is the number of transitions per second from the state $|\mathbf{k}_0, \mathbf{S}_0, \Psi_0\rangle$ to the state $|\mathbf{k}_\mathrm{f}, \mathbf{S}_\mathrm{f}, \Psi_\mathrm{f}\rangle$ for the combined system of the neutron and sample. At this point it is common to apply "Fermi's golden rule" for $\mathcal{W}_{\mathbf{k}_0,\mathbf{S}_0,\Psi_0\rightarrow\mathbf{k}_\mathrm{f},\mathbf{S}_\mathrm{f},\Psi_\mathrm{f}}$ [106, 107, 109]:

$$\mathcal{W}_{\mathbf{k}_0,\mathbf{S}_0,\Psi_0\rightarrow\mathbf{k}_\mathrm{f},\mathbf{S}_\mathrm{f},\Psi_\mathrm{f}} = \frac{2\pi}{\hbar}\left|\big\langle\mathbf{k}_0,\mathbf{S}_0,\Psi_0\big|\hat{V}\big|\mathbf{k}_\mathrm{f},\mathbf{S}_\mathrm{f},\Psi_\mathrm{f}\big\rangle\right|^2\rho_{\mathbf{k}_\mathrm{f},\mathbf{S}_\mathrm{f}}(E_\mathrm{f}) \;, \tag{1.32}$$

where $\rho_{\mathbf{k}_\mathrm{f},\mathbf{S}_\mathrm{f}}(E_\mathrm{f})$ is the density of final states at energy E_f for a neutron in the momentum and polarization states denoted by $\mathbf{k}_\mathrm{f}$ and $\mathbf{S}_\mathrm{f}$, respectively. In other words, $\rho_{\mathbf{k}_\mathrm{f},\mathbf{S}_\mathrm{f}}(E_\mathrm{f})$ is the number of states between E_f and $E_\mathrm{f}+\mathrm{d}E_\mathrm{f}$ for a neutron in the $\mathbf{k}_\mathrm{f}$ and $\mathbf{S}_\mathrm{f}$ momentum and polarization states, respectively, divided by the energy interval $\mathrm{d}E_\mathrm{f}$. The operator $\hat{V}$ describes the interaction potential, and can be separated into two components: $\hat{V}_\mathrm{N}$, describing the nuclear interaction between the sample and the neutron, and $\hat{V}_\mathrm{M}$, describing the magnetic interaction between the sample and the neutron. The nuclear (magnetic) interaction potential and the nuclear (magnetic) scattering that arise from it are discussed in Section 1.6.2 (1.6.3).

Fermi's golden rule in Eq. (1.32) is an application of first-order perturbation theory which is accurate in the case of neutron scattering due to both the short-ranged nature of the nuclear interaction and the fact that the magnetic interaction is weak (see Refs. [106, 107, 109] for further details). Also due to the relatively weak and short-ranged interaction between neutron and sample, an accurate description is obtained using the Born approximation which treats both the scattered and incident neutrons as plane waves [106, 107, 109]:

$$\big|\mathbf{k}_0,\mathbf{S}_0\big\rangle = \frac{1}{\sqrt{V_0}}e^{i\mathbf{k}_0\cdot\mathbf{r}}\big|\mathbf{S}_0\big\rangle \;, \tag{1.33}$$

and,

$$\big|\mathbf{k}_\mathrm{f},\mathbf{S}_\mathrm{f}\big\rangle = \frac{1}{\sqrt{V_0}}e^{i\mathbf{k}_\mathrm{f}\cdot\mathbf{r}}\big|\mathbf{S}_\mathrm{f}\big\rangle \;, \tag{1.34}$$

for a neutron plane-wave in a box of volume $V_0 = L^3$, where e is Euler's number. Using this box normalization method, which is arbitrary but convenient (see Refs. [13, 106–109] for further details), the allowed neutron states are those where periodicity in each direction is a fraction of the box edge-length L; In the case of the scattered neutrons, this gives, $\mathbf{k}_\mathrm{f} = \frac{2\pi\hbar}{L}(n_x,n_y,n_z)$ for integers n_x, n_y, and n_z. The number of states between E_f and $E_\mathrm{f}+\mathrm{d}E_\mathrm{f}$ for a neutron with momentum and spin states $\mathbf{k}_\mathrm{f}$ and $\mathbf{S}_\mathrm{f}$, respectively, $\rho_{\mathbf{k}_\mathrm{f},\mathbf{S}_\mathrm{f}}(E_\mathrm{f})\,\mathrm{d}E_\mathrm{f}$, is then given by $\rho_{\mathbf{k}_\mathrm{f},\mathbf{S}_\mathrm{f}}(E_\mathrm{f})\,\mathrm{d}E_\mathrm{f} = \frac{V_0}{8\pi^3}\,\mathrm{d}\mathbf{k}_\mathrm{f} = \frac{V_0}{8\pi^3}{k_\mathrm{f}}^2\,\mathrm{d}k_\mathrm{f}\,\mathrm{d}\Omega$. Equation (1.28) gives $\mathrm{d}E_\mathrm{f} = \frac{\hbar^2 k_\mathrm{f}}{m_\mathrm{n}}\,\mathrm{d}k_\mathrm{f}$, and by definition we have $\Phi = v_0\langle\mathbf{k}_\mathrm{f},\mathbf{S}_\mathrm{f}|\mathbf{k}_\mathrm{f},\mathbf{S}_\mathrm{f}\rangle = \frac{\hbar k_0}{m_\mathrm{n}}\frac{1}{V_0}$. Putting this all together with Eqs. (1.31) and (1.32) then gives [106, 107, 109]:

$$\left(\frac{\mathrm{d}\sigma}{\mathrm{d}\Omega}\right)_{\mathbf{k}_0,\mathbf{S}_0,\Psi_0\rightarrow\mathbf{k}_\mathrm{f},\mathbf{S}_\mathrm{f},\Psi_\mathrm{f}} = {V_0}^2\frac{k_\mathrm{f}}{k_0}\left(\frac{m_n}{2\pi\hbar^2}\right)^2\left|\big\langle\mathbf{k}_0,\mathbf{S}_0,\Psi_0\big|\hat{V}\big|\mathbf{k}_\mathrm{f},\mathbf{S}_\mathrm{f},\Psi_\mathrm{f}\big\rangle\right|^2 \;, \tag{1.35}$$

and it is then standard to define:

$$<\mathbf{k}_0,\mathbf{S}_0,\Psi_0\big|\hat{V}\big|\mathbf{k}_\mathrm{f},\mathbf{S}_\mathrm{f},\Psi_\mathrm{f}> \;=\; V_0\big\langle\mathbf{k}_0,\mathbf{S}_0,\Psi_0\big|\hat{V}\big|\mathbf{k}_\mathrm{f},\mathbf{S}_\mathrm{f},\Psi_\mathrm{f}\big\rangle \;, \tag{1.36}$$

where the units of $<\mathbf{k}_0,\mathbf{S}_0,\Psi_0\big|\hat{V}\big|\mathbf{k}_\mathrm{f},\mathbf{S}_\mathrm{f},\Psi_\mathrm{f}>$ are J·m^3 (rather than Joules), and the arbitrary volume V_0 cancels out in the eventual evaluation of $<\mathbf{k}_0, \mathbf{S}_0, \Psi_0|\hat{V}|\mathbf{k}_\mathrm{f}, \mathbf{S}_\mathrm{f}, \Psi_\mathrm{f}> = V_0\langle\mathbf{k}_0, \mathbf{S}_0, \Psi_0|\hat{V}|\mathbf{k}_\mathrm{f}, \mathbf{S}_\mathrm{f}, \Psi_\mathrm{f}\rangle$ due to the $1/\sqrt{V_0}$ terms in Eqs. (1.33) and (1.34). This then gives,

$$\left(\frac{\mathrm{d}\sigma}{\mathrm{d}\Omega}\right)_{\mathbf{k}_0,\mathbf{S}_0,\Psi_0\rightarrow\mathbf{k}_\mathrm{f},\mathbf{S}_\mathrm{f},\Psi_\mathrm{f}} = \frac{k_\mathrm{f}}{k_0}\left(\frac{m_n}{2\pi\hbar^2}\right)^2 \left|<\mathbf{k}_0, \mathbf{S}_0, \Psi_0|\hat{V}|\mathbf{k}_\mathrm{f}, \mathbf{S}_\mathrm{f}, \Psi_\mathrm{f}>\right|^2 . \tag{1.37}$$

The double differential cross section can then be obtained by summing over all possible final states, and averaging over all initial states, for both the neutron polarization, $\mathbf{S}$, and the state of the sample Ψ, giving [106, 107, 109]:

$$\left(\frac{\mathrm{d}^2\sigma}{\mathrm{d}\Omega\mathrm{d}E_\mathrm{f}}\right)_{\mathbf{k}_0\rightarrow\mathbf{k}_\mathrm{f}} = \frac{k_\mathrm{f}}{k_0}\left(\frac{m_n}{2\pi\hbar^2}\right)^2 \sum_{\mathbf{S}_0,\Psi_0} P_{\mathbf{S}_0}P_{\Psi_0} \sum_{\mathbf{S}_\mathrm{f},\Psi_\mathrm{f}} \left[\left|<\mathbf{k}_0, \mathbf{S}_0, \Psi_0|\hat{V}|\mathbf{k}_\mathrm{f}, \mathbf{S}_\mathrm{f}, \Psi_\mathrm{f}>\right|^2 \delta\Big(E_0 - E_\mathrm{f} - (E_{\Psi_\mathrm{f}} - E_{\Psi_0})\Big)\right], \tag{1.38}$$

where $P_{\mathbf{S}_0}$ is the probability of the neutron being in the initial polarization state $\mathbf{S}_0$, and P_{Ψ_0} is the probability of the sample being in the initial state Ψ_0. Equation (1.38) is called the *master formula.* The δ-function in Eq. (1.38) ensures energy conservation; The energy, $\hbar\omega = E_{\Psi_\mathrm{f}} - E_{\Psi_0}$, is equal to zero for the case of elastic measurements, which probe ground state properties in the sample, and otherwise $\hbar\omega$ is equal to the energy of the excitation being measured from the sample in a particular inelastic scattering event. With that being said, it is worth mentioning that the δ-function is essentially a placeholder used in theoretical calculations, and in reality it should be replaced by a more realistic form appropriate to the peak-broadening (and the corresponding peak-shape) associated with the experimental apparatus, which must be limited to some nonzero energy resolution.

As we show in Section 1.6.2 and Section 1.6.3, different material properties generally contribute to the value of $\frac{\mathrm{d}^2\sigma}{\mathrm{d}\Omega\mathrm{d}E_\mathrm{f}}$ with different Q and E dependencies, such that it is possible to identify the different contributions in a neutron scattering measurement. The signals from the different contributions can then be examined in order to gain information on the behavior of atoms inside of the material. It is typical to define the *dynamic structure factor*, $S(\mathbf{Q}, \omega)$ [also commonly referred to as $S(\mathbf{Q}, E)$ where $E = \hbar\omega$], and the *equal-time structure factor*, $S(\mathbf{Q})$, using the definitions [106, 107, 109]:

$$\frac{\mathrm{d}^2\sigma}{\mathrm{d}\Omega\mathrm{d}E_\mathrm{f}} = N\frac{k_\mathrm{f}}{k_0}S(\mathbf{Q}, \omega) , \tag{1.39}$$

and

$$\frac{\mathrm{d}\sigma}{\mathrm{d}\Omega} = N\frac{k_\mathrm{f}}{k_0}S(\mathbf{Q}) , \tag{1.40}$$

respectively.

1.6.2 Nuclear Scattering

The nuclear potential can be accurately-approximated using a δ-function due to the fact that its range is much smaller (∼3 orders of magnitude) than the typical incident neutron wavelength $\lambda_0 = \frac{2\pi}{k_0}$ [106, 107, 109]. Under such an approximation, for a single atom denoted as atom i, we then have the nuclear potential [106, 107, 109]:

$$\hat{V}_\mathrm{N} = \left(\frac{2\pi\hbar^2}{m_n}\right) b_i\ \delta(\mathbf{r} - \mathbf{R}_i) , \tag{1.41}$$

which is commonly known as the *Fermi pseudopotential*, where $\mathbf{r}$ is the position of the neutron and $\mathbf{R}_i$ is the position of atom i. The constant b_i is the nuclear scattering length for atom i, and ${b_i}^2$ is a measure of the relative scattering power of the individual atom and is dependent on its isotopic state, the nuclear spin, and the neutron spin.

In general, b_i is a complex number, $b_i = b_i' - \mathrm{i}b_i''$ with its imaginary part describing the neutron absorption. The real part of the nuclear scattering length b_i' is positive for ions that repel the neutron and negative for ions which provide an attractive potential, while the imaginary part of the nuclear cross section is always negative when nonzero ($b_i' \geq 0$) [106]. Unlike the atomic form factor used for x-ray scattering (for example), b_i does not vary systematically across the periodic table [106, 107, 109].

As eluded to in Section 1.6.1, the total collision cross section σ can be separated into parts describing the scattering and absorption, $\sigma = \sigma_{\text{Scattering}} + \sigma_{\text{Absorption}}$ [106, 107]. Additionally, the total scattering cross section can be separated into one part describing the coherent scattering and a second part describing the incoherent scattering, $\sigma_{\text{Scattering}} = \sigma_{\text{Coherent}} + \sigma_{\text{Incoherent}}$, where σ_{Coherent} contains all correlations between different ions at equal or different times, and $\sigma_{\text{Incoherent}}$ contains all correlations between each ion and itself at equal or different times [106, 107, 109].

Substitution of the single-ion nuclear potential [Eq. (1.41)] into the master formula for neutron scattering [Eq. (1.38)] gives a cross section for unpolarized nuclear scattering, from a single ion, which is constant and is proportional to the square of the scattering length, $\sigma_{\text{Scattering}} = \frac{4\pi}{k_0}\overline{|b_i|^2}$, where the averages are taken over the isotopic states, the nuclear spin states, and the neutron spin states [106, 107, 109]. Additionally, this gives a neutron absorption cross section for a single ion that scales with $1/k_0$ and is proportional to the negative of the imaginary part of the scattering length $\sigma_{\text{Absorption}} = \frac{4\pi}{k_0}\overline{b_i''}$ [106, 107, 109]. It is typical to use the single-ion neutron scattering cross section to define cross sections for particular elements: $\sigma_{\text{Scattering}} = \sigma_{\text{Coherent}} + \sigma_{\text{Incoherent}} = \frac{4\pi}{k_0}\overline{|b_i|^2}$, where $\sigma_{\text{Coherent}} = \frac{4\pi}{k_0}|\overline{b_i}|^2$ and $\sigma_{\text{Incoherent}} = \frac{4\pi}{k_0}(\overline{|b_i|^2} - |\overline{b_i}|^2)$. Similarly, one can define $\sigma_{\text{Absorption}} = \frac{4\pi}{k_0}\overline{b_i''}$ where the average here need only be taken over the different isotopes of the element [106, 107]. The scattering lengths do not depend on the incident or final neutron-energy for the vast majority of isotopes but there does exist some rare cases, highlighted in Ref. [107] for example, of scattering lengths that have a significant energy dependence due to the isotope having a neutron absorption process with resonant energy that is obtainable or near-obtainable in neutron scattering experiments. Scattering lengths and cross sections are typically on the order of femtometres (10^{-15} m) and barns (10^{-28} m^2), respectively [106, 107, 109]. In all following discussions, we consider only the scattering cross section, $\sigma_{\text{Scattering}}$, and contributions to its corresponding differential and double differential cross sections; In doing so, we omit the subscript "Scattering" from the neutron scattering cross section.

For a macroscopic sample of some material of interest, the appropriate nuclear potential is given by summing the single-ion nuclear potential in Eq. (1.41) over all ions in the sample [106, 107, 109]:

$$\hat{V}_{\mathrm{N},i} = \left(\frac{2\pi\hbar^2}{m_n}\right)\sum_i b_i \; \delta(\mathbf{r} - \mathbf{R}_i) \; , \tag{1.42}$$

where i denotes the different ions in the sample. The potential operator in Eq. (1.42) can then be used in the master formula for neutron scattering [Eq. (1.38)] to investigate the different contributions to the nuclear scattering.

In neutron scattering experiments on crystalline materials, one is often interested in the contribution to the scattering from elastic Bragg peaks arising from the long-ranged order of the crystal structure in the sample. For the case of unpolarized neutron scattering from a crystalline sample with reciprocal lattice vectors $\boldsymbol{\tau}$, the differential cross section for the nuclear contribution to the coherent elastic scattering is given by [106, 107, 109]:

$$\left(\frac{\mathrm{d}\sigma}{\mathrm{d}\Omega}\right)_{\text{N, Coherent, Elastic}} = \frac{N(2\pi)^3}{v}\sum_{\boldsymbol{\tau}} |F_{\mathrm{N}}(\boldsymbol{\tau})|^2\ \delta(\mathbf{Q}-\boldsymbol{\tau})\ , \tag{1.43}$$

where v is the volume of the nuclear unit cell, N is the number of unit cells in the sample, and the nuclear unit cell structure factor, $F_{\mathrm{N}}(\boldsymbol{\tau})$, is given by [106, 107, 109],

$$F_{\mathrm{N}}(\boldsymbol{\tau}) = \sum_{d} \overline{b_d}\ \mathrm{e}^{-W_d(\boldsymbol{\tau})}\mathrm{e}^{\mathrm{i}(\boldsymbol{\tau}\cdot\mathbf{R}_d)}\ , \tag{1.44}$$

where the sum is over all atoms within the nuclear unit cell, denoted as d. The vector $\mathbf{R}_d$ corresponds to the position of atom d within the nuclear unit cell, $\overline{b_d}$ is the nuclear scattering length for atom d, averaged over the nuclear spin and isotope distributions of the type d atoms. Values of $\overline{b_d}$ are tabulated for different atoms in Refs. [106, 107, 111] for example. The term $W_d(\boldsymbol{\tau})$ is known as the Debye-Waller factor for atom d and is a temperature-dependent term that describes the reduction in scattered intensity due to atomic vibrations, which become more prevalent at higher temperatures; The Debye-Waller factors $W_d(\boldsymbol{\tau})$ increase with temperature leading to a reduction in scattered intensity at higher temperatures. The Debye-Waller factors, $W_d(\boldsymbol{\tau})$, are tabulated at different temperatures for different atoms in common materials in works like Refs. [112–114] for example, and can be calculated in more complex cases following the methods outlined in Ref. [115] for example. However, at low temperature, it is often sufficient to employ the approximation $W_d(\boldsymbol{\tau}) \approx 0$.

Equation (1.43) describes the occurrence of nuclear Bragg peaks in the elastic scattering due to the long-ranged order of a crystal structure. Specifically, these peaks occur at reciprocal lattice positions, $\boldsymbol{\tau}$, with intensities that are proportional to $|\mathbf{F}_{\mathrm{N}}(\boldsymbol{\tau})|^2$. Similar to the δ-function in energy in Section 1.6.1, the δ-function here is essentially a placeholder used in theoretical calculations and in reality it should be replaced by a more realistic form appropriate to the peak shape of the experimental apparatus. A collection of nuclear Bragg peak locations and their relative scattering intensities can be used to determine the crystal structure responsible for the nuclear Bragg peaks, similar to the x-ray scattering refinement performed in Publication I of this thesis except there $\bar{b}_d$ would be replaced by the atomic form factor relevant to x-ray scattering [13].

We end this subsection with a brief discussion of neutron scattering from phonon excitations. While the scattering from phonons is not the contribution to the measured-signal of main focus for most magnetic investigations, it is important to be able to distinguish phonon excitations from other contributions to the signal which are of higher focus. For unpolarized neutrons, the contribution to the inelastic scattering from scattering events that create single-phonon excitations can be described by the double-differential cross section [106, 107, 109]:

$$\left(\frac{\mathrm{d}^2\sigma}{\mathrm{d}\Omega\,\mathrm{d}E_\mathrm{f}}\right)_{+1\,\mathrm{Phonon}} = \frac{k_\mathrm{f}}{k_0}\,\frac{(2\pi)^3}{v}\,\frac{1}{2}\sum_{\boldsymbol{\tau}}\sum_{j,\mathbf{q}}\frac{\hbar|F_j(\mathbf{Q},\,\mathbf{q})|^2}{\omega_j(\mathbf{q})}\,\langle n_j(\mathbf{q})+1\rangle\,\delta\big(E_0-E_\mathrm{f}-\hbar\omega_j(\mathbf{q})\big)\,\delta(\mathbf{Q}-\boldsymbol{\tau}-\mathbf{q})\ , \tag{1.45}$$

where $\omega_j(\mathbf{q})$ is phonon frequency for the j'th phonon branch at reduced wavevector $\mathbf{q}$, and the sum is over all reciprocal lattice vectors for the nuclear cell (denoted as $\boldsymbol{\tau}$), all phonon branches (denoted as j), and all reduced wavevectors within the first Brillouin zone, quantized according to the Born-von Karman boundary conditions (denoted as $\mathbf{q}$) [13, 106, 107, 109]. The term $\langle n_j(\mathbf{q})\rangle$ is the Bose factor giving the average number of phonons with wavevector $\mathbf{q}$ in branch j, with,

$$\langle n_j(\mathbf{q})+1\rangle = \langle n_j(\mathbf{q})\rangle + 1 = \frac{\mathrm{e}^{\frac{\hbar\omega_j(\mathbf{q})}{k_\mathrm{B}T}}}{\mathrm{e}^{\frac{\hbar\omega_j(\mathbf{q})}{k_\mathrm{B}T}}-1}\ . \tag{1.46}$$

The term $F_j(\mathbf{Q},\,\mathbf{q})$ is called the one-phonon structure factor and is given by:

$$F_j(\mathbf{Q},\,\mathbf{q}) = \sum_d \frac{\overline{b_d}}{\sqrt{M_d}}\,\mathrm{e}^{-W_d(\mathbf{Q})}\,\mathrm{e}^{\mathrm{i}(\mathbf{Q}\,\cdot\,\mathbf{R}_d)}[\mathbf{Q}\,\cdot\,\boldsymbol{\epsilon}_{d,j}(\mathbf{q})]\ , \tag{1.47}$$

where the sum is over all atoms within the nuclear unit cell, M_d is mass of atom d, and $\boldsymbol{\epsilon}_{d,j}(\mathbf{q})$ is the polarization vector of atom d for the j'th phonon branch at reduced wavevector $\mathbf{q}$ [13, 106, 107, 109]. As shown in Eq. (1.45), single-phonon excitations follow dispersion relations $E_j = \hbar\omega_j(\mathbf{q})$, where each branch has intensity that scales with $|F_j(\mathbf{Q},\,\mathbf{q})|^2$ along with other various factors. Importantly, this dependence on $|F_j(\mathbf{Q},\,\mathbf{q})|^2$ dictates that single-phonon excitations have intensity that increases with Q approximately as Q^2, due to the $\mathbf{Q}\,\cdot\,\boldsymbol{\epsilon}_{d,j}(\mathbf{q})$ term in Eq. (1.47), and it is this Q-dependence that makes phonon excitations easily distinguishable from CEF transitions as we discuss further in the following section and in Publication I of thesis.

1.6.3 Magnetic Scattering

The most dominant magnetic interaction between a neutron and a magnetic ion is the dipole-dipole interaction between the neutron and the electrons in the magnetic shell of the ion. This dipole-dipole interaction can be described by the potential [106, 107, 109]:

$$\hat{V}_\mathrm{M} = \sum_i \hat{V}_{\mathrm{M},i} = \frac{-2\gamma\mu_\mathrm{N}\mu_\mathrm{B}\mu_0}{4\pi}\sum_i \hat{\mathbf{S}}\cdot\left[\boldsymbol{\nabla}\times\left(\frac{\hat{\mathbf{s}}_i\times\mathbf{r}}{r^3}\right)+\frac{1}{\hbar}\left(\frac{\hat{\mathbf{p}}_i\times\mathbf{r}}{r^3}\right)\right]\ , \tag{1.48}$$

where $\gamma = 1.913$ is the reduced gyromagnetic ratio for a neutron, $\mu_\mathrm{N} = 5.0508\times10^{-27}\,\mathrm{J\,T^{-1}}$ is the nuclear magneton, $\mu_\mathrm{B} = 9.274\times10^{-24}\,\mathrm{J\,T^{-1}}$ is the Bohr magneton, and $\mu_0 = 1.2566\times10^{-6}\,\mathrm{kg\,m\,s^{-2}\,A^{-2}}$ is the permeability of free space. The vectors $\mathbf{r}$ and $\hat{\mathbf{S}}$ are the position and spin operators of the neutron, respectively, and the vectors $\hat{\mathbf{s}}_i$ and $\hat{\mathbf{p}}_i$ correspond to the spin and momentum operators of electron i, respectively. The sum in Eq. (1.48) is carried out over all magnetic electrons in the sample, denoted as i. Nonmagnetic electrons do not contribute as the sum is zero over a full (nonmagnetic) electronic shell. The potential operator in Eq. (1.48) can then be used in the master formula for neutron scattering [Eq. (1.38)] to investigate the different contributions to the magnetic scattering.

In neutron scattering experiments on magnetic materials, one is often interested in the contribution to the scattering from elastic, magnetic Bragg peaks arising from long-ranged magnetic order in the sample. For the case of unpolarized neutron scattering from a magnetically ordered sample with magnetic reciprocal lattice vectors denoted as $\boldsymbol{\tau}_{\mathrm{M}}$, the differential cross section for the magnetic contribution to the coherent elastic scattering is given by [106, 107, 109]:

$$\left(\frac{\mathrm{d}\sigma}{\mathrm{d}\Omega}\right)_{\mathrm{M,\ Coherent,\ Elastic}} = \left(\frac{\gamma r_0}{2\mu_{\mathrm{B}}}\right)^2 \frac{N_{\mathrm{M}}(2\pi)^3}{v_{\mathrm{M}}} \sum_{\boldsymbol{\tau}_{\mathrm{M}}} |\mathbf{F}_{\mathrm{M},\perp}(\boldsymbol{\tau}_{\mathrm{M}})|^2 \, \delta(\mathbf{Q} - \boldsymbol{\tau}_{\mathrm{M}}) \ , \tag{1.49}$$

where v_{M} is the volume of the magnetic unit cell, N_{M} is the number of magnetic unit cells in the sample, and $r_0 = \frac{\mu_0 e^2}{4\pi m_e} = 2.818 \times 10^{-15}$ m is the classical electron radius. The term $\mathbf{F}_{\mathrm{M},\perp}(\boldsymbol{\tau}_{\mathrm{M}})$ is the component of the magnetic unit cell structure factor that is perpendicular to $\mathbf{Q}$, evaluated at $\boldsymbol{\tau}_{\mathrm{M}}$,

$$\mathbf{F}_{\mathrm{M},\perp}(\boldsymbol{\tau}_{\mathrm{M}}) = \frac{\mathbf{Q} \times \mathbf{F}_{\mathrm{M}}(\boldsymbol{\tau}_{\mathrm{M}}) \times \mathbf{Q}}{|\mathbf{Q}|^2} \ . \tag{1.50}$$

The magnetic unit cell structure factor, $\mathbf{F}_{\mathrm{M}}(\boldsymbol{\tau})$, is given by the equation [106, 107, 109],

$$\mathbf{F}_{\mathrm{M}}(\boldsymbol{\tau}) = \sum_{d} f_d(\mathbf{Q}) \bar{\boldsymbol{\mu}}_d \ \mathrm{e}^{-W_d(\boldsymbol{\tau})} \mathrm{e}^{\mathrm{i}(\boldsymbol{\tau} \cdot \mathbf{R}_d)} \ , \tag{1.51}$$

where the sum here is over all magnetic atoms with the magnetic unit cell, denoted as d, and the vector $\bar{\boldsymbol{\mu}}_d$ is the ordered component of the magnetic moment for site d, which is given by the expectation value of the magnetic moment for a specific atom at site d in a specific unit cell, $\langle \hat{\boldsymbol{\mu}}_d \rangle$, averaged over all unit cells. The term $W_d(\boldsymbol{\tau})$ is the Debye-Waller factor defined in Section 1.6.2. The magnetic form factor $f_d(\mathbf{Q})$ describes the effect on the scattering due to the spatial dependence of the magnetic electrons around atom d, and is given by [106, 107, 109],

$$f_d(\mathbf{Q}) = \int \rho_d(\mathbf{r}) \mathrm{e}^{\mathrm{i}(\mathbf{Q} \cdot \mathbf{r})} \mathrm{d}\mathbf{r} \ , \tag{1.52}$$

where the integral is over all real-space and ρ_d is the normalized density of unpaired electrons for atom d. A useful approximation for the magnetic form factor approximates the scattering as arising only from the dipolar component of the magnetic moment, ignore higher order multipoles such as octupoles which couple much weaker to the neutrons [106, 107, 109]. Under the dipole-approximation, the magnetic form factor may be given by [106, 107, 109],

$$f(\mathbf{Q}) = f(Q) = \bar{j}_0(Q) - \frac{2 - g_J}{g_J} \bar{j}_2(Q) \ , \tag{1.53}$$

where the d subscript has been dropped for clarity, g_J is given by Equation (1.1), and $\bar{j}_n(Q)$ is the weighted-average of the nth spherical Bessel function, $j_n(Q)$, over the ionic wave function, ψ, given by $\bar{j}_n(Q) = \int j_n(Qr) |\psi|^2 \mathrm{d}\mathbf{r}$; This can be well-approximated by the analytical expressions that are given for different ions in Ref. [116].

Equation (1.49) describes the occurrence of magnetic Bragg peaks in the elastic scattering due to the long-ranged order of a magnetic structure. Specifically, these peaks occur at magnetic reciprocal lattice positions, $\boldsymbol{\tau}_{\mathrm{M}}$, with intensities that are proportional to $|\mathbf{F}_{\mathrm{M},\perp}(\boldsymbol{\tau}_{\mathrm{M}})|^2$. Similar to the δ-function in energy in Section 1.6.1, the δ-function here is essentially a placeholder used in theoretical calculations and in reality it should be replaced by a more realistic form appropriate to the peak shape of the experimental apparatus. A collection of magnetic Bragg peak locations and their relative scattering intensities can be used to determine the magnetic structure responsible for the magnetic Bragg peaks, as we do in Publication III of this thesis for $\mathrm{Ce_2Zr_2O_7}$ in a magnetic field. Furthermore, the dependence of $\mathbf{F}_{\mathrm{M}}$ on the ordered-moment size can be used to determine the ordered-moment size for specific magnetic structures by comparing measured nuclear and magnetic Bragg peak ratios to calculated nuclear and magnetic Bragg peak ratios. We do this in Publication II of this thesis to place an upper limit on the size of the ordered magnetic moment of $\mathrm{Ce_2Zr_2O_7}$ in zero magnetic field, for all-in, all-out magnetic order (see Section 1.4).

Along with collective magnetic behavior, such as the aforementioned magnetic order, the single-ion magnetic properties are also often focused on in neutron scattering experiments. As shown in Section 1.2, the single-ion magnetic properties at low temperature are governed by the CEF ground state, which can be inferred from refinement of the CEF Hamiltonian [Eq. (1.4)] to the CEF transition energies and intensities measured in an inelastic neutron scattering experiment, as we now describe further.

The powder-averaged double differential cross section for a general CEF transition, describing the intensity of the specific transition from the CEF state denoted as $|i\rangle$ to the CEF state denoted as $|j\rangle$, as would be measured from a powder sample using unpolarized neutrons, is given by [17, 72]:

$$\left(\frac{\mathrm{d}^2\sigma}{\mathrm{d}\Omega\,\mathrm{d}E_{\mathrm{f}}}\right)_{\mathrm{CEF},\,(i\rightarrow j)} = C\,\frac{k_{\mathrm{f}}}{k_0}\,[f(Q)]^2\,\frac{\sum_\alpha |\langle i|\hat{J}_\alpha|j\rangle|^2\,\mathrm{e}^{\frac{-E_i}{k_{\mathrm{B}}T}}}{Z}\,\delta(E_0-E_{\mathrm{f}}-\hbar\omega)\,, \tag{1.54}$$

where C is a constant, $\alpha = x, y, z$, and $\hbar\omega = E_i - E_j$. Here we give the double differential cross section with powder averaging as neutron scattering experiments which are focused on CEF transitions are most often performed on powder samples, as is the case for CEF-focused experiment in Publication I of this thesis. As mentioned more generally in Section 1.6.1, the δ-function here is essentially a placeholder used in theoretical calculations and in reality it should be replaced by a more realistic form appropriate to the peak shape of the experimental apparatus. Here, $f(Q)$ is the powder average of magnetic form factor for the relevant magnetic ion, and the partition function Z is defined as,

$$Z = \sum_k \mathrm{e}^{\frac{-E_k}{k_{\mathrm{B}}T}}\ , \tag{1.55}$$

where the sum is over all CEF states, denoted here as k. As shown in Equation (1.54), a CEF transition from state $|i\rangle$ to $|j\rangle$ has nonzero intensity when any of the total angular momentum components has a nonzero matrix element between states $|i\rangle$ and $|j\rangle$. Furthermore, Equation (1.54) shows that CEF transitions are dispersionless an appear at isolated energies (apart from peak-broadening of the δ-function induced by experimental considerations), in accordance with CEF transitions being a single-ion property rather than collective behavior. Importantly, the intensity of the CEF transitions intensity falls off with increasing Q as $[f(Q)]^2$, which makes these transitions easily-differentiable from single-phonon excitations [Eq. (1.45)] due to the fact that single-phonons excitations have intensity that increases with Q approximately as Q^2.

It is worth mentioning that the intensities from different degenerate states should be summed together in determining the total intensity of the corresponding transition involving the degenerate state. For example, if states $|0_A\rangle$ and $|0_B\rangle$ are degenerate, and so are $|1_A\rangle$ and $|1_B\rangle$, then to calculate the total intensity for the transition from the $|0_A\rangle$ and $|0_B\rangle$ doublet to the $|1_A\rangle$ and $|1_B\rangle$ doublet, one should sum the intensities for the transitions from $|0_A\rangle$ to $|1_A\rangle$, $|0_A\rangle$ to $|1_B\rangle$, $|0_B\rangle$ to $|1_A\rangle$, and $|0_B\rangle$ to $|1_B\rangle$, with each of these individual intensities calculated using Eq. (1.54). The constant C in Eq. (1.54) cancels out when calculating ratios of transition intensities, which is important because measured intensity ratios and transition energies are often compared with calculated intensity ratios and transition energies to refine the parameters in the CEF Hamiltonian as we do in Publication I of this thesis.

Finally, we end this subsection with a discussion of diffuse neutron scattering, which can be loosely defined as coherent scattering arising from short-ranged correlations. For unpolarized neutrons, the diffuse scattering arising from *disordered* short-ranged correlations, for a system with one type of magnetic ion, can be described by the differential cross section [97, 106]:

$$\left(\frac{\mathrm{d}\sigma}{\mathrm{d}\Omega}\right)_{\mathrm{M,\ Diffuse}} = \left(\frac{\gamma r_0}{2\mu_{\mathrm{B}}}\right)^2 [f(\mathbf{Q})]^2 \mathrm{e}^{-2W(\mathbf{Q})} \sum_{ij} \mathrm{e}^{-\mathrm{i}\mathbf{Q}\cdot(\mathbf{R_i}-\mathbf{R_j})} \left(\hat{\mathbf{n}}_i \cdot \hat{\mathbf{n}}_j - \frac{(\hat{\mathbf{n}}_i \cdot \mathbf{Q})(\hat{\mathbf{n}}_j \cdot \mathbf{Q})}{|\mathbf{Q}|^{\mathbf{2}}}\right) \langle\, ||\hat{\boldsymbol{\mu}}_i||\ ||\hat{\boldsymbol{\mu}}_j||\, \rangle\ , \tag{1.56}$$

where $W(\mathbf{Q})$ and $\mathrm{f}(\mathbf{Q})$ are the Debye-Waller factor and magnetic form factor for the ion, defined in Sections 1.6.2 and 1.6.3 respectively. Here it is assumed that there exists a magnetic anisotropy which allows the magnetic moment of each atom i to be confined to some direction denoted by the normalized vector $\hat{\mathbf{n}}_i$; For example, $\hat{\mathbf{n}}_i$ is either the positive or negative local z-axis, $\pm\hat{\mathbf{z}}_i$, for a pyrochlore with Ising single-ion anisotropy. It is important to reiterate that this is valid for diffuse scattering from disordered short-range correlations and further considerations must be taken to accurately account for the diffuse scattering from short-ranged ordered dipole moments [106]. Nonetheless, such disorder is the case for a quantum spin ice and accordingly, we use Eq. (1.56) to calculate unpolarized diffuse neutron scattering signals in Publication II of this thesis.

1.6.4 Neutron Sources and Neutron Scattering Instrumentation

This subsection is intended to provide a brief introduction to some experimental aspects of neutron scattering, including neutron sources and two types of neutron scattering instrument which are particularity relevant to this thesis: The triple-axis spectrometer and the time-of-flight chopper spectrometer.

In this thesis, we use both reactor neutron sources and spallation neutron sources for our experiments on $\mathrm{Ce_2Zr_2O_7}$. Nuclear reactors produce neutrons through fission chain reactions, most-often involving uranium-235 as the starting point in the reaction, which is a fissionable isotope of uranium that is unstable to the capture of a neutron [106, 107, 117]. When a uranium-235 atom captures a neutron, it spends a very short amount of time as a uranium-236 isotope before decaying into fission products. For example, one of the main fission processes is one in which the short-lived uranium-236 atom decays to form one barium-141 atom, one krypton-92 atom, and three neutrons [117]. When this occurs, the neutrons produced in one fission process are then able to be captured by other fissile uranium-235 atoms, forming a fission chain reaction. The high-energy neutrons leaving the fission processes are slowed down by thermal moderation [106, 107]. For example, thermal neutrons are neutrons with energies in the range from 5 to 100 meV, and sources of thermal neutrons most often use water as the moderating medium, with the water continuously cycled to maintain a temperature near room temperature [107, 109]. The outcome is that the neutrons leaving the moderator have energies within a certain range, such as 5 to 100 meV for neutrons moderated using a room temperature medium (thermal neutrons). The fission chain reaction occurs on a large scale in the uranium-235 fuel rods that are housed in a reactor's core, and the large number of neutrons produced through these reactions can be focused and guided towards neutron scattering instruments, as is done at reactor-source neutron scattering facilities.

Spallation neutron sources produce neutrons through proton-bombardment of a neutron-rich target material [107, 109]. Protons are accelerated to high energies and led towards a target which is typically a heavy metal. The protons excite the nuclei in the target material and neutrons are released in the deexcitation of the nuclei. Unlike reactors, spallation neutron sources typically produce pulses of neutrons rather than continuous neutron beams [107, 109]. This is done intentionally using a pulsed time-structure for the proton beam generating the neutrons, and this is done because pulsed time-structures with short pulse widths in time can be used for determining the energy of the scattered neutrons in time-of-flight neutron scattering experiments. It is worth mentioning that the pulses generated by spallation neutron sources have a relatively large peak flux compared to the flux of reactor sources, resulting in a higher total flux for typical spallation sources compared to typical reactors [107, 109].

In Publications I and III of this thesis, we report neutron scattering data collected using a triple-axis spectrometer. The defining feature of the triple-axis spectrometer is that, along with sample and detector rotation, this instrument allows the user to rotate one crystal called the monochromator, which selects the incident energy of the neutrons, and a second crystal called the analyzer, which selects the energy of the neutrons that are measured by the detector [107, 109]. Both the monochromotor and analyzer select the neutron energy by using Bragg scattering from a set of atomic planes with known interplanar spacing in a high-quality crystal; Different wavelengths will scatter at different angles according to Bragg's law [13, 106, 107, 109], and so the wavelength can be chosen by the isolating the neutrons that have a certain scattering angle, for both the monochromator and analyzer. A schematic diagram of a triple axis spectrometer is shown in Fig. 1.11. We omit the collimation and neutron guides in this simplified diagram but note that neutron guide systems and linear collimators are used to transport the neutrons over longer distances and to control the divergence of the beam, respectively [106, 107].

In Publications I, II, and III of this thesis, we report neutron scattering data collected using a time-of-flight spectrometer. For time-of-flight neutron scattering instruments, rotating disk choppers are used to select the incident energy of the neutrons and prevent any "frame-overlap" of separate neutron pulses being detected within the same pulse channel of the detector [107, 109]. Rotating disk choppers can also be used to introduce a pulsed time-structure to a steady-state neutron source [118]. These neutrons are moderated, focused, and guided towards the sample, and scattering from the sample is measured by a position- and time-sensitive detector which typically covers a large range of scattering angles. The positional information in combination with the pulsed time-structure of the neutrons is used to determine the scattered energy of each neutron according to simple kinematics [107, 109]. A schematic diagram of a time-of-flight chopper spectrometer is shown in Fig. 1.12.

1.7 Overview of Thesis

In this thesis we use neutron scattering and complementary experimental techniques to build an understanding of the magnetic properties and magnetic behavior of the rare-earth pyrochlore $Ce_2Zr_2O_7$ at low temperature in both zero and nonzero external magnetic field:

- Chapter 2 contains two publications focused on the basic magnetic properties of $Ce_2Zr_2O_7$ and its magnetic behavior in zero magnetic field. The first of which establishes $Ce_2Zr_2O_7$ as a dipole-octupole pyrochlore and quantum spin ice candidate. The second of which provides further evidence for quantum spin ice behavior in $Ce_2Zr_2O_7$ at low temperature as well as estimates of the exchange parameters for $Ce_2Zr_2O_7$, which also point towards a quantum spin ice ground state.
- Chapter 3 contains one publication focused on the magnetic behavior of $Ce_2Zr_2O_7$ in magnetic fields along the $[1, \bar{1}, 0]$ and $[0, 0, 1]$ crystallographic directions. This paper also focuses on further-refining previous estimates of

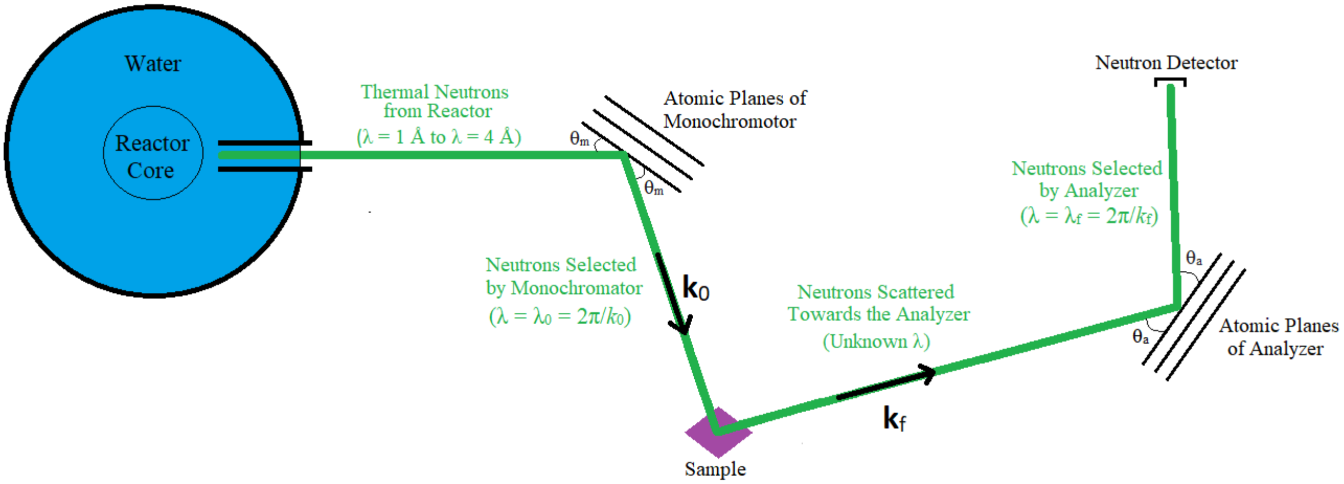

Figure 1.11: A simplified diagram of a neutron triple-axis spectrometer. This is drawn from viewpoint that is looking downward on the scattering plane containing $\mathbf{k}_0$ and $\mathbf{k}_\mathrm{f}$, and is shown for thermal neutrons moderated via water. Neutrons exit the moderating medium with neutrons wavelengths in some specific range determined by the temperature of the moderator ($\lambda \approx 1$ to 4 Å for thermal neutrons for example). Bragg scattering from the monochromotor crystal then directs neutrons of wavevector $\mathbf{k}_0$ (and wavelength $\lambda_0 = 2\pi/k_0$) towards the sample. The analyzer crystal and detector rotate together around the sample in the scattering plane, in order to measure the scattering from the sample for different directions of $\mathbf{k}_\mathrm{f}$. The analyzer and detector also rotate separately in the scattering plane about an axis through the analyzer's center. This latter rotation corresponds to changing the value of θ_a in the diagram by some amount and rotating the detector about the analyzer by twice that amount to ensure that the Bragg scattering from the analyzer is still being measured. This technique, of adjusting θ_a and moving the detector accordingly, allows the user to change the wavelength of neutrons being measured, $\lambda_\mathrm{f} = 2\pi/k_f$. The wavevectors $\mathbf{k}_0$ and $\mathbf{k}_\mathrm{f}$ give the energy transfer E and scattering vector $\mathbf{Q}$ for each orientation via Eqs. (1.29)-(1.31), and neutrons are counted over time by the detector for each desired $\mathbf{Q}$ and E combination.

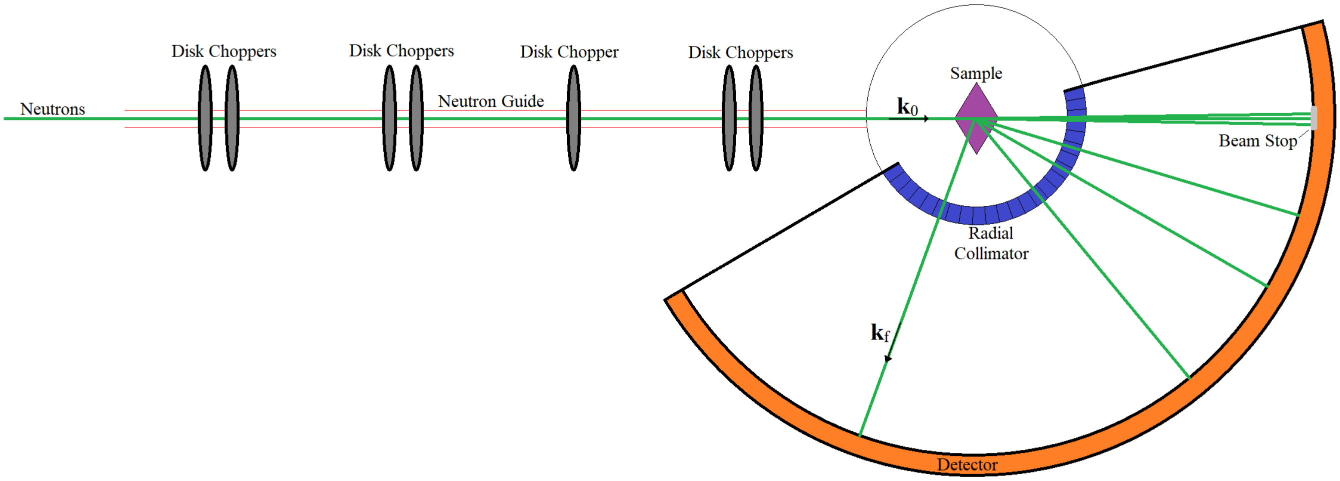

Figure 1.12: A simplified diagram of a neutron time-of-flight chopper spectrometer. Neutrons are led by a neutron guide system through a series of rotating disk choppers, which only allow full-passage for neutrons of the desired incident energy, $E_0 = \hbar^2 k_0^2/(2m_\mathrm{n})$, within resolution. The monochromatic neutron beam is directed towards the sample in the direction of $\mathbf{k}_0$ and neutrons then scatter from the sample in all directions (only shown for some of the scattering towards the detector). Scattering from any sample-environment equipment that is far from the center of sample-rotation is largely captured by a radial collimator designed for removing this scattering before the detector. Neutrons scattered from the sample pass through the radial collimator before striking a position- and time-sensitive detector composed of an array of He^3 tubes. The position on the detector gives the direction of $\mathbf{k}_\mathrm{f}$ and together with this direction, the time measured by detector gives the magnitude k_f. Using the measured $\mathbf{k}_\mathrm{f}$ with the known $\mathbf{k}_0$ then gives the energy transfer E and scattering vector $\mathbf{Q}$ for each scattered neutron via Eqs. (1.29)-(1.31). The neutrons are counted over time by the detector for each measured $\mathbf{Q}$ and E, and often the sample is rotated to access additional $\mathbf{Q}$ directions with respect to the reciprocal space lattice.

the nearest-neighbor exchange parameters for $Ce_2Zr_2O_7$.

- Chapter 4 contains concluding remarks on the current understanding of $Ce_2Zr_2O_7$ and future directions of research which may help better the understanding of $Ce_2Zr_2O_7$ and related dipole-octupole pyrochlores.

Chapter 2

$Ce_2Zr_2O_7$ in Zero Magnetic Field

Despite the large popularity of the rare-earth pyrochlores in the condensed matter community, and especially of those with chemical formula $R_2B_2O_7$ where R^{3+} is a magnetic rare-earth ion and B^{4+} is a nonmagnetic transition metal ion, the Ce^{3+}-based pyrochlores, $Ce_2B_2O_7$, remained largely unstudied until the late 2010s. This is likely due to the added-difficulty in synthesis and growth of $Ce_2B_2O_7$ samples due to the instability of the Ce^{3+} oxidation state in favor of the Ce^{4+} state, which we further discuss in Publication I of this thesis.

The availability of powder and single crystal samples of the $Ce_2B_2O_7$ pyrochlores, beginning with powder samples of $Ce_2Sn_2O_7$ in 2015 [119], has presented a new avenue for investigating rare magnetic phases and exotic excitations, which appear to be relatively plentiful in the rare-earth pyrochlores [5–10, 12]. In fact, our initial focus on $Ce_2Zr_2O_7$ was motivated in large-part by the previous work in Ref. [119] on $Ce_2Sn_2O_7$, where muon spin relaxation and magnetic susceptibility measurements show a lack of magnetic order and a lack of spin freezing in $Ce_2Sn_2O_7$ down to the lowest measured temperatures of $T = 0.02$ K and $T = 0.07$ K respectively, which is also corroborated by heat capacity measurements down to $T = 0.3$ K. This lack of both magnetic order and spin freezing is suggestive of a spin liquid phase at low temperature in $Ce_2Sn_2O_7$ and the implied-likelihood of similar spin liquid behavior in $Ce_2Zr_2O_7$ helped draw our attention to $Ce_2Zr_2O_7$ as an interesting new material to study. Fortunately, the synthesis and crystal-growth efforts of our collaborators (listed in the following section) have allowed for such a study of $Ce_2Zr_2O_7$ to include both powder and single crystal samples.

This chapter contains Publications I and II of this thesis as well as prefaces to these publications on $Ce_2Zr_2O_7$, which provide an initial summary of each publication, and place each publication in the context of other relevant work and theoretical expectations. We also outline the contributions of the co-authors involved in each of these collaborative works. Specifically, the following publications are contained in this chapter:

Publication I:

"*Quantum Spin Ice Dynamics in the Dipole-Octupole Pyrochlore Magnet $Ce_2Zr_2O_7$*",

J. Gaudet, E. M. Smith, J. Dudemaine, J. Beare, C. R. C. Buhariwalla, N. P. Butch, M. B. Stone, A. I. Kolesnikov, G. Xu, D. R. Yahne, K. A. Ross, C. A. Marjerrison, J. D. Garrett, G. M. Luke, A. D. Bianchi, and B. D. Gaulin,

Physical Review Letters **122**, 187201 (2019).

Reproduced from Reference [1] with permission, copyrighted by the American Physical Society.

Publication II:

"*Case for a $U(1)_\pi$ Quantum Spin Liquid Ground State in the Dipole-Octupole Pyrochlore $Ce_2Zr_2O_7$*",

E. M. Smith, O. Benton, D. R. Yahne, B. Placke, R. Schäfer, J. Gaudet, J. Dudemaine, A Fitterman, J. Beare, A. R. Wildes, S. Bhattacharya, T. DeLazzer, C. R. C. Buhariwalla, N. P. Butch, R. Movshovich, J. D. Garrett, C. A. Marjerrison, J. P. Clancy, E. Kermarrec, G. M. Luke, A. D. Bianchi, K. A. Ross, and B. D. Gaulin,

Physical Review X **12**, 021015 (2022).

Reproduced from Reference [2] with permission, copyrighted by the American Physical Society.

2.1 Preface to Publication I: Evidence for a Dipole-Octupole Crystal Electric Field Ground State and Quantum Spin Ice Correlations in the Cerium-Based Pyrochlore Magnet $Ce_2Zr_2O_7$

In this work we report high-energy inelastic neutron scattering data measured on a powder sample of $Ce_2Zr_2O_7$ and we fit the data in order to determine the parameters in the CEF Hamiltonian [see Eq. (1.4)] which best reproduce the measured CEF transition energies and intensities [see Eq. (1.54)] according to the Stevens operator approximation including only the $J = 5/2$ states. The results show that the CEF ground state for Ce^{3+} in $Ce_2Zr_2O_7$ can be approximated by a $|J = 5/2,\ m_J = \pm 3/2\rangle$ doublet, which is separated in energy from the first excited CEF state by ∼55 meV. This is an important starting point for forming an accurate understanding and description of the magnetism at low temperature in $Ce_2Zr_2O_7$. For example, the $|J = 5/2,\ m_J = \pm 3/2\rangle$ doublet corresponds to an Ising single-ion anisotropy where the magnetic moments point along the local z directions. The anisotropic g-factors, $g_{xy} = 0$ and $g_z = 2.57$, for this doublet yield a magnetic moment size of $\mu_{CEF} = 1.29\ \mu_B$ in the CEF ground state [see Eq. (1.8)], which is relatively small compared to the value of value of $\mu_{CEF} \approx 10\ \mu_B$ in the classical spin ices $Ho_2Ti_2O_7$ and $Dy_2Ti_2O_7$ for example [16, 18, 48, 72]. Furthermore, since the CEF ground state is a doublet that is well-separated in energy from the first excited CEF state, the low-temperature magnetic behavior can be accurately described using pseudospin-1/2 degrees of freedom [Eqs. (1.5)-(1.7)]. As elucidated in Refs. [51, 52], the pseudospin-1/2 description is particularly interesting for the case of the $|J = 5/2,\ m_J = \pm 3/2\rangle$ doublet due to the fact that this doublet has dipole-octupole symmetry with a peculiar splitting of dipolar and octupolar properties between the different pseudospin components (see Section 1.5). In fact, similar investigations on $Ce_2Sn_2O_7$ in Ref. [30, 119] and on

$Ce_2Hf_2O_7$ in Ref. [61] also conclude a CEF ground state doublet which is dominated by the $|J = 5/2,\ m_J = \pm 3/2\rangle$ states, however the refinements to the inelastic neutron scattering spectra in Ref. [30, 119] for $Ce_2Sn_2O_7$ and in Ref. [61] for $Ce_2Hf_2O_7$ each include minor contributions to the CEF ground state doublet from states with $J = 7/2$, which we discuss in further detail in Chapters 3 and 4.

Here we also report new magnetic susceptibility measurements on $Ce_2Zr_2O_7$, which show a lack of both magnetic order and spin freezing down to the lowest measured temperature of $T = 0.5$ K. This is corroborated by our time-of-flight neutron scattering measurements which show a lack of magnetic order down to the lowest measured temperature of $T = 0.06$ K, and a snowflake-like pattern of diffuse magnetic scattering at low energy which is typical for spin ice correlations [71, 93]. For example, the classical spin ices $Ho_2Ti_2O_7$ (Refs. [69, 88]) and $Dy_2Ti_2O_7$ (Refs. [120, 121]), as well as the quantum spin ice candidates $Pr_2Zr_2O_7$ (Refs. [43, 122, 123]) and $Pr_2Hf_2O_7$ (Ref. [66]), each show a snowflake-like pattern of diffuse scattering in the (H, H, L) scattering plane similar to $Ce_2Zr_2O_7$, with the finer details of the signals giving further information on the magnetic interactions at play in the corresponding materials [71, 93].

In Publication I we compare the measured snowflake-like diffuse scattering signal from $Ce_2Zr_2O_7$ to predictions for emergent photon excitations in a quantum spin ice. However, it is worth mentioning that in Publication II of this thesis, we show that the emergent photon excitations in $Ce_2Zr_2O_7$ are not expected to give a significant neutron scattering signal within the Q range of these measurements due to the dipole-octupole nature of the Ce^{3+} pseudospins in combination with the exchange parameters relevant for $Ce_2Zr_2O_7$, and instead, spinon excitations should dominate the signal and generate a snowflake-like pattern of diffuse scattering that is also consistent with measurements.

During the publication process for Publication I, we became aware of a separate work on $Ce_2Zr_2O_7$ in Ref. [22] which also estimates a $|J = 5/2,\ m_J = \pm 3/2\rangle$ CEF ground state doublet, a lack of magnetic order down to the lowest measured temperature, and a diffuse scattering signal at low energy, with the latter being less informative than ours due to the lessened Q-coverage in their time-of-flight neutron scattering experiment compared to our experiment. Importantly, the data and interpretation in Ref. [22] is consistent with that presented in our work. While the results are similar, the work in Ref. [22] has less focus on controlling the oxidation level in their samples compared our significant focus on controlling this issue as much as possible in Publication I (and all following publications to date). In further detail, we report the sample oxidation as function of time for a powder sample of $Ce_2Zr_2O_7$ and show that significant sample oxidation occurs at room temperature in just the first couple hours of exposure to air, meaning it is important to store samples in an inert atmosphere or vacuum, while no mention is made of such considerations in Ref. [22]. Along with this storage procedure, we anneal our samples in hydrogen gas after synthesis and crystal growth to reduce any undesired sample oxidation and Ce^{4+} content remaining after initial synthesis or growth of each sample, as discussed further in Publications I, II, and III.

While quantum spin ice correlations are reported in neutron scattering data on $Ce_2Sn_2O_7$ in Refs. [30, 60, 124] and for $Ce_2Hf_2O_7$ in Refs. [61], the first reports of quantum spin ice correlations in a cerium-based pyrochlore were for $Ce_2Zr_2O_7$ in 2019 in Publication I of this thesis and in Ref. [22]; Of course, this is not including the initial report for a lack of magnetic order and lack of spin freezing in $Ce_2Sn_2O_7$ at low temperature in 2015 (Ref. [119]). With that in mind, the neutron scattering measurements that we present in Publication I of this thesis, along with those in Ref. [22], represent a significant breakthrough in the elucidation of quantum spin ice behavior in the cerium-based pyrochlores. Furthermore, this snowflake-like pattern of diffuse scattering measured from single crystal $Ce_2Zr_2O_7$ has additional importance considering that all neutron scattering data published on $Ce_2Sn_2O_7$ and $Ce_2Hf_2O_7$ to date has been measured on powder samples, and the powder-averaging of the neutron signal leads to a far less robust comparison between measurement and theory in such cases, with all directional information lost in these measurements on powder samples.

Fits of the magnetic susceptibility measured from $Ce_2Zr_2O_7$ in Publication I and in Ref. [22] each yield a negative Curie-Weiss temperature around -0.5 K, characteristic of antiferromagnetic interactions and typically suggestive of an all-in, all-out magnetically ordered ground state for Ising pyrochlores such as $Ce_2Zr_2O_7$. However, these magnetic susceptibility measurements only have significant sensitivity to the z components of the pseudospins and their magnetic dipole moments, and lack significant sensitivity to the x and y components of pseudospins and their magnetic octupoles. It is now well-understood in the literature that J_x-dominant and J_y-dominant quantum spin ice ground states are possible even for $J_z < 0$, and so a negative Curie-Weiss temperature does not imply an all-in, all-out phase for the dipole-octupole pyrochlores (see Section 1.5 for further details, for example). Moreover, we now understand that the curvature of the inverse susceptibility (shown in Publication I) results in a Curie-Weiss temperature that gives an inaccurate representation of the correlations in the low-temperature ground state. This point is elucidated by our fits to the heat capacity measured from $Ce_2Zr_2O_7$ at low temperature in Publications II and III of this thesis, which each give a more-accurate estimate of J_z compared to estimates using the Curie-Weiss temperature, and which each give $J_z > 0$. In fact, our diffuse neutron scattering data in Publication III also gives strong evidence for $J_z > 0$. With all of this in mind, we reiterate that the Curie-Weiss temperature and its usual implications are far less significant for $Ce_2Zr_2O_7$ than we were aware of at the time of writing Publication I.

I contributed to Publication I by leading two single-crystal neutron scattering experiments and the corresponding preparation, preparing a sample for magnetic susceptibility measurements, as well as taking part in the corresponding measurement process for the magnetic susceptibility. I characterized both the crystallinity and phase purity of the single crystal samples used in this work using x-ray diffraction and I performed the x-ray characterization included in the supplemental material. I analyzed all of the experimental data presented in this paper and supplemental material except for the high-energy inelastic neutron scattering measurements focused on probing the CEF levels. I was responsible for annealing the single crystal samples used in this work, in hydrogen gas, before storing each sample in an inert atmosphere until measurement. Finally, I designed and generated all-but-two of the figures included in this work and wrote ~50% of the text. The contributions of each author are summarized below.

Author Contributions for Publication I:

Experimental Concept:

J. Gaudet, **E. M. Smith**, B. D. Gaulin

Sample Preparation:

J. Dudemaine, **E. M. Smith**, J. Gaudet, C. A. Marjerrison, J. D. Garrett, B. D. Gaulin, A. D. Bianchi

Neutron Scattering Experiments:

E. M. Smith, J. Gaudet, C. R. C. Buhariwalla, N. P. Butch, M. B. Stone, A. I. Kolesnikov, Guangyong Xu, B. D. Gaulin

Magnetic Susceptibility Measurements:

J. Beare, **E. M. Smith**, B. D. Gaulin, G. M. Luke

X-Ray Scattering Characterization:

E. M. Smith, B. D. Gaulin

Data Analysis:

E. M. Smith, J. Gaudet, B. D. Gaulin

Calculations and Modeling:

J. Gaudet, B. D. Gaulin

Manuscript:

J. Gaudet, **E. M. Smith**, B. D. Gaulin

Quantum Spin Ice Dynamics in the Dipole-Octupole Pyrochlore Magnet $Ce_2Zr_2O_7$

J. Gaudet,[1,2,3] E. M. Smith,[1] J. Dudemaine,[4] J. Beare,[1] C. R. C. Buhariwalla,[1] N. P. Butch,[3] M. B. Stone,[5]
A. I. Kolesnikov,[5] Guangyong Xu,[3] D. R. Yahne,[6] K. A. Ross,[6,7] C. A. Marjerrison,[8] J. D. Garrett,[8]
G. M. Luke,[1,7] A. D. Bianchi,[4,9] and B. D. Gaulin[1,7,8]
[1]Department of Physics and Astronomy, McMaster University, Hamilton, Ontario, L8S 4M1, Canada
[2]Institute for Quantum Matter and Department of Physics and Astronomy, Johns Hopkins University, Baltimore, Maryland 21218, USA
[3]Center for Neutron Research, National Institute of Standards and Technology, MS 6100 Gaithersburg, Maryland 20899, USA
[4]Département de Physique, Université de Montréal, 2900 Boulevard Édouard-Montpetit, Montréal, Quebec, H3T 1J4, Canada
[5]Neutron Scattering Division, Oak Ridge National Laboratory, Oak Ridge, Tennessee 37831, USA
[6]Department of Physics, Colorado State University, 200 West Lake Street, Fort Collins, Colorado 80523-1875, USA
[7]Canadian Institute for Advanced Research, 661 University Avenue, Toronto, Ontario, M5G 1M1, Canada
[8]Brockhouse Institute for Materials Research, McMaster University, Hamilton, Ontario, L8S 4M1, Canada
[9]Regroupement Québécois sur les Matériaux de Pointe (RQMP), Quebec, H3T 3J7, Canada

(Received 28 November 2018; revised manuscript received 15 March 2019; published 7 May 2019)

Neutron scattering measurements on the pyrochlore magnet $Ce_2Zr_2O_7$ reveal an unusual crystal field splitting of its lowest $J = 5/2$ multiplet, such that its ground-state doublet is composed of $m_J = \pm 3/2$, giving these doublets a dipole-octupole (DO) character with local Ising anisotropy. Its magnetic susceptibility shows weak antiferromagnetic correlations with $\theta_{CW} = -0.4(2)$ K, leading to a naive expectation of an all-in, all-out ordered state at low temperatures. Instead, our low-energy inelastic neutron scattering measurements show a dynamic quantum spin ice state, with suppressed scattering near $|\mathbf{Q}| = 0$, and no long-range order at low temperatures. This is consistent with recent theory predicting symmetry-enriched U(1) quantum spin liquids for such DO doublets decorating the pyrochlore lattice. Finally, we show that disorder, especially oxidation of powder samples, is important in $Ce_2Zr_2O_7$ and could play an important role in the low-temperature behavior of this material.

DOI: 10.1103/PhysRevLett.122.187201

The rare-earth pyrochlore oxides $R_2B_2O_7$, where R^{3+} and B^{4+} consist generally of rare-earth and transition-metal ions, respectively, display a wealth of both exotic and conventional magnetic ground states. Their R^{3+} ions decorate a network of corner-sharing tetrahedra, one of the archetypes for geometrical frustration in three dimensions. Because of strong crystal electric field (CEF) effects, the nature of the magnetic interactions in such materials are strongly influenced by their single-ion physics [1–3]. A naive theoretical description of the magnetic interactions in rare-earth pyrochlores is generally performed by introducing an *ad hoc* effective single-ion term in addition to Heisenberg exchange interactions. For example, Heisenberg antiferromagnetism with an effective Ising anisotropy leads to nonfrustrated all-in, all-out (AIAO) magnetic order, as seen in several heavy rare-earth iridate pyrochlores [4,5] and illustrated in the insert of Fig. 1(a). Heisenberg ferromagnetism and an effective Ising anisotropy give rise to a classical spin ice ground state [6], as seen in $(Ho, Dy)_2Ti_2O_7$ [7,8] and illustrated as the two-in, two-out (2I2O) local structure in the inset of Fig. 1(a). However, the magnetic interactions should be projected into pseudospin operators acting solely on the low-energy CEF states [3,9–13]. This procedure has been applied, e.g., in the Yb^{3+} [11,14,15] and Er^{3+} [12,16–18] *XY* pyrochlores, where CEF effects give rise to effective $S = 1/2$ quantum degrees of freedom that interact via anisotropic exchange interactions.

More recently, it has been realized that the precise composition of the ground-state crystal field doublets in rare-earth pyrochlores is crucial in determining the form of the microscopic Hamiltonian, and in itself, diversifies the possibility of quantum magnetic states [3,19]. This has been appreciated for some time in the case of non-Kramers doublets, based on magnetic ions with an even number of electrons, such as the $4f^2$ configuration in Pr^{3+}. Only the local z component of the spin operators transforms as a dipole, with the transverse components transforming as quadrupoles [20–22]. This restricts the form of the effective spin Hamiltonian and can stabilize quadrupolar phases that are not present in the phase diagram for dipolar doublets [23,24]. For Kramers ions with an odd number of electrons, such as $4f^1$ in Ce^{3+}, $4f^3$ in Nd^{3+}, and $4f^5$ in Sm^{3+}, a crystal field ground-state doublet with dipole-octupole (DO) character can be realized where the local z and x components transform as a dipole, but the local y component transforms as an octupole [19,25–27]. After a rotation of the pseudospins about the y axis, the DO exchange Hamiltonian on the pyrochlore lattice can be reduced to an *XYZ* model with

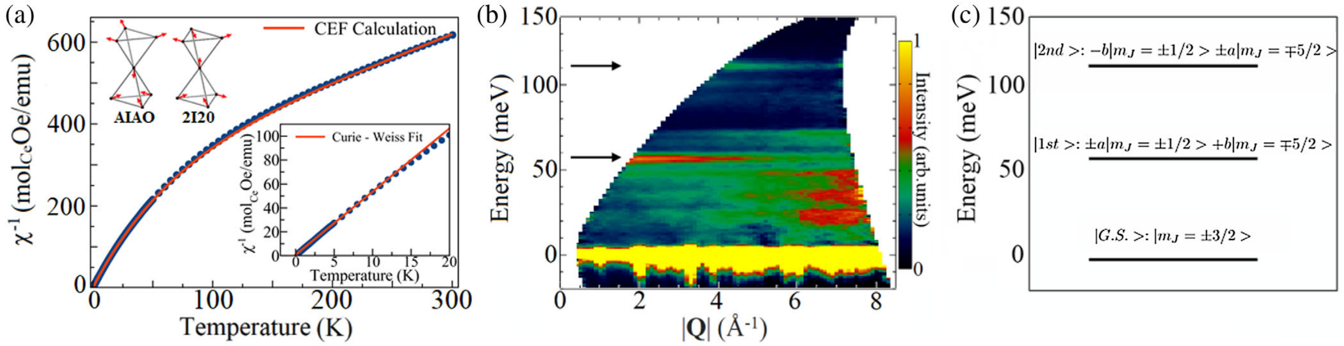

FIG. 1. (a) The inverse magnetic susceptibility of a powder sample of $Ce_2Zr_2O_7$. The red curve is the Van Vleck susceptibility calculated with the CEF Hamiltonian of $Ce_2Zr_2O_7$. (Top left inset) The AIAO and 2I2O magnetic ground-state spin configurations on a pair of tetrahedra. (Bottom right inset) The low-temperature magnetic susceptibility that yields $\theta_{\mathrm{CW}} = -0.4(2)$ K and a paramagnetic moment of $1.3(1)$ μ_B and shows no signature of magnetic order or spin freezing down to 0.5 K. (b) Inelastic neutron scattering spectra of $Ce_2Zr_2O_7$ at $T = 5$ K with incident neutron energy $E_i = 150$ meV. Two strong excitations can be identified as magnetic in origin at $E \sim 56$ and ~ 112 meV, as their intensity decreases as a function of $|\mathbf{Q}|$, consistent with the Ce^{3+} magnetic form factor. (c) The energy eigenvalues corresponding to the CEF states belonging to the spin-orbit ground-state manifold of $Ce_2Zr_2O_7$. The composition of the CEF eigenfunctions are also presented in (c), revealing the DO nature of the ground-state doublet—that is, it corresponds to pure $m_J = \pm 3/2$ states.

three independent exchange parameters ($J_{\tilde{x}}$,$J_{\tilde{y}}$,$J_{\tilde{z}}$) [19,25]. This Hamiltonian allows for multiple phases to emerge, such as an AIAO order, octupolar ordered phases, and also for moment fragmentation, as observed in $Nd_2Zr_2O_7$, where static AIAO order coexists with dynamic spin ice fluctuations [19,25,28,29]. In the limit of dominant antiferromagnetic interactions and strong easy-axis exchange anisotropy, a dipolar quantum spin ice is stabilized so long as the easy axis is along one of the dipolar components of the DO doublet ($J_{\tilde{x}} \gg J_{\tilde{z}}$,$J_{\tilde{y}}$ or $J_{\tilde{z}} \gg J_{\tilde{x}}$,$J_{\tilde{y}}$). An octupolar quantum spin ice is favored if the easy axis is along the octupole component ($J_{\tilde{y}} \gg J_{\tilde{x}}$,$J_{\tilde{z}}$) [19,25].

A promising family of candidate materials for dipolar or octupolar quantum spin ice physics originating from DO doublets are the cerium pyrochlores $Ce_2B_2O_7$. The Ce^{3+} ions in the pyrochlore $Ce_2Sn_2O_7$ are believed to have a DO CEF ground state and to interact via dominant antiferromagnetic interactions, but do not magnetically order down to $T = 20$ mK [25,30]. The low-energy spin dynamics of the cerium pyrochlores remains unexplored and their characterization is key in determining the nature of their possible spin liquid states. In this Letter, we report new inelastic neutron scattering experiments on powder and single crystal samples of $Ce_2Zr_2O_7$. Using high-energy inelastic neutron scattering, we first confirmed the DO nature of the Ce^{3+} single-ion ground-state wave functions in $Ce_2Zr_2O_7$. We also present low-energy inelastic neutron scattering measurements performed on a single crystal of $Ce_2Zr_2O_7$ and observe diffuse, inelastic magnetic scattering that emerges at low temperatures. The $\mathbf{Q}$ dependence of this diffuse scattering is consistent with a symmetry-enriched U(1) quantum spin ice state at low but finite temperatures. Furthermore, we show the quantum spin-ice correlations remain dynamic down to at least 60 mK with no sign of static magnetic order. Our results demonstrate $\mathbf{Q}$ signatures of a dynamic quantum spin ice ground state in $Ce_2Zr_2O_7$, with associated emergent quantum electrodynamics and elementary excitations based on magnetic and electric monopoles, as well as emergent photons [31–34].

Single crystal and powder samples of $Ce_2Zr_2O_7$ have been grown using floating zone techniques and solid-state synthesis. Stabilizing the Ce^{3+} oxidation state in $Ce_2Zr_2O_7$ is not simple and requires growth and annealing in strong reducing conditions to minimize Ce^{4+} [35]. As discussed in the Supplemental Material [36], which includes Refs. [37–44], this is a serious issue, especially in powder samples, where oxidization is observed to occur in powders exposed to air on a timescale on the order of minutes, complicating the exact characterization of the material's stoichiometry. The oxidization process can be tracked through high-resolution x-ray diffraction measurements of the lattice parameter, and it is much slower for single crystal samples. There we can make an estimate of the stoichiometry of the single crystal used in our experiments as $Ce_2Zr_2O_{7+\delta}$ with $\delta \sim 0.1$.

We first present high-energy inelastic neutron scattering measurements, which probe the single-ion properties of the Ce^{3+} ions. To do so, we used the SEQUOIA high-resolution inelastic chopper spectrometer [45] at the Spallation Neutron Source of Oak Ridge National Laboratory and employed neutrons with incident energies (E_i) of 150 and 500 meV. The $E_i = 150$ meV instrument setting was chosen to resolve the CEF states that belong to the spin-orbit ground-state manifold ($J = 5/2$). The CEF interaction lifts the Ce^{3+} spin-orbit ground-state degeneracy into three different eigenstates that are each doubly degenerate. We also estimated a CEF Hamiltonian for $Ce_2Zr_2O_7$ using a scaling procedure based on the Er^{3+} pyrochlore CEF scheme [46]. This predicts two CEF excited states near 80 and 100 meV with similar inelastic neutron scattering intensity at $T = 5$ K. As seen in Fig. 1(b), this scenario is in qualitatively good agreement with our 150 meV inelastic neutron experimental spectra, where two strong magnetic excitations are observed at ∼56 and ∼112 meV. The relative scattered intensity of these CEF transitions can be obtained giving $I_{56\text{ meV}}/I_{112\text{ meV}} = 1.2(1)$, in good agreement with our expectations based on this scaling argument.

Additional weak inelastic scattering whose **Q** dependence is inconsistent with phonons is also visible in the spectra, e.g., weak scattering near ∼100 meV in Fig. 1(b). It is not clear if this weak inelastic scattering is due to the influence of Ce^{3+} or Zr^{3+} in defective sites [47], on residual Ce^{4+}, or on the possible presence of hybridized phonon-crystal field excitations known as vibronic bound states, as has been recently observed in holmium and terbium pyrochlores [48,49]. In any case, this unidentified contribution to the inelastic scattering yields a small fraction of the spectral weight and we conclude the features at 56 and 112 meV are the CEF excitations corresponding to the main Ce^{3+} site.

The details of the crystal field analysis determining the full set of eigenvalues and eigenfunctions for Ce^{3+} are summarized in Fig. 1(c) and further discussed in the Supplemental Material [36]. The key conclusion is that the ground-state Kramers doublet appropriate to Ce^{3+} is well separated from all excited crystal field states (by ∼56 meV) and is composed of pure $m_J = \pm 3/2$ states. A large CEF gap is consistent with the high-temperature heat capacity of $Ce_2Zr_2O_7$ measured in Ref. [50], where no Schottky anomaly is observed between 5 and 300 K. These pure $m_J = \pm 3/2$ states have a dipole-octupole character with a dipolar moment whose anisotropy is purely Ising and whose magnitude must be 1.286 μ_B. This result does not originate from a fine-tuning of the CEF parameters, but is instead a property protected by the point-group symmetry of the A site in the pyrochlore lattice.

Figure 1(a) shows the inverse magnetic susceptibility of a 107 mg powder sample of $Ce_2Zr_2O_7$ measured with a Quantum Design magnetic property measurement system magnetometer equipped with a ^{3}He insert. The main panel of Fig. 1(a) shows the high-temperature susceptibility of $Ce_2Zr_2O_7$ and reveals strong nonlinearity. Assuming a dilution of the Ce^{3+} moments by nonmagnetic Ce^{4+} ions at the ∼8% level in this powder sample, the Van Vleck susceptibility calculated with the CEF Hamiltonian of $Ce_2Zr_2O_7$ reproduces the high-temperature susceptibility data well and yields an antiferromagnetic Curie constant of $-0.4(2)$ K. We expect conventional and unfrustrated AIAO order in $Ce_2Zr_2O_7$ based on the effective antiferromagnetic interactions and the Ising anisotropy associated with its magnetism. However, our magnetic susceptibility measurements [inset of Fig. 1(a)], as well as both powder and single crystal neutron diffraction experiments, show no indication of long-range magnetic order down to $T = 0.06$ K. In particular, and as shown in the Supplemental Material [36], no new Bragg scattering or enhancement of the Bragg scattering associated with any $\mathbf{k} = 0$ magnetic structure is observed, including at those wave vectors characteristic of the AIAO, Γ_3 structure. $Ce_2Zr_2O_7$ therefore remains disordered to $T = 0.06$ K, our lowest temperature measured.

We examined the low-temperature spin dynamics in $Ce_2Zr_2O_7$ using the low energy disk chopper spectrometer (DCS) neutron instrument at NCNR with $E_i = 3.27$ meV incident neutrons giving an energy resolution of ∼0.09 meV at the elastic line. One experiment was performed on a ∼6 g powder sample and a second one was performed on a ∼5 g single crystal, which was mounted with its $[HHL]$ plane coincident with the horizontal plane of the spectrometer. Figure 2(a) shows the DCS measurements on our powder, where the integration in $|\mathbf{Q}|$ is $0.35 - 0.85$ Å^{-1}. This integration in momentum transfer $|\mathbf{Q}|$ corresponds to integrating over the $|\mathbf{Q}| = |(001)|$ position (∼0.59 Å^{-1}), where quantum spin ice correlations are expected to be strongest [34]. A buildup of inelastic spectral weight below ∼0.4 meV is observed on decreasing the temperature.

Low-energy inelastic neutron scattering from our single crystal is shown in Figs. 2(b)–2(d) and 3(a). All this data were acquired using the same $E_i = 3.27$ meV instrument configuration of DCS, and Figs. 2(b)–2(d) shows *powder-averaged* single crystal data. Figure 2(b) shows the full

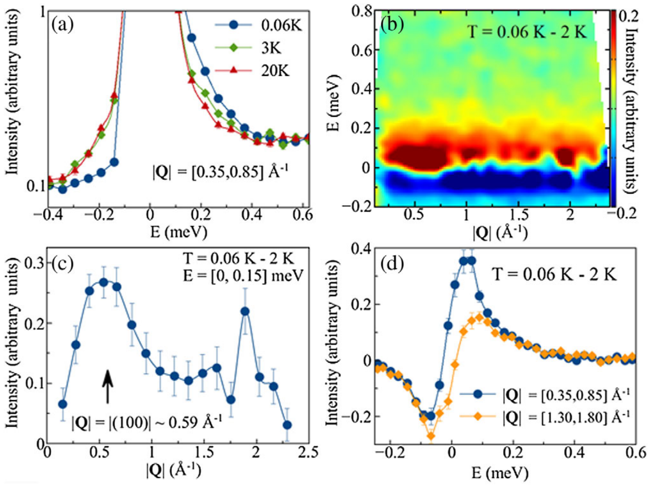

FIG. 2. (a) The onset of dynamic spin ice correlations with decreasing temperature in an annealed $Ce_2Zr_2O_7$ powder sample. (b) The powder-averaged *difference* neutron scattering spectra for an annealed single crystal sample of $Ce_2Zr_2O_7$. A dataset at $T = 2$ K has been subtracted from that at $T = 0.06$ K. (c) A cut along $|\mathbf{Q}|$ through this difference spectra showing that the dominant quasielastic signal, integrated in energy between 0 and 0.15 meV, is centered on $|\mathbf{Q}| = |(001)|$ (∼0.59 Å^{-1}) and (d) a comparison of two cuts in energy through the difference spectra shown in (b), with one of these cuts taken with a $|\mathbf{Q}|$ integral centered on $|(001)|$ (0.35–0.85 Å^{-1}), and one removed from $|(001)|$, integrating between 1.3 and 1.8 Å^{-1}. For all these panels, the error bars correspond to 1 standard deviation.

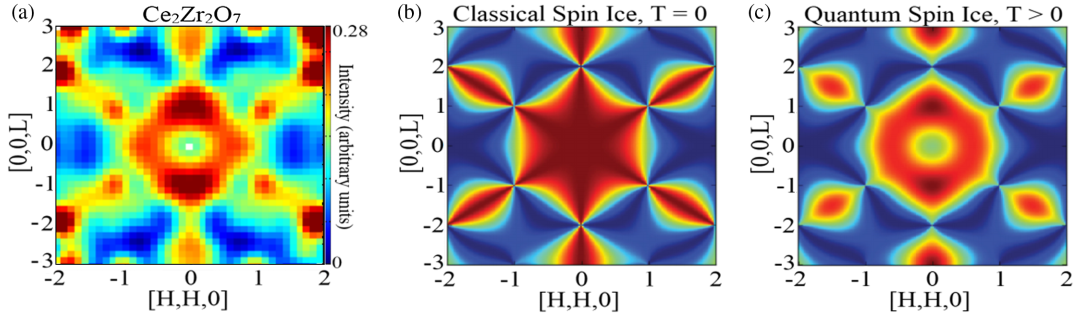

FIG. 3. Comparison of the measured low-energy inelastic neutron scattering from (a) an annealed single crystal sample of $Ce_2Zr_2O_7$ with the calculated quasielastic neutron scattering for (b) the classical near-neighbor spin ice model at $T = 0$ K and (c) a quantum spin ice at finite T. Data in (a) are the symmetrized difference between inelastic scattering at $T = 0.06$ K and $T = 2$ K, integrated between 0 and 0.15 meV. (b),(c) Simulations taken from Benton *et al.* [34]. The lack of intensity around $\mathbf{Q} = (000)$ and the fact that the ring of diffuse inelastic scattering peaks along $(00L)$ provides evidence for $Ce_2Zr_2O_7$ displaying a dynamic quantum spin ice state at these low temperatures. Also, the observed diffuse inelastic scattering at $\mathbf{Q} = (003)$ is more pronounced than that at $\mathbf{Q} = (\frac{3}{2}\frac{3}{2}\frac{3}{2})$, again consistent with the expectations of quantum spin ice, and not consistent with classical near-neighbor spin ice. Note the extra features centered at the Bragg peak positions such as (111) likely originate from leakages of the structural Bragg peaks, due to the subtraction of two large intensities.

powder-averaged spectrum at $T = 0.06$ K with a $T = 2$ K dataset subtracted from it. This result shows enhanced inelastic scattering at low temperature, which peaks up at $|\mathbf{Q}| \sim 0.59$ Å^{-1}, that is, the magnitude of the $\mathbf{Q} = (001)$ position in reciprocal space. This is explicitly shown via the $|\mathbf{Q}|$ cut of the data presented in Fig. 2(c). Importantly, Fig. 2(c) shows no enhancement of the low-energy inelastic scattering around $|\mathbf{Q}| = 0$, consistent with expectations for a U(1) quantum spin ice. Finally, Fig. 2(d) shows energy cuts through the full difference spectrum shown in Fig. 2(b), taken by integrating in $|\mathbf{Q}|$ from 0.35 to 0.85 Å^{-1}, so around $|\mathbf{Q}| = |(001)|$, and also well away from $|\mathbf{Q}| = |(001)|$, integrating from 1.3 to 1.8 Å^{-1}. This clearly shows the quantum spin ice correlations to be dynamic in nature, characterized by an energy less than ~0.15 meV.

With the energy range of the dynamic quantum spin ice correlations identified, we can look explicitly at this scattering from the single crystal, but now comparing $\mathbf{Q}$ maps of these correlations to the expectations of both classical near-neighbor spin ice (without dipolar interactions) and a U(1) quantum spin ice. Figure 3(a) shows $T = 0.06$–2 K data integrated between 0 and 0.15 meV, folded into a single quadrant of the $[HHL]$ map and further symmetrized. The details of this data symmetrization are in the Supplemental Material [36]. For reference, a theoretical simulation of the structure factor expected for classical near-neighbor spin ice [34] is shown in Fig. 3(b) and that for a U(1) quantum spin ice at low but finite temperature [34] is shown in Fig. 3(c). While these theoretical predictions have similarities, the structure factor for U(1) quantum spin ice has minima in intensity near $\mathbf{Q} = 0$, while the intensity of the structure factor is maximal there for classical near-neighbor spin ice.

Clearly, the measured dynamic $S(\mathbf{Q})$ shows a qualitatively stronger resemblance to the expectations of the symmetry-enriched U(1) quantum spin ice [31–34]. The quantum spin ice ground state is one of various spin liquids that are supported by a model of well isolated DO CEF doublets on the pyrochlore lattice [19,25]. A similar dynamic $S(\mathbf{Q})$ is expected in the case of classical *dipolar* spin ice (here dipolar refers to long-range dipolar interactions between magnetic dipoles), which also shows the suppression of diffuse scattering near $|\mathbf{Q}| = 0$ [51,52]. Although a definitive conclusion can only be reached once a full spin Hamiltonian is parametrized, the Ce^{3+} ions in $Ce_2Zr_2O_7$ have a moment of 1.286 μ_B, which is roughly a factor 8 smaller than those associated with Ho^{3+} or Dy^{3+} in the classical dipolar spin ices $Ho_2Ti_2O_7$ and $Dy_2Ti_2O_7$. The resulting long-range dipole terms are expected to be ~64 times weaker in $Ce_2Zr_2O_7$, making such a scenario unlikely. This suggests the spin-ice correlations in $Ce_2Zr_2O_7$ originate from quantum effects. An octupolar ordered state is also consistent with the lack of magnetic dipole order in $Ce_2Zr_2O_7$. However, the neutron scattering spectra associated with such an octupolar ordered phase has yet to be calculated; thus we cannot compare it to our data in Fig. 3(a).

The effect of disorder in $Ce_2Zr_2O_7$ is still an open question as we are aware that our single crystals have some low levels of oxidation. Furthermore, stuffing [53–56] (site mixing) is expected to be important in $Ce_2Zr_2O_7$, because both undesired Ce^{4+} and Zr^{3+} ions are chemically stable. It is known that small amounts of disorder can have a drastic impact on the physical properties of frustrated pyrochlore magnets [53,54,56]. It will then be important to further optimize the growth procedure and annealing techniques of $Ce_2Zr_2O_7$. However, we believe that our inelastic neutron scattering results rule out the scenario of a sensitive AIAO order. Indeed, the conventional impact of quenched disorder on a pyrochlore antiferromagnet would be spin glass physics with diffuse scattering peaked for $\mathbf{Q}$'s corresponding to the Bragg positions of the AIAO state. Here, we observe strong diffuse scattering at $\mathbf{Q} = (001)$, which is not only strictly zero for an AIAO state, but also forbidden for all $\mathbf{k} = 0$ long-range ordered magnetic structures allowed by symmetry of the pyrochlore lattice. We thus conclude that our Letter demonstrates $Ce_2Zr_2O_7$ to be one of a very few candidates for quantum spin ice physics. Other candidates for quantum spin ice physics are based on Pr^{3+} and Tb^{3+} pyrochlores [57–61]. However, in contrast to Pr^{3+} and Tb^{3+}, Ce^{3+} is a Kramers ion and its magnetism is thus further protected against disorder, which in and of itself can drive a spin liquid state for non-Kramers doublets [22,62–64]. Furthermore, Tb^{3+} and Pr^{3+} pyrochlores display low-lying CEF field states, which complicate their theoretical understanding due to multipolar interactions [24,65,66]. For all these reasons, the cerium pyrochlores are an excellent theoretical and experimental template to investigate quantum spin ice physics.

We acknowledge useful conversations with Allen Scheie, Alannah Hallas, and Owen Benton. We greatly appreciate the technical support from Alan Ye and Yegor Vekhov at the NIST Center for Neutron Research. This work was supported by the Natural Sciences and Engineering Research Council of Canada (NSERC). A portion of this research used resources at the High Flux Isotope Reactor and Spallation Neutron Source, a DOE Office of Science User Facility operated by the Oak Ridge National Laboratory. We also acknowledge the support of the National Institute of Standards and Technology, U.S. Department of Commerce. Certain commercial equipment, instruments, or materials (or suppliers, or software, etc.) are identified in this Letter to foster understanding. Such identification does not imply recommendation or endorsement by the National Institute of Standards and Technology, nor does it imply that the materials or equipment identified are necessarily the best available for the purpose.

Note added in the proof.—Recently, we became aware of Ref. [67], which reports on a related experimental study on $Ce_2Zr_2O_7$.

[1] J. S. Gardner, M. J. P. Gingras, and J. E. Greedan, Rev. Mod. Phys. **82**, 53 (2010).

[2] A. M. Hallas, J. Gaudet, and B. D. Gaulin, Annu. Rev. Condens. Matter Phys. **9**, 105 (2018).

[3] J. G. Rau and M. J. P. Gingras, Annu. Rev. Condens. Matter Phys. **10**, 357 (2018).

[4] H. Sagayama, D. Uematsu, T. Arima, K. Sugimoto, J. J. Ishikawa, E. O'Farrell, and S. Nakatsuji, Phys. Rev. B **87**, 100403(R) (2013).

[5] S. M. Disseler, Phys. Rev. B **89**, 140413(R) (2014).

[6] S. T. Bramwell and M. J. P. Gingras, Science **294**, 1495 (2001).

[7] M. J. Harris, S. T. Bramwell, D. F. McMorrow, T. H. Zeiske, and K. W. Godfrey, Phys. Rev. Lett. **79**, 2554 (1997).

[8] D. J. P. Morris, D. A. Tennant, S. A. Grigera, B. Klemke, C. Castelnovo, R. Moessner, C. Czternasty, M. Meissner, K. C. Rule, J.-U. Hoffmann, K. Kiefer, S. Gerischer, D. Slobinsky, and R. S. Perry, Science **326**, 411 (2009).

[9] S. H. Curnoe, Phys. Rev. B **78**, 094418 (2008).

[10] S. Onoda, J. Phys. Conf. Ser. **320**, 012065 (2011).

[11] K. A. Ross, L. Savary, B. D. Gaulin, and L. Balents, Phys. Rev. X **1**, 021002 (2011).

[12] L. Savary, K. A. Ross, B. D. Gaulin, J. P. C. Ruff, and L. Balents, Phys. Rev. Lett. **109**, 167201 (2012).

[13] J. G. Rau and M. J. P. Gingras, Phys. Rev. B **92**, 144417 (2015).

[14] J. Robert, E. Lhotel, G. Remenyi, S. Sahling, I. Mirebeau, C. Decorse, B. Canals, and S. Petit, Phys. Rev. B **92**, 064425 (2015).

[15] J. D. Thompson, P. A. McClarty, D. Prabhakaran, I. Cabrera, T. Guidi, and R. Coldea, Phys. Rev. Lett. **119**, 057203 (2017).

[16] S. Petit, J. Robert, S. Guitteny, P. Bonville, C. Decorse, J. Ollivier, H. Mutka, M. J. P. Gingras, and I. Mirebeau, Phys. Rev. B **90**, 060410(R) (2014).

[17] A. M. Hallas, J. Gaudet, N. P. Butch, G. Xu, M. Tachibana, C. R. Wiebe, G. M. Luke, and B. D. Gaulin, Phys. Rev. Lett. **119**, 187201 (2017).

[18] S. Petit, E. Lhotel, F. Damay, P. Boutrouille, A. Forget, and D. Colson, Phys. Rev. Lett. **119**, 187202 (2017).

[19] Y.-P. Huang, G. Chen, and M. Hermele, Phys. Rev. Lett. **112**, 167203 (2014).

[20] S. B. Lee, S. Onoda, and L. Balents, Phys. Rev. B **86**, 104412 (2012).

[21] G. Chen, Phys. Rev. B **96**, 085136 (2017).

[22] N. Martin, P. Bonville, E. Lhotel, S. Guitteny, A. Wildes, C. Decorse, M. Ciomaga Hatnean, G. Balakrishnan, I. Mirebeau, and S. Petit, Phys. Rev. X **7**, 041028 (2017).

[23] S. Onoda and Y. Tanaka, Phys. Rev. B **83**, 094411 (2011).

[24] H. Takatsu, S. Onoda, S. Kittaka, A. Kasahara, Y. Kono, T. Sakakibara, Y. Kato, B. Fåk, J. Ollivier, J. W. Lynn, T. Taniguchi, M. Wakita, and H. Kadowaki, Phys. Rev. Lett. **116**, 217201 (2016).

[25] Y.-D. Li and G. Chen, Phys. Rev. B **95**, 041106(R) (2017).

[26] E. Lhotel, S. Petit, S. Guitteny, O. Florea, M. Ciomaga Hatnean, C. Colin, E. Ressouche, M. R. Lees, and G. Balakrishnan, Phys. Rev. Lett. **115**, 197202 (2015).

[27] C. Mauws, A. M. Hallas, G. Sala, A. A. Aczel, P. M. Sarte, J. Gaudet, D. Ziat, J. A. Quilliam, J. A. Lussier, M. Bieringer, H. D. Zhou, A. Wildes, M. B. Stone, D. Abernathy, G. M. Luke, B. D. Gaulin, and C. R. Wiebe, Phys. Rev. B **98**, 100401(R) (2018).

[28] O. Benton, Phys. Rev. B **94**, 104430 (2016).

[29] S. Petit, E. Lhotel, B. Canals, M. C. Hatnean, J. Ollivier, H. Mutka, E. Ressouche, A. Wildes, M. Lees, and G. Balakrishnan, Nat. Phys. **12**, 746 (2016).

[30] R. Sibille, E. Lhotel, V. Pomjakushin, C. Baines, T. Fennell, and M. Kenzelmann, Phys. Rev. Lett. **115**, 097202 (2015).

[31] M. Hermele, M. P. A. Fisher, and L. Balents, Phys. Rev. B **69**, 064404 (2004).

[32] L. Savary and L. Balents, Phys. Rev. Lett. **108**, 037202 (2012).

[33] L. Savary and L. Balents, Phys. Rev. B **87**, 205130 (2013).

[34] O. Benton, O. Sikora, and N. Shannon, Phys. Rev. B **86**, 075154 (2012).

[35] H. Otobe, A. Nakamura, T. Yamashita, and K. Minato, J. Phys. Chem. Solids **66**, 329 (2005).

[36] See Supplemental Material at http://link.aps.org/supplemental/10.1103/PhysRevLett.122.187201 for details on experimental methods, crystal-field calculations and analysis of the neutron scattering experiments.

[37] J. B. Thomson, A. R. Armstrong, and P. G. Bruce, J. Solid State Chem. **148**, 56 (1999).

[38] J. B. Thomson, A. R. Armstrong, and P. G. Bruce, Chem. Commun. (Cambridge) 10 (**1996**) 1165.

[39] J. Gaudet, D. D. Maharaj, G. Sala, E. Kermarrec, K. A. Ross, H. A. Dabkowska, A. I. Kolesnikov, G. E. Granroth, and B. D. Gaulin, Phys. Rev. B **92**, 134420 (2015).

[40] A. J. Freeman and R. E. Watson, Phys. Rev. **127**, 2058 (1962).

[41] M. Blume, A. Freeman, and R. Watson, Phys. Rev. **134**, A320 (1964).

[42] J. H. VanVleck, *The Theory of Electronic and Magnetic Susceptibilities* (Oxford University Press, London, 1932).

[43] R. Azuah, L. Kneller, Y. Qiu, C. Brown, J. Copley, R. Dimeo, and P. Tregenna-Piggott, J. Res. Natl. Inst. Stand. Technol. **114**, 341 (2009).

[44] A. M. Hallas, J. Gaudet, M. N. Wilson, T. J. Munsie, A. A. Aczel, M. B. Stone, R. S. Freitas, A. M. Arevalo-Lopez, J. P. Attfield, M. Tachibana, C. R. Wiebe, G. M. Luke, and B. D. Gaulin, Phys. Rev. B **93**, 104405 (2016).

[45] G. E. Granroth, A. I. Kolesnikov, T. E. Sherline, J. P. Clancy, K. A. Ross, J. P. C. Ruff, B. D. Gaulin, and S. E. Nagler, J. Phys. Conf. Ser. **251**, 012058 (2010).

[46] J. Gaudet, A. M. Hallas, A. I. Kolesnikov, and B. D. Gaulin, Phys. Rev. B **97**, 024415 (2018).

[47] G. Sala, D. D. Maharaj, M. B. Stone, H. A. Dabkowska, and B. D. Gaulin, Phys. Rev. B **97**, 224409 (2018).

[48] J. Gaudet, A. M. Hallas, C. R. C. Buhariwalla, G. Sala, M. B. Stone, M. Tachibana, K. Baroudi, R. J. Cava, and B. D. Gaulin, Phys. Rev. B **98**, 014419 (2018).

[49] M. Ruminy, E. Pomjakushina, K. Iida, K. Kamazawa, D. T. Adroja, U. Stuhr, and T. Fennell, Phys. Rev. B **94**, 024430 (2016).

[50] K. Popa, R. Konings, F. Wastin, E. Colineau, N. Magnani, and P. Raison, J. Phys. Chem. Solids **69**, 70 (2008).

[51] B. C. den Hertog and M. J. P. Gingras, Phys. Rev. Lett. **84**, 3430 (2000).

[52] S. T. Bramwell, M. J. Harris, B. C. Den Hertog, M. J. P. Gingras, J. S. Gardner, D. F. McMorrow, A. R. Wildes, A. Cornelius, J. D. M. Champion, R. G. Melko, and T. Fennell, Phys. Rev. Lett. **87**, 047205 (2001).

[53] K. A. Ross, T. H. Proffen, H. A. Dabkowska, J. A. Quilliam, L. R. Yaraskavitch, J. B. Kycia, and B. D. Gaulin, Phys. Rev. B **86**, 174424 (2012).

[54] S. M. Koohpayeh, J.-J. Wen, B. A. Trump, C. L. Broholm, and T. M. McQueen, J. Cryst. Growth **402**, 291 (2014).

[55] K. Baroudi, B. D. Gaulin, S. H. Lapidus, J. Gaudet, and R. J. Cava, Phys. Rev. B **92**, 024110 (2015).

[56] K. E. Arpino, B. A. Trump, A. O. Scheie, T. M. McQueen, and S. M. Koohpayeh, Phys. Rev. B **95**, 094407 (2017).

[57] H. D. Zhou, C. R. Wiebe, J. A. Janik, L. Balicas, Y. J. Yo, Y. Qiu, J. R. D. Copley, and J. S. Gardner, Phys. Rev. Lett. **101**, 227204 (2008).

[58] K. Fritsch, K. A. Ross, Y. Qiu, J. R. D. Copley, T. Guidi, R. I. Bewley, H. A. Dabkowska, and B. D. Gaulin, Phys. Rev. B **87**, 094410 (2013).

[59] K. Kimura, S. Nakatsuji, J.-J. Wen, C. L. Broholm, M. B. Stone, E. Nishibori, and H. Sawa, Nat. Commun. **4**, 1934 (2013).

[60] R. Sibille, E. Lhotel, M. C. Hatnean, G. Balakrishnan, B. Fåk, N. Gauthier, T. Fennell, and M. Kenzelmann, Phys. Rev. B **94**, 024436 (2016).

[61] R. Sibille, N. Gauthier, H. Yan, M. C. Hatnean, J. Ollivier, B. Winn, U. Filges, G. Balakrishnan, M. Kenzelmann, N. Shannon, and T. Fennell, Nat. Phys. **14**, 711 (2018).

[62] L. Savary and L. Balents, Phys. Rev. Lett. **118**, 087203 (2017).

[63] J.-J. Wen, S. M. Koohpayeh, K. A. Ross, B. A. Trump, T. M. McQueen, K. Kimura, S. Nakatsuji, Y. Qiu, D. M. Pajerowski, J. R. D. Copley, and C. L. Broholm, Phys. Rev. Lett. **118**, 107206 (2017).

[64] O. Benton, Phys. Rev. Lett. **121**, 037203 (2018).

[65] H. R. Molavian, M. J. P. Gingras, and B. Canals, Phys. Rev. Lett. **98**, 157204 (2007).

[66] S. Petit, E. Lhotel, S. Guitteny, O. Florea, J. Robert, P. Bonville, I. Mirebeau, J. Ollivier, H. Mutka, E. Ressouche, C. Decorse, M. Ciomaga Hatnean, and G. Balakrishnan, Phys. Rev. B **94**, 165153 (2016).

[67] B. Gao *et al.*, arXiv:1901.10092.

SUPPLEMENTAL MATERIAL:
Quantum Spin Ice Dynamics in the Dipole-Octupole Pyrochlore Magnet $Ce_2Zr_2O_7$

J. Gaudet,[1, 2, 3] E. M. Smith,[1] J. Dudemaine,[4] J. Beare,[1] C. R. C. Buhariwalla,[1] N. P. Butch,[3] M. B. Stone,[5] A. I. Kolesnikov,[5] Guangyong Xu,[3] D. R. Yahne,[6] K. A. Ross,[6, 7] C. A. Marjerrison,[8] J. D. Garrett,[8] G. M. Luke,[1, 7] A. D. Bianchi,[4, 9] and B. D. Gaulin[1, 7, 8]

[1] *Department of Physics and Astronomy, McMaster University, Hamilton, ON, L8S 4M1, Canada*
[2] *Institute for Quantum Matter and Department of Physics and Astronomy,*
Johns Hopkins University, Baltimore, MD 21218, USA
[3] *Center for Neutron Research, National Institute of Standards and Technology, MS 6100 Gaithersburg, Maryland 20899, USA*
[4] *Département de Physique, Université de Montréal,*
2900 Boul.Édouard-Montpetit, Montréal, QC, H3T 1J4, Canada
[5] *Neutron Scattering Division, Oak Ridge National Laboratory, Oak Ridge, Tennessee 37831, USA*
[6] *Department of Physics, Colorado State University,*
200 W. Lake St., Fort Collins, CO 80523-1875, USA
[7] *Canadian Institute for Advanced Research, 661 University Ave., Toronto, ON, M5G 1M1, Canada*
[8] *Brockhouse Institute for Materials Research, McMaster University, Hamilton, ON L8S 4M1 Canada*
[9] *Regroupement Québécois sur les Matériaux de Pointe (RQMP), Quebec, QC H3T 3J7 Canada*

POWDER SYNTHESIS AND SINGLE CRYSTAL GROWTH

The polycrystalline and powder samples of $Ce_2Zr_2O_7$ used in this work were first prepared by arc melting stoichiometric amounts of CeO_2, Zr, and ZrO_2 in an argon atmosphere, followed by a regrinding and firing at 1000°C for two days in flowing hydrogen. Prior to any measurements, the powder samples were further annealed in flowing hydrogen at 1000°C for several hours. An x-ray refinement against the $Fd\bar{3}m$ space group is shown in Fig.S1(a) for one of the $Ce_2Zr_2O_7$ powder samples, synthesized and annealed using this protocol. Previous studies have characterized the level of oxidation of $Ce_2Zr_2O_{7+\delta}$ powder samples using the value of the lattice parameter, a, refined from x-ray diffraction measurements. For example, the values $a \sim 10.735$ Å has been refined for $\delta = 0$ and $a \sim 10.66$ Å has been refined for $\delta = 0.5$. A linear relationship has been observed between these limits [1–3]. Our materials synthesis and powder x-ray diffraction is consistent with these previous works, and, as shown in Fig.S1(a), our stoichiometric powder sample has a lattice parameter of $a = 10.735(5)$ Å. As we will discuss, we observe the oxidation of the powder sample left exposed to air to begin to occur on the order of minutes. There is an obvious colour change which occurs between the stoichiometric (annealed) and oxidized samples, wherein a light green/yellow sample is obtained for the $\delta = 0$ annealed sample, and a black powder is obtained for the $\delta = 0.5$ oxidized sample.

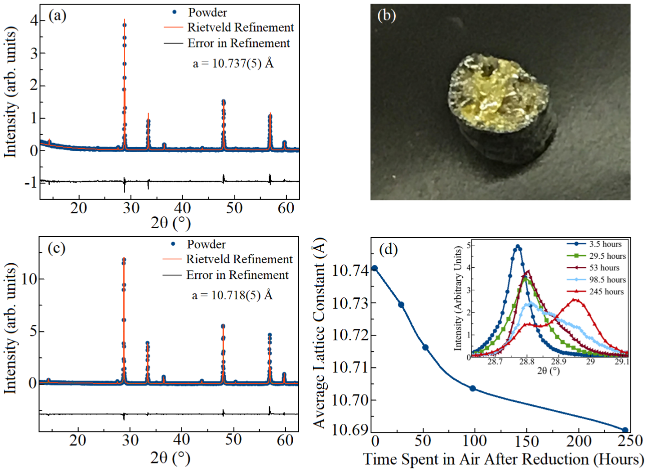

FIG. 1. (a) Powder x-ray refinement of a typical powder sample of $Ce_2Zr_2O_7$ synthesized for this work. A lattice parameter of 10.735(5) Å has been refined. (b) A photograph of an annealed single crystal sample of $Ce_2Zr_2O_7$, broken with an exposed surface, and showing a bright yellow color on the inside and a thin black oxidized surface on the outside. (c) Powder x-ray refinement of a crushed single crystal of $Ce_2Zr_2O_7$ against the pyrochlore structure. (d) The time dependence of the lattice parameter is shown for a polycrystalline sample of $Ce_2Zr_2O_7$, annealed in hydrogen at 1200°C for 6 hours, and then left exposed to air. The exposure to air produces oxidation of the sample over time and a decreasing lattice parameter. The inset shows typical x-ray diffraction scans collected at different times of exposure to air, following the annealing protocol.

Single crystals of $Ce_2Zr_2O_7$ were obtained using optical floating zone growth, with Xe lamps, from polycrystalline feed stock. The powder rods were first prepared through a solid state reaction using high purity materials. Stoichiometric mixtures of Ce_2O_3 (99.995%) and ZrN (99.5%) were mixed in a ball mill and pressed into rods. The rods were heated in air to 900°C in a covered alumina crucible for 5 h. The solidified rods were then re-ground in a ball mill, repressed into rods 8 cm and 6 cm in length to be used as the feed and seed rods for the optical floating zone growth. These rods were then heated to 1550°C for 3 h in an atmosphere containing a ratio of 95/5 argon to hydrogen. During the actual optical floating zone

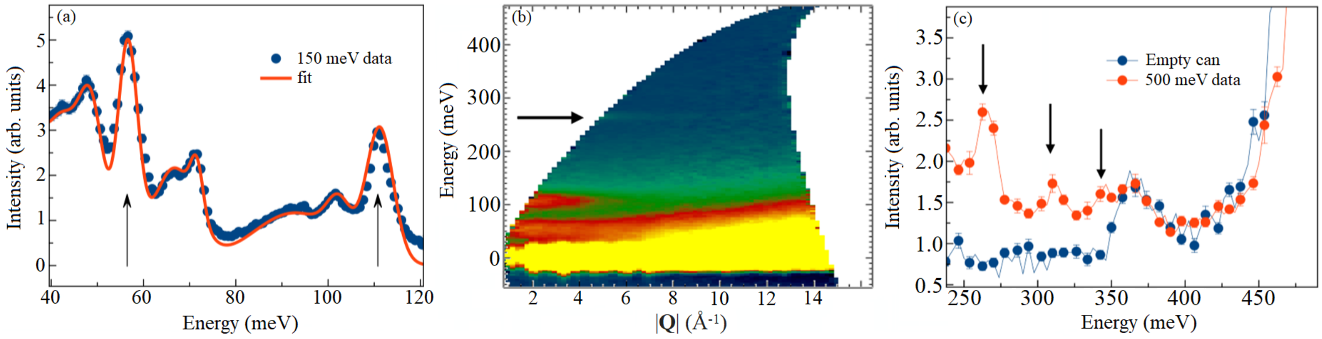

FIG. 2. (a) Inelastic neutron scattering spectra obtained for an incident energy of 150 meV for $Ce_2Zr_2O_7$, and integrated between $|\mathbf{Q}| = 4.5$ and 5.5 Å^{-1} (this is a cut of the data shown in Fig.1(a) of the main manuscript). The two black arrows indicate the energy position of the CEF transitions originating from the main Ce^{3+} site. (b) High energy inelastic neutron scattering spectra of $Ce_2Zr_2O_7$ obtained with an incident energy of 500 meV. The arrow highlights the relatively weaker magnetic excitations near 275 meV. c) A constant energy cut of the data shown in b), integrated in $|\mathbf{Q}|$ between 7 and 10 Å^{-1}, is shown, along with data from the empty sample can. We identify three CEF transitions from the ground state to the highest J manifold at $\sim$ 270 meV, 310 meV and 340 meV. These energies are sufficiently high, such that no optic phonons are expected to be nearby in energy.

growth, we employed a growth rate of 2.5 mm/hour while counter-rotating feed and seed rods at 15 rpm in an argon atmosphere containing 5% hydrogen. Further annealing of the single crystals for 36 hours at 1200°C was also performed prior to all experiments. A photograph of a typical single crystal of $Ce_2Zr_2O_7$ obtained through this protocol is shown in Fig.S1(b). A broken surface is shown and one can see that the inside of the single crystal piece is bright yellow while the surface exposed to air is black, indicating some remaining oxidation at the surface after the annealing process. Refinement of a yellow single crystal piece from the unexposed inner layer of the crystal is shown in Fig.1(c). Such x-ray diffraction measurements on crushed single crystals give a lattice parameter refinement of $a = 10.718(5)$ Å for the bulk inner layer of the crystal, as shown in Fig.1(c), and this can be use to estimate the oxidation state of our annealed single crystal sample, $Ce_2Zr_2O_{7+\delta}$, to be $\delta \sim 0.1$.

Finally, we characterized the time dependence of $Ce_2Zr_2O_{7+\delta}$ by collecting several powder diffraction patterns from a broken, ceramic rod of material, for differing exposure times in air following a 1200°C, 6 hour hydrogen annealing protocol. The lattice parameter extracted from x-ray diffraction measurements is shown as a function of time in Fig.S1(d) for this polycrystalline sample, whose oxidation rate should be between the fast rate of the powder samples of $Ce_2Zr_2O_{7+\delta}$ and slow rate of the relatively-well behaved single crystal samples of $Ce_2Zr_2O_{7+\delta}$. The inset shows x-ray diffraction scans of the $\mathbf{Q} = (222)$ Bragg peak as a function of scattering angle and exposure time. Not only do the Bragg peaks shift higher in 2θ with exposure (sample oxidation), they also significantly broaden and eventually split into multiple distinguishable peaks. This broadening and splitting corresponds to a distribution of oxidation in the sample, and to the eventual formation of separate majority and minority phases with different levels of oxidation, such as the bulk inner and thin outer layers of differing color in the case of single crystal $Ce_2Zr_2O_{7+\delta}$. The x-ray intensity at the $\mathbf{Q} = (222)$ Bragg position for each data set was fit to Lorentzian peak shapes according to the number of peaks present around that Bragg position. The average lattice constant for each data set with multiple distinguishable peaks ($>$ 29.5 hours) was determined by using a weighted average of the lattice constants determined from these peaks, with the integrated intensity of the peaks used as the weights for this average. Figure S1(d) should then give the time dependence of the volume-averaged lattice constant in this polycrystalline sample.

DETERMINATION OF THE CEF HAMILTONIAN

As discussed in the main manuscript, the CEF eigenstates for Ce^{3+} in $Ce_2Zr_2O_7$ were expressed in the $|J = 5/2, m_J\rangle$ manifold and fitted using the low energy CEF transitions observed in the $E_i = 150$ meV neutron scattering spectra. We refined a CEF Hamiltonian for $Ce_2Zr_2O_7$ by constraining the relative scattered intensities and energies of the CEF transitions observed in our $E_i = 150$ meV spectra (Fig.1(a) of the main letter). The following CEF Hamiltonian was used in this work:

$$\mathcal{H}_{CEF} = B_2^0\hat{O}_2^0 + B_4^0\hat{O}_4^0 + B_4^3\hat{O}_4^3 \qquad (1)$$

The protocol and the expression of the CEF Hamiltonian in terms of Stevens operators used in this work is identical to ref. [4, 5] and we refer the reader to these works for further details. It is worthwhile mentioning that the CEF Hamiltonian appropriate for the $R^{3+}(D_{3d})$ site of the pyrochlore lattice includes six Stevens operators (B_2^0, B_4^0, B_4^3, B_6^0, B_6^3, B_6^6), however the three B_6^n terms are zero for Ce^{3+}.

The B_2^0, B_4^0 and B_4^3 terms of the CEF Hamiltonian were refined using the observed energies and scattered neutron intensities of the magnetic excitations near 58 and 110 meV. It was possible to extract this information using a constant $|\mathbf{Q}|$-cut from the 150 meV data. We obtain this by integrating the 150 meV spectra (Fig.1(a) of the main letter) between $|\mathbf{Q}|$ = 4.5 and 5.5 Å^{-1}. The resulting integration is shown in Fig.S2(a). The two CEF transitions, so-identified by their $|\mathbf{Q}|$-dependence, are indicated by the black arrows in Fig.S2(a), while other features observed in Fig.S2(a) are likely optical phonon excitations. The CEF transitions as well as the phonon excitations were fitted using a Lorentzian function in energy. The resulting fit of the 150 meV data set is plotted in Fig.S2(a). From this fit, we determined that the energies of the CEF levels within the spin-orbit J-manifold are $E_1 = 55.9(1)$ and $E_2 = 110.5(1)$ meV. The relative intensity of the CEF transitions between the CEF ground state to the first (I_1) and the second (I_2) excited state is found to be $I_1/I_2 = 1.2(1)$. Using these three constraints (E_1, E_2, I_1/I_2), we refined $B_2^0 = 0.835$ meV, $B_4^0 = 0.299$ meV and $B_4^3 = 2.875$ meV. Comparison between the calculation and data is shown in Table.S1. The calculated eigenstates and eigenfunctions using this CEF Hamiltonian are reported in Table.S2.

In the main letter, we also reported a weaker magnetic excitation near 100 meV, so just below E_2. It is possible that magneto-elastic coupling between the CEF ground state and the 2nd excited CEF state (E_2) is sufficiently strong to drive a vibronic bound state, which would effectively split the single-ion CEF excitation at E_2 into two different excitations [6]. Here, these two excitations would correspond to the one at 110 meV and the one at 100 meV. Thus, within the scenario of a vibronic bound state as the origin of the inelastic scattering at 100 meV, we underestimated I_2. We can compensate for this by adding the integrated intensity of the 100 meV transition. By doing so, a new optimization of the CEF Hamiltonian could be refined, leading to $B_2^0 = 0.455$ meV, $B_4^0 = 0.295$ meV and $B_4^3 = 2.582$ meV. Table.S1 also shows the comparison between the data and the calculation within such a scenario. This scenario in which a vibronic bound state is responsible for the weak inelastic intensity near 100 meV also leads to a CEF ground state that is a pure $m_J = \pm 3/2$ state. Thus the conclusion that the CEF ground state doublet for $Ce_2Zr_2O_7$ is a pure $m_J = \pm 3/2$ doublet with dipolar octupolar character is robust.

We also present the $E_i = 500$ meV inelastic neutron scattering spectra of $Ce_2Zr_2O_7$ in Fig.S2(b). This inelastic scattering data shows a clear magnetic feature near 275 meV that corresponds to a transition originating from the CEF ground state to the highest J-manifold ($J = 7/2$). Two additional, albeit weaker, excitations can be identified by taking appropriate $|\mathbf{Q}|$ cuts of this data and comparing to the measured empty can, background scattering. This is shown in Fig.S2(c), where a $|\mathbf{Q}|$ integration from $|\mathbf{Q}|$ = 7 to 10 Å^{-1} is performed. This reveals three CEF transitions ~ 260, 310 and possibly 340 meV. The location in energy of these highest $J = 7/2$ states is consistent with estimates of the spin-orbit coupling strength (λ) for Ce^{3+} [7, 8].

TABLE I. Comparison between the observed (Obs_1,Obs_2) and calculated ($Calc_1$,$Calc_2$) energies and intensities of the CEF excitations in $Ce_2Zr_2O_7$. Scenario 1 refers to the case where no vibronic bound state is present, while Scenario 2 is the case where weak inelastic scattering near 100 meV is identified as arising due to a vibronic bound state.

	Obs$_1$	**Calc$_1$**	**Obs$_2$**	**Calc$_2$**
E_1 (meV)	55.9(2)	55.92	55.9(1)	56.06
E_2 (meV)	110.5(3)	110.55	106.1(4)	105.97
I_1/I_2 (arb.units)	1.2(1)	0.98	0.99(15)	0.92

TABLE II. Eigenstates and eigenfunctions of the spin-orbit ground state manifold written within the $|J = 5/2, m_J\rangle$ basis. These eigenfunctions correspond to the scenario of no vibronic bound-state. A $m_J = \pm 3/2$ CEF ground state is stabilized for both scenarios (without and with a vibronic bound state).

E(meV)	**-5/2**	**-3/2**	**-1/2**	1/2	**3/2**	**5/2**
E_1	0	1	0	0	0	0
E_2	0	0	0	0	1	0
E_3	0.725	0	0	0.688	0	0
E_4	0	0	-0.688	0	0	0.725
E_5	0	0	-0.725	0	0	-0.688
E_6	0.688	0	0	-0.725	0	0

Finally, the determination of our CEF Hamiltonian appropriate for $Ce_2Zr_2O_7$ was further validated via calculation of its Van-Vleck susceptibility that can be compared with the temperature dependence of its measured magnetic susceptibility. The following Van-Vleck susceptibility term (ref.[9]) was computed for a powder sample:

$$\chi_{CEF} = \frac{N_A g_J^2 \mu_B^2 X}{k_B Z} \sum_{\alpha} \Big(\sum_{n} \frac{|\langle n|J_\alpha|n\rangle|^2 e^{-E_n/T}}{T} + \sum_{n} \sum_{m \neq n} \frac{|\langle m|J_\alpha|n\rangle|^2 (e^{-E_n/T} - e^{-E_m/T})}{E_m - E_n} \Big) \quad (2)$$

where $\alpha = x, y, z$, N_A is the Avogadro constant, g_J is the Landé g-factor, k_B is the Boltzman constant, μ_B is the Bohr magneton and $Z = \sum_n e^{-E_n/T}$ is the partition function. The factor X was used to parametrize the dilution of the Ce^{3+} ions into non-magnetic Ce^{4+} and was refined to 0.92(2), which is in good agreement with our estimate of the oxidation level in our samples using the refined lattice parameters (see section 1 of the SM).

DETAILS ON THE LACK OF MAGNETIC ORDER IN $CE_2ZR_2O_7$

An orange cryostat with a dilution refrigerator insert was used for both of our DCS experiments. The powder sample was wrapped in of a copper foil inside a copper can sealed under 10 atm of He. For the single crystal experiment, the sample was aligned and mounted on a copper mount. For the data collection of our single crystal DCS experiment, the single crystal was rotated for a total of 270° with steps of 0.5 ° and we counted for 5 minutes per angle at $T = 0.06$ K and 3 minutes per angle at $T = 2$ K. The data was analyzed and plotted using DAVE [10].

We demonstrate the evidence for no magnetic order in $Ce_2Zr_2O_7$ to temperatures as low as $T = 0.06$ K using our single crystal DCS experiment. We do this by noting that no new Bragg peaks are observed at $T = 0.06$ K compared with $T = 2$ K, and by explicitly isolating the elastic scattering for each $\mathbf{k} = 0$ Bragg peak accessible in our experiment. This elastic scattering is shown in Fig.S3 at both $T = 0.06$ K and $T = 2$ K for the $\mathbf{Q} =$ (220),(113),(111),(222) and (002) positions of reciprocal space, with $E_i = 3.27$ meV incident neutrons and energy integration in the range from -0.1 to 0.1 meV. None of these selected $\mathbf{k} = 0$ positions in reciprocal space show any significant changes in intensity with temperature as can be seen by the subtraction of the $T = 2$ K data set from the $T = 0.06$ K data set in each plot of Fig.S3. The elastic cuts through the $\mathbf{Q} =$ (220),(113) and (111) positions were taken along the (HH0) direction with integration in (00L) from L = -0.1 to 0.1 r.l.u., 2.9 to 3.1 r.l.u., and 0.9 to 1.1 r.l.u. respectively and the elastic cuts through the $\mathbf{Q} =$ (222) and (002) positions were taken along the (00L) direction with integration in (HH0) from H = 1.9 to 2.1 r.l.u. and -0.1 to 0.1 r.l.u. respectively. Figure S3(f) shows a table qualitatively outlining which of these positions is expected to show magnetic intensity for each $\mathbf{k} = 0$ magnetic structure permitted by the pyrochlore lattice [11]. A green check mark indicates the presence of magnetic intensity at that location due to the corresponding ordered structure, while the red symbol indicates that the corresponding structure results in no magnetic intensity at that location. For example, the Γ_3 structure corresponding to AIAO order generates magnetic intensity at the (220) and (113) positions only. As can be seen from this Table, the fact that we have measured no magnetic intensity at each of the (220), (111), (113), (222) and (002) positions, signifies a lack of $\mathbf{k} = 0$ magnetic order in $Ce_2Zr_2O_7$ down to $T = 0.06$ K. Furthermore, the whole elastic $\mathbf{Q}$ map within the (HHL) plane can be plotted for 0.06 K and this is shown in Fig.S3(g). Only the expected structural Bragg peaks are visible in Fig.S3(g), which confirms the lack of $\mathbf{k}$=0 magnetic order.

We note that our powder and single crystal DCS experiments that both show no magnetic order in $Ce_2Zr_2O_7$ are further corroborated with cold neutron triple-axis experiment using the SPINS instrument, also at NIST. For this experiment, the sample was also mounted on a copper mount and aligned within the (HHL) plane. An orange cryostat with an He3 insert was used for this experiment. Figure S4 shows θ-2θ scans for several Bragg peaks at both 5.2 K and 0.3 K collected with neutron incident energies of 5 meV. It is clear from the temperature difference data that our triple-axis experiment also does not support the existence of $\mathbf{k} = 0$ magnetic order in $Ce_2Zr_2O_7$ down to 0.3 K.

Finally, low temperature magnetic susceptibility measurements of $Ce_2Zr_2O_7$ were performed in several fields with both field cooled (FC) and zero field cooled (ZFC) protocol. As seen in Fig.S5, our low temperature susceptibility measurements do not reveal any sign of magnetic ordering or spin freezing down to ~ 0.5 K. Furthermore, the general behaviour of the susceptibility is not impacted by the field value used for these measurements.

DETAILS OF THE SYMMETRIZATION PROCESS IN OUR LOW ENERGY INELASTIC NEUTRON SCATTERING (DCS) EXPERIMENT ON A SINGLE CRYSTAL

In this section, we outline the symmetrization process used to average the $\mathbf{Q}$-dependence of the inelastic temperature difference data from an annealed single crystal sample of $Ce_2Zr_2O_7$ using the DCS instrument, shown in Fig.3 of the main manuscript. Figure S6(a) displays the subtraction of a $T = 2$ K data set from a $T = 0.06$ K data set, integrated in energy over the range from 0 to 0.15 meV , with $E_i = 3.27$ meV incident neutrons. This is the unsymmetrized data that was used to produce the symmetrized data shown in Fig.3(a) of the main letter. The intermediate steps in this symmetric averaging are shown in Fig.S6(b) and Fig.S6(c) where the data has been folded upon itself and averaged with respect to the (00L) and (HH0) lines of symmetry. The fully symmetrized data is displayed in Fig.S6(d) to further illustrate the process. Only one quadrant of this data set is truly independent; the other three quadrants are required to impose the symmetry of the reciprocal lattice. No other constraints are imposed on the data. This data set corresponds to symmetric averaging with respect to both the (00L) and (HH0) lines of symmetry. This symmetrization helps to bring out relatively weak signals, as such signals are measured at more than one equivalent $\mathbf{Q}$ position, and averaged over. Non-symmetric features in the scattering, resulting from, for example self-absorption, are also averaged over and hence diminished in the process.

[1] H. Otobe, A. Nakamura, T. Yamashita, and K. Minato, J. Phys. Chem. Solids **66**, 329 (2005).

[2] J. B. Thomson, A. R. Armstrong, and P. G. Bruce, J. Solid State Chem. **148**, 56 (1999).

[3] J. B. Thomson, A. R. Armstrong, and P. G. Bruce, Chem. Comm. , 1165 (1996).

[4] J. Gaudet, D. D. Maharaj, G. Sala, E. Kermarrec, K. A. Ross, H. A. Dabkowska, A. I. Kolesnikov, G. E. Granroth, and B. D. Gaulin, Phys. Rev. B **92**, 134420 (2015).

[5] J. Gaudet, A. M. Hallas, A. I. Kolesnikov, and B. D. Gaulin, Phys. Rev. B **97**, 024415 (2018).

[6] J. Gaudet, A. M. Hallas, C. R. C. Buhariwalla, G. Sala, M. B. Stone, M. Tachibana, K. Baroudi, R. J. Cava, and B. D. Gaulin, Phys. Rev. B **98**, 014419 (2018).

[7] A. J. Freeman and R. E. Watson, Phys. Rev. **127**, 2058 (1962).

[8] M. Blume, A. Freeman, and R. Watson, Phys. Rev. **134**, A320 (1964).

[9] J. H. VanVleck, *The Theory of Electronic and Magnetic Susceptibilities* (Oxford Univ. Press, London, 1932).

[10] R. Azuah, L. Kneller, Y. Qiu, C. Brown, J. Copley, R. Dimeo, and P. Tregenna-Piggott, J. Res. Natl. Inst. Stan. Technol. **114** (2009).

[11] A. M. Hallas, J. Gaudet, M. N. Wilson, T. J. Munsie, A. A. Aczel, M. B. Stone, R. S. Freitas, A. M. Arevalo-Lopez, J. P. Attfield, M. Tachibana, C. R. Wiebe, G. M. Luke, and B. D. Gaulin, Phys. Rev. B **93**, 104405 (2016).

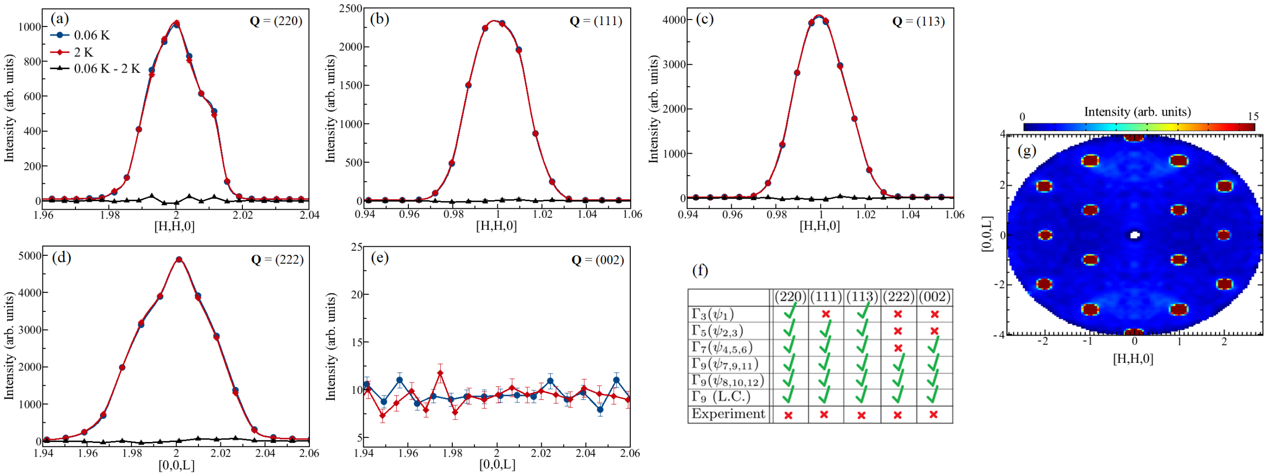

	(220)	(111)	(113)	(222)	(002)
$\Gamma_3(\psi_1)$	✓	✗	✓	✗	✗
$\Gamma_5(\psi_{2,3})$	✓	✓	✓	✗	✗
$\Gamma_7(\psi_{4,5,6})$	✓	✓	✓	✗	✓
$\Gamma_9(\psi_{7,9,11})$	✓	✓	✓	✓	✓
$\Gamma_9(\psi_{8,10,12})$	✓	✓	✓	✓	✓
Γ_9 (L.C.)	✓	✓	✓	✓	✓
Experiment	✗	✗	✗	✗	✗

FIG. 3. Elastic neutron scattering data from an annealed single crystal of $Ce_2Zr_2O_7$ collected using a time-of-flight neutron spectrometer. Elastic cuts in reciprocal space are shown at $T = 0.06$ K (blue) and $T = 2$ K (red) as well as the $T = 2$ K data set subtracted from the $T = 0.06$ K data set (black). This elastic data has been integrated from -0.1 meV to 0.1 meV in energy. No significant changes in intensity were measured at the (a) (220), (b) (111), (c) (113), (d) (222), or (e) (002) positions of reciprocal space. (f) A table qualitatively outlining which of these $\mathbf{Q}$ positions is expected to show magnetic intensity for the different $\mathbf{k} = 0$ magnetic structures permitted by the pyrochlore lattice [11]. The green check marks indicate the presence of magnetic intensity at that location due to the corresponding ordered structure while the red symbols indicate that the structure results in no magnetic intensity at that location. As can be seen from this table, the fact that the measured positions showed no systematic change of intensity with temperature indicates a lack of $\mathbf{k} = 0$ magnetic order down to $T = 0.06$ K. (g) A $T = 0.06$ K map showing the elastic scattering for momentum transfer within the (HHL) plane, which rules out the possible presence of magnetic Bragg peaks with non $\mathbf{k} = 0$ ordering vector.

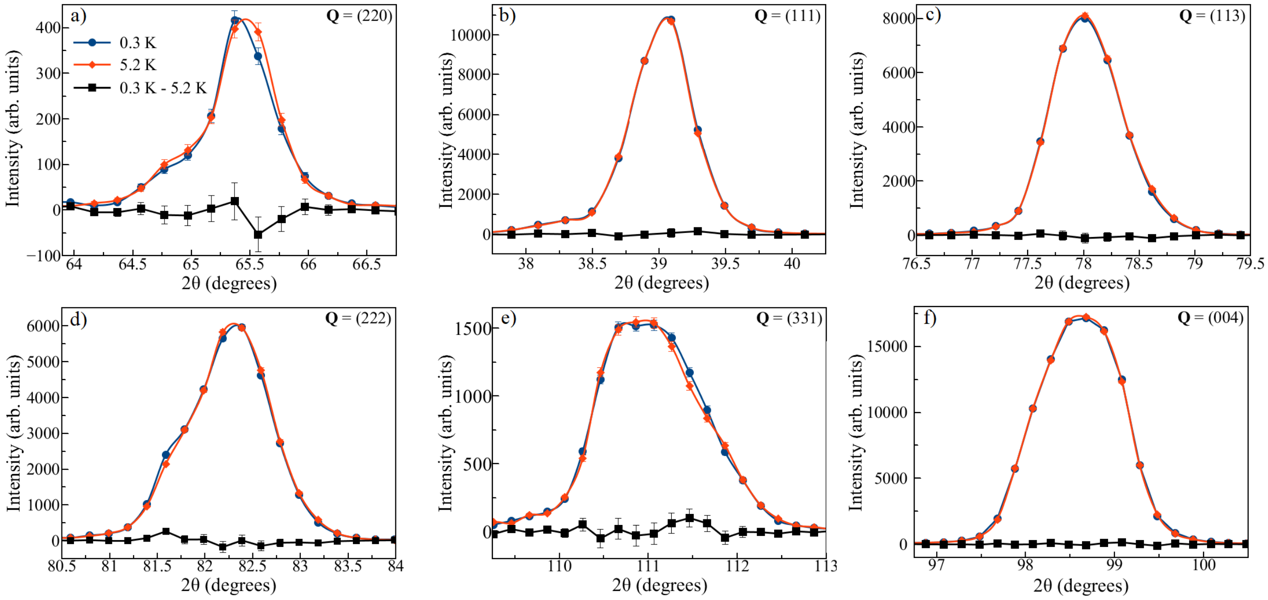

FIG. 4. θ-2θ scans for (a) $\mathbf{Q} = (220)$, (b) $\mathbf{Q} = (111)$, (c) $\mathbf{Q} = (113)$, (d) $\mathbf{Q} = (222)$, (e) $\mathbf{Q} = (004)$ and (f) $\mathbf{Q} = (331)$ collected on an annealed single crystal of $Ce_2Zr_2O_7$. These measurements were performed using a neutron triple-axis instrument at a temperature of 5.2 K (red) and 0.3 K (blue). The difference plots between the two data sets at different temperatures are also shown in each panels (black line) and further confirmed that our single crystal of $Ce_2Zr_2O_7$ does not magnetically order at low temperature.

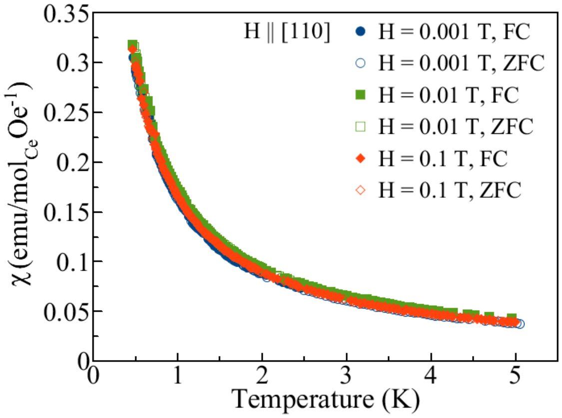

FIG. 5. The DC magnetic susceptibility measurements on annealed single crystals of $Ce_2Zr_2O_7$ collected in fields of 0.1 T, 0.01 T and 0.001 T for both field cooled (FC) and zero field cooled (ZFC) protocol. The absence of features in any of these measurements indicates that our single crystal of $Ce_2Zr_2O_7$ does not undergo a transition to long range magnetic order, or spin freezing down to T ∼ 0.5 K.

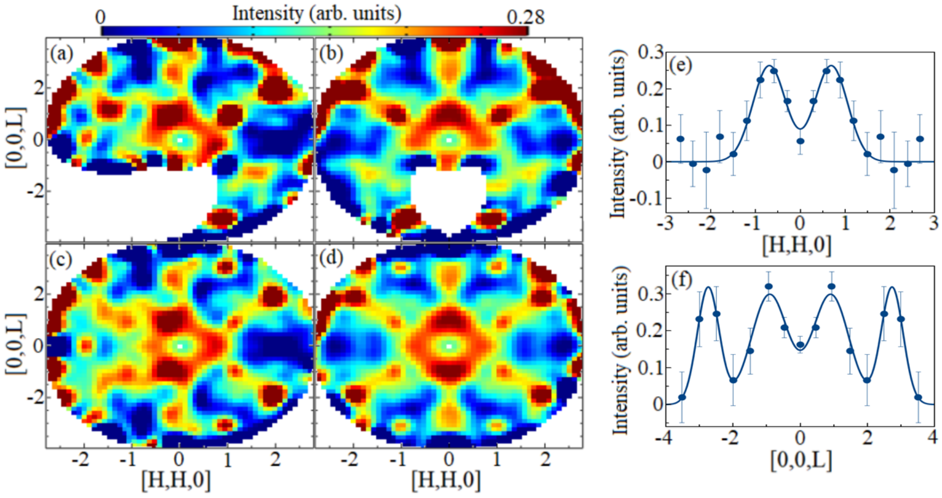

FIG. 6. The low energy inelastic neutron scattering difference from an annealed single crystal sample of $Ce_2Zr_2O_7$. This displays the subtraction of a $T = 2$ K data set from a $T = 0.06$ K difference data set integrated in energy over the range from 0 to 0.15 meV , with $E_i = 3.2$ meV incident neutrons. (b) The same neutron scattering difference after being symmetrically averaged about the line of symmetry along the (00L) axis of reciprocal space. The data is folded across the (00L) axis and averaged at points where this results in an overlap of the data with itself. (c) The same neutron scattering difference after being symmetrically averaged across the line of symmetry along the (HH0) axis of reciprocal space. (d) The same neutron scattering difference after being fully symmetrized in accordance with both the (00L) and (HH0) lines of symmetry in reciprocal space (also shown in Fig.3(a) of the main letter). This symmetrization brings out relatively weak signals measured in multiple, equivalent **Q** positions and can help minimize non-symmetric features, such as self-absorption effects. (e) A cut through the symmetrized data of (d) along the [H,H,0] direction is shown. This cut integrates [-0.4,0.4] in the perpendicular [00L] direction. (f) A cut through the symmetrized data of (d) along the [0,0,L] direction is shown. This cut integrates [-0.4,0.4] in the perpendicular [HH0] direction.

2.2 Preface to Publication II: Estimating the Nearest-Neighbor Exchange Parameters and Further Evidence for a Quantum Spin Ice Ground State in the Dipole-Octupole Pyrochlore $Ce_2Zr_2O_7$

In Publication II we extend our previous work in Publication I by showing further evidence for a lack of both magnetic order and spin freezing combined with quantum spin ice correlations at low temperature in $Ce_2Zr_2O_7$. We also perform estimates of the nearest-neighbor exchange parameters for $Ce_2Zr_2O_7$ in the XYZ Hamiltonian relevant for dipole-octupole pyrochlores at the nearest-neighbor level [Eq. (1.21)], with the results pointing towards a quantum spin ice ground state.

Our heat capacity measurements show a lack of magnetic order down to the lowest measured temperature, $T = 58$ mK. This not only confirms the findings of the neutron scattering and magnetic susceptibility measurements in Publication I, but this also provides evidence for an absence of octupolar magnetic order down to ∼58 mK, which the previous neutron scattering and magnetic susceptibility measurements lack sensitivity towards [52, 103, 105]. Our measured heat capacity data are consistent with that reported for $Ce_2Zr_2O_7$ in Ref. [22], but we perform a separate, more-sophisticated analysis than performed in Ref. [22], which involves showing that the low-temperature extrapolation used in Ref. [22] is inappropriate to the form of the measured heat capacity. The zero-field magnetic heat capacity measurements that we present in our work are similar to measurements reported on $Ce_2Sn_2O_7$ in Refs. [30, 60, 66, 119] and on $Ce_2Hf_2O_7$ in Refs. [32, 61], where in each case the zero-field magnetic heat capacity shows a broad hump below $T \approx 10$ K with the finer details of this anomaly, such as the exact height and width of the hump, differing with the values of the exchange parameters in each material [2, 37, 60, 61].

We estimate the nearest-neighbor exchange parameters by fitting the measured heat capacity and magnetic susceptibility using the numerical linked cluster (NLC) method in order to determine the set of nearest-neighbor exchange parameters which best-describe the measured data. The temperature dependence of the integrated neutron scattering signal is used to definitively rule out a locally optimal set of nearest-neighbor exchange parameters from our fitting to the heat capacity and magnetic susceptibility. This sub-optimal set of parameters describes the heat capacity and magnetic susceptibility reasonably well over the range of measured temperatures but clearly fails to describe the neutron scattering. Importantly, the best-fitting nearest-neighbor exchange parameters from our analysis correspond to a quantum spin ice ground state according to the zero-field magnetic ground state phase diagram predicted for dipole-octupole pyrochlores at the nearest-neighbor level [56, 57, 96–98]. In further detail, our estimates predict that J_x and J_y are approximately equal and are much stronger than J_z, corresponding to a quantum spin ice ground state that is near the boundary between dipolar and octupolar symmetry [56, 57, 96–98]. Much work is spent in fitting extrapolations and interpolations to the measured heat capacity and the corresponding recovered-entropy in order to show the measurements can be simultaneously consistent with the expected recovered-entropy for a CEF ground state doublet and the form of the specific heat expected at low temperature for a U(1) quantum spin ice [52, 93, 98, 125, 126].

Our new polarized neutron diffraction measurements provide further evidence for quantum spin ice correlations at low temperature in $Ce_2Zr_2O_7$ and elucidate the significance of further-than-nearest neighbor magnetic interactions. Specifically, the spin-flip channel of the measured scattering shows a snowflake-like signal that agrees reasonably-well with predictions using our best-fitting nearest-neighbor exchange parameters, while the non-spin-flip channel shows increased scattering at the Brillouin zone boundaries which is not present in calculations at the nearest-neighbor level. We compare our new polarized neutron diffraction measurements on $Ce_2Zr_2O_7$ with well-acclaimed polarized neutron diffraction measurements that were taken on the classical spin ice $Ho_2Ti_2O_7$ in Ref. [88] using the same diffraction instrument.

Typically exchange parameters are estimated in the rare-earth pyrochlores by fitting the spin-wave spectra obtained in inelastic neuron scattering experiments (see Refs. [35, 38, 59, 62–64] for examples), which requires the application of a magnetic field in cases where the zero-field magnetic ground state is disordered and shows no well-defined spin waves. In the case of $Ce_2Zr_2O_7$, no well-defined spin waves (no sharp single-magnon excitations) are detected in either zero or nonzero magnetic field as we mention in Publication II and show further in Publication III, and so the exchange parameters must be estimated through other means as is done using the measured heat capacity and magnetic susceptibility in Publication II, and extended in Publication III using higher-order calculations that yield best-fitting exchange parameters that are near-identical to those in Publication II. Importantly and as mentioned in these works, no well-defined spin waves are expected for the best-fitting exchange parameters obtained in Publications II and III due to the partially-octupolar character of the Ce^{3+} pseudospins, consistent with our measurements on $Ce_2Zr_2O_7$.

This paper was published two weeks before a similar work on $Ce_2Zr_2O_7$ (Ref. [37]) in which the authors fit the measured heat capacity and magnetization from Ref. [22] in order to yield separate estimates for the exchange parameters than what we achieve through our work. The exchange parameters suggested in Ref. [37] are near to ours in magnitude and in phase space but are clearly within the octupolar quantum spin ice region of the corresponding ground state phase diagram [56, 57], whereas our parameters reside near the boundary separating quantum spin ices with octupolar symmetry (of the emergent electric field) from those with dipolar symmetry. Despite this difference in the estimates, the separate estimates in Ref. [37] and in Publication III complement each other well in that they both suggest a π-flux quantum spin ice which is novel in the sense that the underlying two-in, two-out rule is a rare two-plus, two-minus rule associated with the configurations of magnetic octupoles rather than dipoles (see Section 1.5.2). In Publication III we plot our estimates for the nearest-neighbor exchange parameters and those from Ref. [37] on the ground state phase diagram predicated for dipole-octupole pyrochlores at the nearest-neighbor level [56, 57]. In fact, the nearest-neighbor exchange parameters suggested in Ref. [37] were arrived at through averaging parameter sets determined using different fitting schemes, and one of the *individual* parameter sets from Ref. [37] agrees remarkably well with our exchange parameters, as we further discuss in Chapter 3. We also compare our parameter estimates for $Ce_2Zr_2O_7$ to available estimates of the exchange parameters for $Ce_2Hf_2O_7$ (Ref. [61]) and $Ce_2Sn_2O_7$ (Refs. [30, 60, 124]) in Publication III of this thesis.

In addition to this estimation of the nearest-neighbor exchange parameters for $Ce_2Zr_2O_7$, Bhardwaj *et al.*

(Ref. [37]) also calculate the equal-time neutron scattering structure factor in the (H, H, L) plane and show that a weak second-nearest neighbor interaction between magnetic dipole moments is able to generate the majority of the finer details from the measured signals in Publication I and Ref. [22], which are unaccounted-for via calculations at the nearest-neighbor level. This finding in Ref. [37], and our analysis of the polarized neutron diffraction signals measured from $Ce_2Zr_2O_7$ in Publication II, complement each other well in that they both point towards the significance of weak further-than-nearest neighbor interactions at low temperature. The second-nearest-neighbor interaction parameter estimated in Ref. [37] is antiferromagnetic as expected for the dipole-dipole interaction between second-nearest neighbors in the pyrochlore lattice. However, this next-nearest-neighbor interaction estimated in Ref. [37] is ∼4 times stronger than the second-nearest-neighbor coupling predicted for the dipole-dipole interaction in $Ce_2Zr_2O_7$ (see Table 1.3). This latter point highlights the remaining need for a further understanding of interactions beyond nearest-neighbors in $Ce_2Zr_2O_7$, which we discuss further in Section 4.2.

In this paper we discuss the different U(1) quantum spin liquid ground states known to be available to the dipole-octupole pyrochlores and we do so while avoiding the terminology "quantum spin ice". After gaining a better appreciation for the implications of the dipole-octupole CEF ground state than we had in Publication I, we chose this wording to avoid causing confusion between the U(1) quantum spin liquids that arise in the dipole-octupole pyrochlores (described in Section 1.5) and the U(1) quantum spin ices that can be associated with the *conventional* two-in, two-out rule described in Section 1.4. With that being said, the nomenclature used in the literature has since evolved to accept these multipolar U(1) quantum spin liquids as new quantum spin ices [3, 30, 32, 52, 57, 61, 96, 99, 124], due to the many similarities between these multipolar U(1) quantum spin liquids and conventional quantum spin ices, as outlined in Sections 1.5.2 and 1.5.3.

I contributed to Publication II by leading a polarized neutron scattering experiment and the corresponding preparation, cutting a single crystal sample for heat capacity measurements, preparing a sample for magnetic susceptibility measurements, as well as taking part in the corresponding measurement process for the magnetic susceptibility. I analyzed the entirety of the experimental data presented in the paper and appendices, which included writing a code using the Python coding language in order to extract the recovered entropy from the measured heat capacity. I performed cubic and exponential extrapolations to the measured heat capacity and further theoretical calculations were performed by our collaborators as listed below. I synthesized powder samples of $Ce_2Zr_2O_7$ and $La_2Zr_2O_7$ and performed x-ray characterization measurements on each sample used in this work. I was responsible for annealing the $Ce_2Zr_2O_7$ samples in hydrogen gas before each experiment and storing the samples in an inert atmosphere until measurement. Finally, I designed and generated all-but-one of the figures included in this work and wrote ∼70% of the text. The contributions of each author are summarized below.

Author Contributions for Publication II:

Experimental Concept:

E. M. Smith, J. Gaudet, B. D. Gaulin

Sample Preparation:

J. Dudemaine, **E. M. Smith**, J. Gaudet, A. Fitterman, J. Beare, C. A. Marjerrison, J. D. Garrett, G. M. Luke, B. D. Gaulin, A. D. Bianchi

Neutron Scattering Experiments:

E. M. Smith, J. Gaudet, A. R. Wildes, S. Bhattacharya, C. R. C. Buhariwalla, N. P. Butch, J. P. Clancy, E. Kermarrec

Magnetic Susceptibility Measurements:

J. Beare, **E. M. Smith**, B. D. Gaulin, G. M. Luke

X-Ray Scattering Characterization:

E. M. Smith, B. D. Gaulin

Heat Capacity Measurements:

D. R. Yahne, T. DeLazzer, **E. M. Smith**, R. Movshovich, B. D. Gaulin, K. A. Ross

Data Analysis:

E. M. Smith, B. D. Gaulin

Theoretical Calculations and Modeling:

O. Benton, B. Placke, R. Schäfer

Manuscript:

E. M. Smith, O. Benton, B. Placke, B. D. Gaulin

Case for a $\mathrm{U}(1)_{\pi}$ Quantum Spin Liquid Ground State in the Dipole-Octupole Pyrochlore $\mathrm{Ce_2Zr_2O_7}$

E. M. Smith,[1,2,*] O. Benton,[3] D. R. Yahne,[4] B. Placke,[3] R. Schäfer,[3] J. Gaudet,[1] J. Dudemaine,[5,6] A. Fitterman,[5,6]
J. Beare,[1] A. R. Wildes,[7] S. Bhattacharya,[8] T. DeLazzer,[4] C. R. C. Buhariwalla,[1] N. P. Butch,[9] R. Movshovich,[10]
J. D. Garrett,[2] C. A. Marjerrison,[2] J. P. Clancy,[1,2] E. Kermarrec,[8] G. M. Luke,[1,2] A. D. Bianchi,[5,6]
K. A. Ross,[4,11] and B. D. Gaulin[1,2,11]

[1]*Department of Physics and Astronomy, McMaster University, Hamilton, Ontario L8S 4M1, Canada*
[2]*Brockhouse Institute for Materials Research, McMaster University, Hamilton, Ontario L8S 4M1, Canada*
[3]*Max Planck Institute for the Physics of Complex Systems, Nöthnitzer Straße 38, Dresden 01187, Germany*
[4]*Department of Physics, Colorado State University,*
200 West Lake Street, Fort Collins, Colorado 80523-1875, USA
[5]*Département de Physique, Université de Montréal, Montréal, Quebec H2V 0B3, Canada*
[6]*Regroupement Québécois sur les Matériaux de Pointe (RQMP), Quebec H3T 3J7, Canada*
[7]*Institut Laue-Langevin, 71 Avenue des Martyrs CS 20156, 38042 Grenoble Cedex 9, France*
[8]*Université Paris-Saclay, CNRS, Laboratoire de Physique des Solides, 91405 Orsay, France*
[9]*Center for Neutron Research, National Institute of Standards and Technology,*
MS 6100 Gaithersburg, Maryland 20899, USA
[10]*Los Alamos National Laboratory, Los Alamos, New Mexico 87545, USA*
[11]*Canadian Institute for Advanced Research, 661 University Avenue, Toronto, Ontario M5G 1M1, Canada*

(Received 4 August 2021; revised 8 December 2021; accepted 18 February 2022; published 20 April 2022)

The $\mathrm{Ce^{3+}}$ pseudospin-1/2 degrees of freedom in the pyrochlore magnet $\mathrm{Ce_2Zr_2O_7}$ are known to possess dipole-octupole character, making it a candidate for novel quantum spin liquid ground states at low temperatures. We report new polarized neutron diffraction at low temperatures, as well as heat capacity (C_p) measurements on single crystal $\mathrm{Ce_2Zr_2O_7}$. The former bears both similarities and differences with that measured from the canonical dipolar spin ice compound $\mathrm{Ho_2Ti_2O_7}$, while the latter rises sharply at low temperatures, initially plateauing near 0.08 K, before falling off toward a high temperature zero beyond 3 K. Above ~ 0.5 K, the C_p dataset can be fit to the results of a quantum numerical linked cluster calculation, carried out to fourth order, that allows estimates for the terms in the near-neighbor XYZ Hamiltonian expected for such dipole-octupole pyrochlore systems. Fits of the same theory to the temperature dependence of the magnetic susceptibility and unpolarized neutron scattering complement this analysis. A comparison between the resulting best-fit numerical linked cluster calculation and the polarized neutron diffraction shows both agreement and discrepancies, mostly in the form of zone-boundary diffuse scattering in the non-spin-flip channel, which are attributed to interactions beyond near neighbors. The lack of an observed thermodynamic anomaly and the constraints on the near-neighbor XYZ Hamiltonian suggest that $\mathrm{Ce_2Zr_2O_7}$ realizes a $\mathrm{U}(1)_{\pi}$ quantum spin liquid state at low temperatures, and one that likely resides near the boundary between dipolar and octupolar character.

DOI: 10.1103/PhysRevX.12.021015

Subject Areas: Condensed Matter Physics, Magnetism, Strongly Correlated Materials

I. INTRODUCTION

The rare-earth pyrochlore oxides, $R_2B_2\mathrm{O}_7$, where R^{3+} is a trivalent rare-earth ion and B^{4+} is a nonmagnetic tetravalent transition-metal ion, display a wealth of both exotic and conventional magnetic ground states. Their R^{3+} ions decorate a network of corner-sharing tetrahedra, one of the archetypes for geometrical frustration in three dimensions, and this crystalline architecture underlies many of their exotic properties [1]. A separation of energy scales, with crystal electric field (CEF) effects dominating over

---

[*] smithem4@mcmaster.ca

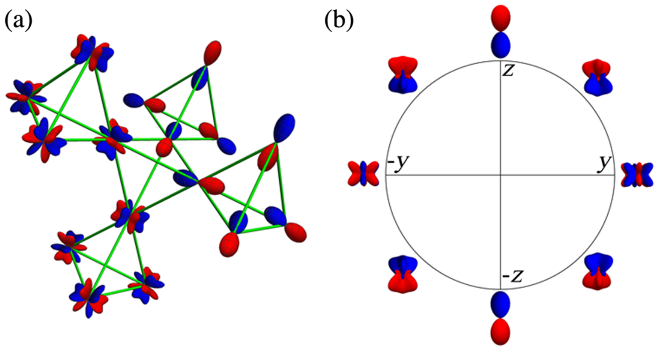

FIG. 1. (a) The magnetic charge distributions associated with octupoles (left) and dipoles (right) are depicted at the vertices of five corner-sharing tetrahedra, making up part of the pyrochlore lattice. (b) Octupolar and dipolar components inhabit the same Ce^{3+} pseudospin-1/2 degrees of freedom in $Ce_2Zr_2O_7$, such that y components behave as octupoles, while the x and z components of each pseudospin-1/2 behave as dipoles, as schematically illustrated here using the magnetic charge distributions associated with different directions of pseudospin in the yz plane.

exchange interactions, often results in a well-separated CEF ground-state doublet for the R^{3+} ion and interacting pseudospin-1/2 degrees of freedom at low temperatures [2–4].

It is well appreciated that the CEF Hamiltonian determines both the size of the magnetic moment at the R^{3+} site and its anisotropy, but less well appreciated that the symmetry of the CEF ground state can imprint itself on the exchange Hamiltonian [4–6]. The possible symmetries of the ground-state doublets then lead to an important classification of the rare-earth pyrochlores, which depends on how their CEF doublet transforms under time-reversal symmetry and the point group symmetry of the R^{3+} site. Three classes of doublets arise, one for non-Kramers ions with an even number of electrons and two for Kramers ions with an odd number of electrons. The non-Kramers case gives rise to a pseudospin wherein one component of the pseudospin transforms as a magnetic dipole and two transform as quadrupoles. For Kramers ions, we have the familiar case where all three components of the pseudospin in the ground-state doublet transform as magnetic dipoles, as well as the more exotic one where two components transform as magnetic dipoles and one transforms as an octupole. This latter case is known to describe the CEF Kramers ground state of $4f^1$ Ce^{3+} in $Ce_2Zr_2O_7$ [7,8], a dipole-octupole (DO) ground-state doublet, and also that of its sister pyrochlore, $Ce_2Sn_2O_7$ [9]. Figure 1(a) pictorially displays the magnetic charge distributions associated with both magnetic dipoles and octupoles decorating the tetrahedra on part of a cubic pyrochlore lattice. As discussed above, for the dipole-octupole doublets relevant to $Ce_2Zr_2O_7$, a single component of the pseudospin-1/2 degree of freedom (the y component) behaves as an octupole, while the x and z components behave as dipoles under the symmetry of the lattice and time-reversal symmetry, as schematically illustrated in Fig. 1(b).

Such DO doublets decorating pyrochlore lattices are theoretically known to allow for at least six distinct quantum disordered and ordered ground states, with three in each of the dipole and octupole sectors [10–12]. Recent neutron scattering measurements on single crystal $Ce_2Zr_2O_7$ have uncovered a signal that strongly resembles predictions for the energy integration of emergent photon excitations in a U(1) quantum spin ice [7], while recent experiments on powder samples of $Ce_2Sn_2O_7$ have been interpreted in terms of a U(1) quantum spin ice ground state in the octupole sector [9].

II. OUTLINE OF THE PAPER

In this paper, we present new polarized neutron diffraction and heat capacity measurements on single crystal $Ce_2Zr_2O_7$. The former bears both similarities and differences with that measured from the canonical dipolar spin ice compound, $Ho_2Ti_2O_7$, while the latter shows no sign of a thermodynamic phase transition above $T = 0.06$ K. C_p rises sharply at low temperatures, initially plateauing near 0.08 K, before falling off toward a high temperature zero beyond 3 K, consistent with previous measurements [8]. We have modeled the high temperature C_p and the powder-averaged magnetic susceptibility using quantum numerical linked cluster (NLC) expansions. This allows us to estimate and constrain the parameters of the anticipated near-neighbor XYZ Hamiltonian. To the extent that interactions beyond near neighbor do not alter ground state selection, we constrain the nature of the ground state itself, with the results indicating a $U(1)_\pi$ quantum spin liquid (QSL) ground state is selected at low temperature.

We use the resulting near-neighbor exchange parameters to calculate the equal-time spin-flip (SF) and non-spin-flip (NSF) structure factors in the $[HHL]$ scattering plane. This calculation resembles the new polarized neutron diffraction measurements in the SF channel from single crystal $Ce_2Zr_2O_7$, but cannot account for the observed zone-boundary diffuse scattering in the NSF channel. We attribute this discrepancy to interactions beyond near neighbor in the Hamiltonian, which are expected to be small, and a full study of which is beyond the scope of our present work. The same discrepancy exists for spin-polarized neutron diffraction from $Ho_2Ti_2O_7$, where it was ascribed to expected long-range dipolar interactions [13]. NLC calculations using the same near-neighbor exchange Hamiltonian were also carried out to seventh order. While these agree with the fourth-order calculations above ~0.5 K, they depart from the measured C_p at lower temperatures. We interpret this as arising from the same interactions beyond near neighbor in $Ce_2Zr_2O_7$ that were revealed by the NSF zone-boundary scattering. As these are relatively weak, they only manifest themselves at low temperatures.

A further consistency check is carried out via semi-classical Monte Carlo and molecular spin dynamics using the best-fit near-neighbor Hamiltonian. This calculation accounts for the energy dependence of the inelastic spectral weight making up the diffuse scattering at low temperatures without further adjustment of the NLC-determined near-neighbor Hamiltonian. We further show that the full $R\ln(2)$ entropy of the DO ground-state doublet can be accounted for to 10 K with a smooth extrapolation of C_p from the lowest temperature data point at $T = 0.06$ K, to zero at $T = 0$ K, using a theoretical form which is simultaneously consistent with both the expected behavior of a U(1) QSL at low temperature and the high temperature limit of the NLC calculations. Interestingly, the Pauling, classical spin ice entropy $R\ln(2)$ less $(R/2)\ln(\frac{3}{2})$ is recovered from the peak in the C_p data at ~0.08 K, to 10 K.

III. POLARIZED NEUTRON DIFFRACTION

We have carried out new polarized diffraction measurements on single crystal $Ce_2Zr_2O_7$ using the D7 diffractometer at the Institute Laue Langevin [14]. This diffractometer employs a spin-polarized monochromatic incident beam, which was $E_i = 3.47$ meV for this experiment. This configuration effectively integrates over $-15\text{ meV} \lesssim E < 3.47$ meV during the course of a diffraction measurement, giving a signal that is directly proportional to the equal-time structure factor. A single polarization direction, perpendicular to the $[HHL]$ scattering plane, was employed, and as such the spin-flip and non-spin-flip diffuse scattering profiles can be independently measured. The diffuse scattering associated with these two cross sections, SF and NSF, are shown in the $[HHL]$ scattering plane for $Ce_2Zr_2O_7$ in Figs. 2(a) and 2(b), respectively for the temperature-difference dataset $T = 0.045\text{ K} - T = 10$ K. For comparison, the corresponding SF and NSF diffuse scattering patterns as measured on single crystal $Ho_2Ti_2O_7$ at $T = 1.7$ K are shown in Figs. 2(c) and 2(d), respectively [13]. These earlier spin-polarized diffuse scattering measurements on $Ho_2Ti_2O_7$ (Ref. [13]) played a formative role in the development of classical spin ice physics, as they drew clear attention to "pinch point" scattering within the SF cross section at (0,0,2) and (1,1,1) and equivalent wave vectors, due to the presence of a classical Coulomb phase at low temperature. These measurements on $Ho_2Ti_2O_7$ also observed zone-boundary diffuse scattering in the NSF channel, which was later attributed to the long-range dipolar interactions relevant to the large Ho^{3+} dipole moments.

The comparison between the spin-polarized diffuse scattering from $Ce_2Zr_2O_7$ and $Ho_2Ti_2O_7$ in Fig. 2 is interesting both in what is similar and where the discrepancies between the two materials lie. One may note, however, that the comparison is made at quite different temperatures, 0.045 K for $Ce_2Zr_2O_7$ but only 1.7 K for $Ho_2Ti_2O_7$. In fact, the large Ho^{3+} moments and effective ferromagnetic coupling cause $Ho_2Ti_2O_7$ to depolarize the beam at lower temperatures, whereas no such issue is present for $Ce_2Zr_2O_7$ due to its much smaller Ce^{3+} moments. Quasi-pinch-point SF scattering is observed near (0,0,2) Bragg positions for $Ce_2Zr_2O_7$, but it is not as constricted as that observed at (0,0,2) for $Ho_2Ti_2O_7$, even though the earlier measurements on $Ho_2Ti_2O_7$ were taken at much higher temperature. Furthermore, while diffuse SF scattering extends out in (1,1,1) and equivalent directions in a snowflakelike pattern for $Ce_2Zr_2O_7$, pinch points appear to be absent in these directions.

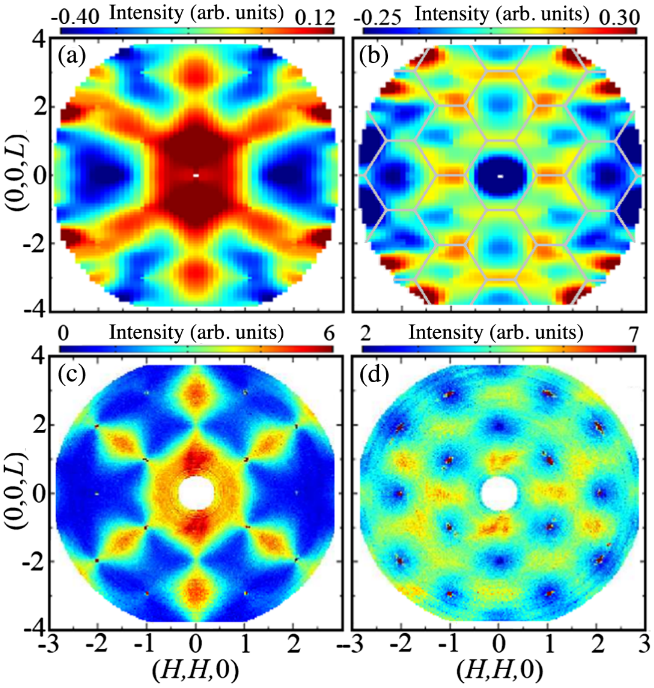

FIG. 2. The symmetrized $T = 45\text{ mK} - T = 10$ K temperature-difference neutron signal measured in the (a) SF and (b) NSF channels of our polarized neutron diffraction experiment on $Ce_2Zr_2O_7$. The (c) SF and (d) NSF scattering signals in the $[HHL]$ plane measured in a polarized neutron scattering experiment on $Ho_2Ti_2O_7$ at $T = 1.7$ K [13]. The data in this figure are shown in arbitrary units.

In contrast, and somewhat surprisingly, the observed NSF diffuse scattering from $Ce_2Zr_2O_7$ is quite similar to that measured from $Ho_2Ti_2O_7$. In both cases the diffuse scattering tends to follow the face-centered cubic Brillouin zone boundaries, outlined in gray in Fig. 2(b). For $Ho_2Ti_2O_7$, this was ascribed to interactions beyond near neighbor [13], which was not surprising, given that dipolar interactions are expected to dominate over exchange interactions even for near neighbors in $Ho_2Ti_2O_7$. However, the Ce^{3+} moments are ~8 times smaller than those of Ho^{3+} and hence dipolar interactions are expected to be ~64 times smaller in $Ce_2Zr_2O_7$. We revisit our new polarized neutron diffraction data in Sec. V, where we compare the measured SF and NSF signals to NLC calculations using the near-neighbor exchange parameters yielded in this work.

IV. ESTIMATING THE NEAR-NEIGHBOR EXCHANGE PARAMETERS IN THE SPIN HAMILTONIAN

The gold standard for determining the microscopic spin Hamiltonian of magnetic materials is inelastic neutron scattering studies of spin wave spectra. This technique can and has been successfully applied to pyrochlore magnets with pseudospin-1/2 degrees of freedom arising from well-separated ground-state CEF doublets, including $Yb_2Ti_2O_7$ and $Er_2Ti_2O_7$ [15–20]. For disordered ground states, it is necessary to perform measurements in a sufficiently strong magnetic field, so as to polarize the ground state, thus giving rise to well-defined spin wave spectra. However, this is not always possible. For example, the classical spin ice ground state as appears in $Ho_2Ti_2O_7$ does not allow transverse spin fluctuations; hence, no well-defined spin wave excitations are observed due to Ho^{3+}'s non-Kramers CEF doublet eigenvectors [21]. No evidence for well-defined spin waves has been observed to date in either zero or nonzero magnetic field in $Ce_2Zr_2O_7$, a likely consequence of the form of Ce^{3+}'s DO CEF ground-state doublet and spin Hamiltonian. Hence estimates for the microscopic spin Hamiltonian parameters for such materials can only come from sophisticated modeling of other data, such as the high temperature thermodynamic data presented here. We note that a related work has appeared coincident with this paper which performs independent modeling of heat capacity, magnetization, and neutron scattering measurements on $Ce_2Zr_2O_7$, and reaches similar conclusions [22].

A. Introduction to the exchange parameters in the XYZ Hamiltonian

The near-neighbor XYZ Hamiltonian appropriate to DO pyrochlores in a magnetic field may be written as [5,6]

$$\begin{aligned}\mathcal{H}_{\mathrm{XYZ}} = {}& \sum_{\langle ij\rangle}[J_{\tilde{x}} S_i^{\tilde{x}} S_j^{\tilde{x}} + J_{\tilde{y}} S_i^{\tilde{y}} S_j^{\tilde{y}} + J_{\tilde{z}} S_i^{\tilde{z}} S_j^{\tilde{z}}] \\ & - g_z \mu_B \sum_i \mathbf{h}\cdot\hat{\mathbf{z}}_i (S_i^{\tilde{z}}\cos\theta + S_i^{\tilde{x}}\sin\theta).\end{aligned} \tag{1}$$

In this equation, $S_i^{\tilde{\alpha}}$ ($\alpha = \tilde{x}$, $\tilde{y}$, $\tilde{z}$) are the pseudospin components of atom i in the local $\tilde{x}$, $\tilde{y}$, $\tilde{z}$ coordinate frame. This coordinate frame arises from rotation of the local x, y, z coordinate frame, with the z anisotropy axis connecting near-neighbor tetrahedra in the pyrochlore structure, by θ about the y axis [5,6]. The magnetic field is denoted as $\mathbf{h}$, and $\hat{\mathbf{z}}_i$ is the local anisotropy axis for the site i. The g factor g_z is fixed by the wave functions of the lowest CEF doublet, giving $g_z = 2.57$ for Ce^{3+} [7–9]. $S_i^{\tilde{x}}$ and $S_i^{\tilde{z}}$ are distinguished from $S_i^{\tilde{y}}$ by how they transform under the point group of the lattice and time-reversal symmetry. $S_i^{\tilde{x}}$ and $S_i^{\tilde{z}}$ transform like a magnetic dipole while $S_i^{\tilde{y}}$ transforms like a component of the magnetic octupole tensor, as schematically illustrated in Fig. 1.

The nearest-neighbor exchange Hamiltonian in Eq. (1) has only three independent exchange parameters $(J_{\tilde{x}}, J_{\tilde{y}}, J_{\tilde{z}})$ in zero magnetic field. Theory has predicted the ground-state phase diagram for such a zero-field XYZ Hamiltonian, uncovering both quantum spin liquid as well as ordered ground states [10,11]. Each of these can have either dipolar or octupolar nature. A QSL phase has octupolar nature if $|J_{\tilde{y}}| > |J_{\tilde{x}}|, |J_{\tilde{z}}|$ and dipolar nature if $|J_{\tilde{z}}| > |J_{\tilde{y}}|$ or $|J_{\tilde{x}}| > |J_{\tilde{y}}|$. An ordered phase has octupolar nature if $J_{\tilde{y}} < J_{\tilde{x}}, J_{\tilde{z}}$ and dipolar nature if $J_{\tilde{z}} < J_{\tilde{y}}$ or $J_{\tilde{x}} < J_{\tilde{y}}$. One final classification comes about for U(1) QSL ground states, based on whether the U(1) flux that penetrates the hexagonal plaquettes embedded in the pyrochlore structure is equal to 0 or π. This leads to a distinction between $\mathrm{U}(1)_0$ and $\mathrm{U}(1)_\pi$ QSLs. The aforementioned theoretical studies then uncover six phases within the ground-state phase diagram: all-in, all-out (AIAO) order, $\mathrm{U}(1)_0$ QSL, and $\mathrm{U}(1)_\pi$ QSL, each of which can have dipolar or octupolar nature. A separate theory study has provided evidence for a small portion of the ground-state phase diagram corresponding to a $\mathbb{Z}_2$ QSL phase [12]. It is worth noting that inter-Ce^{3+} interactions beyond near neighbor are allowed, but are expected to be weak. Long-range, three-dimensional dipolar interactions must be present in $Ce_2Zr_2O_7$; however, they are expected to be weak due to the small dipole moment associated with the Ce^{3+} CEF ground-state doublet in $Ce_2Zr_2O_7$ [7,8]. Exchange interactions beyond near neighbor are also expected to be weak due to the localized nature of $4f$ electron wave functions in rare-earth insulators.

B. Heat capacity and numerical linked cluster calculations

The single crystal and powder samples of $Ce_2Zr_2O_7$ used in this study are from the same growth and synthesis employed in Ref. [7]. As reported there, stabilizing the Ce^{3+} oxidation state in $Ce_2Zr_2O_7$ requires growth and annealing in strong reducing conditions to minimize the Ce^{4+} content. The amount of sample oxidation (the value of δ in $Ce^{3+}_{2-2\delta}Ce^{4+}_{2\delta}Zr_2O_{7+\delta}$) can be tracked through x-ray diffraction measurements of the lattice parameter [23], and we estimate an oxidation level of $\delta \sim 0.05$ for the single crystal samples in the present work. Heat capacity measurements on a polished single crystal were carried out on a Quantum Design PPMS with dilution insert using the conventional quasiadiabatic thermal relaxation technique.

Heat capacity measurements were performed on our single crystal $Ce_2Zr_2O_7$ sample, along with a polycrystalline

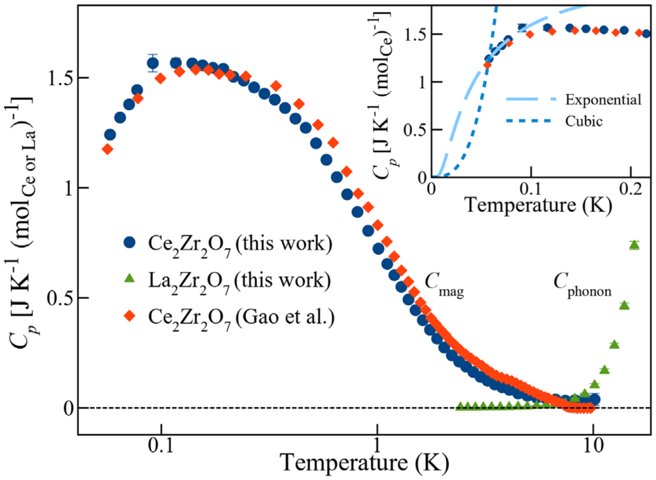

FIG. 3. The magnetic contribution to the heat capacity (C_{mag}) for the $Ce_2Zr_2O_7$ single crystal measured in the present work (blue) and in previous work by Gao *et al.* (red) [8]. The phonon contribution to the heat capacity, estimated from measurements on a $La_2Zr_2O_7$ sample (green), was removed from C_p to obtain C_{mag}. The inset shows the best-fit simple exponential and cubic extrapolations to $T = 0$ K for the present $Ce_2Zr_2O_7$ C_{mag}. An exponential extrapolation, with an energy gap of ~0.035 K, can smoothly connect to the finite temperature data, while a cubic extrapolation cannot.

sample of $La_2Zr_2O_7$ (see the Appendix A), which is used as a $4f^0$ analog of $Ce_2Zr_2O_7$. The results are shown in Fig. 3, where the temperature axis is logarithmic. C_p results on another $Ce_2Zr_2O_7$ single crystal from Ref. [8] are also overlaid for ease of comparison. One can see that the phonon contribution to C_p, as measured from the $La_2Zr_2O_7$ sample, is negligible below ~10 K, and thus C_{mag} is easily isolated. These results show that C_{mag} rises on decreasing temperature below ~3 K, and then drops off sharply below ~0.08 K, consistent with the earlier measurements (Ref. [8]) and a disordered ground state, as no sharp features associated with a phase transition can be identified.

The order of the quantum NLC calculations, which were used to model the experimental results, refers to the maximum number of tetrahedra considered in a cluster. We have carried out NLC calculations for orders of 7 and less to model the magnetic heat capacity at temperatures above an order-dependent threshold. This threshold is set by the temperature above which the nth-order calculation for a particular set of near-neighbor exchange parameters is consistent with the corresponding $(n-1)$th-order calculation. NLC calculations become progressively more time-consuming to carry out at higher order. For this reason, calculations of the high temperature C_{mag} with varying exchange parameters were carried out only to order 4, while calculations of other observables [integrated $S(\mathbf{Q}, T)$ and susceptibility] were calculated at lower order. NLC calculations at order 7, the highest order reported here, were carried out for C_{mag} with a single set of exchange couplings only. Going beyond sixth order is significant, because this is the first order at which the expansion contains nontrivial loops.

At temperatures of $T \sim 0.5$ K and above, the measured C_{mag} data can be compared with fourth-order NLC (NLC-4) calculations for C_{mag} in order to model and constrain $Ce_2Zr_2O_7$'s microscopic near-neighbor Hamiltonian. As the zero-field heat capacity contains no directional information, we define a new set of axes, $\{a, b, c\}$, to be the permutation of $\{\tilde{x},\ \tilde{y},\ \tilde{z}\}$ such that $|J_a| \geq |J_b|, |J_c|$ and $J_b \geq J_c$. This allows for a unique fit to C_{mag} but does not specify which values correspond to which exchange constants. Accordingly, the fit does not distinguish between the octupolar or dipolar nature of the ground state. Nonetheless, knowledge of J_a, J_b, and J_c suffices to determine whether the ground state is an ordered phase or a QSL phase [10].

This J_a, J_b, J_c Hamiltonian can also be written in terms of raising and lowering operators with respect to ${S_i}^a$, giving

$$\begin{aligned}\mathcal{H}_{\mathrm{ABC}} &= \sum_{\langle ij\rangle}[J_a {S_i}^a {S_j}^a + J_b {S_i}^b {S_j}^b + J_c {S_i}^c {S_j}^c] \\ &= \sum_{\langle ij\rangle}[J_a {S_i}^a {S_j}^a - J_{\pm}({S_i}^+ {S_j}^- + {S_i}^- {S_j}^+) \\ &\quad + J_{\pm\pm}({S_i}^+ {S_j}^+ + {S_i}^- {S_j}^-)] \qquad (2)\end{aligned}$$

in zero field, where $J_{\pm} = -\frac{1}{4}(J_b + J_c)$, $J_{\pm\pm} = \frac{1}{4}(J_b - J_c)$.

The set of exchange parameters (J_a, J_b, J_c) best reproducing C_{mag} was obtained from a fourth-order NLC calculation with an Euler transformation to improve convergence. Heat capacity curves were calculated for values of $-1 \leq J_b \leq 1$ and $-1 \leq J_c \leq J_b$ in increments of 0.01, with $J_a = 1$. Each curve was then rescaled for best agreement with experiment to determine the value of J_a, according to the goodness-of-fit measure $\langle \delta^2/\epsilon^2 \rangle_{C\mathrm{mag}} \propto \sum\{[C_{\mathrm{mag}}^{\mathrm{NLC}}(T_{\mathrm{expt}}) - C_{\mathrm{mag}}^{\mathrm{expt}}(T_{\mathrm{expt}})]^2/\epsilon(T_{\mathrm{expt}})^2\}$, where the sum is over measured temperatures T_{expt} above the low temperature threshold $(0.7J_a)/k_B$, restricting the fit to the regime where the NLC calculations converge, and $\epsilon(T_{\mathrm{expt}})$ is the experimental uncertainty on the heat capacity at temperature T_{expt}. The values of $\langle \delta^2/\epsilon^2 \rangle_{C\mathrm{mag}}$ over the entire phase space, after optimization of the scale J_a for each parameter set, are shown in Fig. 4(a). This displays two extended regions in which there is good agreement with the experimental C_{mag}. Both regions are entirely within one single phase in the predicted ground-state phase diagram for the near-neighbor XYZ model Hamiltonian [Fig. 4(b)] [10].

Some parameter sets within these regions can however be excluded due to their inability to describe the experimental magnetic susceptibility data. This is shown in Fig. 5 and explained in further detail in Sec. IV C. The best fits within each region which are also consistent with the susceptibility data are found at the points $(J_a, J_b, J_c) = (0.064, 0.063, 0.011)$ and $(0.089, -0.007, -0.027)$ meV,

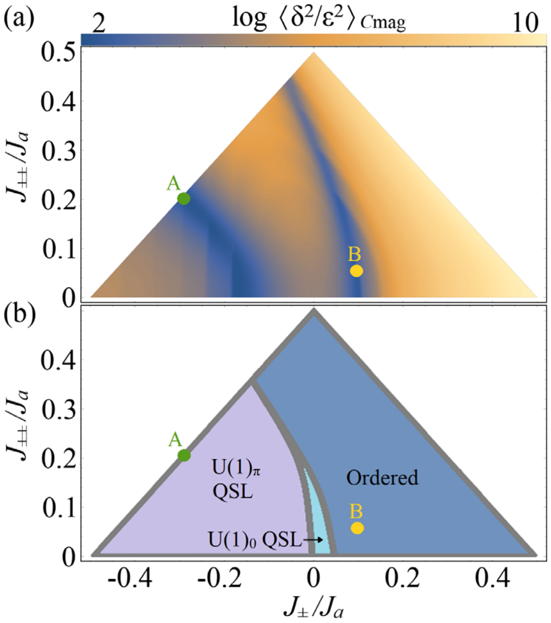

FIG. 4. (a) The goodness-of-fit parameter ($\langle\delta^2/\epsilon^2\rangle_{C\mathrm{mag}}$) for the fourth-order NLC calculation compared to the measured C_{mag}, as a function of the exchange parameters, J_a, $J_{\pm} = -\frac{1}{4}(J_b + J_c)$, and $J_{\pm\pm} = \frac{1}{4}(J_b - J_c)$. This displays two local minima of $\langle\delta^2/\epsilon^2\rangle_{C\mathrm{mag}}$. The best-fit parameters are labeled as parameter set A and parameter set B. The global minimum corresponds to set A while set B is only locally optimal. (b) The best-fit parameters from the NLC calculations (A and B) overlaid on the zero-field ground-state phase diagram predicted for the XYZ model Hamiltonian and DO pyrochlores [10]. The set A exchange parameters are well within the region of the phase diagram that is attributed to the U(1)$_\pi$ QSL, while the set B parameters are well within the region attributed to an ordered ground state.

which we label as A and B, respectively. In Fig. 4(b) we overplot the optimal exchange parameters on top of the predicted ground-state phase diagram for the near-neighbor XYZ model Hamiltonian [10]. The set A (B) exchange parameters reside within the region corresponding to the π-flux U(1) QSL (ordered phase). Of these two parameter sets, parameter set A gives a better fit to the heat capacity. The calculated C_{mag}'s using the fourth-order NLC with sets A and B are shown in Fig. 6.

The fourth-order NLC C_{mag} calculation and fit was redone assuming 5% vacancies, and $\langle\delta^2/\epsilon^2\rangle_{C\mathrm{mag}}$ again shows two locally optimal regions of parameter space. The best-fitting parameter sets that are also able to describe the measured susceptibility, A′ and B′, are very near to A and B in parameter space, respectively (see Appendix B). The global (local) minima at A′ (B′) lies within the region corresponding to the π-flux U(1) QSL (ordered phase). We therefore conclude that these results are robust to the presence of at least 5% Ce^{4+} in $Ce_2Zr_2O_7$.

Seventh-order NLC (NLC-7) calculations for C_{mag} converge above ~0.2 K, and these have been carried out for the

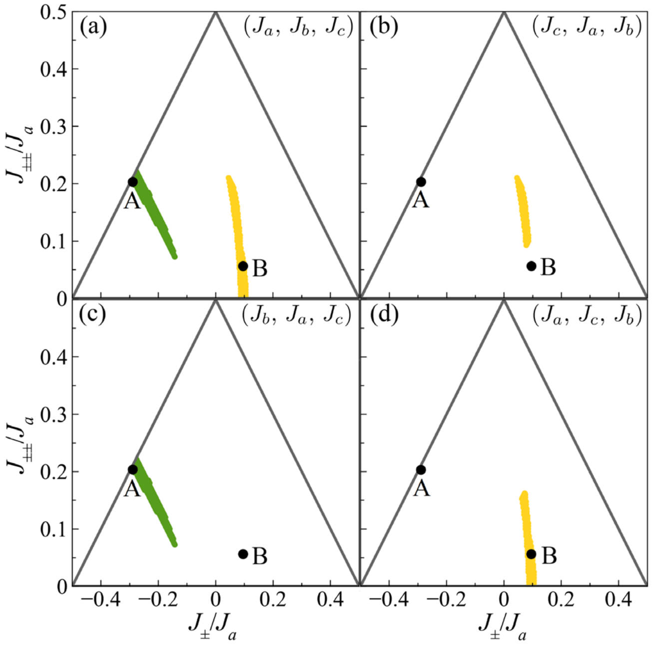

FIG. 5. The regions of the XYZ phase diagram for which it is possible to obtain simultaneous reasonable NLC descriptions of χ and C_{mag} are indicated in green and yellow for $(J_{\tilde{x}}, J_{\tilde{y}}, J_{\tilde{z}})$ equal to the different permutations of (J_a, J_b, J_c). We define the thresholds for reasonable χ and C_{mag} descriptions in Appendix C. Specifically, we show the regions of simultaneous χ and C_{mag} descriptions for the permutation in which $(J_{\tilde{x}}, J_{\tilde{y}}, J_{\tilde{z}})$ is equal to (a) (J_a, J_b, J_c), (b) (J_c, J_a, J_b), (c) (J_b, J_a, J_c), and (d) (J_a, J_c, J_b). The overall best-fit A parameters require that $(J_{\tilde{x}}, J_{\tilde{y}}, J_{\tilde{z}})$ is equal to (J_a, J_b, J_c) or (J_b, J_a, J_c); that is, $J_{\tilde{z}} = J_c$.

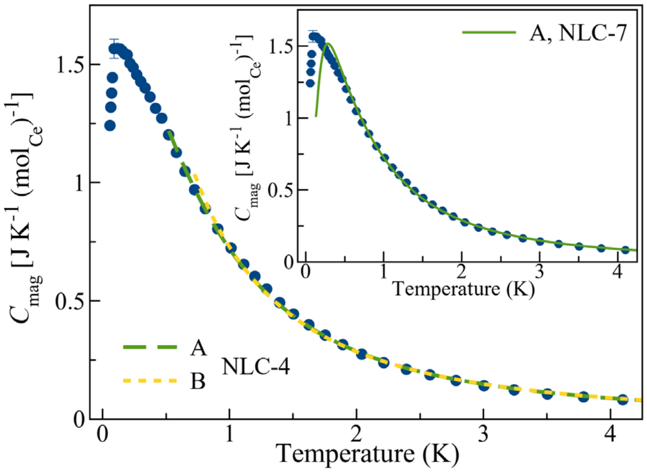

FIG. 6. The results of the fourth-order NLC C_{mag} calculation for zero sample oxidation, using the near-neighbor exchange parameters $J_a = 0.064$ meV, $J_b = 0.063$ meV, $J_c = 0.011$ meV (set A) and $J_a = 0.089$ meV, $J_b = -0.007$ meV, $J_c = -0.027$ meV (set B), overlaid on top of the measured C_{mag} for our $Ce_2Zr_2O_7$ sample. The inset shows the results of the seventh-order NLC C_{mag} calculation for zero sample oxidation, using the set A near-neighbor exchange parameters.

optimal, set A, near-neighbor exchange parameters, as shown in the inset of Fig. 6. These higher-order calculations are consistent with the NLC-4 calculations above ~0.5 K. However, at temperatures between ~0.2 and ~0.5 K, the NLC-7 calculations do not quantitatively describe the measured C_{mag}. We attribute this to interactions not included in the XYZ Hamiltonian [Eqs. (1) and (2)], those beyond near neighbor, which are relatively weak and therefore only manifest themselves at the lowest temperatures. This is also consistent with the zone-boundary diffuse scattering observed in the NSF structure factor discussed above and shown in Fig. 2. Including the next-nearest-neighbor part of the dipole-dipole interaction in the NLC-7 calculation did not significantly improve the agreement between theory and experiment, suggesting that either dipole-dipole interactions beyond next-nearest-neighbor or additional exchange interactions are important.

C. DC magnetic susceptibility

While the zero-field C_{mag} contains no directional information, the temperature-dependent dc magnetic susceptibility (χ) does because it is sensitive to the magnetic moment, which distinguishes between pseudospin components. Specifically, χ is dependent on the values of $J_{\tilde{x}}$, $J_{\tilde{y}}$, $J_{\tilde{z}}$, and θ. A second-order NLC expansion (NLC-2) is used to calculate χ (see Appendix C). Specifically, we use NLC-2 to fit measurements of χ from a powder sample of $Ce_2Zr_2O_7$ in order to narrow down the possible parameter sets and to distinguish between possible permutations of the exchange parameters.

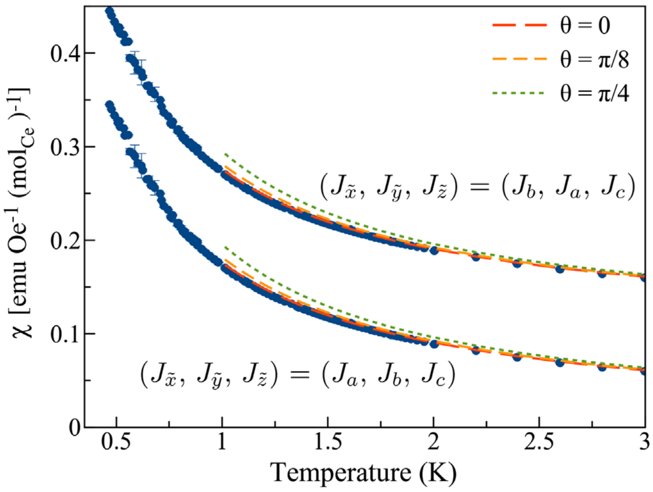

FIG. 7. The measured powder magnetic susceptibility data plotted alongside the second-order NLC-calculated susceptibility for values of θ between 0 and $\pi/4$, and for $(J_{\tilde{x}}, J_{\tilde{y}}, J_{\tilde{z}})$ equal to the two permutations of the A parameters that are able to provide a reasonable fit to the data. Specifically, we show calculations for values of θ given by $\theta = 0$ (red), $\theta = \pi/8$ (yellow), and $\theta = \pi/4$ (green). This shows that the NLC calculations for the magnetic susceptibility agree well with the data when $(J_{\tilde{x}}, J_{\tilde{y}}, J_{\tilde{z}}) = (0.064, 0.063, 0.011)$ meV, or $(J_{\tilde{x}}, J_{\tilde{y}}, J_{\tilde{z}}) = (0.063, 0.064, 0.011)$ meV, so long as the value of θ is near $\theta = 0$. The $(J_{\tilde{x}}, J_{\tilde{y}}, J_{\tilde{z}}) = (0.063, 0.064, 0.011)$ meV calculations are shifted upward by 0.1 emu Oe^{-1} $(\mathrm{mol}_{\mathrm{Ce}})^{-1}$ for visibility.

As mentioned above, some parameter sets within the region of good agreement for C_{mag} cannot be made to agree with χ, for any choice of θ or permutation of parameters, and are therefore excluded. Figure 5 shows the regions of the phase diagram for which it is possible to obtain simultaneous agreement with C_{mag} and χ, for $(J_{\tilde{x}}, J_{\tilde{y}}, J_{\tilde{z}})$ equal to the different permutations of (J_a, J_b, J_c).

For the B parameters, we can rule out the possibility of $J_{\tilde{z}}$ being the largest exchange parameter, and we find different optimal values of θ for the remaining permutations. For the A parameter set, and all nearby parameter sets for which a good fit can be found, the results of the NLC-2 fitting to χ suggest that $\theta \sim 0$ and that $J_{\tilde{z}}$ is the weakest exchange parameter, as Figs. 5 and 7 demonstrate. Accordingly, the only allowed permutations of exchange parameters from the A set satisfy $J_{\tilde{x}} \sim J_{\tilde{y}}$, implying that $Ce_2Zr_2O_7$ resides near the boundary between dipolar and octupolar nature.

V. CONSISTENCY OF ESTIMATED EXCHANGE PARAMETERS WITH NEUTRON SCATTERING RESULTS

The combined analyses of the measured C_{mag} and χ give experimental estimates for the near-neighbor exchange constants for $Ce_2Zr_2O_7$, yielding $\theta \sim 0$ and $(J_{\tilde{x}}, J_{\tilde{y}}, J_{\tilde{z}}) = (0.064, 0.063, 0.011)$ meV or $(J_{\tilde{x}}, J_{\tilde{y}}, J_{\tilde{z}}) = (0.063, 0.064, 0.011)$ meV. While neutron scattering measurements were *not* modeled in order to constrain the microscopic spin Hamiltonian for $Ce_2Zr_2O_7$, it is interesting and important to see to what extent the measured neutron scattering from $Ce_2Zr_2O_7$ is consistent with calculations using the near-neighbor spin Hamiltonian so derived.

A. Elastic neutron scattering

The $U(1)_\pi$ ground state, determined by these best-fitting near-neighbor exchange parameters, is consistent with the nature of the previously reported diffuse inelastic neutron scattering from single crystals of $Ce_2Zr_2O_7$ [7,8]. Additionally, the earlier neutron scattering work is inconsistent with an ordered state, at least in the dipolar sector, as magnetic Bragg peaks would be expected. We have revisited our earlier elastic neutron scattering data to place an upper limit on possible AIAO dipole order in the ground state of $Ce_2Zr_2O_7$, the form expected to reside within the XYZ DO pyrochlore phase diagram. We conclude that no such AIAO dipole order occurs in $Ce_2Zr_2O_7$, with an upper limit on the Ce^{3+} ordered moment of $\mu_{\mathrm{ordered}} \leq 0.04\mu_B$ (see Appendix D).

B. Polarized neutron diffraction

We can also compute the spin-flip and non-spin-flip structure factors using this best-fitting A parameter set and compare with the polarized neutron diffraction measurements on an annealed single crystal sample of $Ce_2Zr_2O_7$ shown in Sec. III. The calculations are carried out at $T = 0.5$ K (see Appendix E), as that is the lowest temperature for which the NLC-3 calculation converges, while the new polarized neutron diffraction measurements were performed at lower temperatures, $T = 0.045$ K. Nonetheless, we assume that this calculation will capture most of the features at lower temperatures, as the ground state is disordered.

The measured (NLC-calculated) SF scattering in the $[HHL]$ scattering plane is shown in Fig. 8(a) [Fig. 8(b)] and the measured (NLC-calculated) NSF scattering in the $[HHL]$ scattering plane is shown in Fig. 8(c) [Fig. 8(d)]. The comparison between measurement and theory for the SF channel in Figs. 8(a) and 8(b) is good, although sharper features are present in the lower temperature, SF polarized diffraction, such as the broad pinch point scattering near (0,0,2). The measured NSF structure factor in the $[HHL]$ scattering plane [Fig. 8(c)] shows intensity that is maximal along Brillouin zone boundaries [shown as gray lines in Fig. 8(c)] and minimal at zone centers. As discussed in Sec. III, this zone-boundary scattering is similar to that measured in the NSF channel of polarized neutron diffraction measurements on $Ho_2Ti_2O_7$, shown in Fig. 2(d) [13], and associated with interactions beyond the nearest neighbor. The calculated NSF structure factor is featureless for the near-neighbor-only XYZ spin Hamiltonian employed here, with a $\mathbf{Q}$ dependence originating from the Ce^{3+} magnetic form factor only, as Fig. 8(d) illustrates.

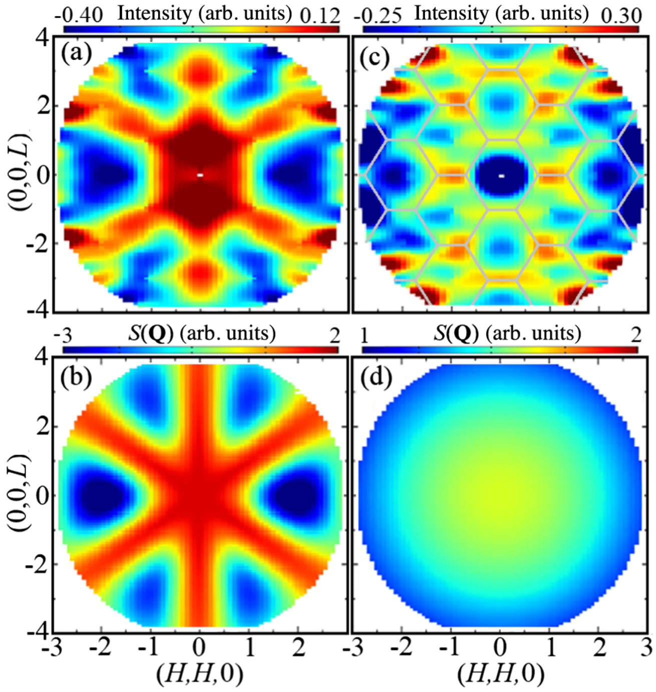

FIG. 8. (a) The symmetrized $T = 45$ mK $- T = 10$ K temperature-difference neutron signal measured in the SF channel of our polarized neutron diffraction experiment. (b) The NLC-calculated equal-time structure factor for SF scattering in the $[HHL]$ plane at $T = 0.5$ K with a $T = 10$ K temperature subtraction. (c) The symmetrized $T = 45$ mK $- T = 10$ K temperature-difference neutron signal measured in the NSF channel of our polarized neutron diffraction experiment. The gray lines show the Brillouin zone boundaries. (d) The NLC-calculated equal-time structure factor for NSF scattering in the $[HHL]$ plane at $T = 0.5$ K with a $T = 10$ K temperature subtraction. Both (b) and (d) are calculated using the experimental estimates for the A near-neighbor exchange parameters yielded in this work (see main text).

C. Inelastic neutron scattering from powder samples

Low energy, unpolarized inelastic neutron scattering measurements were performed on powder samples of $Ce_2Zr_2O_7$ as shown in Figs. 9(a)–9(c); this shows the temperature-difference neutron scattering spectra measured for a $T = 0.06$, 0.5, and 3 K dataset with a $T = 9.6$ K dataset used as background. These measurements were taken on the low energy disk chopper spectrometer neutron instrument at NIST Center for Neutron Research with $E_i = 3.27$ meV incident neutrons giving an energy resolution of $\sim$0.09 meV at the elastic line. This larger dataset was

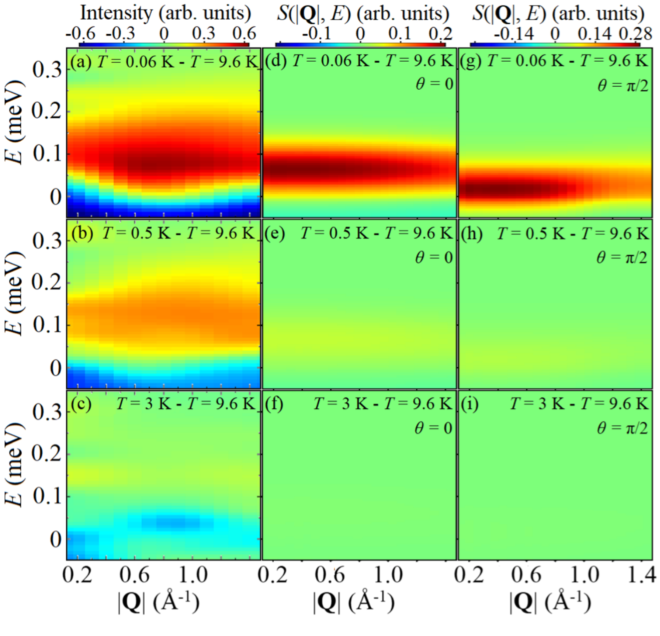

FIG. 9. The measured inelastic neutron scattering from an annealed powder sample of $Ce_2Zr_2O_7$ is shown in panels (a)–(c) for temperature-subtracted data relative to $T = 9.6$ K. The corresponding powder-averaged neutron scattering structure factors $[S(|\mathbf{Q}|, E, T)]$ calculated from semiclassical molecular dynamics calculations based on Monte Carlo simulations using near-neighbor exchange parameters from the A regime, $(J_{\tilde{x}}, J_{\tilde{y}}, J_{\tilde{z}}) = (0.064, 0.063, 0.011)$ meV, are shown in panels (d)–(i). The temperatures of the measured and calculated datasets ($T = 0.06$, 0.5, and 3 K) and the θ values used in the calculations ($\theta = 0$ and $\pi/2$) are as indicated in the individual panels.

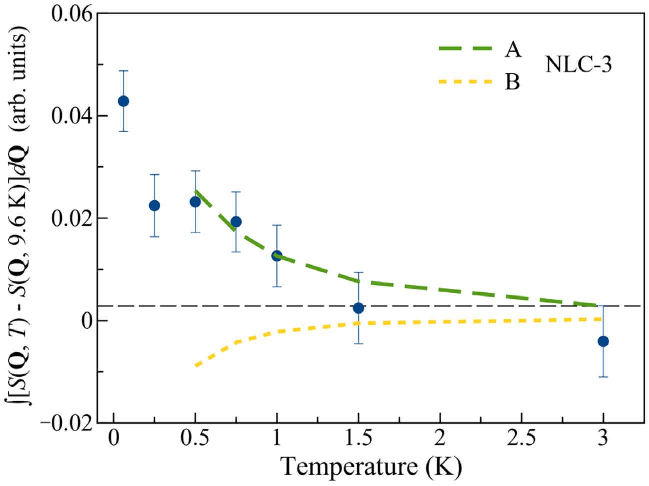

FIG. 10. The results of the NLC $S(\mathbf{Q},T)$ calculation to third order using the A and B exchange parameters, overlaid on top of the measured neutron scattering intensity from our $Ce_2Zr_2O_7$ sample. Here we compare the temperature dependence of the measured and calculated integrated intensities for the $T = 9.6$ K temperature subtraction, with integration over the energy-transfer range $E = [-0.2, 0.4]$ meV and integration in wave vector over the range $|\mathbf{Q}| = [0.46, 0.93]$ Å^{-1}. The temperature dependence of the NLC-calculated integrated $S(\mathbf{Q},T)$ agrees well with that of the measured data when using parameter set A, but clearly does not for set B.

previously discussed in Ref. [7] and we perform two sets of analyses with this dataset. First, in Fig. 10, we examine the temperature dependence of the measured and calculated integrated intensities for the $T = 9.6$ K temperature subtraction, with integration in energy transfer over the range $E = [-0.2, 0.4]$ meV and integration in scattering vector over the range $|\mathbf{Q}| = [0.46, 0.93]$ Å^{-1}. This integration range was chosen to enclose the dominant portion of the measured magnetic intensity, while avoiding nuclear Bragg peaks. The NLC calculations are carried out to third order (see Appendix F). For the A (B) exchange parameters, we use $\theta = 0$ (0.561 rad), but it is important to note that there is no choice of θ for which the calculations using the B parameters agree with the temperature dependence of the experimental data over the range $|\mathbf{Q}| = [0.46, 0.93]$ Å^{-1}.

We also compare these measurements with the corresponding spectra obtained via semiclassical molecular dynamics (MD) calculations based on Monte Carlo simulations (see Appendix H) using the near-neighbor exchange parameters from the A regime, $(J_{\tilde{x}}, J_{\tilde{y}}, J_{\tilde{z}}) = (0.064, 0.063, 0.011)$ meV, for $\theta = 0$ [Figs. 9(d)–9(f)] and $\theta = \pi/2$ [Figs. 9(g)–9(i)].

The temperature dependence of the measured signal is most consistent with that obtained from the semiclassical MD and Monte Carlo simulations using $(J_{\tilde{x}}, J_{\tilde{y}}, J_{\tilde{z}}) = (0.064, 0.063, 0.011)$ meV when $\theta = 0$. Furthermore, the energy dependence of the predicted signal is only consistent with the measured data for values of θ near $\theta = 0$; as θ increases from $\theta = 0$ to $\theta = \pi/2$, the spectral weight in the simulated signal shifts from $E \sim 0.1$ meV to $E \sim 0$ meV, as illustrated in Figs. 9(d) and 9(g).

VI. DISCUSSION

A. Low temperature heat capacity and entropy

The new C_p measurements also provide better definition of the low temperature C_{mag}, below ~0.1 K, where C_{mag} falls off sharply toward zero. The lowest-temperature data points can be used to model how C_{mag} approaches zero at $T = 0$ K. This is interesting to do because an extrapolation of C_{mag} below experimentally accessible temperatures to $T = 0$ K allows us to evaluate the entropy $S_{\text{mag}}(T) = \int_0^T (C_{\text{mag}}/T)dT$.

The two simple forms for the low temperature C_{mag}, an exponential form and a cubic form, are shown in the inset of Fig. 3. Both forms are too simple to be related to the spin Hamiltonian or $U(1)_\pi$ ground state in any sophisticated manner; however, one can smoothly extrapolate the low temperature C_{mag} data to zero using an exponentially activated form. A simple power law, such as the cubic form in the inset of Fig. 3, does not smoothly meet up with the low temperature data at the lowest measured temperature, $T = 0.058$ K; doing so would require a nonphysical sublinear C_{mag} at the lowest temperatures. A cubic extrapolation was used in the previous work on the C_{mag} of $Ce_2Zr_2O_7$ (Ref. [8]); however, our new results, consistent with the previous measurements, show that such a low temperature extrapolation is inappropriate.

The cubic form would be appropriate for emergent gapless photon excitations associated with U(1) QSLs [5,12,24]. However, depending on the speed of light for these emergent photons, their T^3 contribution may only enter at very low temperatures [25]. Furthermore, the bending of the photon dispersion toward the zone boundary, combined with contributions from gapped spinons and visons, can easily mimic the exponentially activated form at intermediate temperatures. Interactions between visons and photons can also cause the photons to develop an effective temperature-dependent gap [26]. To address these subtleties, we use a low T form for C_{mag} which is based on an interpolation scheme connecting the $T >$ ~0.5 K C_{mag} regime described by the NLC calculations, and hence consistent with the proposed spin Hamiltonian, to a low temperature form consistent with a T^3 C_{mag} from U(1) emergent photons at sufficiently low temperatures. This involves an interpolation scheme for C_{mag} and S_{mag} following the method of Padé approximants in Ref. [27] (see Appendix I). The resulting theoretical curve, now covering all temperatures, is shown as the solid line in Figs. 11(a) and 11(b). Clearly the low temperature portion of this curve smoothly connects to the low temperature

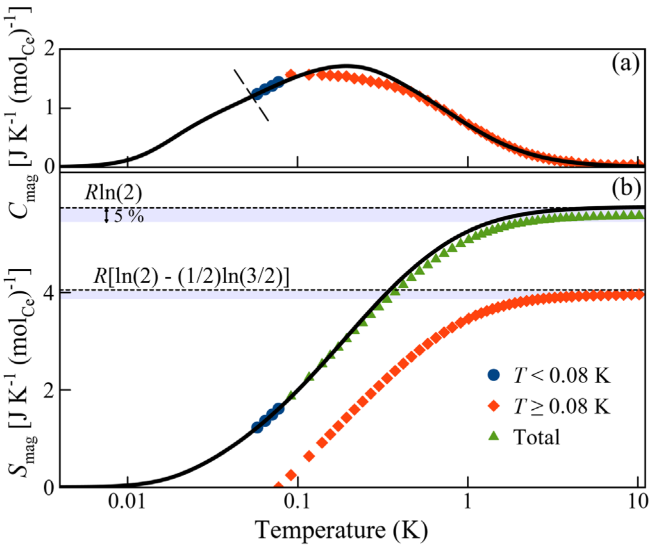

FIG. 11. (a) The measured $C_{\rm mag}$ and best-fit $C_{\rm mag}$ interpolation for the $\rm Ce_2Zr_2O_7$ sample of the present work. The data are divided into high and low T regimes around $T = 0.08$ K, which separates the plateau regime from the rapidly decreasing $C_{\rm mag}$ regime. (b) The magnetic entropy recovered from $S_{\rm mag} = \int_{T_0}^{T}(C_{\rm mag}/T)dT$ over the full temperature range ($T_0 = 0$ K) and above the onset of the plateau ($T_0 = 0.08$ K) are shown. This is derived from the integration of $C_{\rm mag}$ shown in (a), and employs the $C_{\rm mag}$ interpolation below the lowest measured temperature, accounting for gapless photons as well as gapped spinons and visons. $R\ln(2)$ in entropy is recovered over the full temperature range, to within 5%, which is the approximate deficiency expected for $\rm Ce^{4+}$ in this sample. The Pauling spin ice entropy $R[\ln(2) - \frac{1}{2}\ln(\frac{3}{2})]$ is recovered from the onset of the plateau, $T = 0.08$ K, to $T = 10$ K to within approximately the same tolerance.

$C_{\rm mag}$ data. The point of this exercise is to provide a physically motivated form of $C_{\rm mag}$ which extrapolates smoothly between the lowest-temperature $C_{\rm mag}$ data point and zero at $T = 0$ K.

With a good minimal description of $C_{\rm mag}$ for $\rm Ce_2Zr_2O_7$ at the lowest temperatures in place, we can look to account for the entropy associated with the DO doublet, which must be $R\ln(2)$, as this ground-state doublet is well separated, by ~55 meV, from the first excited CEF state [7,8]. Figure 11(b) shows the integration of the $C_{\rm mag}/T$ data to give the entropy $S_{\rm mag}$ to ~10 K. The experimental entropy of $R\ln(2)$ is recovered, to within 5%, which may be associated with $4f^0$ $\rm Ce^{4+}$ impurities. Interestingly, Fig. 11(b) also shows that accounting for the entropy from the only feature in the temperature dependence of $C_{\rm mag}$, the beginning of the $C_{\rm mag}$ plateau at $T = 0.08$ K, to 10 K gives $\sim R[\ln(2) - \frac{1}{2}\ln(\frac{3}{2})]$, the Pauling entropy associated with both spin ice and proton disorder in solid ice. Note that this latter argument is independent of the low temperature extrapolation of $C_{\rm mag}$.

B. Implications of small θ

In the case where $J_{\tilde{x}}$ is the largest exchange parameter in the XYZ Hamiltonian, the resulting $\mathrm{U}(1)_\pi$ QSL is dipolar from a symmetry perspective. Its emergent electric field transforms like a magnetic dipole. However, the small value of θ suppresses coupling between the emergent field and external magnetic fields. Therefore, for this case, we expect weak coupling between neutrons and emergent photons at low $|\mathbf{Q}|$. In the case of $J_{\tilde{y}} > J_{\tilde{x}}$, there would be no low-$|\mathbf{Q}|$ coupling between photons and neutrons regardless of the value of θ. It is therefore unlikely that the inelastic neutron scattering signal observed at low energy in Refs. [7,8] (and in this work) originates from an integration over emergent photons, despite the similarity to predictions in Ref. [25]. The dominant neutron scattering signal should then come from gapped spinons.

A further implication of the small value for θ is that spin waves in finite magnetic field will be difficult to observe. This may be important to note as modeling spin wave dispersion and intensity in a field-polarized state has been effectively applied to understanding the microscopic ground state in several pyrochlore magnets based on Kramers doublet CEF ground states [15–20]. It may also underlie the lack of observation of well-defined spin waves in studies of $\rm Ce_2Zr_2O_7$ published to date. A finite value of θ implies that the local magnetic moment operator possesses components transverse to the expectation value of the pseudospins in the high field state. It is the finite transverse matrix elements which allow the observation of single spin waves by inelastic neutron scattering. In contrast, when $\theta = 0$, the magnetic moment operator is parallel to the pseudospin directions in the high field state, and the matrix element connecting the ground state to single spin wave excitations is zero.

VII. SUMMARY AND CONCLUSIONS

To conclude, we report new spin-polarized neutron diffraction and $C_{\rm mag}$ measurements on single crystal $\rm Ce_2Zr_2O_7$ in zero magnetic field. Our modeling of $C_{\rm mag}$, χ, and $S(\mathbf{Q}, T)$ with NLC calculations provides strong constraints on the exchange terms in the microscopic near-neighbor XYZ Hamiltonian. We arrive at best-fit Hamiltonian parameters $\theta \sim 0$ and $(J_{\tilde{x}}, J_{\tilde{y}}, J_{\tilde{z}}) = (0.064, 0.063, 0.011)$ meV or $(J_{\tilde{x}}, J_{\tilde{y}}, J_{\tilde{z}}) = (0.063, 0.064, 0.011)$ meV, which indicates that a $\mathrm{U}(1)_\pi$ QSL ground state is selected near the boundary between dipolar and octupolar character.

The best-fitting exchange parameters from this work largely describe the SF neutron diffraction signal measured from single crystal $Ce_2Zr_2O_7$, while zone-boundary scattering in the NSF channel indicates the significance of interactions beyond near neighbor, including long-ranged dipolar interactions. The seventh-order NLC calculations for C_{mag} evaluated at the best-fit Hamiltonian parameters do not describe the measured C_{mag} at the lowest temperatures, again consistent with weak interactions in $Ce_2Zr_2O_7$'s Hamiltonian beyond near neighbor and beyond the scope of the present calculations.

The new C_{mag} data extend to temperatures as low as $T = 0.058$ K and can be smoothly extrapolated to zero temperature using a form consistent both with the XYZ spin Hamiltonian estimated from fitting the NLC calculations to the data and with a T^3 form for C_{mag} at sufficiently low temperatures, appropriate to emergent gapless photons. With such a low T form for C_{mag} in place we show the $R\ln(2)$ entropy associated with Ce^{3+}'s DO doublet ground state is recovered to 10 K. Phenomenologically, we observe that the Pauling entropy for spin ice is recovered above the onset of the $T \sim 0.08$ K plateau in C_{mag}.

ACKNOWLEDGMENTS

We greatly appreciate the technical support from Alan Ye and Yegor Vekhov at the NIST Center for Neutron Research. This work was supported by the Natural Sciences and Engineering Research Council of Canada (NSERC). We also acknowledge the support of both the Institut Laue-Langevin and the National Institute of Standards and Technology, U.S. Department of Commerce for neutron beam time as well as administrative and technical assistance during the course of our experiments. D. R. Y. and K. A. R. acknowledge the use of the Analytical Resources Core at Colorado State University. B. P. and R. S. acknowledge support by the Deutsche Forschungsgemeinschaft under Grant No. SFB 1143 (Project No. 247310070) and the cluster of excellence ct.qmat (EXC 2147, Project No. 390858490). Work at LANL was supported by the U.S. Department of Energy, Office of Science, Basic Energy Sciences, Materials Sciences and Engineering Division (R. M.). We thank Paul McClarty for a critical reading of the manuscript.

APPENDIX A: SYNTHESIS AND CHARACTERIZATION

The powder and single crystal samples of $Ce_2Zr_2O_7$ used in this work were prepared and characterized as described in Ref. [7]. $La_2Zr_2O_7$ was synthesized in order to estimate the phonon contribution to the C_p of $Ce_2Zr_2O_7$. The powder samples of $La_2Zr_2O_7$ measured in this work were first prepared by mixing stoichiometric amounts of La_2O_3 (Alfa Aesar 99.99%) and ZrO_2 (Alfa Aesar 99.7%). The La_2O_3 (ZrO_2) powder was precalcined (dried) at 800 °C (200 °C) prior to mixing. The stoichiometric mixture was pelletized and sintered in air at 1350 °C for 36 h, 3 times, with regrinding and repelletization between sinterings. Figure 12 shows an x-ray Rietveld refinement against the $Fd\bar{3}m$ space group for a typical powder sample of $La_2Zr_2O_7$ synthesized for this work.

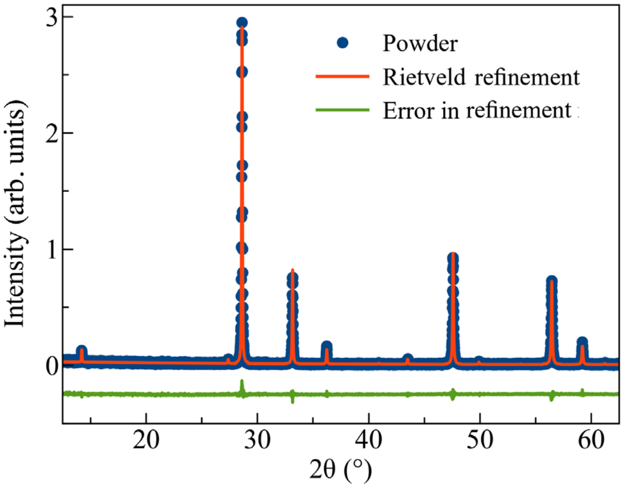

FIG. 12. Powder x-ray refinement of the $La_2Zr_2O_7$ sample synthesized for this work. The difference between the measured and calculated diffraction patterns is shown in green and indicates phase purity; this line has been shifted downward by 0.25 units for visibility.

APPENDIX B: HEAT CAPACITY AND NUMERICAL LINKED CLUSTER CALCULATIONS WITH 5% OXIDATION

We provide further details on the results of our fourth-order NLC calculations for C_{mag} with a 5% oxidation level included in the calculations. The calculated C_{mag} with 5% oxidation using the globally (locally) best-fitting exchange parameters that are also able to describe the measured susceptibility, A′ (B′), is shown in Fig. 13(a) [Fig. 13(b)]. To improve convergence of the NLC calculations, we used the Euler transformation to the third (Euler 3) and fourth (Euler 4) orders (see Appendix J). While the parameter sets A′ and B′ are both locally optimal, the A′ description of the C_{mag} data is clearly superior.

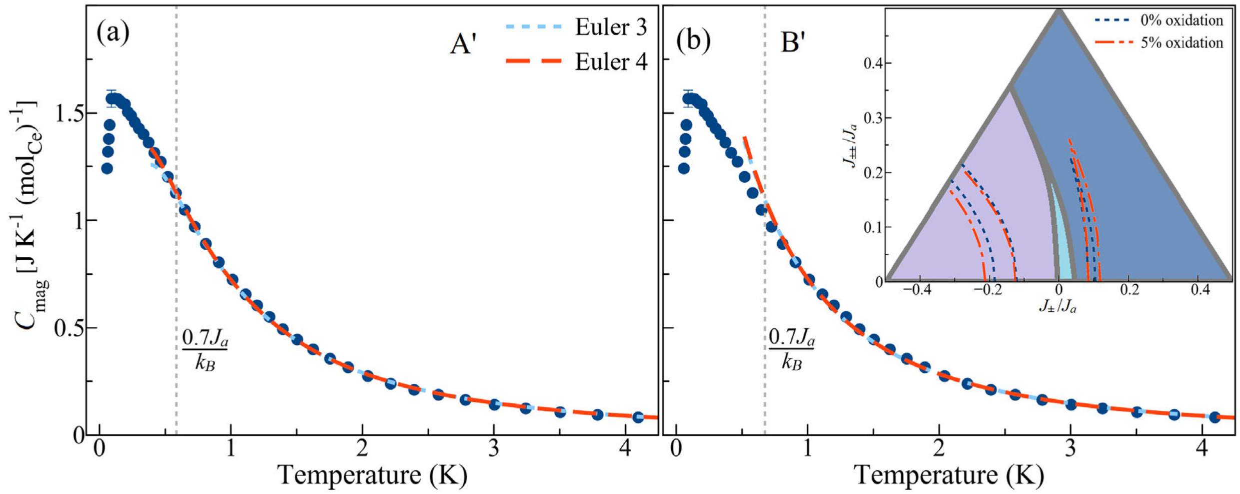

FIG. 13. (a) The results of the fourth-order NLC $C_{\rm mag}$ calculation for 5% sample oxidation, using the near-neighbor exchange parameters $J_a = 0.067$ meV, $J_b = 0.067$ meV, and $J_c = 0.012$ meV (set A′), overlaid on top of the measured $C_{\rm mag}$ for our $Ce_2Zr_2O_7$ sample. (b) The results of the fourth-order NLC $C_{\rm mag}$ calculation for 5% sample oxidation, using the near-neighbor exchange parameters $J_a = 0.089$ meV, $J_b = 0.006$ meV, and $J_c = -0.037$ meV (set B′), overlaid on top of the measured $C_{\rm mag}$ for our $Ce_2Zr_2O_7$ sample. We have used Euler transformations to the third (Euler 3) and fourth (Euler 4) orders to improve convergence of the NLC $C_{\rm mag}$ calculations (see Appendix J). The inset of (b) shows a comparison of the locally optimal fitting regions obtained from NLC calculations with an oxidation level of 0% (blue) and 5% (red). For visualization purposes, the optimal fitting regions in this plot are defined by $\log\langle\delta^2/\epsilon^2\rangle_{C\rm mag} < 2.7$, where $\langle\delta^2/\epsilon^2\rangle_{C\rm mag}$ is the goodness-of-fit parameter for the NLC calculations as described in the main text. We overplot this on the predicted ground-state phase diagram for the XYZ model Hamiltonian [10], but omit the labels for aesthetic purposes [see Fig. 4(b) for labels]. Conclusions from fitting the NLC calculations to the data are robust to at least a 5% oxidation level.

The inset of Fig. 13(b) shows the two locally optimal regions of parameter space for the fourth-order NLC calculations of $C_{\rm mag}$, for both a 0% oxidation level and a 5% oxidation level, defined by $\log\langle\delta^2/\epsilon^2\rangle_{C\rm mag} < 2.7$ for the purposes of the visualization. From the similarity of these regions and their local minima (A and A′, B and B′), we conclude that the results of the NLC calculations for $C_{\rm mag}$ are robust to the sample oxidation up to oxidation levels of at least 5%. In Table 1 we summarize the results of our NLC fittings to $C_{\rm mag}$ and list the best-fitting exchange parameters corresponding to each fitting.

TABLE I. A summary of the different sets of near-neighbor exchange constants discussed throughout this work. Each set of exchange constants was determined according to the minimization of the goodness-of-fit parameter $\langle\delta^2/\epsilon^2\rangle_{C\rm mag}$ corresponding to fourth-order NLC calculations for $C_{\rm mag}$ with a low temperature threshold of $0.7J_a/k_B$ in the evaluation of $\langle\delta^2/\epsilon^2\rangle_{C\rm mag}$. We also list the level of sample oxidation considered in each calculation.

Set	Oxidation	J_a (meV)	J_b (meV)	J_c (meV)
A	0%	0.064	0.063	0.011
A′	5%	0.067	0.067	0.012
B	0%	0.089	−0.007	−0.027
B′	5%	0.089	0.006	−0.037

APPENDIX C: NLC FITTING TO χ

In this Appendix, we discuss the results of the NLC fitting to the magnetic susceptibility measured from a powder sample of $Ce_2Zr_2O_7$. The magnetic susceptibility is dependent on the values of $J_{\tilde{x}}$, $J_{\tilde{y}}$, $J_{\tilde{z}}$, and θ. The exchange parameters $(J_{\tilde{x}}, J_{\tilde{y}}, J_{\tilde{z}})$ are given by some permutation of (J_a, J_b, J_c). We allow θ to vary in the range from 0 to $\pi/4$. This is enough to cover all distinguishable scenarios, since changing the sign of θ does not affect any quantity considered here, and shifting θ to $\theta + \pi/2$ is the same as reversing the sign of θ and swapping the values of $J_{\tilde{x}}$ and $J_{\tilde{z}}$, which is already covered by considering all six permutations of exchange parameters.

NLC calculations up to second order were performed to compute the powder-averaged magnetic susceptibility and to compare the calculations to the corresponding measurement on $Ce_2Zr_2O_7$. A constant term was added to the NLC calculations to account for the effect of mixing in higher crystal-field levels due to an applied magnetic field. This term is calculated from the low temperature limit of single ion susceptibility using the crystal-field scheme of Ce^{3+} in $Ce_2Zr_2O_7$ reported in Ref. [7]. The level of sample oxidation for the measured powder sample had an upper limit of ∼14%. This upper limit was estimated from fits to the single ion susceptibility at high temperature using the crystal-field scheme of Ce^{3+} in $Ce_2Zr_2O_7$ reported in Ref. [7]. Accordingly, a 14% oxidation level is included in our NLC calculations of the magnetic susceptibility.

NLC calculations of the magnetic susceptibility were performed for parameter sets throughout the A and B regions identified by the C_{mag} fittings. The calculations were compared with experimental data between 1 and 10 K. Figure 5 shows the regions of the phase diagram for which it is possible to obtain simultaneous agreement with C_{mag} and χ, for $(J_{\tilde{x}}, J_{\tilde{y}}, J_{\tilde{z}})$ equal to the different permutations of (J_a, J_b, J_c). We define these regions by the simultaneous satisfaction of $\log\langle\delta^2/\epsilon^2\rangle_{C\mathrm{mag}} < 2.7$ and $\log\langle\delta^2/\epsilon^2\rangle_{\chi} < 12.1$. The goodness-of-fit measure $\langle\delta^2/\epsilon^2\rangle_{C\mathrm{mag}}$ is defined in the main text, and $\langle\delta^2/\epsilon^2\rangle_{\chi} \propto \sum\{[\chi^{\mathrm{NLC}}(T_{\mathrm{expt}}) - \chi^{\mathrm{expt}}(T_{\mathrm{expt}})]^2/\epsilon(T_{\mathrm{expt}})^2\}$, where the sum is over measured temperatures T_{expt} between 1 and 10 K and $\epsilon(T_{\mathrm{expt}})$ is the experimental uncertainty on the magnetic susceptibility at temperature T_{expt}. We allow θ to vary in the range from 0 to $\pi/4$ in finding the best agreement with the susceptibility data for each permutation. The relatively small experimental uncertainties on the magnetic susceptibility contribute to the larger upper limit for $\langle\delta^2/\epsilon^2\rangle_{\chi}$ in comparison to the upper limit used for $\langle\delta^2/\epsilon^2\rangle_{C\mathrm{mag}}$.

APPENDIX D: ELASTIC NEUTRON SCATTERING

In this Appendix, we discuss the analysis of our elastic neutron scattering data, measured on an annealed powder sample of $Ce_2Zr_2O_7$ and used to place an upper limit of $\mu_{\mathrm{ordered}} \leq 0.04\mu_B$ on the ordered moment corresponding to any all-in, all-out dipole order in $Ce_2Zr_2O_7$'s magnetic ground state. The strongest magnetic Bragg peaks associated with AIAO order are expected to reside at the $\mathbf{Q} = (2,2,0)$ and $\mathbf{Q} = (1,1,3)$ positions of reciprocal space. Accordingly, we can examine the temperature dependence of the scattered intensity at these locations in order to look for increases of intensity with decreasing temperature, which would signal the onset of a magnetic Bragg peak and associated magnetic order. As shown in Fig. 14(a), no such increase in intensity is detected upon lowering temperature.

In Fig. 14(b), we show the measured intensity around the $\mathbf{Q} = (2,2,0)$ (left) and $\mathbf{Q} = (1,1,3)$ (right) positions at $T = 0.06$ K (blue) and as averaged over the temperatures $T = 0.25$ K, $T = 0.5$ K, $T = 0.75$ K, $T = 1$ K, and $T = 1.5$ K (red). Gaussian fits to the peak at each of the locations are also shown for each temperature (or temperature average) and the area underneath of these Gaussian peaks was used in order to determine the corresponding integrated intensity for each peak. From these values for the integrated intensity, we place an upper limit of $\mu_{\mathrm{ordered}} \leq 0.04\mu_B$ for the Ce^{3+} ordered moment corresponding to any AIAO magnetic dipole ordering in $Ce_2Zr_2O_7$.

For each selected Bragg peak position $\mathbf{Q}$, an upper limit is calculated in accordance with the equation

$$\mu_{\mathrm{ordered}} = \left(\frac{I^{\mathrm{expt}}_{\mathrm{mag}}}{I^{\mathrm{expt}}_{\mathrm{nuc}}}\right)^{1/2} \frac{|F(\mathbf{Q})|}{|\mathbf{F}^{\mathrm{mag}}_{\perp}(\mathbf{Q})/\mu|}, \tag{D1}$$

where $I^{\mathrm{expt}}_{\mathrm{mag}}$ and $I^{\mathrm{expt}}_{\mathrm{nuc}}$ are the measured magnetic and nuclear contributions to the integrated Bragg intensity, respectively. $F(\mathbf{Q})$ is the nuclear structure factor and $\mathbf{F}^{\mathrm{mag}}_{\perp}(\mathbf{Q})/\mu$ is the component of the magnetic structure factor that is perpendicular to $\mathbf{Q}$, after dividing out the magnitude of the ordered moment (μ) from the calculation [28].

APPENDIX E: POLARIZED NEUTRON SCATTERING MEASUREMENTS AND CALCULATIONS

We have used third-order NLC calculations to compute the energy-integrated scattering signals corresponding to a polarized neutron scattering experiment with sample

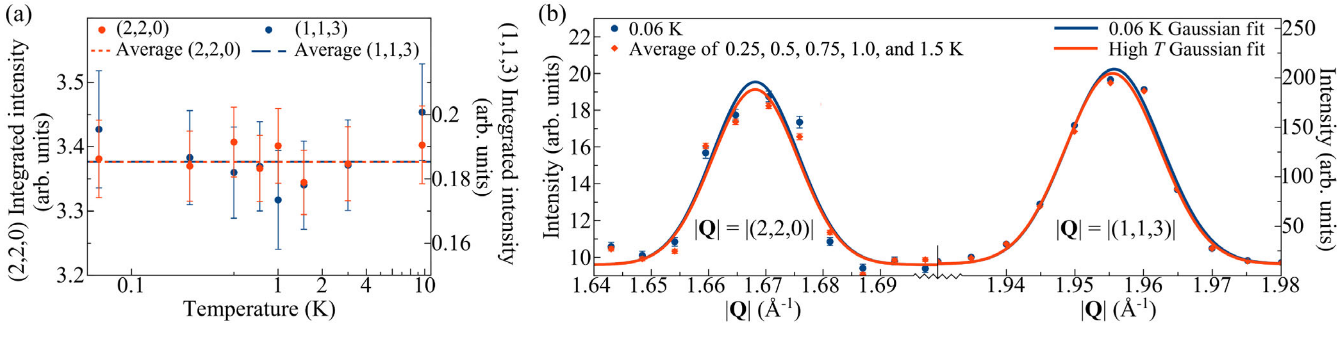

FIG. 14. (a) The temperature dependence of the integrated intensity for the Bragg peaks at the $\mathbf{Q} = (2,2,0)$ (red) and $\mathbf{Q} = (1,1,3)$ (blue) positions. No significant temperature dependence is discernible. (b) Elastic Q cuts through the $\mathbf{Q} = (2,2,0)$ (left) and $\mathbf{Q} = (1,1,3)$ (right) positions at $T = 0.06$ K (blue) and averaged over the higher temperature data points $T = 0.25, 0.5, 0.75, 1, 1.5$ K (red). The Gaussian fitting to each of these datasets, used to determine a corresponding integrated intensity, is also shown for each Bragg peak in (b). From these integrated intensities, we conclude that no AIAO dipole order occurs in $Ce_2Zr_2O_7$, with an upper limit on the Ce^{3+} ordered moment of $\mu_{\mathrm{ordered}} \leq 0.04\mu_B$.

alignment in the $[HHL]$ scattering plane. The exchange parameters are set to $\theta = 0$ and $(J_{\tilde{x}}, J_{\tilde{y}}, J_{\tilde{z}}) = (0.064, 0.063, 0.011)$ meV for the calculation and we perform the NLC-3 calculation with $T = 0.5$ K, as that is the lowest temperature for which the NLC expansion converges. Specifically, we compute

$$S^{\mathrm{SF}}(\mathbf{Q}) = \frac{1}{N}|f(|\mathbf{Q}|)|^2\sum_{ij}\{e^{i\mathbf{Q}\cdot(\mathbf{r}_i-\mathbf{r}_j)}[\hat{\mathbf{u}}(\mathbf{Q})\cdot\hat{\mathbf{z}}_i][\hat{\mathbf{u}}(\mathbf{Q})\cdot\hat{\mathbf{z}}_j] \times [\sin^2(\theta)\langle S_i^{\tilde{x}}S_j^{\tilde{x}}\rangle + \cos^2(\theta)\langle S_i^{\tilde{z}}S_j^{\tilde{z}}\rangle]\} \tag{E1}$$

and

$$S^{\mathrm{NSF}}(\mathbf{Q}) = \frac{1}{N}|f(|\mathbf{Q}|)|^2\sum_{ij}\{e^{i\mathbf{Q}\cdot(\mathbf{r}_i-\mathbf{r}_j)}(\hat{\mathbf{n}}\cdot\hat{\mathbf{z}}_i)(\hat{\mathbf{n}}\cdot\hat{\mathbf{z}}_j) \times [\sin^2(\theta)\langle S_i^{\tilde{x}}S_j^{\tilde{x}}\rangle + \cos^2(\theta)\langle S_i^{\tilde{z}}S_j^{\tilde{z}}\rangle]\}, \tag{E2}$$

where $S^{\mathrm{SF}}(\mathbf{Q})$ $[S^{\mathrm{NSF}}(\mathbf{Q})]$ denotes the energy-integrated structure factor for SF (NSF) scattering. N is the number of spins in the lattice, $f(|\mathbf{Q}|)$ is the magnetic form factor for Ce^{3+} (calculated using the analytical approximation in Ref. [29]), $\hat{\mathbf{n}}$ is the neutron polarization direction, $\hat{\mathbf{z}}_i$ is the local anisotropy axis for the site i, and

$$\hat{\mathbf{u}}(\mathbf{Q}) = \frac{\hat{\mathbf{n}}\times\mathbf{Q}}{|\hat{\mathbf{n}}\times\mathbf{Q}|}. \tag{E3}$$

We compute $S^{\mathrm{SF}}(\mathbf{Q})$ and $S^{\mathrm{NSF}}(\mathbf{Q})$ at $T = 0.5$ K, and in each case we subtract the corresponding calculation at $T = 10$ K for better comparison with the temperature-subtracted experimental data. In Figs. 8(a) and 8(b) [Figs. 8(c) and 8(d)] of the main text, we compare the NLC-calculated $S^{\mathrm{SF}}(\mathbf{Q})$ $[S^{\mathrm{NSF}}(\mathbf{Q})]$ to polarized neutron scattering measurements performed on an annealed ~1.5 g single crystal sample of $\mathrm{Ce_2Zr_2O_7}$ using the D7 diffractometer at the Institut Laue-Langevin with an incident energy of $E_i = 3.47$ meV and a dilution refrigerator sample environment. The sample was aligned in a copper sample holder in the $[HHL]$ scattering plane with the uniaxial polarization direction perpendicular to the $[HHL]$ plane, and the sample was rotated in 0.5° steps over a total of 250°. The data are subsequently folded into a single quadrant of the $[HHL]$ plane and further symmetrized. We have further discussed this symmetrization process in the Supplemental Material of Ref. [7]. For each dataset, we reduce the data in a manner that avoids adding artifacts arising from the subtraction of strong nuclear Bragg peaks. Allowed nuclear Bragg peaks are located at $\mathbf{Q} = (1,1,1), (2,2,2), (1,1,3), (2,2,0), (0,0,4)$, and symmetrically equivalent locations. The intensity at each Bragg peak location is masked in performing the temperature subtraction, and we then show the intensity at these masked Bragg peak locations as the average intensity of the surrounding points in reciprocal space.

APPENDIX F: NLC FITTING TO INTEGRATED $S(\mathbf{Q}, T)$

The microscopic spin Hamiltonian parameters A and B can be employed in third-order NLC calculations to calculate equal-time (energy-integrated) structure factors, and these can be compared to inelastic neutron scattering measurements on $\mathrm{Ce_2Zr_2O_7}$. The energy-integrated structure factor is

$$S(\mathbf{Q}) = |f(|\mathbf{Q}|)|^2\sum_{ij}\left(\hat{\mathbf{z}}_i\cdot\hat{\mathbf{z}}_j - \frac{(\hat{\mathbf{z}}_i\cdot\mathbf{Q})(\hat{\mathbf{z}}_j\cdot\mathbf{Q})}{|\mathbf{Q}|^2}\right) [\cos^2(\theta)\langle S_i^{\tilde{x}}(-\mathbf{Q})S_j^{\tilde{x}}(\mathbf{Q})\rangle + \sin^2(\theta)\langle S_i^{\tilde{z}}(-\mathbf{Q})S_j^{\tilde{z}}(\mathbf{Q})\rangle], \tag{F1}$$

where i, j, are sublattice indices and $f(|\mathbf{Q}|)$ is the magnetic form factor for Ce^{3+}. Averaging over directions at fixed magnitude $|\mathbf{Q}| = Q$ gives the powder structure factor $S(Q)$. We integrate over $Q = [0.46, 0.93]$ Å^{-1} and the result represents the energy-integrated neutron scattering response of a powder sample integrated over that momentum range, as a function of T. The structure factor at $T = 9.6$ K is subtracted to replicate the background subtraction used in the experiment. Lines in Fig. 10 of the main text represent the powder integrated equal-time structure factor calculated in third-order NLC using parameter sets A with $\theta = 0$ and B with $\theta = 0.561$ rad.

We compare the NLC calculations to the experimentally measured neutron scattering response of a powder sample, integrated over the energy range $[-0.2, 0.4]$ meV. This integration range is chosen to enclose the low-lying excitations of the system while avoiding unnecessary contamination to the temperature-subtracted signal, which often becomes more prevalent at higher energies. To further reduce the effect of noise on the experimental data, we integrate in momentum transfer over the range $|\mathbf{Q}| = [0.46, 0.93]$ Å^{-1}. This integration range is chosen to avoid nuclear Bragg peaks while still enclosing the dominant portion of the measured magnetic signal. We find that parameter sets from region A correctly predict the observed increase in scattering over the range $|\mathbf{Q}| = [0.46, 0.93]$ Å^{-1} with decreasing temperature, while parameter sets from region B do not, as shown in Fig. 10 of the main text.

Figure 15(a) [Figs. 15(b)–15(g)] shows the temperature-difference neutron scattering spectra measured from an annealed powder sample of $\mathrm{Ce_2Zr_2O_7}$ for a $T = 0.06$ K $[0.25, 0.5, 0.75, 1, 1.5, 3$ K$]$ dataset with a $T = 9.6$ K dataset used as background. The data in Fig. 15(a) [Figs. 15(c) and 15(g)] are also shown in Figs. 9(a) [Figs. 9(b) and 9(c)] with different $|\mathbf{Q}|$ range and $|\mathbf{Q}|, E$ pixel size. These datasets were used to compute the measured integrated intensity over the energy range $[-0.2, 0.4]$ meV and the momentum range $[0.46, 0.93]$ Å^{-1}, forming the data points shown in Fig. 10 of the main text.

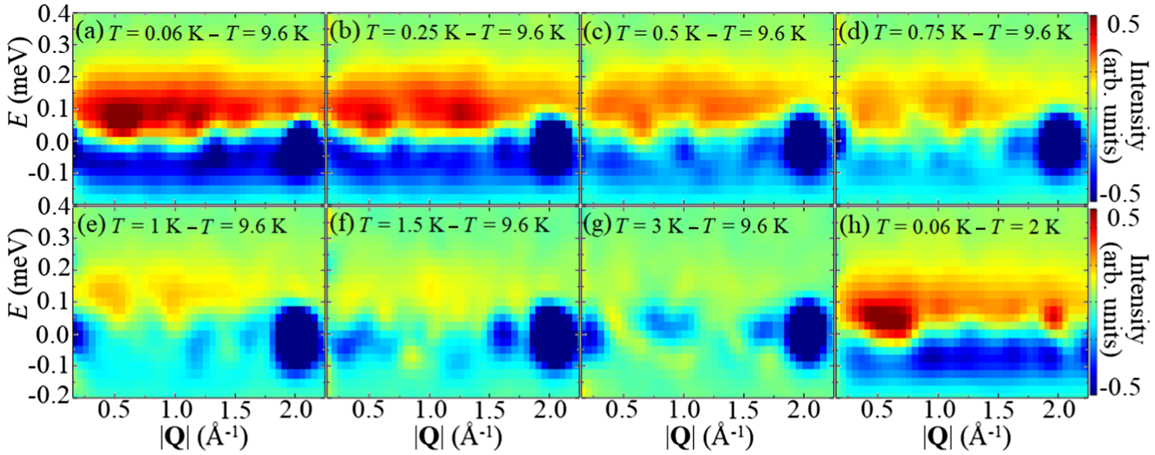

FIG. 15. The temperature evolution of the low energy inelastic neutron scattering from a powder sample of $Ce_2Zr_2O_7$. A dataset measured at 9.6 K has been subtracted from a dataset measured at $T = 0.06$ K (a), 0.25 K (b), 0.5 K (c), 0.75 K (d), 1 K (e), 1.5 K (f), and 3 K (g). (h) The powder-averaged neutron scattering signal measured at $T = 0.06$ K from a single-crystal sample of $Ce_2Zr_2O_7$, with a $T = 2$ K dataset subtracted, is shown for comparison.

APPENDIX G: COMPARISON OF TEMPERATURE DEPENDENCE OF C_{mag} WITH POWDER-AVERAGED INELASTIC NEUTRON SCATTERING

The new measured C_{mag} data also allow for a comparison with the temperature-dependent inelastic neutron scattering signal measured on an annealed powder sample of $Ce_2Zr_2O_7$ [7]. Specifically, we compare the C_{mag} data with the imaginary part of the dynamic spin susceptibility $\chi''(\mathbf{Q}, E)$ calculated from our previously reported neutron data. As shown in Figs. 15(a)–15(g), a signal with the approximate energy range $E = [0, 0.15]$ meV is seen to onset in the inelastic neutron scattering spectra with decreasing temperature. The dominant intensity within this signal was used to calculate $\langle \chi''(\mathbf{Q}, E) \rangle$ for each temperature, giving rise to the data points shown in Fig. 16 and allowing us to further examine the temperature dependence of the measured neutron scattering signal. $\chi''(\mathbf{Q}, E)$ was calculated via $\chi''(\mathbf{Q}, E) = S_0(\mathbf{Q}, E, T)(1 - e^{-E/k_B T})$, where $S_0(\mathbf{Q}, E, T) = S(\mathbf{Q}, E, T) - S(\mathbf{Q}, E, \quad T = 9.6 \text{ K})$. This subtraction is used to isolate the magnetic contribution to the measured neutron scattering spectra, and assumes that $\chi''(\mathbf{Q}, E) = 0$ at $T = 9.6$ K. This was used to calculate the average of $\chi''(\mathbf{Q}, E)$ over $|\mathbf{Q}| = [0.46, 0.93]$ Å^{-1}, $E = [0, 0.15]$ meV, denoted as $\langle \chi''(\mathbf{Q}, E) \rangle$. As shown in Fig. 16, the temperature onset of $\langle \chi''(\mathbf{Q}, E) \rangle$ coincides well with that of the broad hump in C_{mag}, and $\langle \chi''(\mathbf{Q}, E) \rangle$ continues to grow, separating from C_{mag}, below $T \sim 0.3$ K.

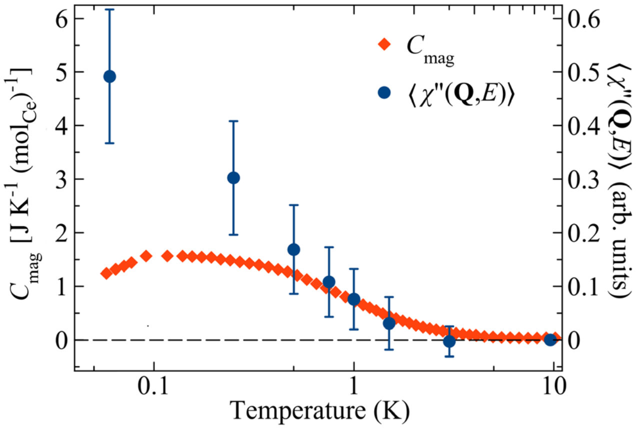

FIG. 16. The low energy dynamic susceptibility $\chi''(\mathbf{Q}, E)$, averaged over $|\mathbf{Q}| = [0.46, 0.93]$ Å^{-1} and $E = [0, 0.15]$ meV, is plotted alongside the measured C_{mag} for the $Ce_2Zr_2O_7$ sample of the present work.

Recent theory work on the XYZ model Hamiltonian with $J_{\tilde{x}} = J_{\tilde{y}}$ (which is a relevant approximation for the best-fitting exchange parameters found in this work) has predicted that a U(1) quantum spin ice ground state can be realized upon decreasing temperature through a classical spin ice regime [12,24,30]. Furthermore, these works predict that a broad hump in C_{mag} onsets slowly on entrance into the classical spin ice regime upon decreasing temperature. This prediction is consistent with the coincidence of the temperature onsets of $\langle \chi''(\mathbf{Q}, E) \rangle$ and C_{mag} shown in Fig. 16.

APPENDIX H: SEMICLASSICAL MOLECULAR DYNAMICS CALCULATION OF $S(|\mathbf{Q}|, E, T)$

Here we discuss the semiclassical molecular dynamics calculations of $S(|\mathbf{Q}|, E, T)$ that lead to the calculated spectra shown in Figs. 9(d)–9(i) of the main text. First, classical Monte Carlo simulations were performed using the best-fit A exchange parameters, to obtain an ensemble of spin configurations sampled at temperature T. We then use these configurations as initial configurations and solve the semiclassical Landau-Lifshitz equation $[d/(dt)]\mathbf{S}_i = -\mathbf{S}_i \times \mathbf{h}_i$, where $\mathbf{h}_i$ is the effective magnetic field on the spin $\mathbf{S}_i$. The dynamical structure factor is obtained as the time-space Fourier transform of the time-evolved magnetic moments, averaged over the ensemble of initial states.

The molecular dynamics solution computes the classical dynamics. That is, it treats the spins as classical magnetic moments precessing in their local field. To compare this to the (quantum) experiment or a theoretical method such as linear spin wave theory, one has to rescale the classical calculation. This is because the classical dynamical structure factor is symmetric with respect to neutron energy transfer E, and it vanishes as T approaches zero for all $E > 0$. Neither of these is the case for the dynamical structure factor of the quantum system. Another, more quantitative, way to think about this is via the fluctuation-dissipation theorem by comparing the version for classical and quantum systems [31]. In particular, for a classical system we get $(\beta E)S_{\mathrm{classical}}(\mathbf{Q}, E, T) = \chi''(\mathbf{Q}, E, T)$, while for the quantum system it reads $(1-e^{-\beta E})S_{\mathrm{quantum}}(\mathbf{Q},E,T) = \chi''(\mathbf{Q},E,T)$, where $\beta = 1/(k_B T)$. It is then reasonable to equate the imaginary part of the susceptibility, $\chi''(\mathbf{Q}, E, T)$, as this quantity is real and symmetric for both the classical and the quantum system. Furthermore, as shown in Ref. [32], $\chi''_{\mathrm{quantum}} = \chi''_{\mathrm{classical}}$ within linear spin wave theory. Using the quantum and classical fluctuation dissipation theorem for the respective sides then yields

$$S_{\mathrm{quantum}}(\mathbf{Q}, E, T) = \frac{\beta E}{1 - e^{-\beta E}} S_{\mathrm{classical}}(\mathbf{Q}, E, T), \qquad \text{(H1)}$$

which is what we use to estimate the dynamical structure factor of the (quantum) experiment using our classical simulation. The dynamical structure factor is then powder averaged to obtain $S_{\mathrm{quantum}}(|\mathbf{Q}|, E, T)$, and convolved with the experimental resolution. In Figs. 9(d)–9(i) of the main text, we show the calculated powder-averaged dynamical structure factor at 0.06, 0.5, and 3 K, with the powder-averaged dynamical structure factor at $T = 9.6$ K subtracted from the result.

Note that Eq. (H1) accounts for detailed balance, $S_{\mathrm{quantum}}(\mathbf{Q}, -E, T) = e^{-\beta E} S_{\mathrm{quantum}}(\mathbf{Q}, E, T)$, since $S_{\mathrm{classical}}(\mathbf{Q}, E, T) = S_{\mathrm{classical}}(\mathbf{Q}, -E, T)$. Zhang *et al.* [32] derive the conversion factor βE by comparing the classical spin wave theory at finite temperature with the quantum spin wave theory at zero temperature. It is thus valid in the case $\beta E \gg 1$, which is well fulfilled in their case, but not applicable to a large part of our energy and temperature range. However, note that our factor $[\beta E/(1 - e^{-\beta E})]$ reduces to βE for $\beta E \gg 1$, so our calculation is entirely consistent with this argument.

APPENDIX I: HEAT CAPACITY MEASUREMENTS AND LOW TEMPERATURE C_{mag} EXTRAPOLATIONS

Heat capacity measurements were performed on our single crystal $Ce_2Zr_2O_7$ sample, along with a polycrystalline sample of $La_2Zr_2O_7$, which is used as a $4f^0$ analog of $Ce_2Zr_2O_7$. Heat capacity measurements on a polished single crystal of $Ce_2Zr_2O_7$ (smooth-surfaced pressed powder pellet of $La_2Zr_2O_7$) were carried out on a Quantum Design PPMS down to $T = 0.058$ K ($T = 2.5$ K) using the conventional quasiadiabatic thermal relaxation technique. The heat capacity of $La_2Zr_2O_7$ is very small at ~2.5 K, and there was no need to pursue measurements at lower temperatures.

We provide further details on the analysis of C_{mag}'s approach to zero at $T = 0$ K. Figure 17(a) shows the results of fitting simple cubic and exponential extrapolations to the measured C_{mag} data, as well as the low temperature extrapolation to C_{mag} which is based upon an interpolation between the results of NLC calculations at $T >$ ~0.5 K and a T^3 low temperature form appropriate to emergent photons in a U(1) QSL. These extrapolations are also shown in Figs. 3 and 11(a) of the main text, respectively. We label the latter extrapolation as "interpolation" in Fig. 17 and the following discussion. This interpolation method is introduced in Ref. [27] and discussed for the current context below.

The interpolation method first involves performing a high temperature expansion of the magnetic heat capacity $C_{\mathrm{mag}}(T)$ corresponding to the XYZ Hamiltonian and the A set exchange parameters, and then turning this into an expansion for the entropy density as a function of energy density $s(e)$ around $e = 0$. If $C_{\mathrm{mag}}(T) \propto T^3$ at low temperature, then for e close to the ground-state energy density e_0, $s(e) \propto (e - e_0)^{3/4}$. A Padé approximant is used to interpolate between those two limits, to obtain $s(e)$ over the region $e = [e_0, 0]$, which can then be converted to $C_{\mathrm{mag}}(T)$ over the range $T = [0, \infty]$. This approach requires an estimate of the ground-state energy per site, e_0. We treat this estimate as an adjustable parameter and set $e_0 = -0.385 J_a$ for best agreement with experiment, which is in a physically plausible range.

The approach based on $s(e)$ is generally better behaved than performing the interpolation on $C_{\mathrm{mag}}(T)$ directly, and it obeys the physical constraints on the total energy and entropy $\int_0^\infty C_{\mathrm{mag}}(T) dT = -e_0$, $\int_0^\infty \{[C_{\mathrm{mag}}(T)]/T\} dT = R\ln(2)$, respectively, by construction. The choice of Padé approximant $P(m, n)$ is constrained to $m + n \leq k$, where k is the maximum order obtained for the high temperature expansion of $C_{\mathrm{mag}}(T)$. In our case $k = 13$, and we take the approximant $P(7, 6)$, again guided by best agreement with experiment. The estimate of e_0 and the choice of m, n are the only adjustable parameters in the comparison, with the exchange parameters equal to the set A parameters (see main text or Table 1). The comparison between theory and experiment is good, particularly for the entropy curve $S_{\mathrm{mag}}(T)$, when one considers that the experimental entropy is missing ~5% of the expected $R\ln(2)$, due to Ce^{4+} substitution which is

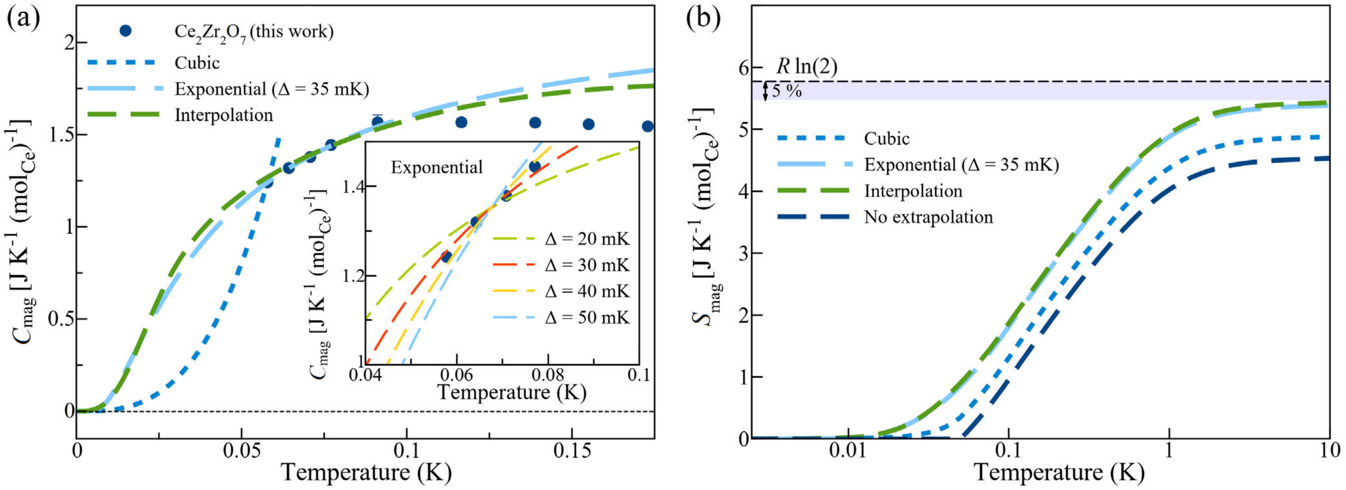

FIG. 17. (a) The best-fitting naive cubic and exponential extrapolations to the measured C_{mag} data, as well as the low temperature extrapolation which is consistent with the NLC fit for $T > \sim 0.5$ K and a T^3 C_{mag} at sufficiently low temperature, as described in the text. A simple best-fitting cubic extrapolation forms a sharp cusplike connection with the data while the simple best-fitting exponential extrapolation and the interpolation (as discussed in the text) both run smoothly through the lowest-temperature data points. The inset of (a) shows the simple exponential extrapolations for different values of the gap energy. Such an analysis yields an estimate of $\Delta = 35(5)$ mK for the gap energy. (b) A comparison of the entropy recovered via $S_{\mathrm{mag}} = \int_0^T (C_{\mathrm{mag}}/T)dT$ using the different low temperature extrapolation schemes of C_{mag} that are shown in (a).

not incorporated in the interpolation calculation. This demonstrates that the observed $C_{\mathrm{mag}}(T)$ can be consistent with a smooth crossover to a T^3 form, even though we do not reach the T^3 regime with the present experimental data.

As shown in Fig. 17(a), the cubic extrapolation cannot be made to connect smoothly to the data at the lowest-temperature data points, while the best-fitting exponential extrapolation and the interpolation both meet the data in a smooth manner. The inset of Fig. 17(a) shows the best-fitting simple exponential extrapolation when locking the gap energy to the values $\Delta = 20$, 30, 40, and 50 mK, and a gap of $\Delta = 35(5)$ mK results from such a naive analysis.

Using each of these extrapolations for C_{mag} in order to describe the data below the lowest-temperature data point, we calculate the entropy recovered via $S_{\mathrm{mag}} = \int_0^T (C_{\mathrm{mag}}/T)dT$ and show the results in Fig. 17(b). As shown in Fig. 17(b), the best-fitting cubic extrapolation grossly underestimates the $R\ln(2)$ entropy associated with the CEF ground-state doublet, while the exponential extrapolation and the interpolation both saturate to $R\ln(2)$ within the ~5% tolerance associated with the sample oxidation.

APPENDIX J: NLC CALCULATIONS AND DISORDER AVERAGING

We use the NLC method to calculate thermodynamic quantities throughout this work. The method is described in Refs. [33–35] (for example). Extensive quantities per site $\langle \mathcal{O} \rangle / N$ are represented as sums over contributions from clusters c:

$$\frac{1}{N}\langle \mathcal{O} \rangle = \sum_c M_c W_c, \tag{J1}$$

where M_c is the cluster multiplicity, defined as the number of times c can be embedded in the lattice, per site N. W_c is the cluster weight:

$$W_c = \langle \mathcal{O} \rangle_c - \sum_{s \subset c} W_s, \tag{J2}$$

where $\langle \mathcal{O} \rangle_c$ is the expectation value of the quantity $\mathcal{O}$ taken from exact diagonalization on cluster c with open boundary conditions. The second term in Eq. (J2) is a sum over the weights of all subclusters of c. The sum in Eq. (J1) is arranged in order of increasing cluster size. At high temperatures, terms from larger clusters vanish faster with increasing temperature and the series converges in the same manner as high temperature expansion. At sufficiently high temperature, one can then justify truncating the sum at finite cluster size.

We employ a series of clusters starting with a single site and then all further clusters are constructed from full tetrahedra. The nth order of the expansion incorporates clusters of size up to n tetrahedra. We denote the nth-order calculation as "NLC-n." For the heat capacity we have performed calculations up to fourth order (NLC-4). For the A parameter set we additionally performed NLC calculations of C_{mag} up to seventh order (see inset of Fig. 6). The methodology for these seventh-order calculations is described in Ref. [36]. For $S(Q)$ and $S(\mathbf{Q})$ we have performed calculations up to third order (NLC-3).

For the susceptibility we have performed calculations up to second order (NLC-2).

For example, to estimate $S(\mathbf{Q})$ using Eq. (F1) and the NLC method, we define for each cluster c entering the expansion, the extensive quantities:

$$C_c(\mathbf{Q}) = |f(|\mathbf{Q}|)|^2 \sum_{i,j\in c}\left(\hat{\mathbf{z}}_i \cdot \hat{\mathbf{z}}_j - \frac{(\hat{\mathbf{z}}_i \cdot \mathbf{Q})(\hat{\mathbf{z}}_j \cdot \mathbf{Q})}{|\mathbf{Q}|^2}\right)$$
$$[\cos^2(\theta)\langle S_i^{\tilde{x}}(-\mathbf{Q})S_j^{\tilde{x}}(\mathbf{Q})\rangle + \sin^2(\theta)\langle S_i^{\tilde{z}}(-\mathbf{Q})S_j^{\tilde{z}}(\mathbf{Q})\rangle], \quad \text{(J3)}$$

The NLC estimate of $S(\mathbf{Q})$ is then

$$S_{\mathrm{NLC}}(\mathbf{Q}) = \sum_c M_c W_c(\mathbf{Q}), \quad \text{(J4)}$$

where in this case (third-order NLC) we truncate the sum at a maximum cluster size of three tetrahedra. M_c are the cluster multiplicities and $W_c(\mathbf{Q})$ are the cluster weights,

$$W_c(\mathbf{Q}) = C_c(\mathbf{Q}) - \sum_{s\subset c} W_s(\mathbf{Q}), \quad \text{(J5)}$$

where the sum on the right-hand side is over sub-clusters of c.

To improve convergence of the C_{mag} calculations, we have used Euler transformation to the third and fourth orders [35]. The Euler transformed results at third and fourth order are

$$\langle \mathcal{O} \rangle_{\mathrm{Euler\,3}} = \frac{1}{2}\langle \mathcal{O} \rangle_{\text{NLC-2}} + \frac{1}{2}\langle \mathcal{O} \rangle_{\text{NLC-3}} \quad \text{(J6)}$$

and

$$\langle \mathcal{O} \rangle_{\mathrm{Euler\,4}} = \frac{1}{4}\langle \mathcal{O} \rangle_{\text{NLC-2}} + \frac{1}{2}\langle \mathcal{O} \rangle_{\text{NLC-3}} + \frac{1}{4}\langle \mathcal{O} \rangle_{\text{NLC-4}}, \quad \text{(J7)}$$

where $\langle \mathcal{O} \rangle_{\text{NLC-}n}$ is the estimate of $\langle \mathcal{O} \rangle$ up to nth order in NLC.

For the susceptibility calculations we included a population of 14% vacancies in the calculation, with disorder averaging. The disorder average can be taken as order by order in NLC. Since vacancy disorder is binary, the disorder average can be done exactly [34]. We have also performed heat capacity calculations with 5% vacancy disorder, as a point of comparison to the calculations with the clean model. The fits of these calculations to the experimental data produce very similar results to those found for the clean model, as shown in Fig. 13.

---

[1] J. S. Gardner, M. J. P. Gingras, and J. E. Greedan, *Magnetic Pyrochlore Oxides*, Rev. Mod. Phys. **82**, 53 (2010).

[2] M. J. P. Gingras and P. A. McClarty, *Quantum Spin Ice: A Search for Gapless Quantum Spin Liquids in Pyrochlore Magnets*, Rep. Prog. Phys. **77**, 056501 (2014).

[3] A. M. Hallas, J. Gaudet, and B. D. Gaulin, *Experimental Insights into Ground-State Selection of Quantum XY Pyrochlores*, Annu. Rev. Condens. Matter Phys. **9**, 105 (2018).

[4] J. G. Rau and M. J. Gingras, *Frustrated Quantum Rare-Earth Pyrochlores*, Annu. Rev. Condens. Matter Phys. **10**, 357 (2019).

[5] Y.-D. Li and G. Chen, *Symmetry Enriched U(1) Topological Orders for Dipole-Octupole Doublets on a Pyrochlore Lattice*, Phys. Rev. B **95**, 041106(R) (2017).

[6] Y.-P. Huang, G. Chen, and M. Hermele, *Quantum Spin Ices and Topological Phases from Dipolar-Octupolar Doublets on the Pyrochlore Lattice*, Phys. Rev. Lett. **112**, 167203 (2014).

[7] J. Gaudet, E. M. Smith, J. Dudemaine, J. Beare, C. R. C. Buhariwalla, N. P. Butch, M. B. Stone, A. I. Kolesnikov, G. Xu, D. R. Yahne, K. A. Ross, C. A. Marjerrison, J. D. Garrett, G. M. Luke, A. D. Bianchi, and B. D. Gaulin, *Quantum Spin Ice Dynamics in the Dipole-Octupole Pyrochlore Magnet* $\mathrm{Ce_2Zr_2O_7}$, Phys. Rev. Lett. **122**, 187201 (2019).

[8] B. Gao, T. Chen, D. Tam, C.-L. Huang, K. Sasmal, D. Adroja, F. Ye, H. Cao, G. Sala, M. Stone, C. Baines, J. Barker, H. Hu, J.-H. Chung, X. Xu, S.-W. Cheong, M. Nallaiyan, S. Spagna, M. Maple, and P. Dai, *Experimental Signatures of a Three-Dimensional Quantum Spin Liquid in Effective Spin-*$1/2$ $\mathrm{Ce_2Zr_2O_7}$ *Pyrochlore*, Nat. Phys. **15**, 1052 (2019).

[9] R. Sibille, N. Gauthier, E. Lhotel, V. Pore, V. Pomjakushin, R. Ewings, T. Perring, J. Ollivier, A. Wildes, C. Ritter, T. Hansen, D. Keen, G. Nilsen, L. Keller, S. Petit, and T. Fennell, *A Quantum Liquid of Magnetic Octupoles on the Pyrochlore Lattice*, Nat. Phys. **16**, 546 (2020).

[10] O. Benton, *Ground-State Phase Diagram of Dipolar-Octupolar Pyrochlores*, Phys. Rev. B **102**, 104408 (2020).

[11] A. S. Patri, M. Hosoi, and Y. B. Kim, *Distinguishing Dipolar and Octupolar Quantum Spin Ices Using Contrasting Magnetostriction Signatures*, Phys. Rev. Research **2**, 023253 (2020).

[12] C.-J. Huang, C. Liu, Z. Meng, Y. Yu, Y. Deng, and G. Chen, *Extended Coulomb Liquid of Paired Hardcore Boson Model on a Pyrochlore Lattice*, Phys. Rev. Research **2**, 042022(R) (2020).

[13] T. Fennell, P. P. Deen, A. R. Wildes, K. Schmalzl, D. Prabhakaran, A. T. Boothroyd, R. J. Aldus, D. F. McMorrow, and S. T. Bramwell, *Magnetic Coulomb Phase in the Spin Ice* $\mathrm{Ho_2Ti_2O_7}$, Science **326**, 415 (2009).

[14] E. M. Smith, Q. Barthélemy, S. Bhattacharya, B. D. Gaulin, E. Kermarrec, R. K. Sharma, and A. Wildes, *Polarization Analysis of the Dynamic Quantum Spin Ice Correlations in the Ground State of a Pyrochlore Magnet*, Institut Laue-Langevin (ILL) (2021) 10.5291/ILL-DATA.5-42-537.

[15] K. A. Ross, L. Savary, B. D. Gaulin, and L. Balents, *Quantum Excitations in Quantum Spin Ice*, Phys. Rev. X **1**, 021002 (2011).

[16] L. Savary, K. A. Ross, B. D. Gaulin, J. P. C. Ruff, and L. Balents, *Order by Quantum Disorder in* $\mathrm{Er_2Ti_2O_7}$, Phys. Rev. Lett. **109**, 167201 (2012).

[17] K. A. Ross, Y. Qiu, J. R. D. Copley, H. A. Dabkowska, and B. D. Gaulin, *Order by Disorder Spin Wave Gap in the XY Pyrochlore Magnet* $\mathrm{Er_2Ti_2O_7}$, Phys. Rev. Lett. **112**, 057201 (2014).

[18] A. Scheie, J. Kindervater, S. Zhang, H. Changlani, G. Sala, G. Ehlers, A. Heinemann, G. Tucker, S. Koohpayeh, and C. Broholm, *Multiphase Magnetism in* $Yb_2Ti_2O_7$, Proc. Natl. Acad. Sci. U.S.A. **117**, 27245 (2020).

[19] J. D. Thompson, P. A. McClarty, D. Prabhakaran, I. Cabrera, T. Guidi, and R. Coldea, *Quasiparticle Breakdown and Spin Hamiltonian of the Frustrated Quantum Pyrochlore* $Yb_2Ti_2O_7$ *in a Magnetic Field*, Phys. Rev. Lett. **119**, 057203 (2017).

[20] J. Robert, E. Lhotel, G. Remenyi, S. Sahling, I. Mirebeau, C. Decorse, B. Canals, and S. Petit, *Spin Dynamics in the Presence of Competing Ferromagnetic and Antiferromagnetic Correlations in* $Yb_2Ti_2O_7$, Phys. Rev. B **92**, 064425 (2015).

[21] J. P. Clancy, J. P. C. Ruff, S. R. Dunsiger, Y. Zhao, H. A. Dabkowska, J. S. Gardner, Y. Qiu, J. R. D. Copley, T. Jenkins, and B. D. Gaulin, *Revisiting Static and Dynamic Spin-Ice Correlations in* $Ho_2Ti_2O_7$ *with Neutron Scattering*, Phys. Rev. B **79**, 014408 (2009).

[22] A. Bhardwaj, S. Zhang, H. Yan, R. Moessner, A. H. Nevidomskyy, and H. J. Changlani, *Sleuthing Out Exotic Quantum Spin Liquidity in the Pyrochlore Magnet* $Ce_2Zr_2O_7$, arXiv:2108.01096.

[23] H. Otobe, A. Nakamura, T. Yamashita, and K. Minato, *Oxygen Potential and Defect Structure of Oxygen-Excess Pyrochlore* $Ce_2Zr_2O_{7+x}$, J. Phys. Chem. Solids **66**, 329 (2005).

[24] Y. Kato and S. Onoda, *Numerical Evidence of Quantum Melting of Spin Ice: Quantum-to-Classical Crossover*, Phys. Rev. Lett. **115**, 077202 (2015).

[25] O. Benton, O. Sikora, and N. Shannon, *Seeing the Light: Experimental Signatures of Emergent Electromagnetism in a Quantum Spin Ice*, Phys. Rev. B **86**, 075154 (2012).

[26] M. P. Kwasigroch, *Vison-Generated Photon Mass in Quantum Spin Ice: A Theoretical Framework*, Phys. Rev. B **102**, 125113 (2020).

[27] B. Bernu and G. Misguich, *Specific Heat and High-Temperature Series of Lattice Models: Interpolation Scheme and Examples on Quantum Spin Systems in One and Two Dimensions*, Phys. Rev. B **63**, 134409 (2001).

[28] K. Skold and D. Price, *Neutron Scattering*, 1st ed. (Academic Press, New York, 1986), Vol. 23A.

[29] E. J. Lisher and J. B. Forsyth, *Analytic Approximations to Form Factors*, Acta Crystallogr., Sect. A. **27**, 545 (1971).

[30] C.-J. Huang, Y. Deng, Y. Wan, and Z. Y. Meng, *Dynamics of Topological Excitations in a Model Quantum Spin Ice*, Phys. Rev. Lett. **120**, 167202 (2018).

[31] R. Kubo, *The Fluctuation-Dissipation Theorem*, Rep. Prog. Phys. **29**, 255 (1966).

[32] S. Zhang, H. J. Changlani, K. W. Plumb, O. Tchernyshyov, and R. Moessner, *Dynamical Structure Factor of the Three-Dimensional Quantum Spin Liquid Candidate* $NaCaNi_2F_7$, Phys. Rev. Lett. **122**, 167203 (2019).

[33] B. Tang, E. Khatami, and M. Rigol, *A Short Introduction to Numerical Linked-Cluster Expansions*, Comput. Phys. Commun. **184**, 557 (2013).

[34] B. Tang, D. Iyer, and M. Rigol, *Thermodynamics of Two-Dimensional Spin Models with Bimodal Random-Bond Disorder*, Phys. Rev. B **91**, 174413 (2015).

[35] R. Applegate, N. R. Hayre, R. R. P. Singh, T. Lin, A. G. R. Day, and M. J. P. Gingras, *Vindication of* $Yb_2Ti_2O_7$ *as a Model Exchange Quantum Spin Ice*, Phys. Rev. Lett. **109**, 097205 (2012).

[36] R. Schäfer, I. Hagymási, R. Moessner, and D. J. Luitz, *Pyrochlore* $S = \frac{1}{2}$ *Heisenberg Antiferromagnet at Finite Temperature*, Phys. Rev. B **102**, 054408 (2020).

Chapter 3

$Ce_2Zr_2O_7$ in a Magnetic Field

The following publication is contained in this chapter:

Publication III:

"*Quantum Spin Ice Response to a Magnetic Field in the Dipole-Octupole Pyrochlore* $Ce_2Zr_2O_7$",

E. M. Smith, J. Dudemaine, B. Placke, R. Schäfer, D. R Yahne, T. DeLazzer, A. Fitterman, J. Beare, J. Gaudet, C. R. C. Buhariwalla, A. Podlesnyak, Guangyong Xu, J. P. Clancy, R. Movshovich, G. M. Luke, K. A. Ross, R. Moessner, O. Benton, A. D. Bianchi, and B. D. Gaulin.

Reproduced from Reference [3] with permission, copyrighted by the American Physical Society.

3.1 Preface to Publication III: Polarized Spin Ice Phases and Quasi-1D Quantum Spin Chains in the Dipole-Octupole Pyrochlore $Ce_2Zr_2O_7$ at Low Temperature in a Magnetic Field

In Publication III, we use neutron scattering and heat capacity measurements to probe single crystal samples of $Ce_2Zr_2O_7$ at low temperature in magnetic fields along the $[1, \bar{1}, 0]$ and $[0, 0, 1]$ directions and we show that the measurements are consistent with the presence of partially-polarized and polarized spin-ice phases in $Ce_2Zr_2O_7$ at low-temperature in magnetic fields along $[1, \bar{1}, 0]$ and $[0, 0, 1]$ directions, respectively. We use a collection of calculation methods in order to help put this data further into context with the relevant theory, which is particularly important for dipole-octupole pyrochlores as such where the different components of pseudospin give significantly different contributions to the neutron scattering [52, 103]. Specifically, we use three-dimensional semiclassical molecular dynamics and one-dimensional quantum calculations for the Bragg, diffuse, and inelastic neutron scattering signals and comparison of the measured neutron scattering data with these calculations provides further evidence that θ is near zero in $Ce_2Zr_2O_7$, corroborating estimates from Publication II and Ref. [37].

Additionally, we use the numerical-linked-cluster method to perform three-dimensional quantum calculations of the magnetic heat capacity at low-temperature for a magnetic field along the $[1, \bar{1}, 0]$ direction, and compare the results with our data in order to estimate the exchange parameters relevant for $Ce_2Zr_2O_7$ in the XYZ Hamiltonian [Eq. (1.21)]. Specifically, we use sixth order NLC calculations of the magnetic heat capacity for zero-field and fifth order NLC calculations of the magnetic heat capacity for nonzero magnetic field along the $[1,\bar{1},0]$ direction in order to estimate the values of $J_{\tilde{x}}$, $J_{\tilde{y}}$, $J_{\tilde{z}}$, and g_z for $Ce_2Zr_2O_7$ in the XYZ Hamiltonian relevant for dipole-octupole pyrochlores at the nearest-neighbor level. Our estimates of $J_{\tilde{x}}$, $J_{\tilde{y}}$, and $J_{\tilde{z}}$ are in strong agreement with our estimates in Publication II and provide further evidence for a $\mathrm{U}(1)_\pi$ quantum spin ice ground state in $Ce_2Zr_2O_7$, and one residing near the $J_{\tilde{x}} = J_{\tilde{y}}$ boundary between dipolar and octupolar symmetry. While the same zero-field heat capacity data from $Ce_2Zr_2O_7$ was fit to estimate the values of $J_{\tilde{x}}$, $J_{\tilde{y}}$, and $J_{\tilde{z}}$ in Publications II and III, it is important to note that the consistency in estimated-parameters between Publications II and III is indeed nontrivial given the difference in fitting procedures used (now using only the heat capacity without including the magnetic susceptibility) and the higher order NLC calculations used in Publication III compared to Publication II. In addition to this, we compare NLC calculations using the exchange parameters determined in Publication III, with those using the different sets of exchange parameters suggested in Ref. [37], and we show that the exchange parameters from Publication III and a very similar parameter set from Ref. [37] provide better descriptions of the measured data compared to the other three parameter sets suggested in Ref. [37]. We perform a similar comparison of these five parameter sets using our semi-classical molecular dynamics calculations for the diffuse scattering in $[1,\bar{1},0]$ magnetic field and again show the exchange parameters from Publication III and the one similar parameter set from Ref. [37] describe the measured data better than the other three parameter sets suggested in Ref. [37].

Our fitting to the heat capacity of $Ce_2Zr_2O_7$ in a magnetic field along the $[1,\bar{1},0]$ direction yields a best-fit value of $g_z = 2.24$ for the anisotropic g-factor, which is only ∼87% of the value of associated with a pure $|J = 5/2,\ m_J = \pm 3/2\rangle$ ground state doublet, $g_z = 2.57$. Some reduction of this g-factor is due to its dependence on the oxidation level; The oxidation level was not included in the fitting procedure and in such cases, the fit value of g_z takes on the oxidation-level dependence of the Zeeman term in Eq. (1.21), which at first-approximation amounts to a simple absorbed-scaling of g_z by the ratio of Ce^{3+} to the combined amount of Ce^{3+} and Ce^{4+}, or by $1-\delta$ in terms of the oxidation level δ. Nonetheless, the estimated oxidation level of our smaller single crystal samples ($\delta \sim 5\%$ [1, 2]) does not fully account for the reduction in g_z from the pure $|J = 5/2,\ m_J = \pm 3/2\rangle$ value, and accordingly, this reduction is indicative towards a small amount of the mixing of the $|J = 5/2,\ m_J = \pm 3/2\rangle$ states with other states in the CEF ground state doublet. While the existing estimates for the CEF states in Publication I and Ref. [22] are good approximations and much-needed starting points, especially due to the importance of the CEF ground state in determining the magnetic behavior in rare-earth pyrochlores, the reduced value of g_z from our study in Publication III elucidates the need for CEF studies of $Ce_2Zr_2O_7$ that extend those in Publication I and Ref. [22], as we discuss in detail in Section 4.2.

In Publication III, we also put our measurements into context with the large amount of experimental literature existing on the renowned classical spin ices $Ho_2Ti_2O_7$ and $Dy_2Ti_2O_7$ in $[1,\bar{1},0]$ and $[0,0,1]$ magnetic fields, as well as the popular, dipole-octupole pyrochlore $Nd_2Zr_2O_7$ for the $[1,\bar{1},0]$ magnetic field direction. In further detail, $Ho_2Ti_2O_7$

and $Dy_2Ti_2O_7$ are each known to display a polarized spin ice phase in $[0,0,1]$ magnetic field that is similar to that observed for $Ce_2Zr_2O_7$ in $[0,0,1]$ magnetic field [127, 128]. Similarly, $Ho_2Ti_2O_7$, $Dy_2Ti_2O_7$, and $Nd_2Zr_2O_7$ are each known to display a partially-polarized spin ice phase in $[1,\bar{1},0]$ magnetic field that are similar to that observed for $Ce_2Zr_2O_7$ in $[1,\bar{1},0]$ magnetic field [79, 83, 127–130]. The similar partially-polarized spin ice phases observed in $[1,\bar{1},0]$ magnetic field for the four materials provides a particularly interesting point of comparison. For the $[1,\bar{1},0]$ field direction, it is convenient to decompose the pyrochlore lattice into two sublattices, with the first containing the R^{3+} ions in the lattice which form chains along the $[1,\bar{1},0]$ direction (conventionally called α chains), and with the second containing the R^{3+} ions in the lattice which form chains along the $[1,1,0]$ direction (conventionally called β chains). For the partially-polarized spin ice phases in $Ce_2Zr_2O_7$, $Ho_2Ti_2O_7$, $Dy_2Ti_2O_7$, and $Nd_2Zr_2O_7$, the α chains exhibit a non-collinear polarization induced by the magnetic field, and the β chains, which are decoupled from the magnetic field and the α chains, display short ranged ferromagnetic order [79, 83, 99, 127–130]. We compare the correlation length for the short-ranged ferromagnetic order in the β chains of each of these materials and discuss likely reasons for the shorter intrachain correlation lengths in $Ce_2Zr_2O_7$ and $Nd_2Zr_2O_7$ compared to $Ho_2Ti_2O_7$ and $Dy_2Ti_2O_7$.

For the best-fitting exchange parameters determined for $Ce_2Zr_2O_7$ in Publications II and III, the expectation for a moderate-strength magnetic field along the $[1,\bar{1},0]$ direction is that the correlations between magnetic octupoles in the field-decoupled β chains should dominate over the coupling between magnetic dipoles and should even lead to a long-ranged, octupolar-ordered chain-phase for each β-chain at zero temperature [99]. With that in mind, it is worth mentioning that the diffuse scattering signal we measure from $Ce_2Zr_2O_7$ in a $[1,\bar{1},0]$ magnetic field in Publication III, attributed to correlations between magnetic dipole moments in the β chains, likely arises due to fluctuations and deviations away from any octupolar order which is expected to be more prevalent in $Ce_2Zr_2O_7$ in a $[1,\bar{1},0]$ magnetic field [99], but also more elusive to the measurements [105], in comparison to dipole-dipole correlations. In fact, as we discuss in Publication III, this is due to the dominance of $J_{\tilde{x}}$ and $J_{\tilde{y}}$ over $J_{\tilde{z}}$, which has some other interesting implications that we point out in Publication III, including contributing to the weakness of the diffuse scattering from the β chains and to the relatively small size of the interchain correlation length for the β chains.

Reference [99] shows that the ground state degeneracy of the different interchain orderings for the β chains is lifted by quantum order by disorder, such that quantum fluctuations provide an effective coupling between β chains. However, Ref. [99] shows that these quantum fluctuations occur on an energy scale that is only 0.01% of the energy scale set by $J_{\tilde{x}}$, $J_{\tilde{y}}$, and $J_{\tilde{z}}$, or less, corresponding to a temperature scale of $T \lesssim 0.1$ mK for the magnitude of the exchange parameters determined from the estimates in Publications II and III as well as in Ref. [37]. Therefore this quantum order by disorder is not expected to be relevant at any realistic temperature for experiments. When considering this result from Ref. [99], along with the fact that the small dipole-moment in $Ce_2Zr_2O_7$ results in a magnetic dipole-dipole interaction for neighboring β chains that is on the order of only 5 mK, it is not particularly surprising that we found a lack of interchain correlations between the β chains; In fact, the closest R^{3+} ions from neighboring β chains are third-nearest-neighbors in general and the value of 5 mK was determined via the third-nearest-neighbor dipole-dipole interaction parameter in Table (1.3). While not surprising, this result in Publication III and the analogous result for $Nd_2Zr_2O_7$ in Ref. [83] are still important to show, as they provide some experimental confirmation to the lack of significant inter-β-chain correlations predicted in Ref. [99]. Albeit this is only partial confirmation in each case due to the insensitivity of the neutrons to the magnetic octupoles in these particular experiments [30, 105], and we return to this latter point in Section 4.2.

As mentioned in Section 2.2, in Publication III we return to using the quantum spin ice terminology in describing the U(1) quantum spin liquids known to be available to the dipole-octupole pyrochlores, due to the growing acceptance of these spin liquids as novel quantum spin ices throughout the collection of literature on dipole-octupole pyrochlores (see Refs. [3, 30, 32, 52, 57, 61, 96, 99, 124] for examples). On a similar note, we take the opportunity in the introduction of Publication III to summarize the growing work on the existing cerium-based pyrochlores $Ce_2Zr_2O_7$, $Ce_2Sn_2O_7$, and $Ce_2Hf_2O_7$; This helps put Publication I and II of this thesis into the context of related experimental work.

As is also discussed in Section 2.2, in-field inelastic neutron scattering data would typically be fit using a relevant exchange Hamiltonian to determine the exchange parameters that best-reproduce the measured spectra. However, this is not a reliable method of parameter-refinement when broad and largely-non-dispersive excitations are the only excitations that are detected, as is the case for our measurements on $Ce_2Zr_2O_7$ in Publication III and in contrast to the sharp spin waves typically used for refining exchange parameters using inelastic neutron scattering data (see Refs. [35, 38, 59, 62–64] for examples).

Publication III was published (as a preprint) shortly after a similar work on $Ce_2Zr_2O_7$ by Gao *et al.* (Ref. [131]) in which the authors investigate the low-temperature magnetic behavior of $Ce_2Zr_2O_7$ in magnetic fields along the $[0, 0, 1]$, $[1, \bar{1}, 0]$, and $[1, 1, 1]$ directions using neutron scattering and magnetization measurements. With that being said, the work in Publication III presents a more-thorough and more-sophisticated analysis of $Ce_2Zr_2O_7$ in $[0, 0, 1]$ and $[1, \bar{1}, 0]$ magnetic fields than that presented in Ref. [131]. Specifically, Gao *et al.* (Ref. [131]) do not report diffuse neutron scattering or inelastic neutron scattering signals in their work, or corresponding calculations for such signals, which are key pieces in the comprehensive analysis presented in our work. The Bragg scattering and corresponding interpretation for the $[0, 0, 1]$ magnetic field direction presented by Gao *et al.* (Ref. [131]) is largely consistent with that presented in our work apart from the fact that Ref. [131] reports a suspicious magnetic Bragg peak at a position which is not expected to contain significant magnetic Bragg scattering for the $[0, 0, 1]$-polarized spin ice phase. On the other hand, we show that no magnetic Bragg scattering is present at this location in our data and speculate that the reported magnetic Bragg intensity at this location in Ref. [131] actually arises from the imperfect subtraction of *nuclear* Bragg peaks in their data. Furthermore, the measured magnetic Bragg scattering for a $[1, \bar{1}, 0]$ magnetic field direction in our work is consistent with that reported in Ref. [131], however, Ref. [131] incorrectly claims that a three-in, one-out magnetic structure is expected for $Ce_2Zr_2O_7$ in $[1, \bar{1}, 0]$ magnetic field and they interpret their data as such, while we show that a partially-polarized spin ice phase is expected and is consistent with the measured Bragg scattering, elastic diffuse scattering, inelastic scattering, and the heat capacity that we present for a $[1, \bar{1}, 0]$ magnetic field direction. In short, our work extends the measured data on $Ce_2Zr_2O_7$ at low-temperature in magnetic fields along the $[0,0,1]$ and $[1,\bar{1},0]$ directions, while also correcting multiple misconceptions regarding the existing data and reported expectations for $Ce_2Zr_2O_7$. This is an additional importance considering the fact that our work in Publication III and the work in Ref. [131] are the only in-field neutron scattering studies published to date for any of the existing cerium-based pyrochlores, $Ce_2Zr_2O_7$, $Ce_2Hf_2O_7$, and $Ce_2Sn_2O_7$.

I contributed to this work by leading three separate neutron scattering experiments and the corresponding preparation, cutting an aligned single crystal sample for heat capacity measurements, and analyzing the entirety of the experimental data presented in the paper and appendices. I synthesized the powder sample of $La_2Zr_2O_7$ used in this work and was responsible for annealing the $Ce_2Zr_2O_7$ samples in hydrogen gas before storing these samples in inert atmosphere until measurement. I characterized both the crystallinity and phase purity of each sample used in this work using x-ray diffraction. I designed and generated the figures included in this work and wrote ~80% of the text. The contributions of each author are summarized below.

Author Contributions for Publication III:

Experimental Concept:

E. M. Smith, J. Gaudet, B. D. Gaulin

Sample Preparation:

J. Dudemaine, **E. M. Smith**, J. Gaudet, A. Fitterman, J. Beare, G. M. Luke, B. D. Gaulin, A. D. Bianchi

Neutron Scattering Experiments:

E. M. Smith, J. Gaudet, C. R. C. Buhariwalla, A. Podlesnyak, Guangyong Xu, J. P. Clancy, B. D. Gaulin

Heat Capacity Measurements:

D. R. Yahne, T. DeLazzer, **E. M. Smith**, R. Movshovich, B. D. Gaulin, K. A. Ross

Data Analysis:

E. M. Smith, B. D. Gaulin

Theoretical Calculations and Modeling:

B. Placke, R. Schäfer, R. Moessner, O. Benton

Manuscript:

E. M. Smith, O. Benton, B. Placke, R. Schäfer, B. D. Gaulin

Quantum spin ice response to a magnetic field in the dipole-octupole pyrochlore $Ce_2Zr_2O_7$

E. M. Smith,[1,2] J. Dudemaine,[3,4] B. Placke,[5] R. Schäfer,[5,6] D. R. Yahne,[7] T. DeLazzer,[7] A. Fitterman,[3,4] J. Beare,[1]
J. Gaudet,[8,9] C. R. C. Buhariwalla,[1] A. Podlesnyak,[10] Guangyong Xu,[8] J. P. Clancy,[1,2] R. Movshovich,[11]
G. M. Luke,[1,2] K. A. Ross,[7,12] R. Moessner,[5] O. Benton,[5] A. D. Bianchi,[3,4] and B. D. Gaulin[1,2,12]
[1]*Department of Physics and Astronomy, McMaster University, Hamilton, Ontario L8S 4M1, Canada*
[2]*Brockhouse Institute for Materials Research, McMaster University, Hamilton, Ontario L8S 4M1, Canada*
[3]*Département de Physique, Université de Montréal, Montréal, Quebec H2V 0B3, Canada*
[4]*Regroupement Québécois sur les Matériaux de Pointe (RQMP), Quebec H3T 3J7, Canada*
[5]*Max Planck Institute for the Physics of Complex Systems, Nöthnitzer Straße 38, Dresden 01187, Germany*
[6]*Department of Physics, Boston University, Boston, Massachusetts 02215, USA*
[7]*Department of Physics, Colorado State University, 200 West Lake Street, Fort Collins, Colorado 80523-1875, USA*
[8]*NIST Center for Neutron Research, National Institute of Standards and Technology, MS 6100 Gaithersburg, Maryland 20899, USA*
[9]*Department of Materials Science and Eng., University of Maryland, College Park, Maryland 20742-2115, USA*
[10]*Neutron Scattering Division, Oak Ridge National Laboratory, Oak Ridge, Tennessee 37831, USA*
[11]*Los Alamos National Laboratory, Los Alamos, New Mexico 87545, USA*
[12]*Canadian Institute for Advanced Research, 661 University Avenue, Toronto, Ontario M5G 1M1, Canada*

(Received 23 June 2023; accepted 7 August 2023; published 28 August 2023)

The pyrochlore magnet $Ce_2Zr_2O_7$ has attracted much attention as a quantum spin ice candidate whose novelty derives in part from the dipolar-octupolar nature of the Ce^{3+} pseudospin-$1/2$ degrees of freedom it possesses. We report heat capacity measurements on single crystal samples of $Ce_2Zr_2O_7$ down to $T \sim 0.1$ K in a magnetic field along the $[1, \bar{1}, 0]$ direction. These measurements show that the broad hump in the zero-field heat capacity moves higher in temperature with increasing field strength and is split into two separate humps by the $[1, \bar{1}, 0]$ magnetic field at $\sim$2 T. These separate features are due to the decomposition of the pyrochlore lattice into effectively decoupled chains for fields in this direction: One set of chains (α chains) is polarized by the field while the other (β chains) remains free. This situation is similar to that observed in the classical spin ices $Ho_2Ti_2O_7$ and $Dy_2Ti_2O_7$, but with the twist that here the strong transverse exchange interactions produce substantial quantum effects. Our theoretical modeling suggests that the β chains are close to a critical state, with nearly-gapless excitations. We also report elastic and inelastic neutron scattering measurements on single crystal $Ce_2Zr_2O_7$ in $[1, \bar{1}, 0]$ and $[0, 0, 1]$ magnetic fields at temperatures down to $T = 0.03$ K. The elastic scattering behaves consistently with the formation of independent chains for a $[1, \bar{1}, 0]$ field, while the $[0, 0, 1]$ field produces a single field-induced elastic magnetic Bragg peak at $(0, 2, 0)$ and equivalent wavevectors, indicating a polarized spin ice state for fields above $\sim$3 T. For both $[1, \bar{1}, 0]$ and $[0, 0, 1]$ magnetic fields, our inelastic neutron scattering results show an approximately-dispersionless continuum of scattering that increases in both energy and intensity with increasing field strength. By modeling the complete set of experimental data using numerical linked cluster and semiclassical molecular dynamics calculations, we demonstrate the dominantly multipolar nature of the exchange interactions in $Ce_2Zr_2O_7$ and the smallness of the parameter θ, which controls the mixing between dipolar and octupolar degrees of freedom. These results support previous estimates of the microscopic exchange parameters and place strong constraints on the theoretical description of this prominent spin ice candidate.

DOI: 10.1103/PhysRevB.108.054438

I. INTRODUCTION

The rare-earth pyrochlores have been of great interest within the condensed matter physics community due to the wealth of exotic magnetic ground states displayed throughout this large family of materials [1–4]. Many rare-earth pyrochlores have the chemical formula $R_2B_2O_7$, where R^{3+} is a trivalent rare-earth ion and B^{4+} is a tetravalent transition metal ion. Much attention has focused on the subset of the pyrochlore family where the B^{4+} site is nonmagnetic, allowing the physics to be driven by interacting multipolar moments at the R^{3+} sites. These form a network of corner-sharing tetrahedra that is one of the archetypes for geometric frustration in three dimensions and which promotes exotic magnetic phases at low temperature [1,2,4–8].

The typical energy hierarchy in rare-earth pyrochlores is such that spin-orbit coupling is the highest energy scale apart from the coulomb interactions that dictate the filling of atomic levels, followed by the crystalline electric field (CEF) at the R^{3+} sites, which then dominates over the exchange and related intersite interactions between the R^{3+} ions [3,4]. Consequently, when the CEF ground state is a doublet that is well separated in energy from the first excited state, which is often the case for the R^{3+} ions in rare-earth pyrochlores, the low-temperature magnetic behavior can be accurately described in terms of interacting pseudospin-1/2 degrees of freedom [3,4].

In such cases, the symmetry of the CEF ground state imprints itself on the R^{3+} pseudospin-1/2 degrees of freedom and the exchange Hamiltonian that describes the interactions between them. This leads to three possible scenarios for the rare-earth pyrochlores, based on how the pseudospin-1/2 degrees of freedom transform under the R^{3+} site symmetries and time-reversal symmetry [4,9–12]. The three scenarios for the CEF ground-state doublets are (1) the "non-Kramers" ground-state doublet, relevant for R^{3+} ions with an even number of electrons, (2) the "effective spin-1/2" dipole doublet, and (3) the "dipolar-octupolar" ground-state doublet, with the latter two being relevant for Kramers R^{3+} ions with an odd number of electrons. Along with governing the form of the nonzero terms allowed in the exchange Hamiltonian, the nature of the CEF ground-state doublet also determines the size and single-ion anisotropy of the magnetic moments at low temperature [4].

In the case of $Ce_2Zr_2O_7$, the Ce^{3+} CEF ground state is well separated in energy from the first excited CEF state, by ∼55 meV, and it is a dipolar-octupolar doublet [13,14], which corresponds to x and z components of pseudospin that transform like magnetic dipoles, and y components that transform like magnetic octupoles, under the point group symmetries of the R^{3+} site and time-reversal symmetry [4,11,12]. This dipolar-octupolar symmetry is accompanied by an Ising single-ion anisotropy in which the magnetic dipole moments are aligned along the local C_3 axes of the R^{3+} sites, labeled as the local z directions. This Ising single-ion anisotropy is the case for all dipolar-octupolar pyrochlores. While the x and z components of pseudospin both *transform* like magnetic dipoles, the x component carries an octupole moment similar to the y component, and the z component carries a dipole moment [4,15].

The dipolar-octupolar symmetry of the CEF ground-state doublet governs the relevant nonzero terms in the general exchange Hamiltonian appropriate for $Ce_2Zr_2O_7$ and other dipolar-octupolar pyrochlores, and at nearest-neighbor level this yields the exchange Hamiltonian [4,11,12],

$$\begin{aligned}\mathcal{H}_{\mathrm{DO}} = \sum_{\langle ij\rangle} \big[& J_x S_i^x S_j^x + J_y S_i^y S_j^y + J_z S_i^z S_j^z \\ & + J_{xz}\big(S_i^x S_j^z + S_i^z S_j^x\big)\big] - g_z \mu_{\mathrm{B}} \sum_i (\mathbf{h}\cdot\hat{\mathbf{z}}_i) S_i^z, \qquad (1)\end{aligned}$$

where S_i^α ($\alpha = x, y, z$) are the pseudospin-1/2 components of rare-earth atom i in the local $\{x, y, z\}$ coordinate frame. The $\{x, y, z\}$ coordinate frame is the local coordinate frame that is typically used for the rare-earth pyrochlores, with the y and z axes along the C_2 and C_3 axes of the R^{3+} site, respectively [4,11,12]. As described above, S_i^z carries a magnetic dipole moment while S_i^x and S_i^y each carry magnetic octupole moments [4,15]. However, both S_i^x and S_i^z transform under the R^{3+} site symmetries and time-reversal symmetry like magnetic dipoles, while only S_i^y transforms like a component of the magnetic octupole tensor. The second sum in Eq. (1) represents the Zeeman interaction between the R^{3+} ion and the magnetic field, where the magnetic field is denoted as $\mathbf{h}$ and $\hat{\mathbf{z}}_i$ is the local z axis for ion i. The constant g_z is determined by the CEF ground-state doublet, which gives $g_z = 2.57$ for the pure $|m_J = \pm 3/2\rangle$ ground-state doublet estimated for Ce^{3+} in $Ce_2Zr_2O_7$ [13,14]. This nearest-neighbor exchange Hamiltonian [Eq. (1)] can then be simplified to the "XYZ" exchange Hamiltonian via rotation of the local $\{x, y, z\}$ coordinate frame by θ about the y axis [11,16],

$$\begin{aligned}\mathcal{H}_{\mathrm{XYZ}} = \sum_{\langle ij\rangle} & \big[J_{\tilde{x}} S_i^{\tilde{x}} S_j^{\tilde{x}} + J_{\tilde{y}} S_i^{\tilde{y}} S_j^{\tilde{y}} + J_{\tilde{z}} S_i^{\tilde{z}} S_j^{\tilde{z}} \big] \\ & - g_z \mu_{\mathrm{B}} \sum_i \mathbf{h}\cdot\hat{\mathbf{z}}_i \big(S_i^{\tilde{z}} \cos\theta + S_i^{\tilde{x}} \sin\theta\big). \qquad (2)\end{aligned}$$

Theoretical studies of this XYZ Hamiltonian [Eq. (2)] for zero field have shown that it permits at least four distinct U(1) quantum spin liquids, with low-energy physics mimicking the theory of quantum electromagnetism, and at least two magnetically-ordered ground states [15,17–20]. We refer to these spin liquids as quantum spin ice (QSI) phases, as they can be obtained from the addition of quantum fluctuations to a classical spin ice model with local "2-in-2-out" constraints on the spins [11,21–24]. Recent studies [25,26] have focused on estimating the exchange parameters, $J_{\tilde{x}}$, $J_{\tilde{y}}$, $J_{\tilde{z}}$, and θ, for $Ce_2Zr_2O_7$ by fitting collections of experimental data, and both analyses yield parameters that correspond to a quantum spin ice ground state for the XYZ Hamiltonian. A quantum spin ice ground state of the XYZ Hamiltonian has octupolar nature if $|J_{\tilde{y}}| > |J_{\tilde{x}}|, |J_{\tilde{z}}|$ and dipolar nature if $|J_{\tilde{z}}| > |J_{\tilde{y}}|$ or $|J_{\tilde{x}}| > |J_{\tilde{y}}|$ [25]. We do not distinguish here between the spin ices appearing for large $J_{\tilde{x}}$ and the spin ices appearing for large $J_{\tilde{z}}$. This is because these ground states can be smoothly deformed into one another, by variation of the parameter θ, so they do not represent distinct phases. In general, the $J_{\tilde{x}}$ or $J_{\tilde{z}}$ dominated spin ices are of mixed dipolar-octupolar character, but we refer to them here as "dipolar" to distinguish them from the purely octupolar spin ices appearing for large $J_{\tilde{y}}$.

The work in Ref. [25] finds experimental estimates for the exchange parameters of $Ce_2Zr_2O_7$ that correspond to a quantum spin ice ground state near the boundary between dipolar and octupolar character, while Ref. [26] also fits next-nearneighbor terms in the Hamiltonian, beyond those contained in Eqs. (1) and (2), and finds exchange parameters for $Ce_2Zr_2O_7$ that correspond to a quantum spin ice ground state with octupolar character. It is worth mentioning that a QSI ground state is also consistent with the lack of evidence for phase transitions in the measured heat capacity and magnetic susceptibility, as well as the snowflake-like pattern of magnetic diffuse scattering and the lack of magnetic Bragg scattering measured in neutron scattering experiments [13,14,19,25,26].

Similarly, recent experiments on powder samples of the dipolar-octupolar pyrochlore $Ce_2Sn_2O_7$ at low temperature have been interpreted in terms of an octupole-based QSI phase [27–29]. However, new results on hydrothermally-grown powder and single crystal samples of $Ce_2Sn_2O_7$ suggest that the magnetic ground state is an "all-in, all-out" ordered phase that is proximate in phase space to a QSI phase whose dynamics persist down to very low temperature [30]. In a recent study on the third existing cerium-based, dipolar-octupolar pyrochlore, $Ce_2Hf_2O_7$ [31], a collection of experimental data was fit to constrain the nearest-neighbor exchange parameters and this analysis concluded that the corresponding ground state is a quantum spin ice ground state [32]. The work in Ref. [32] was unable to constrain the nearest-neighbor exchange parameters further to distinguish between a dominant J_x or a dominant J_y for the proposed quantum spin ice ground state in $Ce_2Hf_2O_7$.

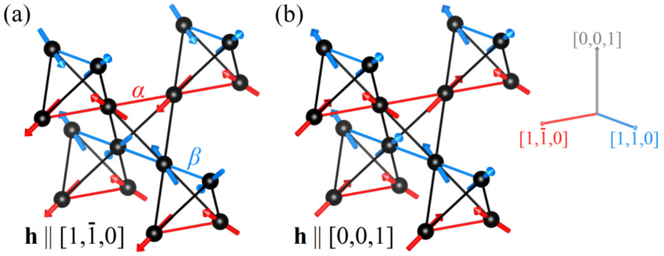

FIG. 1. (a) The magnetic rare-earth ions composing five corner-sharing tetrahedra within the pyrochlore crystal structure, illustrating the magnetic structure expected in a $[1, \bar{1}, 0]$ magnetic field for a spin ice with ferromagnetic coupling of dipole moments. The magnetic moments of the rare-earth ions are confined by the Ising single-ion anisotropy to point directly towards or away from the center of neighboring tetrahedra. The magnetic sublattice can be decomposed into α chains along the $[1, \bar{1}, 0]$ magnetic field direction and β chains perpendicular to the field. The red (blue) colors highlight the α (β) chains along the $[1, \bar{1}, 0]$ ($[1, 1, 0]$) direction parallel (perpendicular) to the magnetic field. The α chains are polarized by the $[1, \bar{1}, 0]$ magnetic field while the β chains show short-ranged ferromagnetic order, which locally establishes the 2-in-2-out spin ice rule for dipoles. There are two possible directions for the short-ranged ferromagnetic order of the β chains due to the fact that the magnetic moments on each β chain can be collectively flipped at zero cost in energy. (b) The magnetic structure for spin ice in the presence of a $[0, 0, 1]$ magnetic field is illustrated. Each tetrahedron takes on a 2-in-2-out configuration, but the component of the magnetic dipole moment along the $[0, 0, 1]$ magnetic field direction is positive for each rare-earth ion, giving rise to a polarized spin ice state.

In this paper, we report heat capacity and neutron scattering studies focused on probing the magnetic behavior of the Ce^{3+} ions in $Ce_2Zr_2O_7$ at low temperature in magnetic fields along the $[1, \bar{1}, 0]$ and $[0, 0, 1]$ directions. Fields along the $[1, \bar{1}, 0]$ direction are of particular interest, because the local anisotropy of the g tensor of the Ce^{3+} ions means two of the four sites in the unit cell are decoupled from fields in this direction, while the other two sites couple to the field strongly. These two sets of spins form chains in the pyrochlore structure [see Fig. 1(a)], conventionally labeled α and β. The α chains are polarized by the field, while the β chains are decoupled from it.

Moreover, the geometry of the interactions on the pyrochlore lattice means that once the α chains are polarized, the exchange field they produce on the sites of the β chains cancels, and the system is thus reduced to a set of independent, quantum, spin chains [33,34]. Reference [34] further shows that any effective interaction between β chains, mediated by quantum fluctuations on the α chains, is extremely small in the nearest-neighbor model. The decoupling of the α and β chains in $[1, \bar{1}, 0]$ magnetic fields has been observed previously in the classical spin ices $Ho_2Ti_2O_7$ [35–37] and $Dy_2Ti_2O_7$ [36,38,39] and in the dipolar-octupolar pyrochlore $Nd_2Zr_2O_7$ [40]. In each of these cases it was found that the β chains develop short-range ferromagnetic intrachain correlations. For $Nd_2Zr_2O_7$, no obvious correlations between β chains were reported [40], while for $Ho_2Ti_2O_7$ [35–37] and $Dy_2Ti_2O_7$ [36,38,39], short-ranged antiferromagnetic correlations develop between the β chains, attributed to long-range dipolar interactions [33].

The ferromagnetic coupling detected within β chains in $Nd_2Zr_2O_7$ [40] is consistent with the dominant ferromagnetic coupling between dipole moments in $Nd_2Zr_2O_7$ [16,40,41], despite the fact that frustration of this dominant ferromagnetic coupling leads to an antiferromagnetic all-in, all-out ground state in zero field [40,42–46]. The short-range ferromagnetic intrachain correlations detected in $Ho_2Ti_2O_7$ [35–37] and $Dy_2Ti_2O_7$ [36,38,39] are consistent with the ferromagnetic coupling of dipole moments that governs the conventional “2-in-2-out” rule for these classical spin ices in zero field [35,47–52].

The results we report here for $Ce_2Zr_2O_7$ also show short-range ferromagnetic intrachain correlations, in agreement with the ferromagnetic coupling between dipole moments ($J_z > 0$) determined from estimates of the exchange parameters in this paper and Refs. [25,26], as well as very weak or vanishing correlations between β chains. However, we also find important differences, compared to previously studied materials. In particular, the intrachain correlation length we observe is much shorter in $Ce_2Zr_2O_7$ than in the classical spin ices, a fact that we attribute both to stronger quantum fluctuations and to the strong multipolar interactions in $Ce_2Zr_2O_7$. The situation here is also somewhat different to that in $Nd_2Zr_2O_7$, where neutron scattering probes the dominant correlations on the β chains, whereas here we find that the dominant multipolar correlations are hidden. We reach this conclusion via fits of the in-field heat capacity data to numerical linked cluster (NLC) calculations based on Eq. (2), finding that $J_{\tilde{x}}$ and $J_{\tilde{y}}$ dominate over $J_{\tilde{z}}$, and that $\theta \approx 0$, reaffirming our conclusions from [25]. We find that the values of $J_{\tilde{x}}$ and $J_{\tilde{y}}$ are closely matched, which in turn implies that the β chains are tuned to the vicinity of a critical point and have nearly gapless excitations.

For fields in the $[0, 0, 1]$ direction we observe the field-induced structure shown in Fig. 1(b). For this magnetic structure, each of the rare-earth magnetic moments are aligned along the local easy-axis direction that has a positive component along $[0, 0, 1]$, so as to collectively minimize the interaction energies of the rare-earth ion with both the crystal electric field and the magnetic field. This corresponds to a field-induced selection of the 2-in-2-out spin ice state that has a net moment along $[0, 0, 1]$, for each tetrahedron, and as such forms a $Q = 0$ magnetic structure [36,38,53]. This $Q = 0$ magnetic structure is known to occur in the classical spin ices $Ho_2Ti_2O_7$ and $Dy_2Ti_2O_7$ at low temperature in moderate magnetic fields along the $[0, 0, 1]$ direction [36,38].

Inelastic neutron scattering performed in both $[1, \bar{1}, 0]$ and $[0, 0, 1]$ does not show any sharp spin wave excitations. This supports the conclusion of a small or vanishing value of θ, as it is this parameter which controls the matrix element to excite spin waves from the high-field polarized state. Modelling the inelastic scattering using molecular dynamics simulations, we find good general agreement. The suite of data presented here, across thermodynamic, static and spectroscopic measurements, strongly constrains any theoretical description of $Ce_2Zr_2O_7$. As such this paper represents an important step in the understanding of this promising spin ice candidate material.

II. OUTLINE

We first present heat capacity measurements of $Ce_2Zr_2O_7$ in a magnetic field along the $[1, \bar{1}, 0]$ direction for field strengths between 0 and 2 T. These measurements are fit to the results of numerical linked cluster (NLC) calculations to further examine experimental estimates of the parameters $(J_{\tilde{x}}, J_{\tilde{y}}, J_{\tilde{z}})$ and g_z for Ce^{3+} in $Ce_2Zr_2O_7$. The results of this fitting are largely consistent with previous estimates for the nearest-neighbor-exchange parameters in Ref. [25], and importantly, with a $U(1)_\pi$ quantum spin ice ground state in $Ce_2Zr_2O_7$ according to the ground-state phase diagrams predicted for dipolar-octupolar pyrochlores at the nearest-neighbor level [15,17–20].

We next present elastic neutron scattering results from our time-of-flight and triple-axis neutron scattering measurements on single crystal $Ce_2Zr_2O_7$ in a $[1, \bar{1}, 0]$ magnetic field. These measurements reveal magnetic Bragg peaks characteristic of field-polarized α chains, as well as sheets of diffuse magnetic scattering characteristic of loosely-correlated β chains that are short-ranged-ordered ferromagnetically within each chain and disordered between the chains, as illustrated in Fig. 1(a). Our elastic neutron scattering measurements in a [0, 0, 1] magnetic field show only the appearance of magnetic Bragg intensity at $\mathbf{Q} = (2, 0, 0)$ and symmetrically-equivalent positions, with no magnetic Bragg intensity at $\mathbf{Q} = (2, 2, 0)$, a signature of the [0, 0, 1]-polarized spin ice state, illustrated in Fig. 1(b). These elastic neutron scattering results are then put into the context of the results on the classical dipolar spin ices, $Ho_2Ti_2O_7$ and $Dy_2Ti_2O_7$ as well as the quantum pyrochlore $Nd_2Zr_2O_7$.

Finally, for both $[1, \bar{1}, 0]$ and $[0, 0, 1]$ magnetic field directions, our time-of-flight inelastic neutron scattering measurements reveal a continuum of relatively dispersionless inelastic scattering, which breaks off from the quasielastic scattering that is characteristic of the zero-field quantum spin ice state, with increasing magnetic field strength.

We compare our neutron scattering measurements with semiclassical molecular dynamics calculations based on Monte Carlo simulations, as well as one-dimensional quantum calculations, using the experimental estimates for $(J_{\tilde{x}}, J_{\tilde{y}}, J_{\tilde{z}})$ and g_z obtained from our fitting to the heat capacity. These calculated neutron scattering intensities are largely consistent with the experimental data and the strong θ dependence of the calculated scattering further suggests that θ is near zero for $Ce_2Zr_2O_7$.

III. EXPERIMENTAL DETAILS

Neutron scattering and heat capacity measurements were performed on three different high-quality single crystal samples of $Ce_2Zr_2O_7$, each grown by floating zone image furnace techniques as described in Ref. [13]. As described in earlier studies, nonstoichiometric oxygen content and the presence of nonmagnetic Ce^{4+} impurities can complicate measurements on as-grown $Ce_2Zr_2O_7$ samples and samples that have been exposed to air after growth [13]. Accordingly, our crystals were subsequently annealed at 1450 C for 72 hours in H_2 gas to reduce the as-grown oxygen content and maximize the Ce^{3+} to Ce^{4+} ratio, and care was taken to store the samples in inert gas after annealing.

Heat capacity measurements were performed on a single crystal piece of $Ce_2Zr_2O_7$ that was removed from one of our larger crystals, along with a polycrystalline sample of $La_2Zr_2O_7$, which is used as a $4f^0$ analog of $Ce_2Zr_2O_7$. Heat capacity measurements on a polished single crystal of $Ce_2Zr_2O_7$ (smooth-surfaced pressed powder pellet of $La_2Zr_2O_7$) were carried out using a Quantum Design PPMS to temperatures as low as $T = 0.058$ K ($T = 2.5$ K) using the conventional quasiadiabatic thermal relaxation technique. The heat capacity of $La_2Zr_2O_7$ is very small at ~2.5 K, and there was no need to pursue measurements at lower temperatures. The heat capacity of our single crystal $Ce_2Zr_2O_7$ sample was measured in a magnetic field along the $[1, \bar{1}, 0]$ direction at field strengths between 0 and 2 T. Our zero-field heat capacity measurements on $Ce_2Zr_2O_7$ and $La_2Zr_2O_7$ are also presented and analyzed in Ref. [25].

Our triple-axis elastic neutron scattering measurements employed the SPINS instrument at the NIST Center for Neutron Research, with a constant incident neutron energy of $E_i = 5$ meV. For this experiment, a ~1.5-gram single crystal of $Ce_2Zr_2O_7$ was aligned in the (H, H, L) scattering plane in a magnetic field along the $[1, \bar{1}, 0]$ direction. The $(0, 0, 2)$ Bragg reflection from pyrolytic graphite was employed for both the monochromator and analyzer of this instrument and a liquid nitrogen cooled beryllium filter was used after the sample to remove higher-order neutrons. The collimation was 0.7° in both the incident and scattered beams, and the overall energy resolution was ~0.22 meV. The single crystal sample was mounted in an aluminum sample holder, and a ^{3}He insert was used in a vertical-field superconducting magnet cryostat with a maximum field strength of 7 T.

Our time-of-flight neutron scattering experiments employed the Cold Neutron Chopper Spectrometer (CNCS) instrument at the Spallation Neutron Source of Oak Ridge National Laboratory [54,55]. We employed an incident neutron energy of $E_i = 3.27$ meV using the high-flux configuration with 300 Hz chopper frequency, yielding an energy resolution of ~0.1 meV at the elastic line. For one experiment, a ~5-gram single crystal sample of $Ce_2Zr_2O_7$ was mounted in a copper sample holder and aligned in the (H, H, L) scattering plane in a magnetic field along the $[1, \bar{1}, 0]$ direction. For the second neutron scattering experiment using the CNCS instrument, a ~1.7-gram single crystal $Ce_2Zr_2O_7$ sample was mounted in a copper sample holder and aligned in the $(H, K, 0)$ scattering plane in a magnetic field along the [0, 0, 1] direction.

For each chosen temperature and field strength of our CNCS experiment with a $[1, \bar{1}, 0]$ magnetic field, the sample was rotated in the (H, H, L) plane in 1° steps through a total of 220° and the data was subsequently symmetrized. We have further discussed this symmetrization process in the supplemental material of Ref. [13]. We reduce the diffuse scattering data in Figs. 4–6 (see below) in a manner that avoids adding artefacts to the diffuse scattering signal arising from the imperfect subtraction of Bragg peaks: The intensity at each Bragg peak location is masked in performing the subtraction of the $h = 0$ T data and we subsequently show the intensity at these masked Bragg peak locations as the average intensity of the surrounding points in reciprocal space. For each chosen temperature and field strength of our CNCS experiment

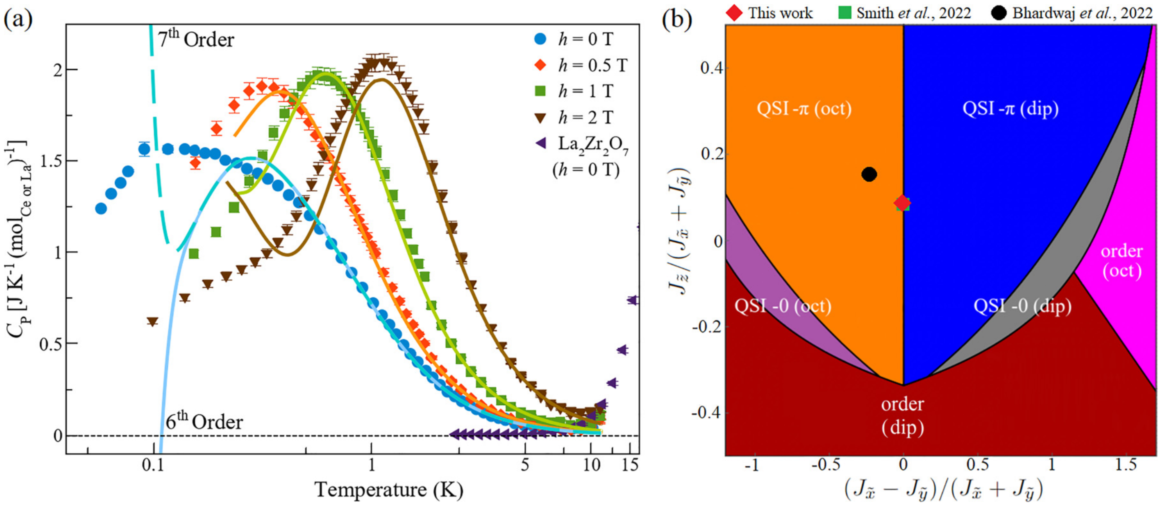

FIG. 2. (a) The temperature dependence of the heat capacity of single crystal $Ce_2Zr_2O_7$ in a $[1, \bar{1}, 0]$ magnetic field is shown for field strengths of 0 T (blue), 0.5 T (orange), 1 T (green), and 2 T (brown), as well as the heat capacity of a $La_2Zr_2O_7$ powder sample in zero magnetic field (purple). The lines in (a) show the magnetic contribution to the heat capacity in a $[1, \bar{1}, 0]$ magnetic field calculated using sixth- and seventh-order NLC calculations for zero magnetic field and fifth-order NLC calculations at each nonzero-field strength of measurement (as labeled). The calculation is shown using $\theta = 0$ and our best-fitting set of nearest-neighbor-exchange parameters $(J_{\tilde{x}}, J_{\tilde{y}}, J_{\tilde{z}}) = (0.063, 0.062, 0.011)$ meV obtained in this paper by fitting the sixth-order NLC calculations to the zero-field $Ce_2Zr_2O_7$ C_P data in this figure. The calculations in this figure use the value $g_z = 2.24$ for the effective g factor, which provides the best-fit to the in-field data for $(J_{\tilde{x}}, J_{\tilde{y}}, J_{\tilde{z}}) = (0.063, 0.062, 0.011)$ meV and $\theta = 0$ according to the fifth-order NLC calculations. (b) The best fit parameters from the NLC calculations in this paper overlaid on the zero-field ground-state phase diagram predicted for the XYZ model Hamiltonian and dipole-octupole pyrochlores [17,30]. We also plot the experimental estimates for the exchange parameters determined in Refs. [25,26]. Part (b) of this figure was adapted from Ref. [30].

with $[0, 0, 1]$ magnetic field, the sample was rotated in the $(H, K, 0)$ plane in 0.5° steps through a total of 280° and the data was subsequently symmetrized. The Data Analysis and Visualization Environment (DAVE) software suite for the reduction, visualization, and analysis of low-energy neutron spectroscopic data [56] was used in analyzing the neutron scattering data presented in this paper.

IV. RESULTS: HEAT CAPACITY AND NUMERICAL-LINKED-CLUSTER CALCULATIONS

New heat capacity measurements taken on a $Ce_2Zr_2O_7$ single crystal in a $[1, \bar{1}, 0]$ magnetic field complement those previously reported from $Ce_2Zr_2O_7$ single crystals in zero magnetic field and in $[1, 1, 1]$ magnetic fields [14,25,26,57]. As discussed previously, the $[1, \bar{1}, 0]$ magnetic field direction is particularly interesting to investigate for $Ce_2Zr_2O_7$ due to the lack of coupling between the magnetic field and the β chains in the pyrochlore lattice for this field direction. Figure 2(a) shows the temperature dependence of heat capacity measured from our single crystal sample of $Ce_2Zr_2O_7$ in a $[1, \bar{1}, 0]$ magnetic field for field strengths between $h = 0$ T and $h = 2$ T, as well as the heat capacity measured from a powder sample of $La_2Zr_2O_7$ down to 2 K. $La_2Zr_2O_7$ is a nonmagnetic analog of $Ce_2Zr_2O_7$ and the measured data from $La_2Zr_2O_7$ in Fig. 2(a) (purple) provides an estimate for the phonon contribution to the heat capacity in $Ce_2Zr_2O_7$. This shows that this lattice contribution to the heat capacity is approximately zero below $T \sim 6$ K, and accordingly, the magnetic contribution to the heat capacity (C_{mag}) is easily isolated below $T \sim 6$ K. Figure 2(a) shows that the broad hump in the zero-field heat capacity, due to C_{mag}, increases in temperature and width with increasing field strength before splitting into two distinct humps, which are visible as separate features by 2 T.

The field-dependent hump at higher temperature has the form of a Schottky anomaly at $h = 2$ T and we attribute this feature to the phase crossover into the low-temperature ordered regime for the α chains, which interact strongly with the magnetic field. On the other hand, the low-temperature shoulder of this peak, most visible in the 2 T data of Fig. 2(a), is attributed to the phase crossover into the low-temperature short-ranged ordered regime for the β chains, which lack significant coupling to the magnetic field. This is similar to the splitting of C_{mag} observed in Ref. [58] for the classical spin ice $Dy_2Ti_2O_7$, where a $[1, \bar{1}, 0]$ magnetic field again splits the hump in the zero-field heat capacity into a field-dependent hump associated with the α chains, which takes the form of a Schottky anomaly for higher fields, and a field-independent phase crossover at lower temperature associated with the β chains, consistent with predictions for $Dy_2Ti_2O_7$ in Ref. [33].

We compare the measured heat capacity of $Ce_2Zr_2O_7$ with C_{mag} calculations using the NLC method [59–63], which allows further refinements of the nearest-neighbor-exchange parameters in the XYZ Hamiltonian relevant to $Ce_2Zr_2O_7$ [25,30]. The NLC method employs a process of calculating C_{mag} (or other physical quantities) by generating a series expansion from the exact diagonalization of clusters containing increasing numbers of tetrahedra. The sum is truncated at some maximum cluster size, and the calculation is expected to be accurate for temperatures such that the correlation length does not exceed that maximum size. The order of these quantum NLC calculations refers to the maximum number of tetrahedra considered in a cluster, and the low-temperature cutoff for the nth-order calculation, using a particular set of exchange parameters, is set by the temperature above which the nth-order calculation is equal to the $(n-1)$th-order calculation up to some small tolerance. We have carried out NLC calculations up to seventh order to model the magnetic heat capacity at temperatures above a low-temperature threshold for each calculation, and below $T = 6$ K where the phonon contribution to the heat capacity is insignificant.

In the following, we use sixth-order NLC and fifth-order NLC to fit the heat capacity in zero and nonzero field, respectively. The reduced order for nonzero field is due to the reduced symmetry of the Hamiltonian in that case, which increases the cost of the exact diagonalization. In addition to that, the number of topologically invariant clusters in the NLC expansion is also increased in the nonzero-field case making calculations even more demanding. We first used sixth-order NLC calculations in order to fit the zero-field heat capacity measured from $Ce_2Zr_2O_7$ and determine the best-fitting nearest-neighbor-exchange parameters $J_{\tilde{x}}$, $J_{\tilde{y}}$, and $J_{\tilde{z}}$ up to permutation of the $\tilde{x}$, $\tilde{y}$, and $\tilde{z}$ axes. This is similar to the sixth-order NLC fitting of the zero-field heat capacity measured from $Ce_2Sn_2O_7$ in Ref. [30], and provides improvement to the fourth-order NLC fitting of the zero-field heat capacity measured from $Ce_2Zr_2O_7$ in Ref. [25]. We then use fifth-order NLC calculations to fit the in-field heat capacity measured from $Ce_2Zr_2O_7$ using the best-fitting values of $J_{\tilde{x}}$, $J_{\tilde{y}}$, and $J_{\tilde{z}}$ determined from our zero-field fitting, in order to determine which permutations of these exchange parameters fit the measured data best, as well as to estimate the effective anisotropic g factor, g_z.

The zero-field heat capacity contains no directional information and as such it does not depend on θ or the permutation of $\tilde{x}$, $\tilde{y}$, and $\tilde{z}$ that is chosen. We compare sixth-order NLC calculations for C_{mag} between $T = 0.3$ K and $T = 4$ K to the measured heat capacity from $Ce_2Zr_2O_7$ in zero field in order to fit the values of $(J_{\tilde{x}}, J_{\tilde{y}}, J_{\tilde{z}})$ up to permutation. Specifically, the set of Hamiltonian parameters, $(J_{\tilde{x}}, J_{\tilde{y}}, J_{\tilde{z}})$, best reproducing C_{mag} was obtained from a sixth-order NLC calculation with an Euler transformation to improve convergence (see Appendix A), and the best-fitting exchange parameters up to permutation are $(J_{\tilde{x}}, J_{\tilde{y}}, J_{\tilde{z}}) = (0.063, 0.062, 0.011)$ meV. The blue lines in Fig. 2(a) shows the magnetic contribution to the heat capacity calculated in zero field via the NLC method at sixth and seventh order, using the best-fitting exchange parameters obtained from our C_{mag}-fitting procedure. These exchange parameters, regardless of their permutation, correspond to a $U(1)_\pi$ QSI in the ground-state phase diagram predicted for dipolar-octupolar pyrochlores [17,19]. However, the nature of the $U(1)_\pi$ QSI ground state (dipolar or octupolar) depends on the permutation of the exchange parameters.

Unlike in zero magnetic field, the magnetic contribution to the heat capacity in nonzero field depends on the permutation of $(J_{\tilde{x}}, J_{\tilde{y}}, J_{\tilde{z}})$, as well as the parameters θ and g_z, which only become relevant in the Hamiltonian of Eq. (2) for nonzero-field strength. We compare fifth-order NLC calculations for C_{mag} between $T = 0.2$ K and $T = 6$ K to the measured heat capacity from $Ce_2Zr_2O_7$ in a $[1, \bar{1}, 0]$ magnetic field for field strengths of $h = 0.5$ T, $h = 1$ T, and $h = 2$ T, in order to fit the value of g_z and the best-fitting permutation of the exchange parameters estimated from our fitting to C_{mag} in zero field using higher-order calculations. The goodness-of-fit parameter for this comparison lacks a significant θ dependence in the region of good agreement for each measured field strength (see Appendix A), and so θ has been set to zero for our fitting of the heat capacity in nonzero magnetic field, in accordance with value of θ estimated in Refs. [25,26] and consistent with the neutron scattering results that we present in Sec. V.

Our fifth-order NLC fitting to the measured heat capacity from $Ce_2Zr_2O_7$ in a $[1, \bar{1}, 0]$ magnetic field yields the estimated value for the effective g factor, $g_z = 2.24$, and signifies that the permutations $(J_{\tilde{x}}, J_{\tilde{y}}, J_{\tilde{z}}) = (0.063, 0.062, 0.011)$ meV and $(J_{\tilde{x}}, J_{\tilde{y}}, J_{\tilde{z}}) = (0.062, 0.063, 0.011)$ meV are the best-fitting permutations and fit much better than the four other possible permutations of $(0.063, 0.062, 0.011)$ meV (see Appendix A). These two best-fitting permutations provide equal fits to the heat capacity due to the interchangeability of $\tilde{x}$ and $\tilde{y}$ in Eq. (2) for $\theta = 0$. Both sets of these best-fitting exchange parameters have $J_{\tilde{x}} \approx J_{\tilde{y}}$, which implies that the corresponding quantum spin ice ground state is proximate to the boundary between dipolar and octupolar character. Furthermore, the near-equality of $J_{\tilde{x}}$ and $J_{\tilde{y}}$ implies that the β chains within $Ce_2Zr_2O_7$ in a $[1, \bar{1}, 0]$ magnetic field are near the critical point $(J_{\tilde{x}} = J_{\tilde{y}})$ where the excitations on the β chains become gapless (see Appendix B).

The orange, green, and brown lines in Fig. 2(a) show the magnetic contribution to the heat capacity calculated via the NLC method at fifth order for $[1, \bar{1}, 0]$ magnetic field strengths of $h = 0.5$ T, $h = 1$ T, and $h = 2$ T, respectively, using the best-fitting exchange parameters obtained from our C_{mag}-fitting procedure, $(J_{\tilde{x}}, J_{\tilde{y}}, J_{\tilde{z}}) = (0.063, 0.062, 0.011)$ meV and $g_z = 2.24$, with θ set to zero. Figure 2(a) shows that the best-fitting nearest-neighbor exchange parameters from this paper are able to accurately describe the temperature dependence of heat capacity measured from $Ce_2Zr_2O_7$ in a $[1, \bar{1}, 0]$ magnetic field up to field strengths of 2 T, at modest and elevated temperatures where the NLC method is expected to be accurate. Specifically, these NLC calculations capture the shifting, widening, and splitting of the broad hump in the measured heat capacity of $Ce_2Zr_2O_7$ in a $[1, \bar{1}, 0]$ magnetic field.

While these NLC calculations provide an accurate qualitative description of the measured data over their respective regions of convergence where they are reliable (above $T \sim 0.15$ K for the zero-field calculations and over the full range shown for the nonzero-field calculations), it is clear that the quantitative descriptions could be improved at lower temperatures within the regions of convergence. This is most evident for zero field, where the hump in calculated heat capacity peaks at a significantly higher temperature than that in the measured data, and for $h = 2$ T, where the calculation suggests a second, distinctive hump at low temperature rather than the broadened feature that resembles more of a low-temperature shoulder to the high-temperature hump in the measured data [Fig. 2(a)]. These inconsistencies suggest the significance of effects beyond the ideal nearest-neighbor Hamiltonians in Eqs. (1) and (2), which are weak effects and hence, only become relevant at the lowest measured temperatures, as would occur, for example, with further-than-nearest neighbor interactions.

Figure 2(b) shows the best-fitting exchange parameters obtained in this paper and the exchange parameters determined in Refs. [25,26] overlaid on the zero-field ground-state phase diagram predicted for dipolar-octupolar pyrochlores at the nearest-neighbor level [17,30]. As shown in Fig. 2(b), the current understanding is that there are six phases in the nearest-neighbor ground-state phase diagram predicted for dipolar-octupolar pyrochlores: Four U(1) spin ice phases, which may be distinguished by an emergent flux of 0 or π on the hexagonal plaquettes of the lattice, and by the dipolar or octupolar nature of the emergent electric field, and two ordered phases distinguished by dipolar and octupolar order parameters [15,17,18]. Each of the estimated exchange parameter sets for $Ce_2Zr_2O_7$ are well within the region of the ground-state phase diagram corresponding to $U(1)_\pi$ quantum spin ice ground states in zero field, with the set from Ref. [26] being within the octupolar regime and the sets from this work and Ref. [25] being on the border between octupolar and dipolar nature.

Our best-fitting exchange parameters are nearly identical to those determined in Ref. [25] but with a reduced anisotropic g factor given by $g_z \sim 2.24$, which is 87% of the value corresponding to a pure $|m_J = \pm 3/2\rangle$ ground-state doublet. The experimental estimates of the exchange parameters in Ref. [26] also yield a reduced g factor value of $g_z \sim 2.4$, while the experimental estimates of the exchange parameters in Ref. [25] did not allow for a variation of g_z from the value of 2.57 corresponding to a pure $|m_J = \pm 3/2\rangle$ ground-state doublet. It is also worth mentioning that our estimated value of $g_z \sim 2.24$ for $Ce_2Zr_2O_7$ is very near the value of $g_z \sim 2.2$ estimated for $Ce_2Sn_2O_7$ in Ref. [30], and attributed to mixing of the $|m_J = \pm 3/2\rangle$ states with states from the $J = 7/2$ spin-orbit manifold in the CEF ground-state doublet for $Ce_2Sn_2O_7$, rather than a pure $|m_J = \pm 3/2\rangle$ ground state [28]. References [13,14] both perform their CEF analysis on $Ce_2Zr_2O_7$ within the $J = 5/2$ spin-orbit ground-state manifold.

V. RESULTS: ELASTIC AND QUASIELASTIC NEUTRON SCATTERING

Here we present our elastic and quasielastic neutron scattering results on single crystal $Ce_2Zr_2O_7$ at low temperature for both $[1, \bar{1}, 0]$ and $[0, 0, 1]$ magnetic fields. We begin with the $[1, \bar{1}, 0]$ field direction where we first analyze the magnetic Bragg scattering from the field-polarized α chains before discussing the quasielastic diffuse scattering in a $[1, \bar{1}, 0]$ magnetic field, which is dominated by scattering from the field-decoupled β chains. We end this section with an analysis of the magnetic Bragg scattering detected from the polarized spin ice phase in a magnetic field along $[0, 0, 1]$. It is worth mentioning that the neutron scattering experiments we present here directly probe only correlations from the z components of the pseudospins, S^z (which equals $S^{\tilde{z}}$ for $\theta = 0$). This is due to the fact that x and y components of pseudospin each carry octupolar magnetic moments and accordingly, give significant scattering signals only at much higher Q than the maximum Q of our measurements [64]. Nonetheless, this paper establishes a clear understanding for the behavior of the magnetic dipole moments in $Ce_2Zr_2O_7$ at low temperature in both $[1, \bar{1}, 0]$ and $[0, 0, 1]$ magnetic fields. Furthermore, and as shown in Ref. [19], the correlation function for z components of the pseudospins indeed depends on the relative values of $J_{\tilde{x}}$, $J_{\tilde{y}}$, and $J_{\tilde{z}}$, and so our neutron scattering experiments are sensitive to all exchange parameters despite only having sensitivity to S^z correlations.

A. Magnetic Bragg peaks from polarized α chains in a $[1, \bar{1}, 0]$ magnetic field

As discussed above, the effect of a moderate $[1, \bar{1}, 0]$ magnetic field on a disordered spin ice ground state is to polarize the α chains to the extent consistent with the Ising single-ion anisotropy [33,35–40,53], which constrains the magnetic moments to point along local $[1, 1, 1]$ and equivalent directions. Accordingly, and as shown in Fig. 1(a), the Zeeman term in Eq. (2) will couple only to two of the four sites in the unit cell (those with easy axes along $[1, \bar{1}, 1]$ and $[1, \bar{1}, \bar{1}]$) while the other two sites will not couple to the external field. The sites which couple to the field form the α chains, while those that do not form the β chains. The α chains polarize in the magnetic field, which then allows the perpendicular β chains to decouple. In the absence of residual β-chain–β-chain interactions, the β chains themselves are expected to behave as one-dimensional spin systems, but weak β-chain–β-chain interactions will tend to induce short-ranged correlations between them [33–39,53].

The field-polarized α chains are then expected to display long-ranged order with magnetic Bragg peaks as a consequence. While all the $Q = 0$ Bragg positions for the FCC pyrochlore structure [all even or all odd h, k, l indices in $\mathbf{Q} = (h, k, l)$] are expected to show nonzero magnetic Bragg intensity, it is the $\mathbf{Q} = (0, 0, \pm 2)$ Bragg positions at which this is immediately obvious, as there is no nuclear contribution to this Bragg peak.

Figures 3(a)–3(d) show the elastic neutron scattering data in the (H, H, L) plane of reciprocal space measured in our time-of-flight neutron scattering experiment using CNCS. Comparison of Fig. 3(a) with Fig. 3(b) shows that there is no discernible change in Bragg peak intensity or appearance of new Bragg peaks in zero field between $T = 30$ K and $T = 0.03$ K in this plane of reciprocal space. This is consistent with the lack of zero-field magnetic order at temperatures above $\sim$0.03 K, as previously reported for $Ce_2Zr_2O_7$ [13,14,25]. Comparison of the $T = 0.03$ K data in Figs. 3(b)–3(d) shows that magnetic Bragg peaks at $\mathbf{Q} = (0, 0, \pm 2)$ appear at low magnetic field and grow in intensity with increasing field strength.

Figure 3(e) shows the field strength and temperature dependence of the $\mathbf{Q} = (0, 0, 2)$ magnetic Bragg peak measured in our triple-axis elastic neutron scattering experiment using SPINS. This is the strongest magnetic Bragg peak corresponding to α-chain polarization within the range of the measurements [40]. We show the $\mathbf{Q} = (0, 0, 2)$ magnetic Bragg peak intensity as a function of magnetic field strength for field strengths between $h = 0$ T and $h = 2.6$ T, at $T = 0.30$ K, $T = 0.65$ K, $T = 0.90$ K, and $T = 1.45$ K. The $T = 0.30$ K (blue) data shows that the $\mathbf{Q} = (0, 0, 2)$ magnetic Bragg peak intensity is saturated for field strengths above

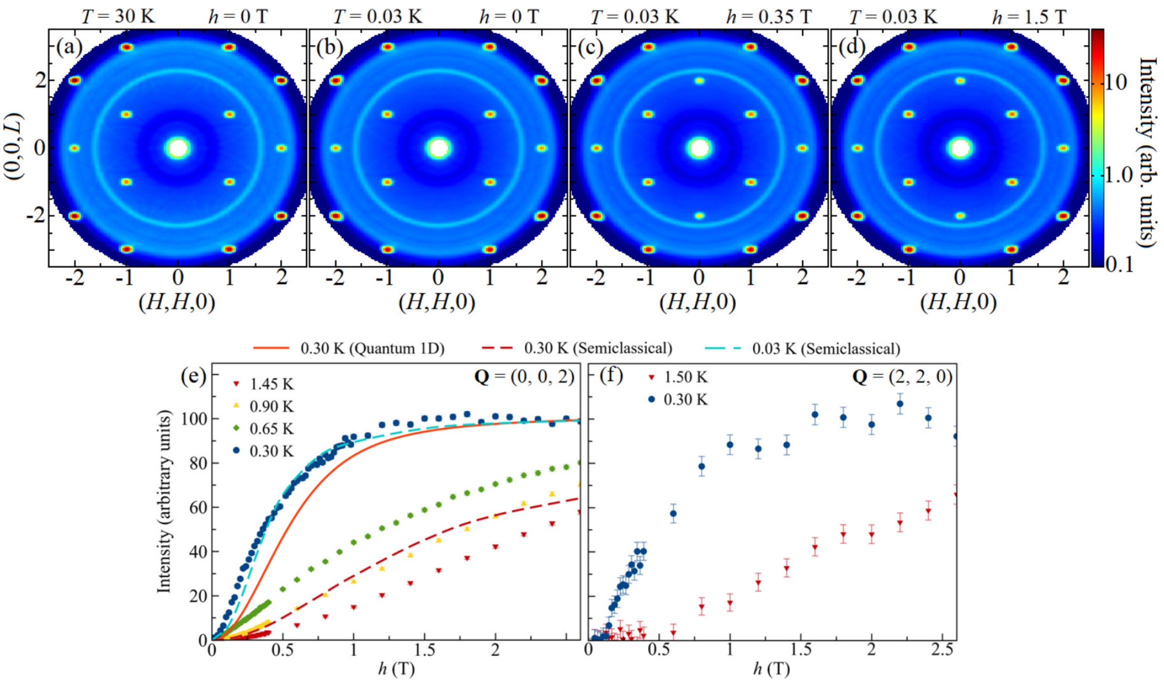

FIG. 3. The symmetrized elastic neutron scattering signal measured from $Ce_2Zr_2O_7$ in the (H, H, L) plane of reciprocal space with integration in the out-of-plane direction, $(K, \bar{K}, 0)$, from $K = -0.1$ to 0.1, and over energy-transfer from $E = -0.2$ to 0.2 meV. (a) and (b) show the elastic neutron scattering signals measured in zero magnetic field at $T = 30$ K and $T = 0.03$ K, respectively. (c) and (d) show the elastic neutron scattering signals measured in a $[1, \bar{1}, 0]$ magnetic field at $T = 0.03$ K for field strengths of $h = 0.35$ T and $h = 1.5$ T, respectively. The intensity here is shown on a logarithmic scale. (e) and (f) show the magnetic field-strength dependence and temperature dependence of the $\mathbf{Q} = (0, 0, 2)$ and $\mathbf{Q} = (2, 2, 0)$ magnetic Bragg peaks, respectively, measured in our triple-axis neutron scattering experiment. Specifically, the data in blue (green, yellow, red) shows the field strength dependence of the magnetic Bragg peak intensity measured at $T = 0.30$ K ($T = 0.65$ K, $T = 0.90$ K, $T \approx 1.45$ K). The lines in (e) show the corresponding semiclassical molecular dynamics calculations (broken lines) and one-dimensional quantum calculations (solid line) for the magnetic Bragg peak intensity as a function of field strength using the experimental estimates of the nearest-neighbor-exchange parameters obtained from this paper, $(J_{\tilde{x}}, J_{\tilde{y}}, J_{\tilde{z}}) = (0.063, 0.062, 0.011)$ meV, $g_z = 2.24$, and $\theta = 0$, where $J_{\tilde{z}}$ is approximated as zero for the one-dimensional quantum calculations. We show the semiclassical and one-dimensional quantum calculations at $T = 0.30$ K (red lines) and we also show the semiclassical calculations at a lower temperature (blue line) where the calculations agree better with the measured data at $T = 0.30$ K. For each data set and calculation, the arbitrary units are such that the average intensity is equal to 100 in the saturated regime at low temperature and high field.

$h \sim 1.5$ T at low temperature. The $\mathbf{Q} = (0, 0, 2)$ magnetic Bragg peak intensity measures the level of α-chain polarization and the intensity saturation indicates full noncollinear polarization for the α chains by $h \sim 1.5$ T at $T = 0.3$ K.

Figure 3(f) shows the field strength and temperature dependence of the $\mathbf{Q} = (2, 2, 0)$ magnetic Bragg peak measured in our triple-axis elastic neutron scattering experiment. The α-chain polarization yields a significant magnetic intensity at the $\mathbf{Q} = (2, 2, 0)$ magnetic Bragg peak, which is second only to $\mathbf{Q} = (0, 0, \pm 2)$ within the range of these measurements. As the (2, 2, 0) nuclear Bragg peak is allowed, this elastic scattering data has had a zero-field high-temperature ($T = 1.5$ K) data set subtracted from it to isolate the magnetic Bragg intensity. We show the $\mathbf{Q} = (2, 2, 0)$ magnetic Bragg peak intensity as a function of magnetic field strength for field strengths between $h = 0$ T and $h = 2.6$ T, at $T = 0.30$ K (blue) and $T = 1.5$ K (red). Like the $\mathbf{Q} = (0, 0, 2)$ magnetic Bragg peak, the intensity of the $\mathbf{Q} = (2, 2, 0)$ magnetic Bragg peak is saturated beyond field strengths of $h \sim 1.5$ T at $T = 0.30$ K. Similar elastic neutron scattering measurements of the (0, 0, 2) and (2, 2, 0) Bragg peaks from $Ce_2Zr_2O_7$ in a $[1, \bar{1}, 0]$ magnetic field have recently been reported [57], and our measurements are consistent with these. However, Ref. [57] incorrectly claims that a three-in-one-out magnetic structure is expected for $Ce_2Zr_2O_7$ in a $[1, \bar{1}, 0]$ magnetic field, in disagreement with the estimated exchange parameters in this paper and in Refs. [25,26], as we show in Appendix C.

In Fig. 3(e), we compare the measured field dependence of the magnetic Bragg intensity to two separate calculations: Semiclassical molecular dynamics calculations based on Monte Carlo simulations (see Appendix D) using the experimental estimates of the nearest-neighbor-exchange parameters obtained from this paper, $(J_{\tilde{x}}, J_{\tilde{y}}, J_{\tilde{z}}) = (0.063, 0.062, 0.011)$ meV, $g_z = 2.24$, and $\theta = 0$, as well as one-dimensional quantum calculations (see Appendix B) that approximate $J_{\tilde{z}}$ as zero and use the best-fitting parameters from this paper otherwise. The approximation of $J_{\tilde{z}}$ as zero is justified as the $\tilde{z}$ components of the α-chain pseudospins interact much more strongly with the magnetic field than with each other except at low fields. This one-dimensional quantum problem is exactly solvable for θ equal to zero using a Jordan-Wigner transformation (further details in Appendix B).

The comparison in Fig. 3(e) shows that quantum calculations are indeed necessary to adequately account for the simultaneous field and temperature dependencies of the magnetic Bragg intensity measured from $Ce_2Zr_2O_7$ in a $[1, \bar{1}, 0]$ magnetic field. Specifically, the semiclassical molecular dynamics calculations, based on Monte Carlo simulations, at $T = 0.30$ K do not account for the measured saturation at ~ 1.5 T, and much lower temperature is required for these semiclassical calculations to describe the measured data adequately (shown for $T = 0.03$ K). On the other hand, the one-dimensional quantum calculations at $T = 0.30$ K provide a good description for the measured saturation at ~ 1.5 T at that temperature [Fig. 3(e)], despite the fact that the one-dimensional quantum calculations underestimate the measured intensity at lower field where the approximation of isolated β chains is less accurate.

B. Quasielastic diffuse scattering from β chains in a $[1, \bar{1}, 0]$ magnetic field

The easy-axes directions for magnetic moments on the β chains are perpendicular to the $[1, \bar{1}, 0]$ magnetic field, resulting in a lack of coupling between the β chains and the $[1, \bar{1}, 0]$ magnetic field at low temperature. In addition to this decoupling with the magnetic field, the β chains are also decoupled from the polarized α chains at the nearest-neighbor level due to a cancellation of the effective exchange field within the polarized state of the α chains [34]. Experimental estimates of the nearest-neighbor exchange parameters for $Ce_2Zr_2O_7$ from this paper and Refs. [25,26], $\theta \sim 0$ and $J_{\tilde{z}} > 0$, are consistent with ferromagnetic interchain correlations for the dipole moments in the β chains (see Appendix C). Placke *et al.* [34] show that interchain correlations between ferromagnetic β chains can be described by a triangular lattice model where each point on the lattice represents a ferromagnetic β chain with one Ising degree of freedom corresponding to the direction of the chain's net magnetic moment. Furthermore, they show that quantum fluctuations mediate an effective interaction between β chains, which can lead to different forms of inter-β-chain magnetic correlations [34]. However, these interactions mediated by fluctuations are extremely weak and therefore not likely to be relevant for the physics here.

The α chains contribute primarily to the elastic scattering through Bragg scattering, and the quasielastic diffuse scattering originates almost entirely from the β chains. We first examine the quasielastic diffuse neutron scattering measured in the (H, H, L) plane with the time-of-flight neutron chopper spectrometer CNCS, and compare this with that predicted for possible magnetic correlations of the β chains. This diffuse β-chain scattering is weak for multiple reasons. First, the one-dimensional magnetic order of the β chains naturally results in planes of diffuse scattering, which will be relatively weak, as it will be distributed over planes perpendicular to the β chains. Furthermore, the small magnetic dipole moment associated with Ce^{3+} in $Ce_2Zr_2O_7$ ($\sim 1\ \mu_B$ [13,14,26], compared to $\sim 10\ \mu_B$ in $Ho_2Ti_2O_7$ for example [65–67]) also leads to weak magnetic scattering, as well as the fact that the dominant intrachain correlations are between octupolar magnetic moments rather than dipoles (as further discussed below). The result is that the diffuse scattering intensity is similar in magnitude to that associated with the background scattering from the magnet cryostat. For that reason, it is necessary to subtract otherwise identical data sets in zero field (where there is no distinction between α and β chains) from data sets in finite $[1, \bar{1}, 0]$ magnetic field. This is what is shown in Figs. 4(a)–4(c), where the (H, H, L) plane of reciprocal space is displayed with a $(K, \bar{K}, 0)$ integration normal to the scattering plane, from $K = -0.3$ to 0.3, and an integration in energy-transfer over the elastic position and any low-lying excitations in the range from $E = -0.2$ meV to 0.2 meV, for $h = 0.35$ T, 1.5 T, and 4 T, all at $T = 0.03$ K.

Figures 4(a)–4(c) clearly show rods of scattering along $(0, 0, L)$ and $(\pm 1, \pm 1, L)$, with less-extended distributions of scattering near $(\pm 2, \pm 2, L)$. While the rod-like scattering due to the β chains is clearly present, its relative weakness gives rise to some degree of interference between it and the undersubtracted and oversubtracted Al powder lines associated with the background from the magnet cryostat. Nonetheless, the overall pattern of diffuse rod-like scattering resembles expectations for the diffuse neutron scattering signal from β chains that are ordered ferromagnetically at short-range within the chains and disordered between the chains, that is, with the most intense rod of scattering along the $(0, 0, L)$ and with no significant peaks in diffuse scattering along the rod. While some patches of increased intensity are detected along the rod, these occur at locations where the rod intersects with an undersubtracted powder ring that accounts for the increase in intensity. As we discuss shortly, the measured rods of scattering extend in the out-of-plane, $(K, \bar{K}, 0)$, direction to form planes of scattering. In other words, the rods of scattering in the (H, H, L) plane are cross-sectional slices through planar scattering.

We compare the measured neutron scattering signal in the (H, H, L) plane to the corresponding prediction according to semiclassical molecular dynamics calculations based on Monte Carlo simulations (see Appendix D). These Monte Carlo simulations use the experimental estimates of the nearest-neighbor-exchange parameters obtained from this paper, $(J_{\tilde{x}}, J_{\tilde{y}}, J_{\tilde{z}}) = (0.063, 0.062, 0.011)$ meV, $g_z = 2.24$, and $\theta \sim 0$, and are consistent with field-polarized α chains and β chains that are short-ranged ordered ferromagnetically within the chains and disordered between the chains. Specifically, we show the calculations using $\theta = 0$ ($\theta = 0.1\pi$) for a $[1, \bar{1}, 0]$ magnetic field strength of $h = 0.35$ T, $h = 1.5$ T, $h = 4$ T in Figs. 4(d)–4(f) [4(g)–4(i)], respectively. Both the $\theta = 0$ and $\theta = 0.1\pi$ calculations are consistent with the data in that the most dominant feature is a rod of scattering along $(0, 0, L)$ direction for each field strength. However, the $\theta = 0.1\pi$ calculations predict a sharp and intense centerpiece to the rod of scattering, which has an intensity that increases with field strength, while the $\theta = 0$ calculations do not, and show much better agreement with the measured data for this reason. Notably, the $\theta = 0$ calculations [Figs. 4(d)–4(f)] predict that the rod-like scattering is weaker at 1.5 T and 4 T compared to 0.35 T, and weaker at 1.5 T compared to 4 T, in agreement with the measured data [Figs. 4(a)–4(c)] and in contrast to the $\theta = 0.1\pi$ calculation [Figs. 4(g)–4(i)], which predicts a rod-like signal with intensity that increases monotonically with field strength.

For the best-fitting exchange parameters obtained in this paper, $(J_{\tilde{x}}, J_{\tilde{y}}, J_{\tilde{z}}) = (0.063, 0.062, 0.011)$ meV, an intense center piece to the calculated neutron scattering signal

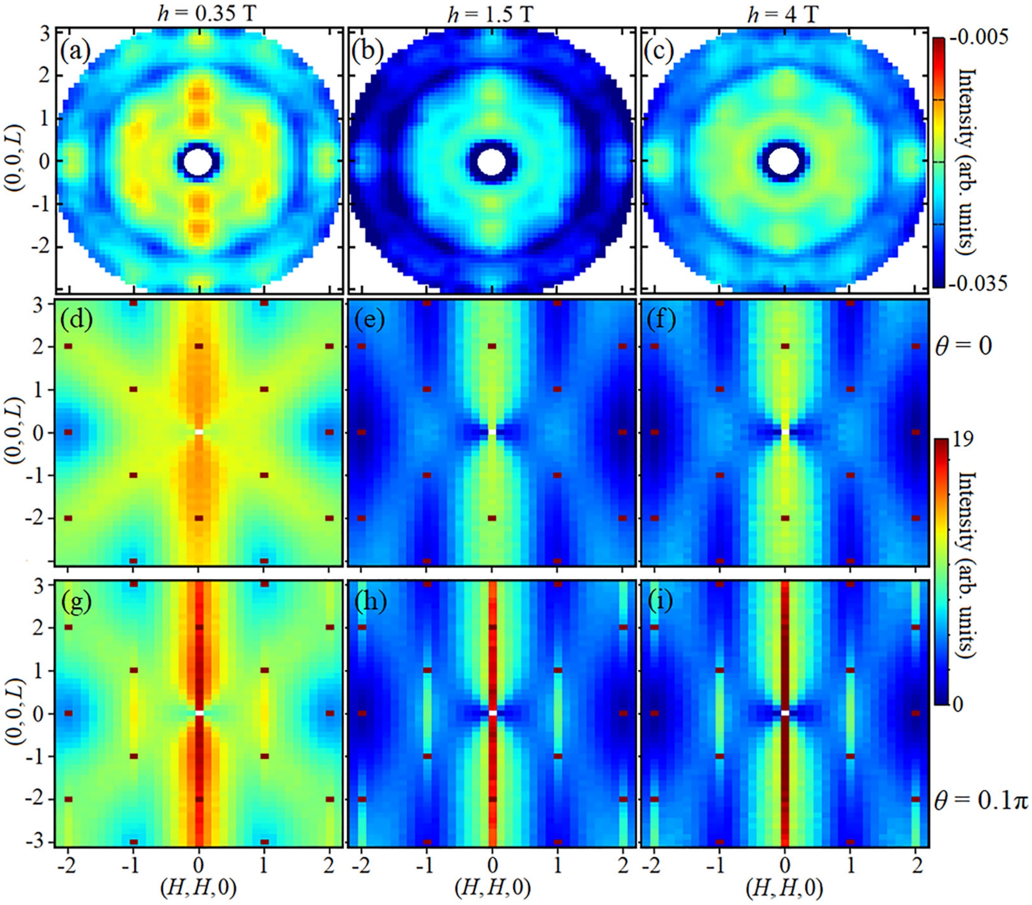

FIG. 4. The symmetrized quasielastic diffuse neutron scattering signal measured at $T = 0.03$ K from a single crystal sample of $Ce_2Zr_2O_7$ aligned in the (H, H, L) scattering plane in a $[1, \bar{1}, 0]$ magnetic field of strength $h = 0.35$ T (a), $h = 1.5$ T (b), and $h = 4$ T (c). In each case, a corresponding data set measured at $h = 0$ T has been subtracted, a $(K, \bar{K}, 0)$ integration range from $K = -0.3$ to 0.3 was used, and integration in energy-transfer was employed over the range -0.2 meV $\leqslant E \leqslant 0.2$ meV. We compare this with the corresponding diffuse neutron scattering signal in the (H, H, L) scattering plane predicted at $T = 0.03$ K according to our semiclassical molecular dynamics calculations using the nearest-neighbor-exchange parameters estimated in this paper. The calculated neutron scattering signal using the exchange parameters $\theta = 0$, $(J_{\tilde{x}}, J_{\tilde{y}}, J_{\tilde{z}}) = (0.063, 0.062, 0.011)$ meV, and $g_z = 2.24$, is shown for a $[1, \bar{1}, 0]$ magnetic field of strength $h = 0.35$ T (d), $h = 1.5$ T (e), and $h = 4$ T (f). The calculated neutron scattering signal using the exchange parameters $\theta = 0.1\pi$ and $(J_{\tilde{x}}, J_{\tilde{y}}, J_{\tilde{z}}) = (0.063, 0.062, 0.011)$ meV, and $g_z = 2.24$ is shown for a $[1, \bar{1}, 0]$ magnetic field of strength $h = 0.35$ T (g), $h = 1.5$ T (h), and $h = 4$ T (i).

becomes visible for nonzero θ, with intensity that increases with θ for $0 \leqslant \theta \leqslant \pi/2$, as we show in Figs. 4(d)–4(i) for $\theta = 0$ and 0.1π. This intense center-piece is not detected in the measured data [Figs. 4(a)–4(c)] and in general, the lack of intense centerpiece to the scattering signal is a signature of correlations between octupolar moments (or S^x and S^y in terms of pseudospin) heavily dominating those between dipole moments (S^z). For example, and as shown in Appendix D, it is possible for this intense centerpiece to be absent even for nonzero θ when $J_{\tilde{y}}$ heavily dominates both $J_{\tilde{x}}$ and $J_{\tilde{z}}$. Accordingly, we reiterate that this lack of intense centerpiece in the measured data is consistent with heavily dominant octupolar correlations.

It is worth mentioning that our one-dimensional quantum calculations for infinite field agree remarkably well with the high-field semiclassical calculations in that the quantum calculations also predict a sharp rod at the center of a broader rod, both along $(0, 0, L)$, for $\theta = 0.1\pi$, and the absence of the sharp and intense centerpiece for $\theta = 0$ (see Appendix B). In contrast to the measured and predicted signals displayed in Fig. 4, the diffuse scattering pattern predicted for a β chain with antiferromagnetically ordered dipole moments has the most intense rods along the $(\pm1, \pm1, L)$ directions of the (H, H, L) plane, with intensities that increase towards larger L for our measurement range, rather than towards $L = 0$ [40].

Figure 5 shows the measured quasielastic diffuse scattering signal in the $(H + K, H - K, 1.5)$ plane of reciprocal space, at $T = 0.03$ K and $h = 0.35$ T (a), $h = 1.5$ T (b), and $h = 4$ T (c), for a $(0, 0, L)$ integration range from $L = 1.25$ to 1.75 [illustrated in Fig. 6(a)]. From Figs. 5(a)–5(c), it is clear that the rod-like feature of diffuse scattering along the $(0, 0, L)$ direction in the (H, H, L) plane also extends out in the perpendicular $(K, \bar{K}, 0)$ direction at each measured field strength, forming the expected plane of scattering perpendicular to the $(H, H, 0)$ direction of the β chains, which is consistent with one-dimensional magnetic correlations for the β chains. We again compare the measured neutron scattering signal in the (H, H, L) plane to the corresponding prediction using semiclassical molecular dynamics

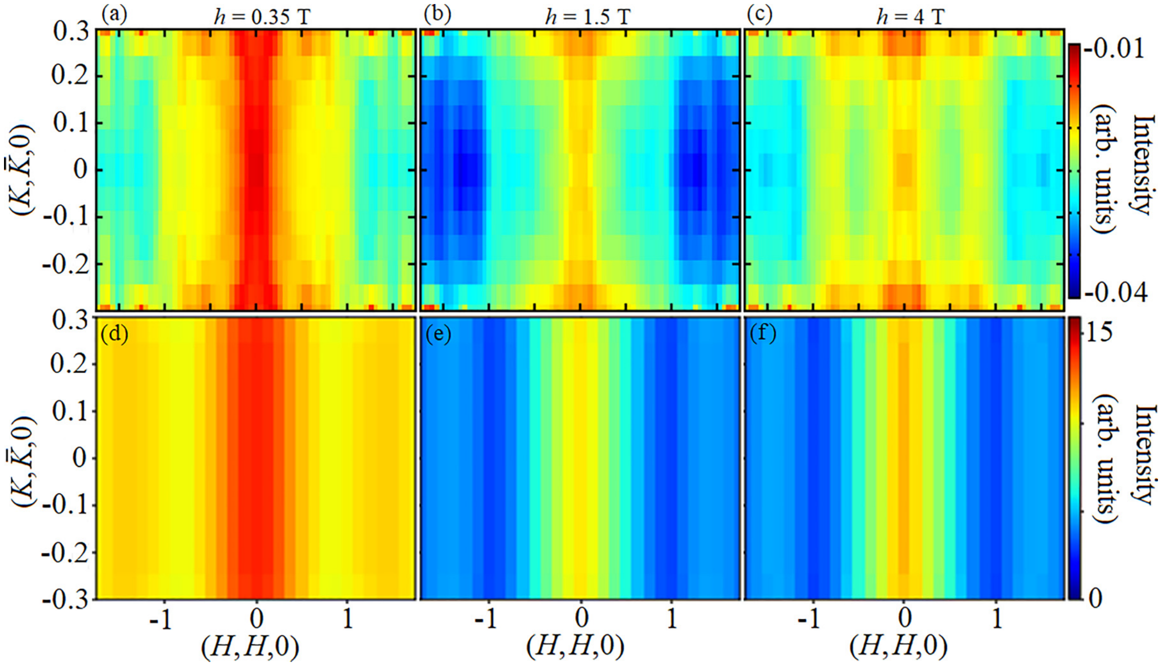

FIG. 5. The symmetrized quasielastic neutron scattering signal measured in our time-of flight neutron scattering experiment at $T = 0.03$ K in the $(H + K, H - K, 1.5)$ plane of reciprocal space for field strengths of $h = 0.35$ T (a), $h = 1.5$ T (b), and $h = 4$ T (c), with the $(0, 0, L)$ integration range from $L = 1.25$ to 1.75 and an energy-transfer integration over the range –0.2 meV $\leqslant E \leqslant$ 0.2 meV. In each case, a data set measured at $h = 0$ T has been subtracted. We compare this with the corresponding diffuse neutron scattering signal in the $(H + K, H - K, 1.5)$ scattering plane with $(0, 0, L)$ integration range from $L = 1.25$ to 1.75, predicted via our semiclassical molecular dynamics calculations using the experimental estimates of the nearest-neighbor-exchange parameters obtained from this paper, $(J_{\tilde{x}}, J_{\tilde{y}}, J_{\tilde{z}}) = (0.063, 0.062, 0.011)$ meV, $g_z = 2.24$, and $\theta = 0$. The calculated signal is shown for $T = 0.03$ K and a $[1, \bar{1}, 0]$ magnetic field of strength $h = 0.35$ T (d), $h = 1.5$ T (e), and $h = 4$ T (f).

calculations based on Monte Carlo simulations. We show the calculations using the experimental estimates of the nearest-neighbor-exchange parameters obtained from this paper, $(J_{\tilde{x}}, J_{\tilde{y}}, J_{\tilde{z}}) = (0.063, 0.062, 0.011)$ meV, $g_z = 2.24$, and $\theta = 0$, for a $[1, \bar{1}, 0]$ magnetic field strength of $h = 0.35$ T, $h = 1.5$ T, $h = 4$ T in Figs. 5(d)–5(f), respectively. Figure 5 shows that these calculations, using the estimated exchange parameters from this paper, capture the planar nature of the measured diffuse scattering signal associated with the one-dimensional nature of the β-chain correlations, and provide a reasonable description for the field dependence of the intensity of this planar scattering.

We do not expect our semiclassical molecular dynamics calculations to capture *all* of the features of the quasielastic diffuse scattering measured from $Ce_2Zr_2O_7$, due in part to weak further-than-nearest neighbor interactions not included in Eqs. (1) and (2), which were shown to be relevant in describing finer features of the zero-field diffuse scattering signal measured from $Ce_2Zr_2O_7$ [25,26], and also due in part to the semiclassical nature of the calculations. Nonetheless, the main, most-dominant features of the measured diffuse scattering are accurately described by these calculations for both zero and nonzero magnetic field as shown in Figs. 4, 5, and Appendix D. Furthermore, since our conclusions based on comparisons with these calculations are drawn from comparing the main features in the diffuse scattering data and calculations, we expect these conclusions, including the estimation of $\theta \sim 0$, to be robust to any finer features missed by the calculations.

We further examine the quasielastic diffuse scattering signal detected in our time-of-flight neutron scattering experiment using cuts along the $(H, H, 0)$ direction of reciprocal space, perpendicular to the rod-like signal detected in the (H, H, L) plane. Figure 6(c) shows the measured diffuse scattering intensity along the $(H, H, 0)$ direction of reciprocal space, for a $(0, 0, L)$ integration range from $L = 1.25$ to 1.75 [illustrated in Fig. 6(a)] and a $(K, \bar{K}, 0)$ integration from $K =$ –0.1 to 0.1 [illustrated in Fig. 6(b)], for field strengths of $h = 0.35$ T (blue), $h = 1.5$ T (orange), and $h = 4$ T (green). Figures 5 and 6(c) show that the intensity of the rod-like feature along $(0, 0, L)$ is more intense in comparison to the scattering elsewhere at $h = 0.35$ T and $h = 1.5$ T than it is at $h = 4$ T. We shall revisit this point shortly.

We fit the $(H, H, 0)$ width of the diffuse scattering around $H = 0$ to a Lorentzian form for the purpose of estimating the correlation length along the β chains, ξ. This fitting assumed a constant background and is shown by the solid-line fits in Fig. 6(c). The reorientation of diffuse scattering at 4 T results in two symmetrically equivalent peaks, which are not present in the cuts along $(H, H, 0)$ direction at 0.35 T and 1.5 T, which we discuss in further detail in the following paragraph. We fit these additional peaks at 4 T to two Gaussian forms, which captured the trend of this measured $H \neq 0$ scattering better than Lorentzian lineshapes. The focus of this analysis is the width of the central peak around $H = 0$, which was fit for each field strength using a resolution-convoluted Lorentzian function (see Appendix E), resulting in a relatively short, ferromagnetic, correlation length of $\xi = 15(2)$ Å for

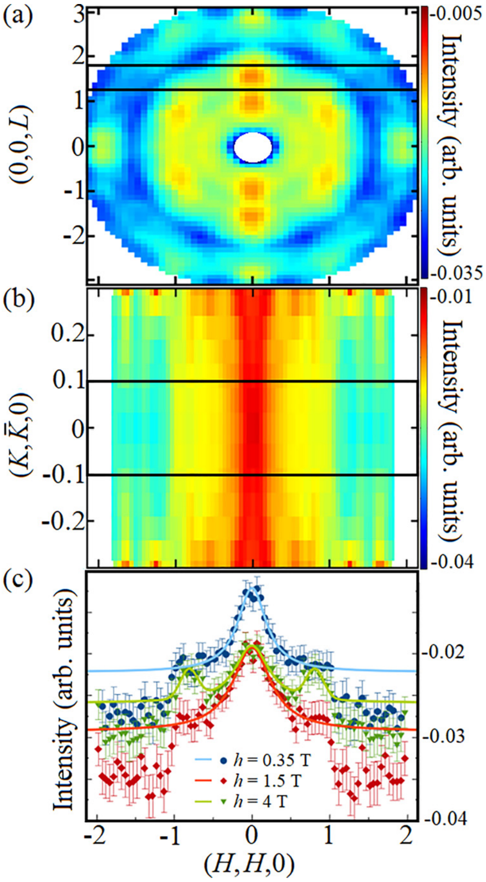

FIG. 6. The symmetrized quasielastic neutron scattering signal measured at $T = 0.03$ K from a single crystal sample of $Ce_2Zr_2O_7$ aligned in the (H, H, L) scattering plane in a $[1, \bar{1}, 0]$ magnetic field. (a) The quasielastic neutron scattering signal in the (H, H, L) plane for a field strength of $h = 0.35$ T, with a $(K, \bar{K}, 0)$ integration from $K = -0.3$ to 0.3, also shown in Fig. 4(a). The black line illustrates the $(0, 0, L)$ integration range from $L = 1.25$ to 1.75. (b) The quasielastic neutron scattering signal in the $(H + K, H - K, 1.5)$ plane of reciprocal space for a field strength $h = 0.35$ T, with $(0, 0, L)$ integration range from $L = 1.25$ to 1.75 [illustrated in (a)]. (c) The quasielastic neutron scattering intensity along the $(H, H, 0)$ direction of reciprocal space, for a $(0, 0, L)$ integration range from $L = 1.25$ to 1.75 [illustrated in (a)], and a $(K, \bar{K}, 0)$ integration from $K = -0.1$ to 0.1 [illustrated in (b)], for field strengths of $h = 0.35$ T (blue), $h = 1.5$ T (orange), and $h = 4$ T (green). The lines in (c) show fits to the intensity that were used to extract the correlation length $\xi = 15(2)$ Å associated with the ferromagnetic intrachain coupling for the z components of the pseudospins within β chains (see main text). In each case, a data set measured at $h = 0$ T has been subtracted and integration over the energy-transfer range -0.2 meV $\leqslant E \leqslant$ 0.2 meV was employed.

the β chains, which varies little as a function of field over the measured field strengths of 0.35 T, 1.5 T, and 4 T. As previously mentioned, this correlation length corresponds to only the correlations for the z components of the pseudospins within the β chains, S^z, due to the fact that x and y components of pseudospin each carry octupolar magnetic moments.

Returning to the magnetic field dependence of the diffuse scattering shown in Figs. 4(a)–4(c), 5(a)–5(c), and 6(c), it is clear the measured diffuse scattering is similar at $h = 0.35$ T and 1.5 T and different at $h = 4$ T, with relatively more diffuse scattering near $H = \pm 1$ and relatively less near $H = 0$ for $h = 4$ T compared to 0.35 T and 1.5 T. This is most apparent in Figs. 5(a)–5(c), and 6(c), which show that the planes of scattering normal to the β chains redistribute to some extent for $[1, \bar{1}, 0]$ magnetic field between $h = 1.5$ T and 4 T, such that stronger planes of scattering develop containing $H = -1$ and $H = 1$ [see Fig. 5(c)], with a relatively weaker plane of scattering at $H = 0$ in comparison to the scattering elsewhere in reciprocal space. This redistribution of the spectral weight between between $h = 1.5$ T and 4 T is not shown by our semiclassical molecular dynamics calculations in Figs. 5(d)–5(f).

C. Magnetic Bragg peaks from $Q = 0$ structure in a [0, 0, 1] magnetic field

The anticipated magnetic structure of a spin ice in a moderate [0, 0, 1] magnetic field is illustrated in Fig. 1(b). Here the system takes on a $Q = 0$ structure (the magnetic structure associated with each tetrahedron is the same) with the 2-in-2-out ice rules satisfied on each tetrahedron and with all magnetic moments canted along the [0, 0, 1] field direction [36,38,53]. This expected $Q = 0$ structure is a polarized spin ice state.

Figure 7 shows the elastic neutron scattering signal in the $(H, K, 0)$ plane of reciprocal space measured in our time-of-flight neutron scattering experiment on CNCS, with a [0, 0, 1] magnetic field applied perpendicular to this plane. Comparison of Fig. 7(a) with Fig. 7(b) shows that there is no discernible change in Bragg peak intensity or appearance of new Bragg peaks in zero field between $T = 10$ K and $T = 0.09$ K in this plane of reciprocal space, again consistent with the lack of zero-field magnetic order reported for $Ce_2Zr_2O_7$ [13,14,25].

As can be seen from Fig. 7, there are only two $Q = 0$ Bragg positions (all even or all odd h, k, l indices) in the field of view of this elastic scattering measurement in the $(H, K, 0)$ plane. These are $(2, 0, 0)$ and equivalent positions, as well as $(2, 2, 0)$ and equivalent positions. Comparison of the $T = 0.09$ K data in Figs. 7(b)–7(e) clearly shows that magnetic Bragg peaks appear at the $\mathbf{Q} = (\pm 2, 0, 0)$ and $(0, \pm 2, 0)$ positions in low-magnetic fields and grow in intensity with field strength. This is obvious as there is no Bragg intensity at $(2, 0, 0)$ and equivalent wavevectors in zero magnetic field, as also observed within the (H, H, L) scattering plane in Fig. 3. This is not the case at $(2, 2, 0)$ and equivalent wavevectors, so differences between data sets in [0, 0, 1] magnetic field and in zero field must be examined for $(2, 2, 0)$.

Figure 7 shows exactly these differences in the form of line scans through the $(0, 2, 0)$ Bragg position [Fig. 7(f)] and through the $(2, 2, 0)$ Bragg position [Fig. 7(g)] at $T = 0.09$ K. As can be seen, only the elastic scattering at the $(0, 2, 0)$ Bragg position shows any [0, 0, 1] magnetic field dependence. The magnetic field dependence of Bragg intensity at $(0, 2, 0)$ in this polarized spin ice state is shown in Fig. 7(h), which shows saturation of the $(0, 2, 0)$ magnetic Bragg peak beyond ~3 T. We compare this to the field dependence of the integrated intensity for the $(0, 2, 0)$ magnetic Bragg peak calculated for $T = 0.09$ K using semiclassical molecular dynamics calculations based on Monte Carlo simulations using the experimental estimates of the nearest-neighbor-

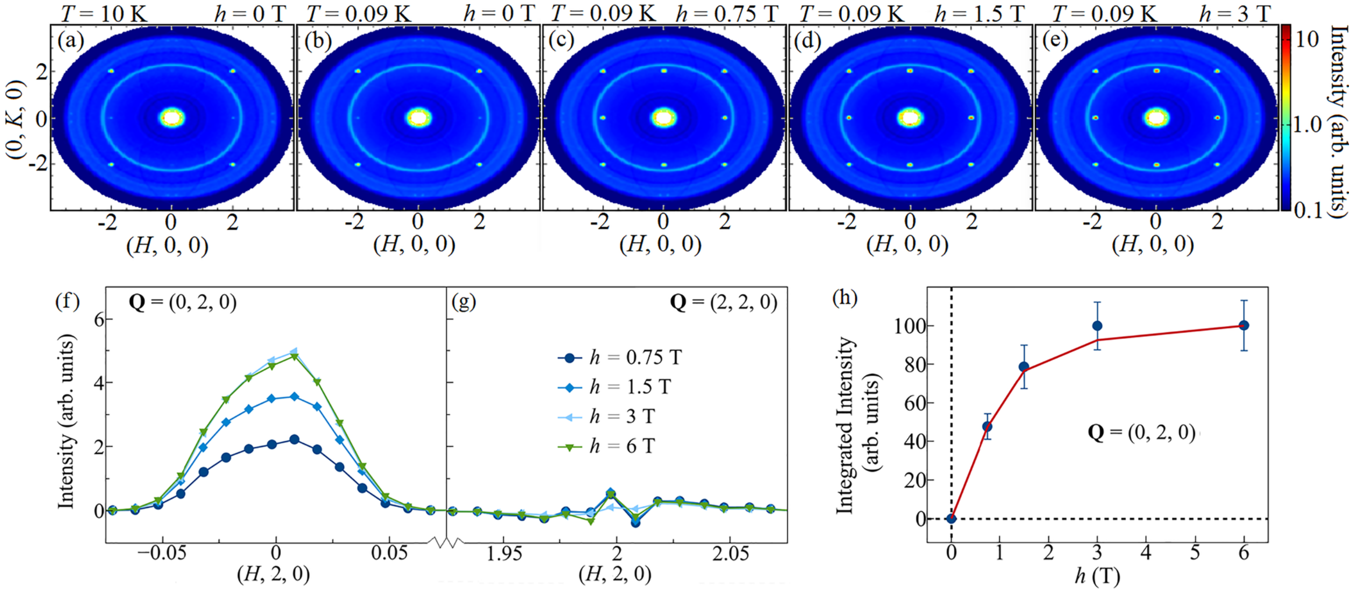

FIG. 7. The symmetrized elastic neutron scattering signal measured in the $(H, K, 0)$ plane of reciprocal space with integration in the out-of-plane direction, $(0, 0, L)$, from $L = –0.1$ to 0.1, and over the energy-transfer range –0.2 meV $\leqslant E \leqslant$ 0.2 meV. (a) and (b) show the elastic neutron scattering signals measured in zero magnetic field at $T = 10$ K and $T = 0.09$ K, respectively. (c), (d), and (e) show the elastic neutron scattering signals measured in a [0, 0, 1] magnetic field at $T = 0.09$ K for field strengths of $h = 0.75$ T, $h = 1.5$ T, and $h = 3$ T, respectively. The intensity here is shown on a logarithmic scale. (f) and (g) show the field strength dependence of the magnetic intensity at $T = 0.09$ K for the $\mathbf{Q} = (0, 2, 0)$ and $\mathbf{Q} = (2, 2, 0)$ reciprocal space positions, respectively. Specifically, the data in dark blue (blue, light blue, green) shows the intensity measured at $h = 0.75$ T ($h = 1.5$ T, $h = 3$ T, $h = 6$ T). In each case, a data set measured at $T = 0.09$ K and $h = 0$ T has been subtracted and integration over $(0, K, 0)$ and $(0, 0, L)$ from $K = 1.9$ to 2.1 and $L = –0.1$ to 0.1 was employed, along with integration over the energy-transfer range –0.2 meV $\leqslant E \leqslant$ 0.2 meV. (h) The integrated intensity of the $\mathbf{Q} = (0, 2, 0)$ magnetic Bragg peak at $T = 0.09$ K as a function of magnetic field strength. The line in (h) shows the calculated integrated intensity at $T = 0.09$ K using the experimental estimates of the nearest-neighbor exchange parameters obtained from this paper, $(J_{\tilde{x}}, J_{\tilde{y}}, J_{\tilde{z}}) = (0.063, 0.062, 0.011)$ meV, $g_z = 2.24$, and $\theta = 0$, according to semiclassical molecular dynamics calculations based on Monte Carlo simulations. For both the data and calculation in (h), the arbitrary units are such that the average intensity is equal to 100 in the saturated regime at low temperature and high field.

exchange parameters obtained from this paper, $(J_{\tilde{x}}, J_{\tilde{y}}, J_{\tilde{z}}) = (0.063, 0.062, 0.011)$ meV, $g_z = 2.24$, and $\theta = 0$. This comparison shows that field dependence of the Bragg intensity in a [0, 0, 1] magnetic field is well accounted for by the semiclassical calculations used throughout this paper, in contrast to the field dependence of the Bragg intensity in a $[1, \bar{1}, 0]$ magnetic field. This suggests that quantum fluctuations are more prevalent in the $[1, \bar{1}, 0]$-polarized α chains compared to the three-dimensional [0, 0, 1]-polarized spin ice phase, as is expected theoretically.

A simple magnetic structure factor calculation for the [0, 0, 1]-polarized spin ice structure is consistent with these results: Magnetic Bragg intensity at (2, 0, 0) and equivalent positions, but not at (2, 2, 0). In fact, the only magnetic structures that are consistent with both the local Ising anisotropy and the measured magnetic Bragg peaks are the $[0, 0, \pm1]$-polarized spin ice structures. Examination of the $h = 0$ T subtracted data yields no convincing signs of diffuse scattering, consistent with expectations for this long-ranged ordered phase. We therefore conclude that $Ce_2Zr_2O_7$ in both [0, 0, 1] and $[1, \bar{1}, 0]$ magnetic fields responds as expected for a material that has a spin ice ground state in zero field.

The [0, 0, 1]-field-induced onset of the magnetic Bragg peak at $\mathbf{Q} = (0, 2, 0)$ is consistent with the data reported in Ref. [57]. However, this previous study [57] claims to detect a [0, 0, 1]-field-induced magnetic Bragg peak at the $\mathbf{Q} = (2, 2, 0)$ position that we do not observe here. Only a single nonzero field value was measured in the previous study and the net intensity surrounding the $\mathbf{Q} = (2, 2, 0)$ position is both positive and negative in the temperature subtraction of the previously reported data. This suggests that the reported increase in intensity may simply be due to an imperfect subtraction of nuclear Bragg peaks at the $\mathbf{Q} = (2, 2, 0)$ position, rather than a field-dependent magnetic Bragg peak.

VI. RESULTS: INELASTIC NEUTRON SCATTERING

In this section, we present our inelastic time-of-flight neutron scattering measurements on single crystal $Ce_2Zr_2O_7$ in magnetic fields oriented along $[1, \bar{1}, 0]$ and [0, 0, 1] directions. For both field directions, a roughly dispersionless narrow band of inelastic scattering is observed, which increases in energy and separates from a quasielastic component with increasing magnetic field strength, in agreement with appropriate theoretical predictions. We compare the field-dependent inelastic scattering to that predicted using semiclassical molecular dynamics calculations based on Monte Carlo simulations. The Monte Carlo simulations apply the experimental estimates of the nearest-neighbor exchange parameters obtained from this paper, $(J_{\tilde{x}}, J_{\tilde{y}}, J_{\tilde{z}}) =$

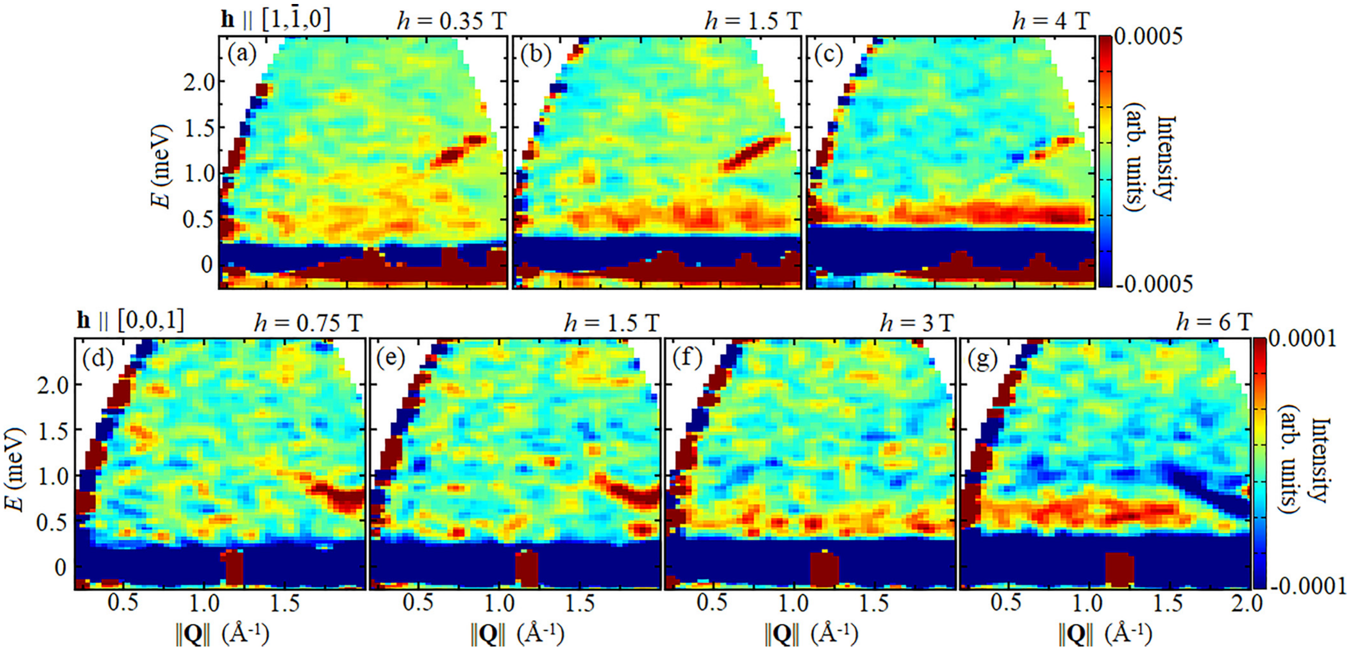

FIG. 8. The magnetic field dependence of the powder-averaged neutron scattering spectra measured at $T = 0.03$ K from our single crystal sample of $Ce_2Zr_2O_7$ aligned in the (H, H, L) scattering plane in a $[1, \bar{1}, 0]$ magnetic field of strength $h = 0.35$ T (a), $h = 1.5$ T (b), and $h = 4$ T (c). We also show the magnetic field dependence of the powder-averaged neutron scattering spectra measured at $T = 0.09$ K from our single crystal sample of $Ce_2Zr_2O_7$ aligned in the $(H, K, 0)$ scattering plane in a $[0, 0, 1]$ magnetic field of strength $h = 0.75$ T (d), $h = 1.5$ T (e), $h = 3$ T (f), and $h = 6$ T (g). In each case, a data set measured at $h = 0$ T has been subtracted.

$(0.063, 0.062, 0.011)$ meV and $g_z = 2.24$, with $\theta \sim 0$, which are consistent with a quantum spin ice ground state in zero field, with a partially-polarized spin ice ground state [Fig. 1(a)] in $[1, \bar{1}, 0]$ magnetic fields, and with a $[0, 0, 1]$-polarized spin ice ground state [Fig. 1(b)] in $[0, 0, 1]$ magnetic fields.

Figures 8(a)–8(c) show the inelastic neutron scattering measured at $T = 0.03$ K from a single crystal sample of $Ce_2Zr_2O_7$ aligned in the (H, H, L) scattering plane in a magnetic field along the $[1, \bar{1}, 0]$ direction for field strengths of $h = 0.35$ T (a), $h = 1.5$ T (b), and $h = 4$ T (c), with a zero-field data set taken at $T = 0.03$ K subtracted in each case. Similarly, Figs. 8(d)–8(g) show the inelastic neutron scattering measured at $T = 0.09$ K from a single crystal sample of $Ce_2Zr_2O_7$ aligned in the $(H, K, 0)$ scattering plane in a magnetic field along the $[0, 0, 1]$ direction for field strengths of $h = 0.75$ T (d), $h = 1.5$ T (e), $h = 3$ T (f), and $h = 6$ T (g), with a zero-field data set taken at $T = 0.09$ K subtracted in each case. In each case, the data has been powder averaged within the scattering plane so as to use all the available scattering as a function of $\|\mathbf{Q}\|$. This was done as the resulting powder-averaged signal from these experiments is similar to measured signal plotted as a function of $\mathbf{Q}$ (see Appendix F), including the lack of any obvious dispersion, but with better statistics. The isolated signal centered on $\|\mathbf{Q}\| = 1.75$ Å^{-1} and slightly above (below) $E = 1$ meV in the net scattering measured for $[1, \bar{1}, 0]$ ($[0, 0, 1]$) field is due to an imperfect subtraction of scattering from the magnet cryostat (superfluid helium) and is not part of the measured signal from the sample.

Figure 8 shows net negative quasielastic scattering is observed at all finite fields in the zero-field-subtracted data, and a narrow band of inelastic scattering with energy of $E \sim 0.5$ meV onsets with increasing field strength and becomes clear at and above $h = 1.5$ T ($h = 3$ T) for a magnetic field in the $[1, \bar{1}, 0]$ ($[0, 0, 1]$) direction. The lack of significant dispersion, and specifically sharp spin waves, in our measurements is consistent with expectations for a small value of θ (see Appendix D).

Figure 9 shows the $\mathbf{Q}$ dependence of the calculated inelastic neutron scattering signal according to our semiclassical molecular dynamics calculations, at $T = 0.03$ K for $\mathbf{Q}$ along different high-symmetry directions in the (H, H, L) scattering plane: $(H, H, 0)$, $(0, 0, L)$, and (H, H, H). Specifically, we show the calculated signal for a $[1, \bar{1}, 0]$ magnetic field of strength $h = 0$ T, $h = 0.35$ T, $h = 1.5$ T, and $h = 4$ T. The calculation is shown for both logarithmic intensity scale [Figs. 9(a)–9(d)], and for linear intensity scales [Figs. 9(e)–9(h)] with the $h = 0$ T calculation subtracted from the in-field calculations [Figs. 9(f)–9(h)]. The calculated spectra are convoluted with a Gaussian lineshape with energy resolution of $\Delta E = 0.25$ meV for best agreement with the measured data from $Ce_2Zr_2O_7$. This resolution is larger than the instrumental resolution of ~0.1 meV, consistent with the fact that viewing the weak signal in the measured data from $Ce_2Zr_2O_7$ requires a smoothing of the data that artificially expands the energy resolution.

As shown in Fig. 9, the quasielastic scattering associated with spinons in the zero-field quantum spin ice ground state is separated by the $[1, \bar{1}, 0]$ magnetic field into three distinct scattering signals: (1) the Bragg scattering due to the long-ranged magnetic order of the polarized α chains, (2) a quasielastic signal centered on $E \sim 0.1$ meV associated with β-chain elastic diffuse scattering, the β-chain spinon

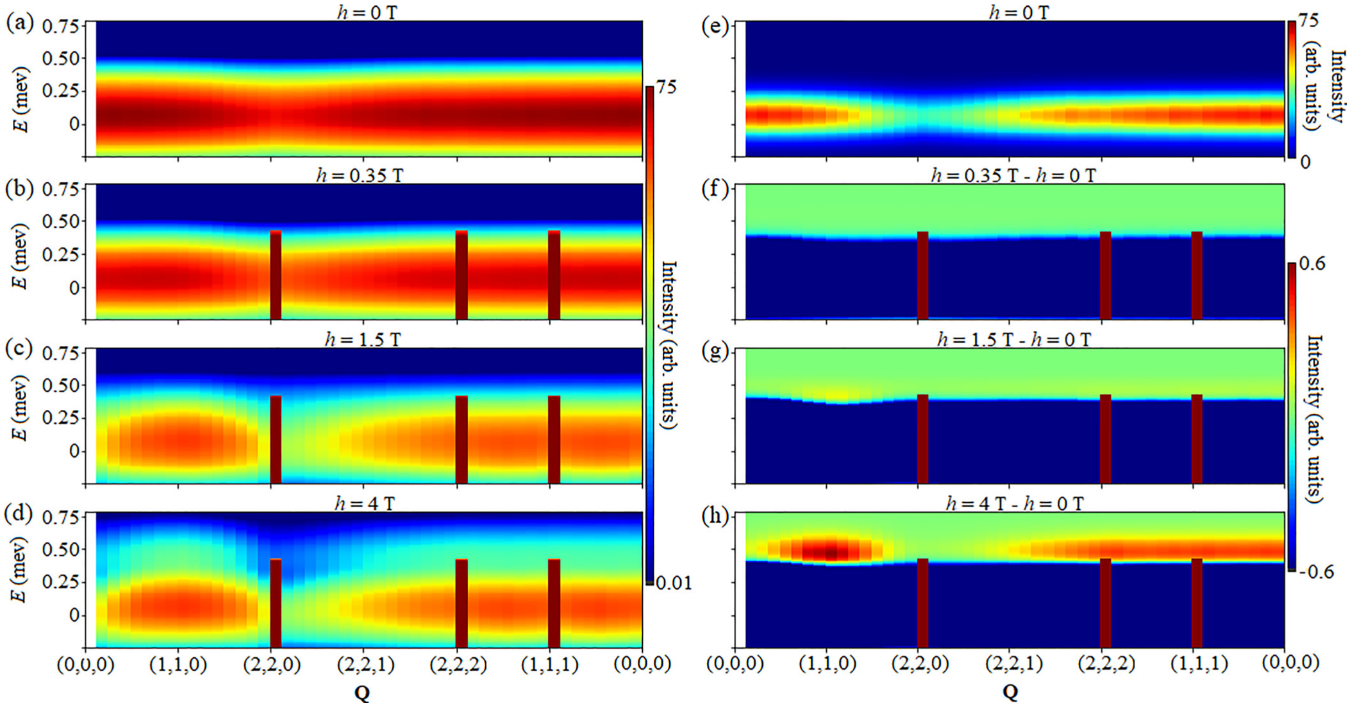

FIG. 9. The calculated inelastic neutron scattering signal, via semiclassical molecular dynamics calculations (see main text) at $T = 0.03$ K using the experimental estimates of the nearest-neighbor-exchange parameters obtained from this paper, $(J_{\tilde{x}}, J_{\tilde{y}}, J_{\tilde{z}}) = (0.063, 0.062, 0.011)$ meV, $g_z = 2.24$, and $\theta = 0$, is shown for a $[1, \bar{1}, 0]$ magnetic field of strength $h = 0$ T [(a),(e)], $h = 0.35$ T [(b),(f)], $h = 1.5$ T [(c),(g)], and $h = 4$ T [(d),(h)] on both logarithmic [(a)–(d)] and linear [(e)–(h)] scales. The $h = 0$ T calculation has been subtracted from the in-field calculation for plots [(f)–(h)].

continuum, and thermally excited magnons, whose signals are merged-together for energy resolutions above ∼0.05 meV, and (3) a signal whose energy center increases with field strength such that the signal is lifted from the quasielastic scattering with increasing field, associated with the two-magnon continuum of the polarized α chains.

Similarly, Fig. 10 shows the **Q** dependence of the calculated inelastic neutron scattering signal according to our semiclassical molecular dynamics calculations, at $T = 0.09$ K for **Q** along different high-symmetry directions in the $(H, K, 0)$ scattering plane: $(H, 0, 0)$, $(0, K, 0)$, and $(H, H, 0)$. Specifically, we show the calculations for a $[0, 0, 1]$ magnetic field of strengths $h = 0$ T, $h = 0.75$ T, $h = 1.5$ T, $h = 3$ T, and $h = 6$ T, and using both a logarithmic intensity scale [Figs. 10(a)–10(e)], and a linear intensity scales [Figs. 10(f)–10(j)] with the $h = 0$ T data subtracted from the in-field data [Figs. 10(g)–10(j)]. The calculated spectra are convoluted with a Gaussian lineshape with energy resolution of $\Delta E = 0.25$ meV for best agreement with the measured data from $Ce_2Zr_2O_7$. The magnetic field along the $[0, 0, 1]$ direction separates the zero-field scattering into Bragg scattering, a field-dependent two-magnon continuum, and low-lying excitations, which consist only of thermally-excited magnons for the $[0, 0, 1]$ field direction. As with the $[1, \bar{1}, 0]$ field direction, sharp single-magnon modes are only expected to be visible in the neutron scattering signal for nonzero θ. However, it is worth mentioning that single-magnon modes, resulting from weak scattering of neutrons off the octupolar moments, are indeed present for $\theta = 0$ but it would require a significantly higher signal-to-noise ratio than achieved here in order to detect these low-intensity octupolar spin waves (see Appendix D).

As shown in Figs. 9(a)–9(d) [10(a)–10(e)], our semiclassical molecular dynamics calculations, using the exchange parameters estimated in this work, predict that a $[1, \bar{1}, 0]$ ($[0, 0, 1]$) magnetic field induces the observed decrease in the quasielastic scattering, concomitant with the appearance of magnetic Bragg scattering centered on $E = 0$ meV, and the appearance of an inelastic signal near $E \sim 0.5$ meV that emerges from the quasielastic scattering at $h = 1.5$ T ($h = 3$ T). Figures 9(f)–9(h) [10(g)–10(j)] show the same semiclassical molecular dynamics calculations with the zero-field calculation subtracted in each case, for better comparison with the zero-field-subtracted data shown in Figs. 8(a)–8(c) [8(d)–8(g)].

Comparison of our calculations in Figs. 9(f)–9(h) [10(g)–10(j)] with our measured neutron scattering data in Figs. 8(a)–8(c) [8(d)–8(g)] shows that our semiclassical molecular dynamics calculations using the exchange parameters estimated in this paper indeed predict the net-negative quasielastic scattering in the zero-field-subtracted signal, as well as the field-induced emergence of an approximately-dispersionless signal at energies above this net-negative quasielastic scattering. The magnetic Bragg peaks shown in Fig. 9 (Fig. 10) are those associated with the polarized α chains (the $[0, 0, 1]$-polarized spin ice structure) expected for a $[1, \bar{1}, 0]$ ($[0, 0, 1]$) magnetic field, and are consistent with the collection of magnetic Bragg peaks detected in our neutron scattering experiment in a $[1, \bar{1}, 0]$ ($[0, 0, 1]$) magnetic field.

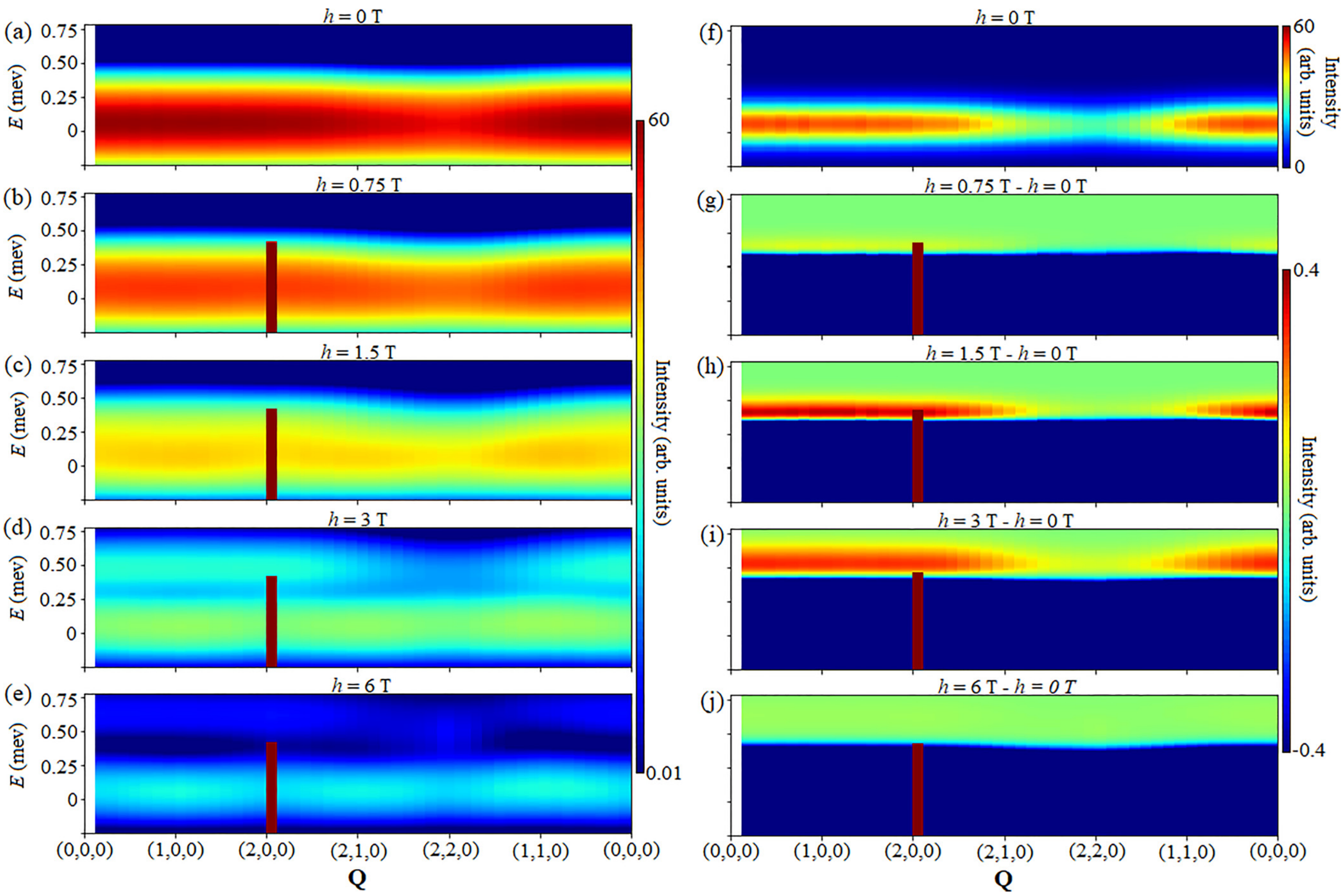

FIG. 10. The calculated inelastic neutron scattering signal, via semiclassical molecular dynamics calculations (see main text) at $T = 0.09$ K using the experimental estimates of the nearest-neighbor-exchange parameters obtained in this paper, $(J_{\tilde{x}}, J_{\tilde{y}}, J_{\tilde{z}}) = (0.063, 0.062, 0.011)$ meV, $g_z = 2.24$, and $\theta = 0$, is shown for a [0, 0, 1] magnetic field of strength $h = 0$ T [(a),(f)], $h = 0.75$ T [(b),(g)], $h = 1.5$ T [(c),(h)], $h = 3$ T [(d),(i)], and $h = 6$ T [(e),(j)] on both logarithmic [(a)–(e)] and linear [(f)–(j)] intensity scales. The $h = 0$ T calculation has been subtracted from the in-field calculation for plots [(g)–(j)].

While our semiclassical molecular dynamics calculations capture the main features in our measured data, there are features in the comparison between theory and experiment which could be improved. For example, the calculated signals near $E \sim 0.5$ meV in Figs. 9 and 10 show a small amount of dispersion that we were unable to convincingly detect in our measured inelastic data. This may be because of the data averaging and smoothing required to view the weak-magnetic signals associated with the small magnetic moment in $Ce_2Zr_2O_7$. This dispersion is also shown in our calculations convoluted with a higher energy-resolution in Appendix D. Also, the field dependence of the measured signal near $E \sim 0.5$ meV in a [0, 0, 1] magnetic field [Figs. 8(d)–8(g)] is not well described by the calculations in [Figs. 10(g)–10(j)], specifically at $h = 6$ T, where the measured signal is most intense, having grown in intensity with increasing field strength. In contrast to this, the calculation for $h = 6$ T shows relatively small intensity at $E \sim 0.5$ meV. This inconsistency between the calculations of the inelastic scattering and the corresponding neutron measurements at $h = 6$ T is currently unexplained, and may point towards additional terms in the Hamiltonian beyond those contained in the ideal nearest-neighbor models of Eqs. (1) and (2), which are relevant for pyrochlores with pure dipolar-octupolar CEF ground states. These discrepancies notwithstanding, we reiterate that our semiclassical molecular dynamics calculations capture the main features associated with each of the Bragg, quasielastic, and inelastic scattering signals presented here on $Ce_2Zr_2O_7$, and in and of itself this is a significant success.

VII. DISCUSSION

Our neutron scattering results on $Ce_2Zr_2O_7$ in magnetic fields oriented along $[1, \bar{1}, 0]$ and $[0, 0, 1]$ directions are consistent with the expectations for a material that has a disordered spin ice ground state in zero field.

We compare the field-induced structures in $Ce_2Zr_2O_7$ with those in the three pyrochlore magnets, $Ho_2Ti_2O_7$, $Dy_2Ti_2O_7$, and $Nd_2Zr_2O_7$, each having Ising anisotropy. The classical dipolar spin ices $Ho_2Ti_2O_7$ and $Dy_2Ti_2O_7$ display disordered spin ice states at low temperatures that can be modelled classically [35,47–52], and have intersite interactions which are dominated by long-ranged dipolar interactions. The dipolar interactions in these materials are responsible for most of the *near-neighbor* intersite interactions [51], due to the relatively large magnetic dipole moments at the Ho^{3+} and Dy^{3+} sites, $\sim 10\ \mu_B$ [65–68].

Their similarities to the behavior reported here for $Ce_2Zr_2O_7$ include both the evidence for the polarized α chains and decoupled β chains in a $[1, \bar{1}, 0]$ field, as well as the polarized spin ice state in a $[0, 0, 1]$ magnetic field [35–39]. However, there is an interesting difference, in that the intra-β-chain correlation length in a $[1, \bar{1}, 0]$ field at low temperatures is relatively short, $\xi = 15(2)$ Å in $Ce_2Zr_2O_7$ ($\sim$4 nearest-neighbor separations), much smaller than the corresponding $\xi \gtrsim 100$ Å correlation lengths measured in the classical spin ices $Ho_2Ti_2O_7$ and $Dy_2Ti_2O_7$ [36,37].

The case of $Nd_2Zr_2O_7$ is also an interesting comparator, as the CEF ground state for $J = 9/2$ Nd^{3+} in the pyrochlore environment is also a dipole-octupole doublet [43]. This system has also been well studied in single crystal form. Its ground-state magnetic structure is a noncollinear all-in, all-out structure [40,42–45], but it shows low-energy fluctuations appropriate to spin ice suggesting that these two states (all-in, all-out, and spin ice) are close in energy [16,41,46,69].

The response of $Nd_2Zr_2O_7$ to a $[1, \bar{1}, 0]$ magnetic field [40] is very similar to $Ce_2Zr_2O_7$ and to other spin ices [35–39], in that planes of scattering associated with approximately decoupled β chains are observed in diffuse neutron scattering measurements. Furthermore, the measured correlation length along the β-chain direction $(H, H, 0)$ in a $[1, \bar{1}, 0]$ magnetic field is $\xi \sim 10$ Å in $Nd_2Zr_2O_7$ [40], similar to what we report here for $Ce_2Zr_2O_7$, and much smaller than the $\xi \gtrsim 100$ Å correlation lengths measured in the classical spin ices $Ho_2Ti_2O_7$ and $Dy_2Ti_2O_7$ [36,37].

Reference [40] has noted that quantum fluctuations in $Nd_2Zr_2O_7$ are likely responsible for its relatively small ξ. In fact, the relatively short correlation lengths along the β chains in $[1, \bar{1}, 0]$ magnetic fields would seem to be a distinguishing feature between the quantum spin ice states proposed for $Ce_2Zr_2O_7$ and $Nd_2Zr_2O_7$ and the classical spin ice states established for $Ho_2Ti_2O_7$ and $Dy_2Ti_2O_7$. However, a subtlety arises when including $Ce_2Zr_2O_7$ in that comparison due to the fact the measured correlation lengths correspond to correlations between the z components of the pseudospins, which for $Ce_2Zr_2O_7$, have corresponding exchange constant ($J_{\tilde{z}}$ for $\theta = 0$) that is by far the weakest of the three exchange constants, $(J_{\tilde{x}}, J_{\tilde{y}}, J_{\tilde{z}}) = (0.063, 0.062, 0.011)$ meV. While the $S^{\tilde{z}}$-$S^{\tilde{z}}$ correlation function does depend on the each of these exchange parameters, the dominant dependence arises from $J_{\tilde{z}}$ [19]. With that in mind, and specifically because $J_{\tilde{z}}$ is much smaller than $J_{\tilde{x}}$ and $J_{\tilde{y}}$, it is likely that octupolar correlations between x components (y components) of pseudospin have significantly longer correlation length than the z-component correlations, which are probed by our neutron scattering. In fact, according to our estimated exchange parameters for $Ce_2Zr_2O_7$, at zero temperature the octupolar correlations in the β chains should dominate to form an octupolar ordered phase close to criticality (with $J_{\tilde{x}} \approx J_{\tilde{y}}$), at the expense of ordering of the magnetic dipole moments associated with the z components of pseudospin [34]. Therefore, the relatively small value of ξ in $Ce_2Zr_2O_7$ is not due just to quantum fluctuations, but also due to the fact that the corresponding neutron scattering measurements primarily probe the pseudospin component that has the weakest magnetic correlations.

In contrast to this, the value of $\theta \sim 1$ rad estimated for $Nd_2Zr_2O_7$ suggests that the dominant contribution to the neutron scattering comes from the correlations between $\tilde{x}$ components of pseudospin, which have a corresponding exchange parameter $J_{\tilde{x}}$ that is the largest by a significant amount in that case [16,70,71]. Similarly, the correlation lengths measured in $Ho_2Ti_2O_7$ and $Dy_2Ti_2O_7$ include significant contribution from the most-dominant magnetic interaction, which is the long-ranged dipolar interaction in that case [51].

For $Ho_2Ti_2O_7$ and $Dy_2Ti_2O_7$ in a $[1, \bar{1}, 0]$ magnetic field, the short-ranged antiferromagnetic correlations between β chains lead to peaks in the diffuse scattering in the (H, H, L) plane, centered on $(0, 0, 1)$ and $(0, 0, 3)$ with broadened widths along the $(0, 0, L)$ direction of the underlying rod of scattering and corresponding interchain correlation lengths of $\xi_\perp \gtrsim 10$ Å [36,37]. These diffuse scattering peaks at $(0, 0, 1)$ and $(0, 0, 3)$ were not observed in our time-of-flight neutron scattering experiment on $Ce_2Zr_2O_7$ in a $[1, \bar{1}, 0]$ magnetic field, as is discussed in Sec. V B and shown in Figs. 4(a)–4(c). Similarly, $Nd_2Zr_2O_7$ in a $[1, \bar{1}, 0]$ magnetic field [40] shows no obvious signs for these peaks in the diffuse scattering at $(0, 0, 1)$ and $(0, 0, 3)$.

Both $Ce_2Zr_2O_7$ and $Nd_2Zr_2O_7$ [40] in a $[1, \bar{1}, 0]$ magnetic field show no clear interchain correlations between their β chains ($\xi_\perp \approx 0$) while both $Ho_2Ti_2O_7$ and $Dy_2Ti_2O_7$ in a $[1, \bar{1}, 0]$ magnetic field exhibit significant short-ranged antiferromagnetic interchain correlations in their β chains, with $\xi_\perp \gtrsim 10$ Å [36,37]. These interchain correlations are thought to arise via long-ranged dipole-dipole interactions [33], which scale with the square of the magnetic moment. The long-ranged dipole interaction is significantly reduced in both $Ce_2Zr_2O_7$ and $Nd_2Zr_2O_7$ compared to $Ho_2Ti_2O_7$ and $Dy_2Ti_2O_7$, as the dipole moments within the CEF ground-states doublets in $Ce_2Zr_2O_7$ ($\sim$1.29 μ_B [13,14]) and $Nd_2Zr_2O_7$ ($\sim$2.65 μ_B [43]) are much smaller than those in $Ho_2Ti_2O_7$ ($\sim$9.85 μ_B [65–67]) and $Dy_2Ti_2O_7$ ($\sim$9.77 μ_B [66,68]).

VIII. SUMMARY

Our heat capacity measurements on single crystal $Ce_2Zr_2O_7$ show that a $[1, \bar{1}, 0]$ magnetic field splits the broad hump in the zero-field heat capacity into two humps that are visible as separate features at $h = 2$ T, with one feature remaining at $T \sim 0.15$ K near the lowest measured temperatures, and the other clearly increasing in amplitude and temperature with increasing field strength, being centered on $T = 1.1$ K at $h = 2$ T. The separation of energy scales implied by the development of these separate features, corresponds to the separate energy scales for the polarized α chains and unpolarized β chains, which emerge in a $[1, \bar{1}, 0]$ field. Fitting the heat capacity measurements to NLC calculations yields results consistent with previous studies [25,26]. In particular, we affirm that the multipolar interactions are strong and frustrated. Of particular interest is the near equality of $J_{\tilde{x}}$ and $J_{\tilde{y}}$, which in turn implies that the β chains are close to a critical state.

We also report triple-axis and time-of-flight elastic neutron scattering measurements on single crystal $Ce_2Zr_2O_7$ at low temperatures in both $[1, \bar{1}, 0]$ and $[0, 0, 1]$ magnetic fields. The measurements in a $[1, \bar{1}, 0]$ magnetic field are consistent with the decoupling of the system into separate quantum spin chains. The field evolution of the Bragg peaks due to the polarized α chains is shown to be consistent with expectations for a 1D quantum system. The magnetic dipole moments in the β chains exhibit short-ranged ($\xi \sim 15$ Å) ferromagnetic intrachain correlations. These intrachain correlations are much shorter ranged than those in classical spin ices, which is a consequence of both quantum fluctuations and dominant multipolar interactions. Direct confirmation of the nearly-gapless excitations predicted for the β chains was not possible with our present experiment, but would be an interesting goal for future high resolution spectroscopic measurements. In a $[0, 0, 1]$ magnetic field, we observe a field-polarized spin ice ground state, with magnetization along the field direction.

Our elastic scattering results are largely consistent with those recently reported in Ref. [57] on a different $Ce_2Zr_2O_7$ single crystal. Gao *et al.* [57] reported $[1, \bar{1}, 0]$-field-induced Bragg peaks at the $(0, 0, 2)$ and equivalent positions, associated with the polarization of the α chains. In a $[0, 0, 1]$ magnetic field, they reported field-induced Bragg peaks at both the $(0, 0, 2)$ and $(2, 2, 0)$ positions. Our study, Fig. 7, shows that there is no field-induced Bragg scattering at $(2, 2, 0)$ and equivalent positions in a $[0, 0, 1]$ magnetic field, a result which is consistent with the expected polarized spin ice state illustrated in Fig. 1(b). We speculate that the relatively weak $(2, 2, 0)$ Bragg scattering reported recently [57] is due to the incomplete cancellation of two large nonmagnetic Bragg signals. Our inelastic scattering results show that both $[1, \bar{1}, 0]$ and $[0, 0, 1]$ magnetic fields result in a separation of the quasielastic scattering, such that a weak and nearly-dispersionless continuum of inelastic scattering emerges from the quasielastic signal with increasing field strength.

We compare our neutron scattering results to both semi-classical molecular dynamics calculations and one dimensional quantum calculations using the best-fitting exchange parameters inferred from the heat capacity. The calculated predictions are largely consistent with the measured elastic scattering, and the θ dependence of the predicted planar scattering from β chains in a $[1, \bar{1}, 0]$ magnetic field provides further evidence that the mixing of the dipolar and octupolar degrees of freedom through the parameter θ [see Eq. (2)], is weak, and importantly, that the correlations between octupolar magnetic moments strongly dominate over dipolar correlations. Furthermore, this means that if $J_{\tilde{x}}$ is the largest exchange parameter, the low-energy fluctuations will be dominantly octupolar, even though the ground state has the same symmetry properties, and can be smoothly deformed into, a dipolar quantum spin ice. The calculated inelastic signal shows field-induced separation of the quasielastic signal that is similar to that detected in the measured data. By modeling the structure factor beyond the dipole approximation we also show that multipolar spin waves in the high-field state can in principle be detected, even though the signal is too weak to detect with the present experiment.

Taken as a whole, the complete set of in-field data provides strong constraints on the theoretical description of $Ce_2Zr_2O_7$. The best description within the nearest-neighbor XYZ model [Eq. (2)] is found for parameters very close to those already proposed in [25]. Future theoretical studies should seek to close the remaining discrepancies between theory and experiment, such as the increase in inelastic scattering intensity at large applied fields and the shape of the low-temperature feature in the heat capacity in $[1, \bar{1}, 0]$ field.

ACKNOWLEDGMENTS

This work was supported by the Natural Sciences and Engineering Research Council of Canada (NSERC). We greatly appreciate the technical support from Alan Ye and Yegor Vekhov at the NIST Center for Neutron Research, from Saad Elorfi at Oak Ridge National Laboratory, and from Marek Kiela, Jim Garrett, and Casey Marjerrison at the Brockhouse Institute for Materials Research, McMaster University. O.B. and B.P. thank Mark Potts for useful discussions. We acknowledge the support of the National Institute of Standards and Technology, U.S. Department of Commerce, in providing neutron research facilities used in this work. A portion of this research used resources at the Spallation Neutron Source, a DOE Office of Science User Facility operated by the Oak Ridge National Laboratory. This work was partially supported by the Deutsche Forschungsgemeinschaft under grants SFB 1143 (Project Id 247310070) and the cluster of excellence ct.qmat (EXC 2147, Project Id 390858490). R.S. acknowledges the AFOSR Grant No. FA 9550-20-1-0235. D.R.Y. and K.A.R. acknowledge the use of the Analytical Resources Core at Colorado State University.

APPENDIX A: NUMERICAL LINKED CLUSTER CALCULATIONS OF THE HEAT CAPACITY

1. Further Details on Numerical Linked Cluster Calculations of the Heat Capacity

Here we discuss the numerical linked cluster (NLC) calculations for the magnetic contribution to the heat capacity, and the fitting analysis that was performed using the data measured from our single crystal sample of $Ce_2Zr_2O_7$ in a $[1, \bar{1}, 0]$ magnetic field. The basic details of the NLC method are outlined in the main text and in Refs. [25,30], and further details are provided in Refs. [59–63]. The methodology specific to the seventh-order calculations is described in Ref. [62].

Throughout this paper, we compare the magnetic heat capacity calculated using nth-order NLC calculations $C_{\rm mag}^{{\rm NLC},n}$ ($n = 4, 5, 6$) to the heat capacity measured from $Ce_2Zr_2O_7$, $C_{\rm P}^{\rm exp}$, using the goodness-of-fit measure,

$$\left\langle \frac{\delta^2}{\epsilon^2} \right\rangle = \sum_{T_{\rm exp}} \frac{\left[C_{\rm mag}^{{\rm NLC},n}(T_{\rm exp}) - C_{\rm P}^{\rm exp}(T_{\rm exp})\right]^2}{\epsilon_{{\rm NLC},n}(T_{\rm exp})^2 + \epsilon_{\rm exp}(T_{\rm exp})^2} , \tag{A1}$$

where $\epsilon_{\rm exp}(T_{\rm exp})$ is the experimental uncertainty on the measured heat capacity at temperature $T_{\rm exp}$, and $\epsilon_{{\rm NLC},n}(T_{\rm exp})$ is the uncertainty associated with the nth-order NLC calculations at temperature $T_{\rm exp}$,

$$\epsilon_{{\rm NLC},n}(T_{\rm exp}) = \max\nolimits_{T \geqslant T_{\rm exp}} \left| C_{\rm mag}^{{\rm NLC},n}(T) - C_{\rm mag}^{{\rm NLC},n-1}(T) \right| . \tag{A2}$$

We first used sixth-order NLC calculations, with Euler transformations to improve convergence (see Ref. [25], for example), in order to fit the zero-field heat capacity measured from $Ce_2Zr_2O_7$ and determine the best-fitting exchange parameters $J_{\tilde{x}}$, $J_{\tilde{y}}$, and $J_{\tilde{z}}$ up to permutation of the exchange parameters as discussed in Sec. III. Heat capacity curves

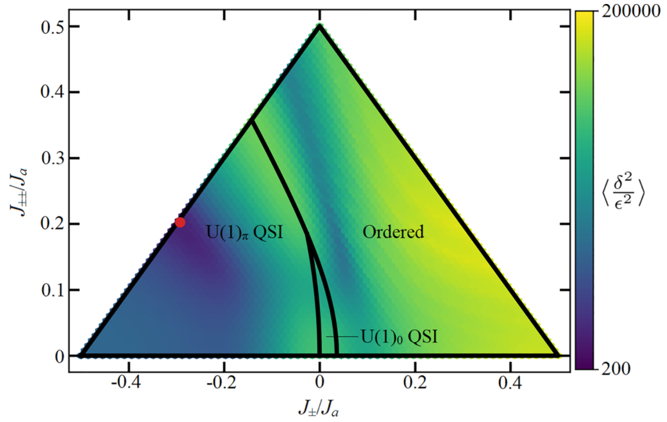

FIG. 11. The goodness-of-fit parameter $\langle \delta^2/\epsilon^2 \rangle$ for our sixth-order NLC fits to the measured C_{mag} of $Ce_2Zr_2O_7$ in zero magnetic field. Here the goodness-of-fit parameter is plotted over the available phase space as a function of the exchange parameters J_a, $J_\pm = -\frac{1}{4}(J_b + J_c)$, and $J_{\pm\pm} = \frac{1}{4}(J_b - J_c)$, where the axes $\{a, b, c\}$ are defined as the permutation of $\{\tilde{x}, \tilde{y}, \tilde{z}\}$ such that $|J_a| \geqslant |J_b|, |J_c|$ and $J_b \geqslant J_c$ (see Refs. [25,30] for further details). The best-fitting exchange parameters obtained in this fitting, $(J_a, J_b, J_c) = (0.063, 0.062, 0.011)$ meV are show as the red point. We also show the phase boundaries and corresponding phases in the ground-state phase diagram predicted at the nearest-neighbor level for dipolar-octupolar pyrochlores [17]. Each phase in this diagram can be dipolar or octupolar in nature and this depends on the permutation giving $(J_{\tilde{x}}, J_{\tilde{y}}, J_{\tilde{z}})$ from (J_a, J_b, J_c). The best-fitting exchange parameters and the entire surrounding region of good agreement (dark-colored) are within the region of the phase diagram corresponding to a U(1)$_\pi$ QSI ground state.

were calculated for values of $(J_{\tilde{x}}, J_{\tilde{y}}, J_{\tilde{z}})$ over the entire available parameter space, and we compare the NLC-calculated heat capacity for each parameter set to the heat capacity measured from $Ce_2Zr_2O_7$ using the goodness-of-fit measure $\langle \frac{\delta^2}{\epsilon^2} \rangle$ in Eq. (A1). The overall energy scale of the exchange parameters was fit to the high-temperature tail of the heat capacity so as to minimize $\langle \frac{\delta^2}{\epsilon^2} \rangle$ summed over the range from $T_{\mathrm{exp}} = 1.9$ K to 4 K (see Ref. [30], for example). The exchange parameters $J_{\tilde{x}}$, $J_{\tilde{y}}$, and $J_{\tilde{z}}$ are then determined up to permutation according to minimization of $\langle \frac{\delta^2}{\epsilon^2} \rangle$ summed over the range from $T_{\mathrm{exp}} = 0.3$ K to 1.9 K. For most parameter sets, and specifically those corresponding to a QSI ground state in the nearest-neighbor ground-state phase diagram [Fig. 2(b)], this restricts the fit to the regime where the NLC calculations converge. The results of this fitting procedure yield $(J_{\tilde{x}}, J_{\tilde{y}}, J_{\tilde{z}}) = (0.063, 0.062, 0.011)$ meV up to permutation. Figure 11 shows the goodness-of-fit measure $\langle \frac{\delta^2}{\epsilon^2} \rangle$ for our sixth-order NLC calculations compared to the measured heat capacity of $Ce_2Zr_2O_7$ in zero magnetic field for $T_{\mathrm{exp}} = 0.3$ K to 1.9 K, as well as the best-fitting exchange parameters that we obtain. We also overplot the ground-state phase diagram predicted for dipolar-octupolar pyrochlores at the nearest-neighbor level [17], showing the regions of phase space corresponding to U(1)$_0$ and U(1)$_\pi$ QSIs as well as a large region corresponding to all-in, all-out magnetic order, where each phase in the diagram of Fig. 11 can be dipolar or octupolar in nature as discussed in the caption of Fig. 11.

We then use NLC calculations to fit the in-field heat capacity for $(J_{\tilde{x}}, J_{\tilde{y}}, J_{\tilde{z}})$ equal to different permutations of $(0.063, 0.062, 0.011)$ meV, and for $\eta = g_z/2.57$ between 0.5 and 1.5. Figure 12 shows the η and θ dependencies of $\langle \frac{\delta^2}{\epsilon^2} \rangle$ for our fourth-order NLC calculations using $(J_{\tilde{x}}, J_{\tilde{y}}, J_{\tilde{z}}) = (0.063, 0.062, 0.011)$ meV, compared to measured heat capacity from $Ce_2Zr_2O_7$ in a $[1, \bar{1}, 0]$ magnetic field of strength $h = 0.5$ T (a), $h = 1$ T (b), and $h = 2$ T (c). Here we use a field-dependent low-temperature cutoff for our evaluation of $\langle \frac{\delta^2}{\epsilon^2} \rangle$ in order to restrict each fitting to its regime of reasonable convergence, as well as a high-temperature cutoff of 6 K in each case. Specifically, we fit the $h = 0.5$ T ($h = 1$ T, $h = 2$ T) data between $T = 0.40$ K ($T = 0.36$ K, $T = 0.29$ K) and 6 K.

Figure 12 shows the lack of significant θ dependence for $\langle \frac{\delta^2}{\epsilon^2} \rangle$ within the dark colored region of best agreement for each measured field strength. While we use $(J_{\tilde{x}}, J_{\tilde{y}}, J_{\tilde{z}}) = (0.063, 0.062, 0.011)$ meV as representative values in Fig. 12, it is worth mentioning that other permutations of $(0.063, 0.062, 0.011)$ meV and nearby parameters also show a lack of significant θ dependence for $\langle \frac{\delta^2}{\epsilon^2} \rangle$ in regions of good agreement. Accordingly, we find it appropriate to set the value of θ to zero consistent with our estimate in Sec. V and with the estimates in Refs. [25,26]. With θ set to zero, we use fifth-order NLC calculations to fit the measured heat capacity from $Ce_2Zr_2O_7$ according to the goodness-of-fit parameter $\langle \frac{\delta^2}{\epsilon^2} \rangle$ evaluated between 0.2 K and 6 K. The low-temperature cutoff used here is lower than that used for the NLC fitting of the zero-field heat capacity due to the fact that our NLC calculations are convergent ($\epsilon_{\mathrm{NLC},n} = 0$) down to lower temperatures for $h = 0.5$ T, $h = 1$ T, and $h = 2$ T compared to zero field. Furthermore, in contrast to the NLC fitting of the heat capacity in zero field, Euler transformations were not used to fit the heat capacity from $Ce_2Zr_2O_7$ for nonzero magnetic field as the bare NLC calculations are more robust than the Euler transformations for $h = 0.5$ T, $h = 1$ T, and $h = 2$ T, and are fully converged for each of these field strengths down to our low-temperature cutoff of $T = 0.2$ K as opposed to the corresponding Euler transformations.

Figure 13 shows the goodness-of-fit parameter $\langle \frac{\delta^2}{\epsilon^2} \rangle$ for our fifth-order NLC calculations compared to the heat capacity measured from $Ce_2Zr_2O_7$ over the fitting range from $T = 0.2$ K to $T = 6$ K, for a $[1, \bar{1}, 0]$ magnetic field of strength $h = 0.5$ T (a), $h = 1$ T (b), and $h = 2$ T (c). For each measured field strength, we show $\langle \frac{\delta^2}{\epsilon^2} \rangle$ for $(J_{\tilde{x}}, J_{\tilde{y}}, J_{\tilde{z}})$ equal to different permutations of $(0.063, 0.062, 0.011)$ meV, and for η between 0.75 and 1 as to highlight the minima in $\langle \frac{\delta^2}{\epsilon^2} \rangle$. As shown by the collection of minima in Fig. 13, the best global fit occurs for $(J_{\tilde{x}}, J_{\tilde{y}}, J_{\tilde{z}}) = (0.063, 0.062, 0.011)$ or $(0.062, 0.063, 0.011)$ meV at $\eta \sim 0.87$ ($g \sim 2.24$).

Permutations $(0.011, 0.062, 0.063)$, $(0.011, 0.063, 0.062)$, $(0.063, 0.011, 0.062)$, and $(0.062, 0.011, 0.063)$ meV are sub-optimal and provide near equal values of $\langle \frac{\delta^2}{\epsilon^2} \rangle$ due to both similarity of the exchange constants 0.062 meV and 0.063 meV, and due to the interchangeability of $\tilde{x}$ and $\tilde{y}$ in Eq. (2) for $\theta = 0$, which results in equal fits for $(J_{\tilde{x}}, J_{\tilde{y}}, J_{\tilde{z}}) = (J_a, J_b, J_c)$ and (J_b, J_a, J_c).

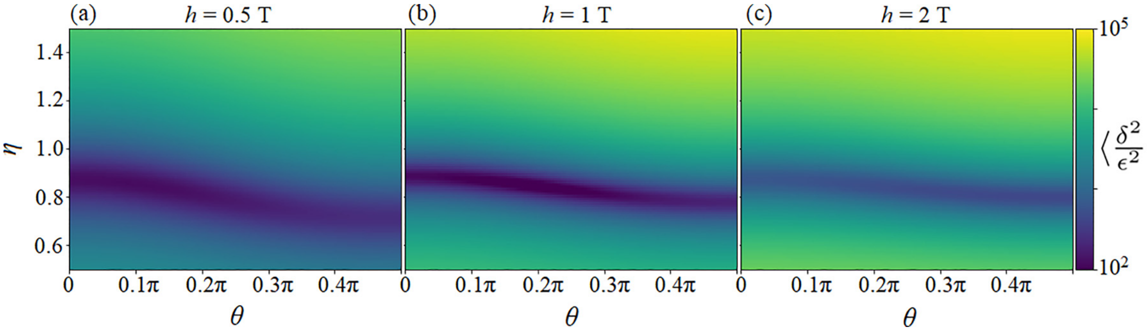

FIG. 12. The η and θ dependencies of the goodness of fit parameter $\langle \frac{\delta^2}{\epsilon^2} \rangle$ for our fourth-order NLC calculations compared to the measured heat capacity from our $Ce_2Zr_2O_7$ sample for $[1, \bar{1}, 0]$ field strengths of $h = 0.5$ T (a), $h = 1$ T (a), and $h = 2$ T (c). The parameter η is defined as $\eta = g_z/2.57$, and we use the best-fitting parameters from this work, $(J_{\tilde{x}}, J_{\tilde{y}}, J_{\tilde{z}}) = (0.063, 0.062, 0.011)$ meV. This plot shows the lack of significant θ dependence for $\langle \frac{\delta^2}{\epsilon^2} \rangle$ in the region of best agreement for each field strength.

2. Numerical linked cluster calculations of the heat capacity with other exchange parameters

Here we present our NLC calculations using the different sets of nearest-neighbor-exchange parameters suggested in Ref. [26]: Set (1) $(J_{\tilde{x}}, J_{\tilde{y}}, J_{\tilde{z}}) = (0.044, 0.087, 0.015)$ meV, $g_z = 2.4$, $\theta = 0$; set (2) $(J_{\tilde{x}}, J_{\tilde{y}}, J_{\tilde{z}}) = (0.039, 0.088, 0.02)$ meV, $g_z = 2.36$, $\theta = -0.03\pi$; set (3) $(J_{\tilde{x}}, J_{\tilde{y}}, J_{\tilde{z}}) = (0.041, 0.081, 0.027)$ meV, $g_z = 2.27$, $\theta = 0.08\pi$; and set (4) $(J_{\tilde{x}}, J_{\tilde{y}}, J_{\tilde{z}}) = (0.069, 0.068, 0.013)$ meV, $g_z = 2.4$, $\theta = 0$. Figure 14 shows these calculations along with the calculations using the best-fitting nearest-neighbor-exchange parameters obtained in this study, and the measured data from $Ce_2Zr_2O_7$, for a $[1, \bar{1}, 0]$ magnetic field of strength $h = 0$ T, 1 T, and 2 T. Each of these parameter-sets provides a reasonable description to the measured data, specifically for $h = 1$ T and 2 T. However, it is worth noting that the exchange parameters obtained in this study and parameter-set 4 from Ref. [26] (which is quite similar to the parameter set obtained in this study) clearly provide better description of the $h = 0$ T data than the other parameter sets.

APPENDIX B: ONE-DIMENSIONAL QUANTUM CALCULATIONS

1. Magnetic Bragg peak intensity

At large magnetic fields along the $[1, \bar{1}, 0]$ direction, the Ising pyrochlore system should be well described by two sets of effectively decoupled one-dimensional chains, called α and β chains [see Fig. 1(a)]. We set θ to zero in accordance with the estimated value in Refs. [25,26] and to simplify the treatment, we neglect the weakest exchange parameter J_z (which is equal to $J_{\tilde{z}}$ for $\theta = 0$). In this case, the Hamiltonian for both α and β chains reduces to the XY model in a staggered field,

$$\mathcal{H} = \sum_j J_x S^x_j S^x_{j+1} + J_y S^y_j S^y_{j+1} + (-1)^j h_0 S^z_j. \tag{B1}$$

with $h_0 = 0$ for the β chains and $h_0 = 2\mu_B g_z h/\sqrt{6}$ for the α chains, where h is the experimentally applied field strength and $2/\sqrt{6}$ is a geometrical factor arising from the projection of the external field on the local easy axis. Here we have used that $(x, y, z) = (\tilde{x}, \tilde{y}, \tilde{z})$ for $\theta = 0$. Rotating the local basis on every second site (sites with odd j) by π around the local x

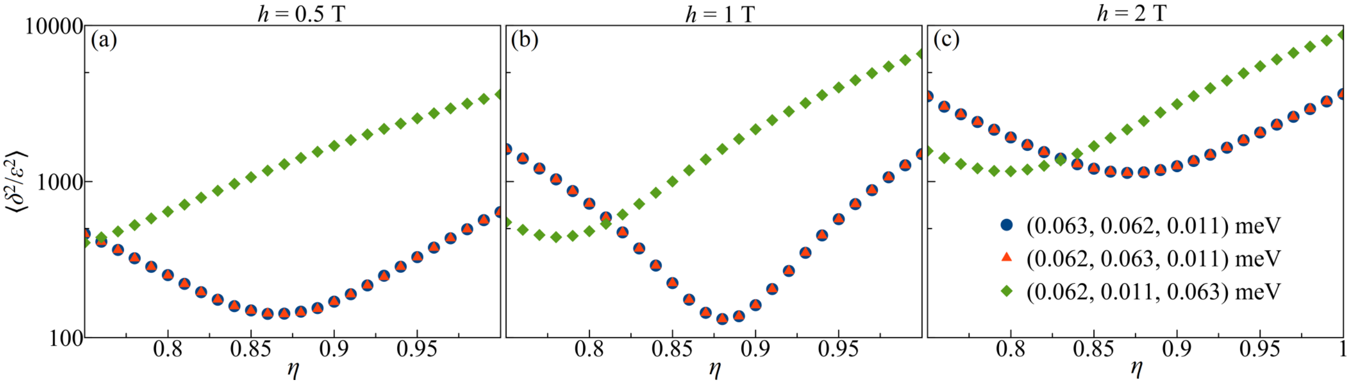

FIG. 13. The η dependence of the goodness of fit parameter $\langle \frac{\delta^2}{\epsilon^2} \rangle$ for our fifth-order NLC calculations compared to the measured heat capacity from our $Ce_2Zr_2O_7$ sample for $[1, \bar{1}, 0]$ field strengths of $h = 0.5$ T (a), $h = 1$ T (b), and $h = 2$ T (c), for $(J_{\tilde{x}}, J_{\tilde{y}}, J_{\tilde{z}})$ equal to different permutations of $(0.063, 0.062, 0.011)$ meV, and with θ set to zero as discussed in the main text. The parameter η is defined as $\eta = g_z/2.57$ (see main text).

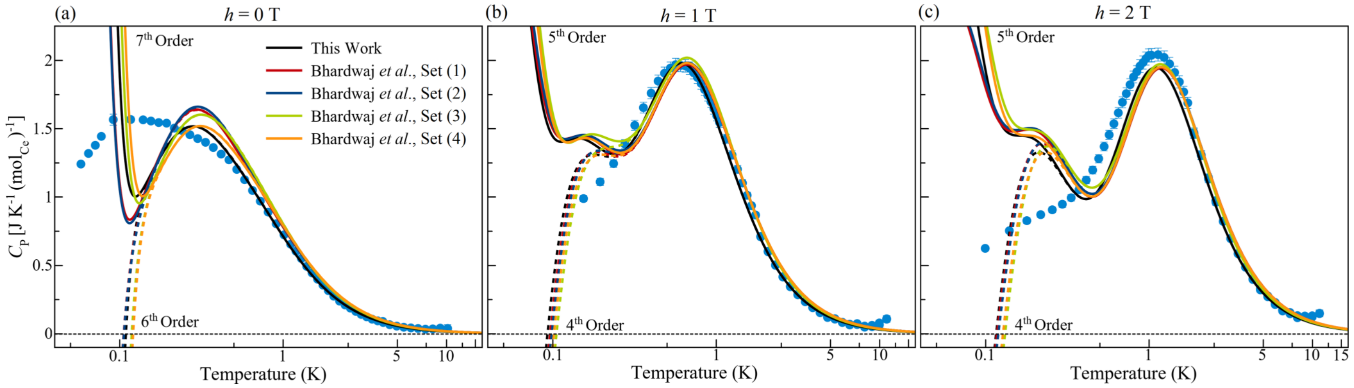

FIG. 14. The temperature dependence of the heat capacity of single crystal $Ce_2Zr_2O_7$ in a $[1, \bar{1}, 0]$ magnetic field is shown for field strengths of 0 T (a), 1 T (b), and 2 T (c). The lines show the magnetic contribution calculated using sixth- and seventh-order NLC calculations for zero magnetic field and fourth- and fifth-order NLC calculations at each nonzero field strength of measurement (as labeled). We show the calculations using the best-fit exchange parameters from this paper, $(J_{\tilde{x}}, J_{\tilde{y}}, J_{\tilde{z}}) = (0.063, 0.062, 0.011)$ meV, $g_z = 2.24$, and $\theta = 0$, as well as the different sets of nearest-neighbor-exchange parameters obtained in Ref. [26]: Set (1) $(J_{\tilde{x}}, J_{\tilde{y}}, J_{\tilde{z}}) = (0.044, 0.087, 0.015)$ meV, $g_z = 2.4$, $\theta = 0$; set (2) $(J_{\tilde{x}}, J_{\tilde{y}}, J_{\tilde{z}}) = (0.039, 0.088, 0.02)$ meV, $g_z = 2.36$, $\theta = -0.03\pi$; set (3) $(J_{\tilde{x}}, J_{\tilde{y}}, J_{\tilde{z}}) = (0.041, 0.081, 0.027)$ meV, $g_z = 2.27$, $\theta = 0.08\pi$; and set (4) $(J_{\tilde{x}}, J_{\tilde{y}}, J_{\tilde{z}}) = (0.069, 0.068, 0.013)$ meV, $g_z = 2.4$, $\theta = 0$.

axis yields $S^y \to -S^{y_0}$ and $S^z \to -S^{z_0}$ on these sites (with odd j), with the local basis remaining the same with $S^y \to S^{y_0}$ and $S^z \to S^{z_0}$ for the other sites (with even j). This transforms Eq. (B1) into the equation for a chain in uniform field but with flipped sign of the J_y exchange term,

$$\mathcal{H} = \sum_j J_x S_j^x S_{j+1}^x - J_y S_j^{y_0} S_{j+1}^{y_0} + h_0 S_j^{z_0}. \tag{B2}$$

This Hamiltonian can now be solved straightforwardly by using the Jordan-Wigner transformation and subsequent Bogolyubov transformation [72],

$$\mathcal{H} = \sum_k \omega(k)\left(\eta_k^\dagger \eta_k + \frac{1}{2}\right), \tag{B3}$$

$$\omega(k) = \sqrt{(\gamma \cos k + h_0)^2 + J^2 \sin^2 k}, \tag{B4}$$

where η_k are Fermionic operators, $J = \frac{1}{2}(J_x + J_y)$, and $\gamma = \frac{1}{2}(J_x - J_y)$. Note that J and γ have switched places in the expression for the dispersion ω compared to the usual result, because of the flipped sign in front of J_y in Eq. (B2). Importantly, inserting $h_0 = 0$ into Eq. (B4) shows that the β chain excitations are gapless with $\omega(0) = 0$ at the critical point where the anisotropy γ vanishes ($J_x = J_y$). We note that the same critical point occurs for $J_{\tilde{x}} = J_{\tilde{y}}$ in the general case where θ is not set to zero.

The magnetic Bragg peak intensity is entirely dominated by the contribution from the α chains, and in particular, the intensity of any nonvanishing magnetic Bragg peak is approximately proportional to the staggered magnetization squared on a single chain, $\langle m^z_{\text{staggered}} \rangle^2$. In the rotated basis of Eq. (B2), this is just the magnetization squared, which is a four-Fermion operator and can be computed exactly according to

$$\left\langle m^z_{\text{staggered}} \right\rangle = \langle m^{z_0} \rangle \tag{B5}$$

$$= \frac{1}{2\pi} \int_0^\pi \tanh\left(\frac{1}{2}\beta\omega(k)\right) \frac{\gamma \cos(k) + h_0}{\omega(k)} dk\,. \tag{B6}$$

We use Eq. (B6) to compute $\langle m^z_{\text{staggered}} \rangle$ and we plot $\langle m^z_{\text{staggered}} \rangle^2$ in Fig. 3(e) using the arbitrary units that are described in the caption of Fig. 3(e).

2. Hidden second-order transition in $[1, \bar{1}, 0]$ magnetic field

In Ref. [34], it was discovered that if exchange in dipolar-octupolar pyrochlores is dominantly octupolar (between octupolar magnetic moments), then the XYZ Hamiltonian undergoes a second-order transition into the high-field chain phase as a function of field strength for fields along the $[1, \bar{1}, 0]$ direction, as opposed to the crossover behavior observed in all other cases. Exchange can be dominantly octupolar for two reasons. First, the case mainly considered in Ref. [34] is the case where $J_y > J_x, J_z$. In the case of $\theta = 0$, as seems to be realized in $Ce_2Zr_2O_7$, this can also occur for $J_x > J_y, J_z$.

In these cases, there is significant competition between the polarization of the magnetic dipole moments, which are coupled to the magnetic field, and the ordering of the octupolar magnetic moments associated with the components of pseudospin which have the strongest exchange coupling. The α chains ground state remains twofold degenerate for some finite field range $h_0 < h_c$, where in this range, the α chains are expected to show noncollinear ferromagnetic octupolar order with one effective degree of freedom per chain corresponding to the two directions of the octupolar order, which are equivalent in energy. As an additional subtlety, the critical field is set by the anisotropy $h_c = \gamma = (J_x - J_y)/2$, and hence we expect it to be small. This is the case because the transition is a gap closing and the spinon gap is set by the anisotropy as shown in Eq. (B4). Since this low-field phase occurs in competition with the polarization of the z components of pseudospin, this indeed affects the value of $\langle m^z_{\text{staggered}} \rangle$ and accordingly, the measured Bragg intensity from the α chains even at low Q where direct contributions from the octupolar components are insignificant to the Bragg intensity.

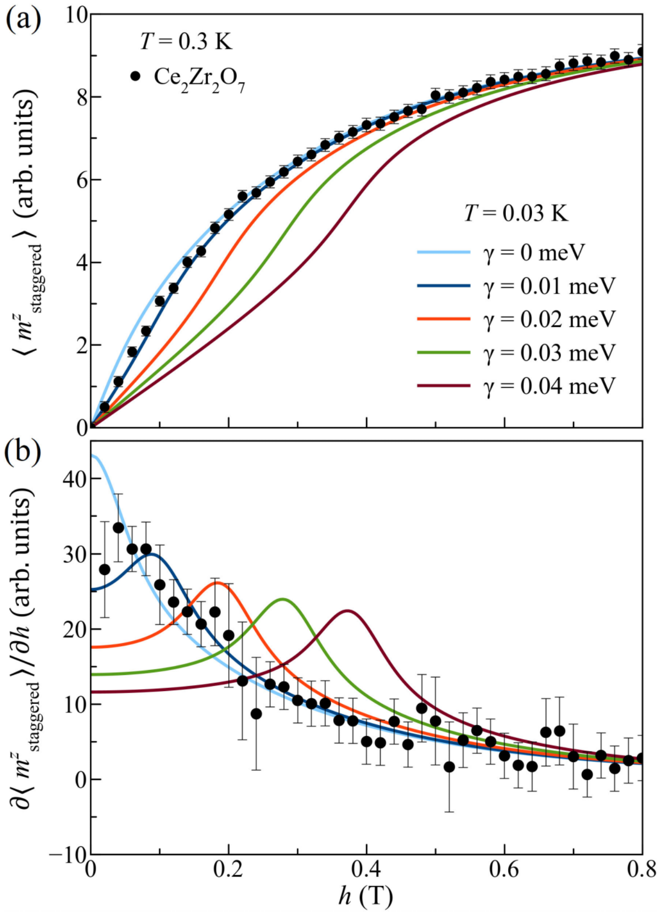

FIG. 15. The staggered magnetization for the α chains $\langle m^z_{\text{staggered}} \rangle$ and its derivative with respect to field strength are shown in (a) and (b) respectively as a function of field strength for a $[1, \bar{1}, 0]$ magnetic field at $T = 0.03$ K, calculated via Eq. (B6) using $J = \frac{1}{2}(J_x + J_y) = 0.0625$ meV and different values of the anisotropy parameter, $\gamma = \frac{1}{2}(J_x - J_y)$, as labeled. The position of the kink in the magnetization marks the transition from the low-field phase to high-field phase (see main text), and corresponds to the position of the peak in $\partial\langle m^z_{\text{staggered}} \rangle/\partial h$. We overplot the values of $\langle m^z_{\text{staggered}} \rangle$ and $\partial\langle m^z_{\text{staggered}} \rangle/\partial h$ obtained experimentally at $T = 0.3$ K by assuming the magnetic Bragg peak intensity at $\mathbf{Q} = (0, 0, 2)$ [shown in Fig. 3(e)] is proportional to $\langle m^z_{\text{staggered}} \rangle^2$. For both the calculations and measured data, we use the arbitrary units described in the caption of Fig. 3(e).

In Fig. 15, we show the calculated value of $\langle m^z_{\text{staggered}} \rangle$ for the α chains, as well as its derivative with respect to field, as a function of field for $\theta = 0$ and J as estimated for $Ce_2Zr_2O_7$ in this paper, for different values of the anisotropy parameter γ. These curves were calculated using Eq. (B6). We show the curves in Fig. 15 for $\gamma \geqslant 0$ only as Eq. (B6) is invariant under $\gamma \to -\gamma$. One way to see this invariance is by using the substitution $k = \pi - k_0$ in Eq. (B6) (with $dk = -dk_0$, and changing the integration limits accordingly).

As shown in Fig. 15, the transition can be diagnosed by a kink in the magnetization curve, or equivalently by a cusp in its derivative, which would be sharp for $T \to 0$. Also in Fig. 15, we overplot the values of $\langle m^z_{\text{staggered}} \rangle$ and $\partial\langle m^z_{\text{staggered}} \rangle/\partial h$ obtained by setting the magnetic Bragg peak intensity of the $\mathbf{Q} = (0, 0, 2)$ peak at $T = 0.3$ K [see Fig. 3(e)] equal to $\langle m^z_{\text{staggered}} \rangle^2$. We note that the measured data at $T = 0.3$ K is described well by the calculations performed at the lower temperature of $T = 0.03$ K for small values of the anisotropy, but noise in the measured $\partial\langle m^z_{\text{staggered}} \rangle/\partial h$ means that a relatively large anisotropy would be needed in order to observe a transition definitively.

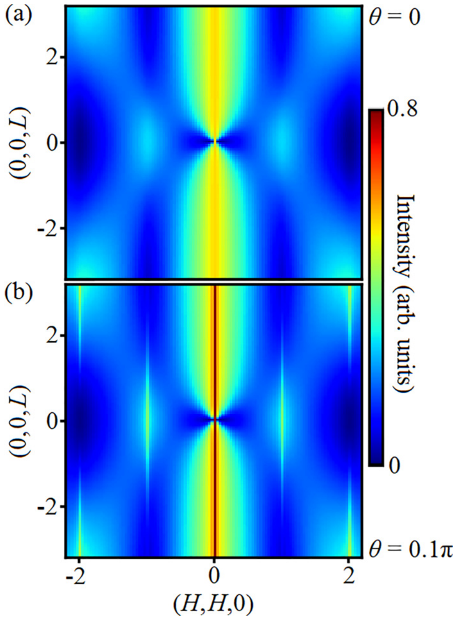

FIG. 16. The β-chain contribution to the energy-integrated dynamical structure factor obtained from our Jordan-Wigner calculations following the numerical procedure in Ref. [73]. Specifically, we show the calculation using the nearest-neighbor-exchange parameters obtained in this paper, $(J_{\tilde{x}}, J_{\tilde{y}}, J_{\tilde{z}}) = (0.063, 0.062, 0.011)$ meV, with $\theta = 0$ (a) and $\theta = 0.1\pi$ (b), for a temperature of $T = 0.03$ K and for a magnetic field in the $[1, \bar{1}, 0]$ direction of infinite strength. The energy-integration for each is over the range $E = [-0.2, 0.2]$ meV.

3. Dynamical structure factor for β chains

We follow the numerical procedure in Ref. [73] to compute the correlations within a single β chain that is 1000 ions long, using the nearest-neighbor-exchange parameters obtained in this paper, $(J_{\tilde{x}}, J_{\tilde{y}}, J_{\tilde{z}}) = (0.063, 0.062, 0.011)$ meV. Incorporating the necessary geometrical factors, one can then obtain the full dynamical structure factor $S(\mathbf{Q}, E)$ of the 3D material, in the infinite field limit $H \to \infty$. In Fig. 16, we show the integrated dynamical structure factor in the (H, H, L) plane obtained from these calculations at $T = 0.03$ K for both $\theta = 0$ and $\theta = 0.1\pi$, integrated in energy over the range from $E = -0.2$ to 0.2 meV. Remarkably, the result is extremely similar to that of the semiclassical Monte Carlo molecular dynamics simulations [Figs. 4(e) and 4(h)], even though the chain is close to criticality at $J_x \approx J_y$. Importantly, both our one-dimensional quantum calculations and our semiclassical molecular dynamics calculations show a sharp and intense centerpiece to the rod of scattering along $(0, 0, L)$ for $\theta = 0.1\pi$, which is not present for $\theta = 0$ and also not present in our measurements.

APPENDIX C: CONSISTENCY BETWEEN EXPERIMENTALLY-ESTIMATED EXCHANGE PARAMETERS AND FERROMAGNETIC β -CHAIN CORRELATIONS IN A $[1, \bar{1}, 0]$ FIELD

We employ the experimental estimates for the exchange parameters of Ce^{3+} in $Ce_2Zr_2O_7$ from this paper and Ref. [25] to conclude that the ferromagnetic intrachain correlations between magnetic dipole moments detected in our time-of-flight neutron scattering experiment are consistent with the expected β-chain correlations in a $[1, \bar{1}, 0]$ magnetic field at finite temperature. We first point out that the estimated exchange parameters give $J_{\tilde{x}} > \max(-3J_\lambda, J_\lambda)$ for $\lambda = \tilde{y}$ and $\tilde{z}$, or $J_{\tilde{y}} > \max(-3J_\lambda, J_\lambda)$ for $\lambda = \tilde{x}$ and $\tilde{z}$, and so at zero temperature all pseudospins in the β chains should be aligned along the local $\tilde{x}$ or local $\tilde{y}$ directions respectively [34], forming a phase of ordered octupolar magnetic moments with two possible directions for the order corresponding to the fact that all pseudospins can be flipped at zero cost in energy. This corresponds to ordering of the octupolar magnetic moments as $S^{\tilde{y}}$ always carries a purely octupolar magnetic moment and the magnetic moment associated with $S^{\tilde{x}}$ is also purely octupolar for $\theta = 0$. This occurs at the expense of any ordering of the $\tilde{z}$ components of pseudospin and their corresponding dipole moments.

However, at nonzero temperature, significant correlations are still expected between the magnetic dipole moments and these expected correlations can be determined from the portion of the Hamiltonian involving the z components of pseudospin. Using $\theta = 0$, and $(x, y, z) = (\tilde{x}, \tilde{y}, \tilde{z})$ for $\theta = 0$, the portion of the exchange Hamiltonian [Eq. (2)] containing the z components of pseudospin is given by $\mathcal{H}_z = \sum_{\langle ij \rangle}[J_z {S_i}^z {S_j}^z]$, where the term in Eq. (2) representing the interaction with the magnetic field vanishes due to the fact that a $[1, \bar{1}, 0]$ magnetic field gives $\mathbf{h} \perp \hat{\mathbf{z}}_i$ for each atom i within the β chains. Each ion in the β chains has four nearest neighbors in α chains and two nearest neighbors in the same β chain. The polarization of the α chains dictates that two of the neighboring α-chain pseudospins are along their local $+z$ direction and two are along their local $-z$ direction. Accordingly, this gives a vanishing exchange field produced from the α chains on the sites of the β chains [33,34]. Furthermore, Ref. [34] further shows that even quantum fluctuations of the α chains are not expected to result in any significant coupling between α and β chains within the nearest-neighbor model. The estimates for the exchange parameters in Refs. [25] and in this paper give $J_z > 0$ and accordingly, the minimum energy state of $\mathcal{H}_z$ corresponds to β chains with noncollinear ferromagnetic order as we discuss in the following paragraph.

Employing $J_z > 0$ to the isolated β chain shows that $\mathcal{H}_z$ is minimized for two neighboring atoms in the β chain when one atom has its magnetic moment in the $+z_i$ $(-z_i)$ direction and the other atom has its magnetic moment in the $-z_j$ $(+z_j)$ direction. These preferred alignments for a β chain then correspond to neighboring magnetic moments aligned along the $[1, 1, 1]$ and $[1, 1, \bar{1}]$ directions, or along the $[\bar{1}, \bar{1}, \bar{1}]$ and $[\bar{1}, \bar{1}, 1]$ directions [11,12], which corresponds to noncollinear ferromagnetism for the β chain, with net dipole moment for the chain in the $[1, 1, 0]$ or $[\bar{1}, \bar{1}, 0]$ direction, respectively. These ferromagnetic correlations between dipole moments in the β chains establish the 2-in-2-out rule locally at finite temperature in $[\bar{1}, \bar{1}, 0]$ magnetic fields. We note that these correlations are also consistent with the estimated nearest-neighbor-exchange parameters in Ref. [26] (see Appendix A, Subsection 2), although for the parameter sets of Ref. [26] with nonzero θ, the ferromagnetic interchain correlations between magnetic dipole moments would involve both the $\tilde{z}$ and $\tilde{x}$ components of pseudospin.

APPENDIX D: SEMICLASSICAL MOLECULAR DYNAMICS CALCULATIONS BASED ON MONTE CARLO SIMULATIONS

1. Further details on semiclassical molecular dynamics calculations based on Monte Carlo simulations

Here we further discuss the semiclassical molecular dynamics calculations based on Monte Carlo simulations, which we have used to calculate Bragg intensities in Figs. 2(e) and 7(g), the quasielastic diffuse scattering signals in the (H, H, L) scattering plane in Figs. 4(d)–4(i) and in the $(H + K, H - K, 1.5)$ scattering plane in Figs. 5(d)–5(f), as well as the inelastic neutron scattering spectra shown in Figs. 9 and 10. The details of these calculations are outlined in Appendix H of Ref. [25].

Figure 17 shows the temperature and $[1, \bar{1}, 0]$-field-strength dependencies of the diffuse neutron scattering signal calculated via our semiclassical molecular dynamics calculations using the experimental estimates of the nearest-neighbor-exchange parameters obtained from this paper, $(J_{\tilde{x}}, J_{\tilde{y}}, J_{\tilde{z}}) = (0.063, 0.062, 0.011)$ meV, $g_z = 2.24$, and $\theta = 0$. The calculated signal for the (H, H, L) scattering plane uses an integration in energy transfer over –0.2 meV $\leqslant E \leqslant$ 0.2 meV and an integration in the $(K, \bar{K}, 0)$ direction over –0.3 $\leqslant K \leqslant$ 0.3, consistent with the integration ranges for the experimental data in Figs. 4(a)–4(c). Figure 17 shows that the predicted diffuse neutron scattering possesses essentially the same field dependence for each temperature, and that for each field strength the signal grows in intensity with decreasing temperature.

The snowflake-like pattern of diffuse scattering in the (H, H, L) plane predicted at low temperature in zero field in Fig. 17 is consistent with the corresponding signals measured from $Ce_2Zr_2O_7$ in Refs. [13,14,25]; however, as discussed in Sec. V B, the calculations miss finer features of the diffuse scattering due to approximations used in Eq. (2) and the semiclassical molecular dynamics calculations themselves (outlined in Appendix H of Ref. [25]). Specifically, previous measurements in Ref. [13] show a snowflake pattern like the one predicted in Fig. 17 but with an increase in scattering centered on (0, 0, 1), less scattering along the (H, H, H) direction compared to the $(0, 0, L)$ direction, and broadened pinch-point features near (1, 1, 1) and (0, 0, 2). None of these are captured by the semiclassical molecular dynamics calculations. Nonetheless, the main features of the diffuse scattering are accurately predicted by these calculations for both zero and nonzero magnetic field as was mentioned in Sec. V.

In Figs. 18 and 19 we show the calculated inelastic neutron scattering spectra via semiclassical molecular dynamics for a higher-energy resolution than used in Sec. V. Here

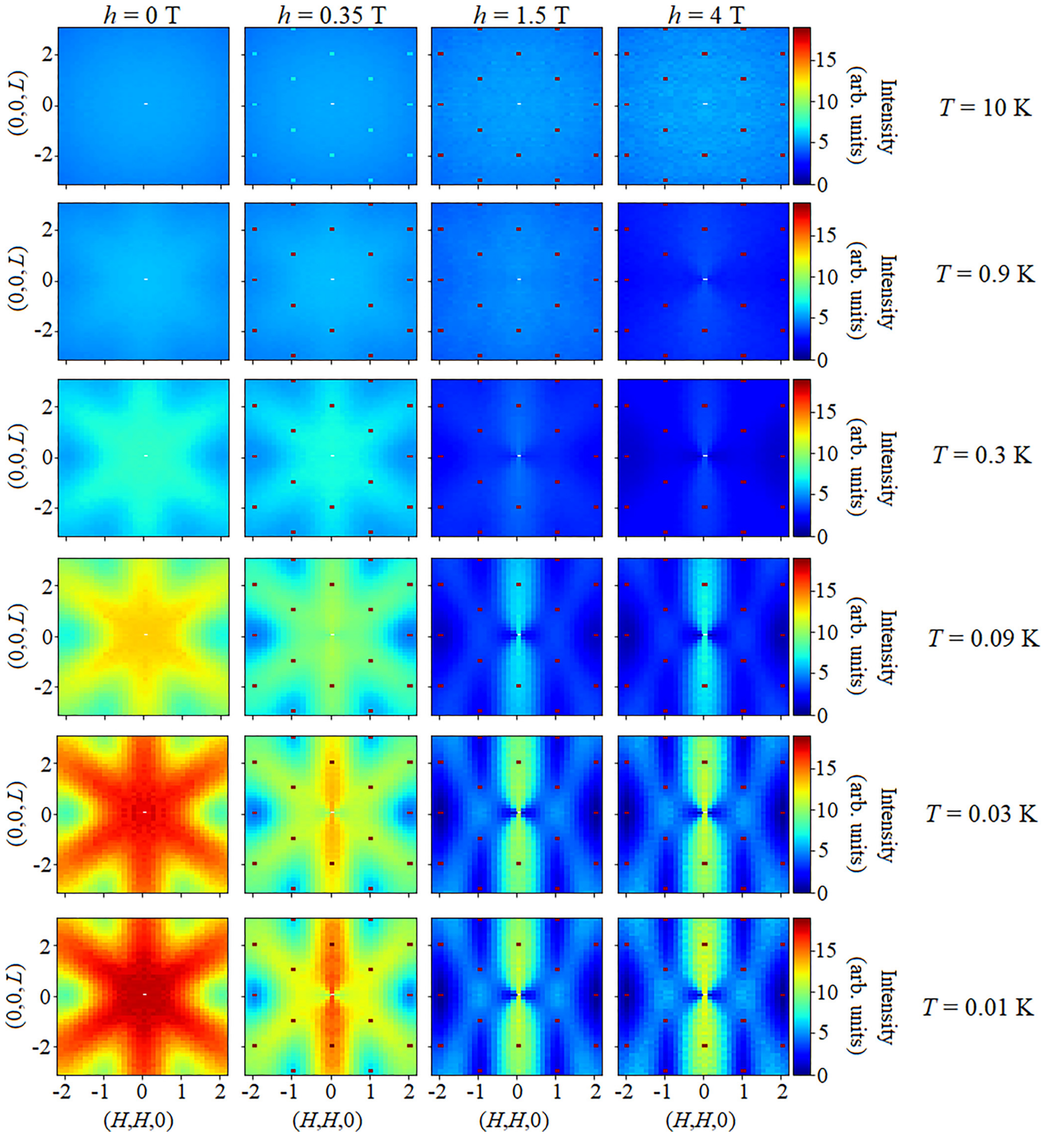

FIG. 17. The temperature and field-strength dependencies of the diffuse neutron scattering signal calculated via semiclassical molecular dynamics calculations using the experimental estimates of the nearest-neighbor exchange parameters obtained from this work, $(J_{\tilde{x}}, J_{\tilde{y}}, J_{\tilde{z}}) = (0.063, 0.062, 0.011)$ meV, $g_z = 2.24$, and $\theta = 0$, for the (H, H, L) scattering plane with an integration in the $(K, \bar{K}, 0)$ direction from -0.3 to 0.3, and with the $[1, \bar{1}, 0]$ magnetic field strength and temperature as labeled for each column and row, respectively.

we show the calculated spectra convoluted with a Gaussian lineshape with energy resolution of $\Delta E = 0.02$ meV. In further detail, Figs. 18 and 19 shows the calculated dispersion for high symmetry directions in the (H, H, L) $[(H, K, 0)]$ plane at $T = 0.03$ K $(T = 0.09$ K$)$ for a $[1, \bar{1}, 0]$ $([0, 0, 1])$ magnetic field. Our calculations again use the nearest-neighbor-exchange parameters obtained from this paper, $(J_{\tilde{x}}, J_{\tilde{y}}, J_{\tilde{z}}) = (0.063, 0.062, 0.011)$ meV and $g_z = 2.24$, and we show the calculations for both $\theta = 0$ (left) and $\theta = 0.1\pi$ (right). As shown in Figs. 18 and 19, sharp single-magnon excitations have extremely weak intensity for $\theta = 0$ and become more visible for nonzero θ.

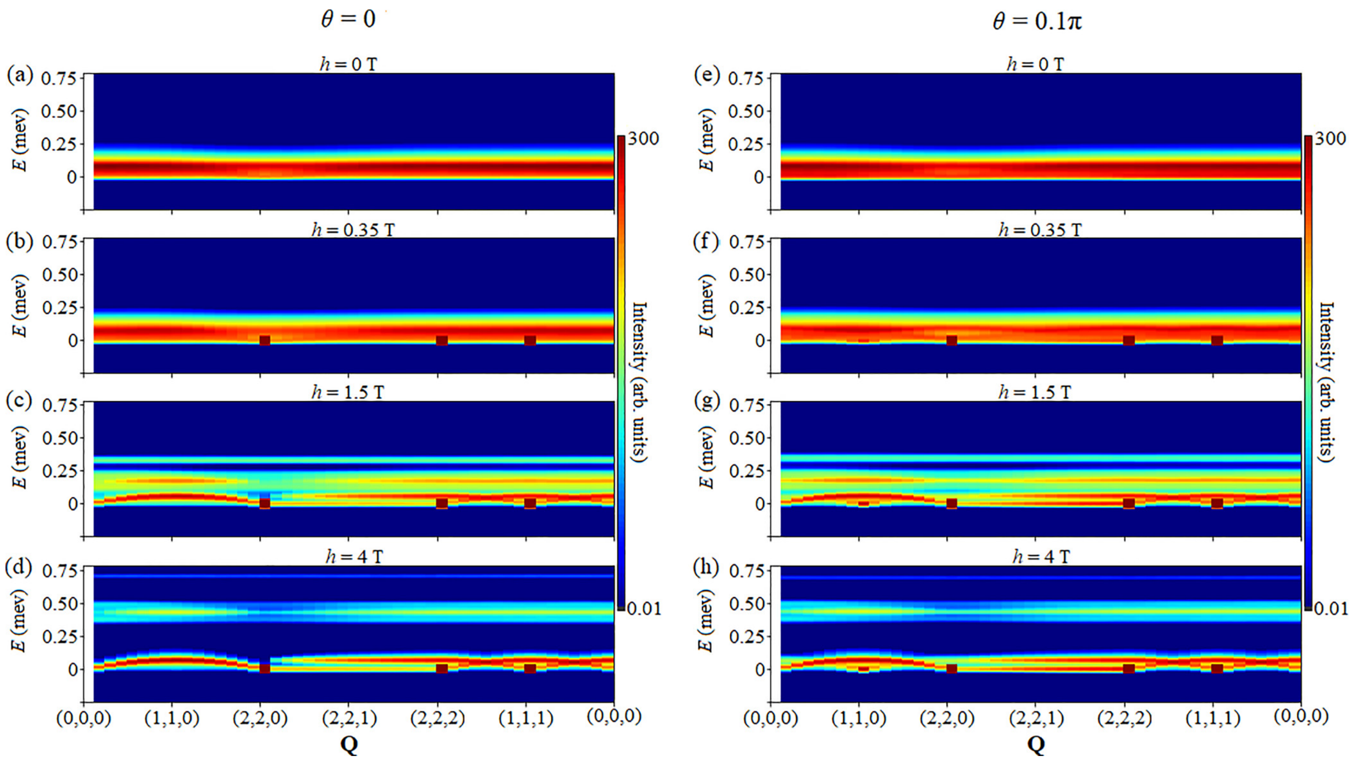

FIG. 18. The calculated inelastic neutron scattering signal, via semiclassical molecular dynamics calculations (see main text) using the experimental estimates of the nearest-neighbor exchange parameters obtained from this work, $(J_{\tilde{x}}, J_{\tilde{y}}, J_{\tilde{z}}) = (0.063, 0.062, 0.011)$ meV, and $g_z = 2.24$, for $\theta = 0$ [(a)–(d)] and $\theta = 0.1\pi$ [(e)–(h)]. Specifically, we show the calculated dispersion along high symmetry directions in the (H, H, L) plane at $T = 0.03$ K for a $[1, \bar{1}, 0]$ magnetic field of strength $h = 0$ T [(a), (e)], $h = 0.35$ T [(b), (f)], $h = 1.5$ T [(c), (g)], and $h = 4$ T [(d), (h)]. The intensity is shown on a logarithmic scale and the calculated spectra are convoluted with a Gaussian lineshape with energy resolution of $\Delta E = 0.02$ meV.

In order to understand why inelastic scattering from single magnon excitations is not expected to be observed in the high-field regime when $\theta = 0$, we must consider both how the neutrons couple to spin waves, and the form of the magnetic ground states. In the dipole approximation, the neutrons couple to the magnetic moment, which in the pseudospin picture means they couple only to $S^z = S^{\tilde{z}} \cos\theta + S^{\tilde{x}} \sin\theta$. At the same time, single-spin waves are excited by spin operators transverse to the direction of the ground-state expectation value of the spin. This means that in order to see single-spin wave scattering in the dipole approximation, the ground-state expectation value of the pseudospin must not be fully aligned with the pseudospin z axis (meaning S^z). For $\theta = 0$, we find that the ground-state energy is minimised by spins aligned with the z axis for all h strong enough to be in the polarized phase. On the other hand, for $\theta \neq 0$, the ground-state expectation value is canted away from the z axis for all fields, only becoming fully aligned as $h \to \infty$. It is this canting which allows for a matrix element for the scattering from single-spin waves in the dipole approximation. Moving beyond the dipole approximation, the scattering becomes sensitive to the S^x and S^y pseudospin components, and single magnons contribute a finite, but small, intensity even for $\theta = 0$. However, the intensity due to octupolar contributions is suppressed by an octupolar form factor and is therefore only expected to be observable at large Q. This effect is visible for example in Figs. 19(d) and 19(e), where a weak sharp magnon dispersion is visible even for $\theta = 0$ at the largest wave vectors plotted. Nonetheless, due to its low intensity, this weak-but-visible signal in the calculations (shown on a logarithmic scale in Fig. 19) is not expected to be observable in the inelastic neutron scattering experiments included in this paper.

We include contributions from all higher-order multipoles relevant to the $J = 5/2$ manifold in our semiclassical molecular dynamics calculations. However, we show the calculated Bragg scattering in Fig. 10 in the dipole approximation for aesthetic purposes and include the higher-order multipole contributions elsewhere. In further detail, our calculations including higher-order multipoles for a $[0, 0, 1]$ magnetic field find a magnetic Bragg peak at $\mathbf{Q} = (2, 2, 0)$ (see Fig. 19), which is ~50 000 times weaker than the magnetic Bragg peak at $\mathbf{Q} = (0, 0, 2)$ and is far from being detectable in experiment due to its weak intensity, especially considering there is a large nuclear Bragg peak at the same position.

2. Monte Carlo molecular dynamics calculations with other exchange parameters

Here we discuss our Monte Carlo molecular dynamics calculations for the neutron scattering signal using the different sets of nearest-neighbor exchange parameters obtained in Ref. [26] through different fitting processes applied to the heat capacity and magnetization measured [57] from $Ce_2Zr_2O_7$ in a $[1, 1, 1]$ magnetic field: Set (1) $(J_{\tilde{x}}, J_{\tilde{y}}, J_{\tilde{z}}) = (0.044, 0.087, 0.015)$ meV, $g_z = 2.4$, $\theta = 0$; set (2) $(J_{\tilde{x}}, J_{\tilde{y}}, J_{\tilde{z}}) = (0.039, 0.088, 0.02)$ meV, $g_z = 2.36$,

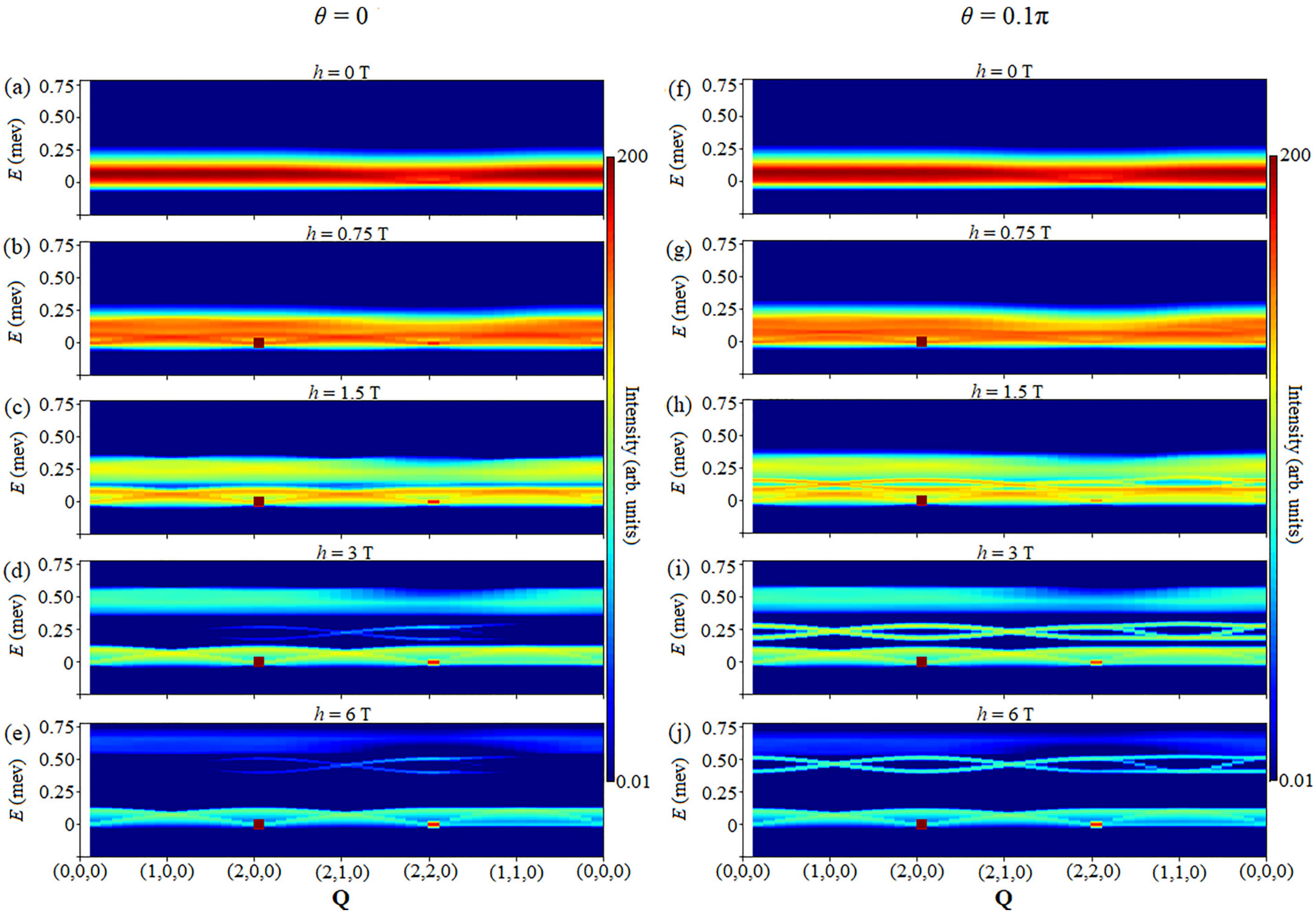

FIG. 19. The calculated inelastic neutron scattering signal, via semiclassical molecular dynamics calculations (see main text) using the experimental estimates of the nearest-neighbor-exchange parameters obtained from this paper, $(J_{\tilde{x}}, J_{\tilde{y}}, J_{\tilde{z}}) = (0.063, 0.062, 0.011)$ meV, and $g_z = 2.24$, for $\theta = 0$ [(a)–(e)] and $\theta = 0.1\pi$ [(f)–(j)]. Specifically, we show the calculated dispersion along high symmetry directions in the $(H, K, 0)$ plane at $T = 0.09$ K for a [0, 0, 1] magnetic field of strength $h = 0$ T [(a),(f)], $h = 0.75$ T [(b),(g)], $h = 1.5$ T [(c),(h)], $h = 3$ T [(d),(i)], and $h = 6$ T [(e),(j)]. The intensity is shown on a logarithmic scale and the calculated spectra are convoluted with a Gaussian lineshape with energy resolution of $\Delta E = 0.02$ meV.

$\theta = -0.03\pi$; set (3) $(J_{\tilde{x}}, J_{\tilde{y}}, J_{\tilde{z}}) = (0.041, 0.081, 0.027)$meV, $g_z = 2.27$, $\theta = 0.08\pi$; and set (4) $(J_{\tilde{x}}, J_{\tilde{y}}, J_{\tilde{z}}) = (0.069, 0.068, 0.013)$ meV, $g_z = 2.4$, $\theta = 0$. The corresponding point shown in Fig. 2(b) was obtained in Ref. [26] as the approximate center point of these four different parameter sets. However, it is worth noting that parameter set 4 from Ref. [26] agree particularly well with the best-fitting exchange parameters obtained in this work. For a nonzero $[1, \bar{1}, 0]$ magnetic field, each of these parameter sets shows quasielastic diffuse scattering which forms a rod along $(0, 0, L)$ in the (H, H, L) scattering plane and is extended in the out-of-plane, $(K, \bar{K}, 0)$ direction as we show in Figs. 4(d)–4(f) and Figs. 5(d)–5(f) for the best-fitting exchange parameters obtained in this paper. Furthermore, each of these parameter sets gives similar inelastic scattering spectra for the energy resolution of our inelastic neutron scattering experiment, shown in Figs. 9 and 10 for the best-fitting exchange parameters obtained in this paper.

Figure 20 shows the diffuse neutron scattering signal in the (H, H, L) scattering plane predicted at $T = 0.03$ K in a $[1, \bar{1}, 0]$ magnetic field for each of these parameter sets and for the exchange parameters estimated in this paper, for an integration in energy over $E = [-0.2, 0.2]$ meV and an integration in the out-of-plane direction over $K = [-0.3, 0.3]$. Each of these parameter sets provides a reasonable description to the measured data in Figs. 4(a)–4(c), specifically for $h = 1.5$ T and 4 T. However, it is worth noting that the exchange parameters obtained in this paper and parameter set 4 from Ref. [26] (which is quite similar to the parameter set obtain in this paper) clearly provide a better description of the $h = 0.35$ T data [Fig. 4(a)] than the other parameter sets, as well as the relative intensity between the signals at $h = 0.35$ T, $h = 1.5$ T, and $h = 4$ T [see Figs. 4(a)–4(c)].

APPENDIX E: ESTIMATING THE CORRELATION LENGTH FOR THE FERROMAGNETIC CORRELATIONS WITHIN β CHAINS

We fit the $(H, H, 0)$ width of the diffuse scattering around $H = 0$ to a Lorentzian form for the purpose of estimating the correlation length along the β chains, ξ. This fitting assumed a constant background and is shown by the solid line

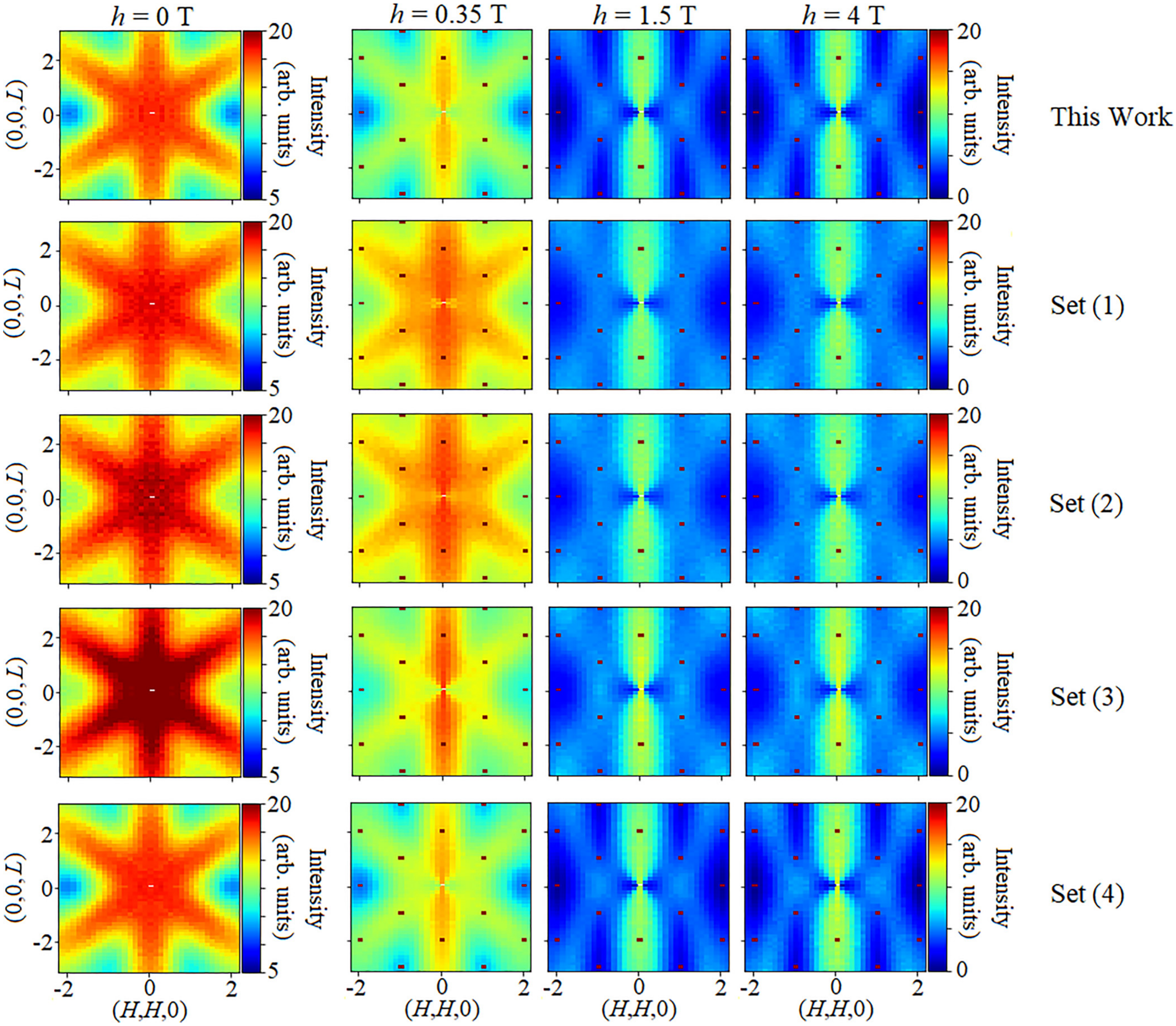

FIG. 20. The diffuse neutron scattering signal in the (H, H, L) scattering plane predicted at $T = 0.03$ K according to our semiclassical molecular dynamics calculations using the nearest-neighbor-exchange parameters estimated in Ref. [26]. Specifically, we show the calculated neutron scattering signal using the best-fit exchange parameters from this paper, $(J_{\tilde{x}}, J_{\tilde{y}}, J_{\tilde{z}}) = (0.063, 0.062, 0.011)$ meV, $g_z = 2.24$, and $\theta = 0$, as well as the different sets of nearest-neighbor-exchange parameters obtained in Ref. [26]: Set (1) $(J_{\tilde{x}}, J_{\tilde{y}}, J_{\tilde{z}}) = (0.044, 0.087, 0.015)$ meV, $g_z = 2.4$, $\theta = 0$; set (2) $(J_{\tilde{x}}, J_{\tilde{y}}, J_{\tilde{z}}) = (0.039, 0.088, 0.02)$ meV, $g_z = 2.36$, $\theta = -0.03\pi$; set (3) $(J_{\tilde{x}}, J_{\tilde{y}}, J_{\tilde{z}}) = (0.041, 0.081, 0.027)$ meV, $g_z = 2.27$, $\theta = 0.08\pi$; and set (4) $(J_{\tilde{x}}, J_{\tilde{y}}, J_{\tilde{z}}) = (0.069, 0.068, 0.013)$ meV, $g_z = 2.4$, $\theta = 0$. For each parameter set, we show the calculated signals for a $[1, \bar{1}, 0]$ magnetic field of strength $h = 0$ T, $h = 0.35$ T, $h = 1.5$ T, and $h = 4$ T (as labeled).

fits in Fig. 6(c). The interest in this analysis is the width of the central peak around $H = 0$, which was fit for each field strength using a resolution-convoluted Lorentzian function with the correlation length along the $(H, H, 0)$ direction calculated using the equation $\xi = a/(\sqrt{2}\Delta_{\text{signal}})$, where $a = 10.7$ Å is the cubic lattice constant for $Ce_2Zr_2O_7$ and $\Delta_{\text{signal}} = \sqrt{\Delta_{\text{total}}^2 - \Delta_{\text{res}}^2}$. In this second equation, Δ_{total} is the full width at half-maximum of the Lorentzian function, and Δ_{res} is the experimental resolution along the $(H, H, 0)$ direction determined by fitting the full-width at half-maximum for nuclear Bragg peaks. This analysis yields correlation lengths of $\xi =$ 17, 13, and 14 Å at $h = 0.35$ T, 1.5 T, and 4 T, respectively, which we describe in the main text using the average value $\xi = 15(2)$ Å. As discussed in Sec. V, this corresponds to the correlations between the z components of the pseudospins in the β chains.

APPENDIX F: INELASTIC SCATTERING DATA WITHOUT POWDER AVERAGING

Here we show the inelastic neutron scattering signal along specific high-symmetry directions of reciprocal space in the scattering plane, measured at low temperature from our sin-

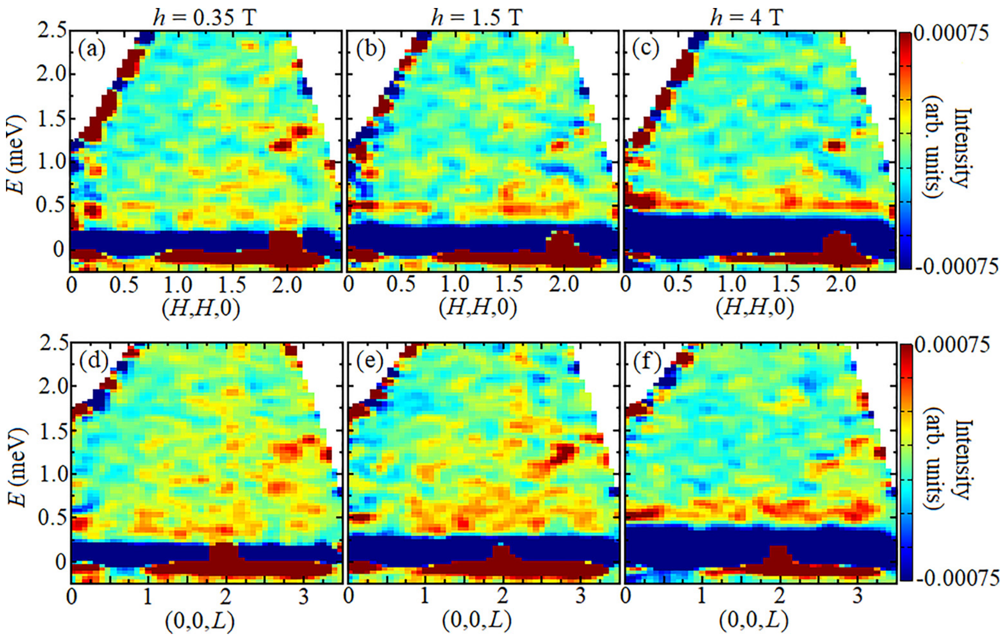

FIG. 21. The symmetrized neutron scattering signal measured at $T = 0.03$ K from a single crystal sample of $Ce_2Zr_2O_7$ aligned in the (H, H, L) scattering plane in a $[1, \bar{1}, 0]$ magnetic field. The energy dependence of the neutron scattering signal along the $(H, H, 0)$ and $(0, 0, L)$ directions of reciprocal space are shown in (a)–(c) and (d)–(f), respectively, for field strengths of $h = 0.35$ T [(a),(d)], $h = 1.5$ T [(b),(e)], and $h = 4$ T [(c),(f)]. The $(0, 0, L)$ and $(H, H, 0)$ integration ranges for (a)–(c) and (d)–(f) are $L = [-0.5, 0.5]$ and $H = [-0.5, 0.5]$, respectively. In each case, an integration in the out-of-plane direction, $(K, \bar{K}, 0)$, from $K = -0.3$ to 0.3 was used and a data set measured at $h = 0$ T has been subtracted.

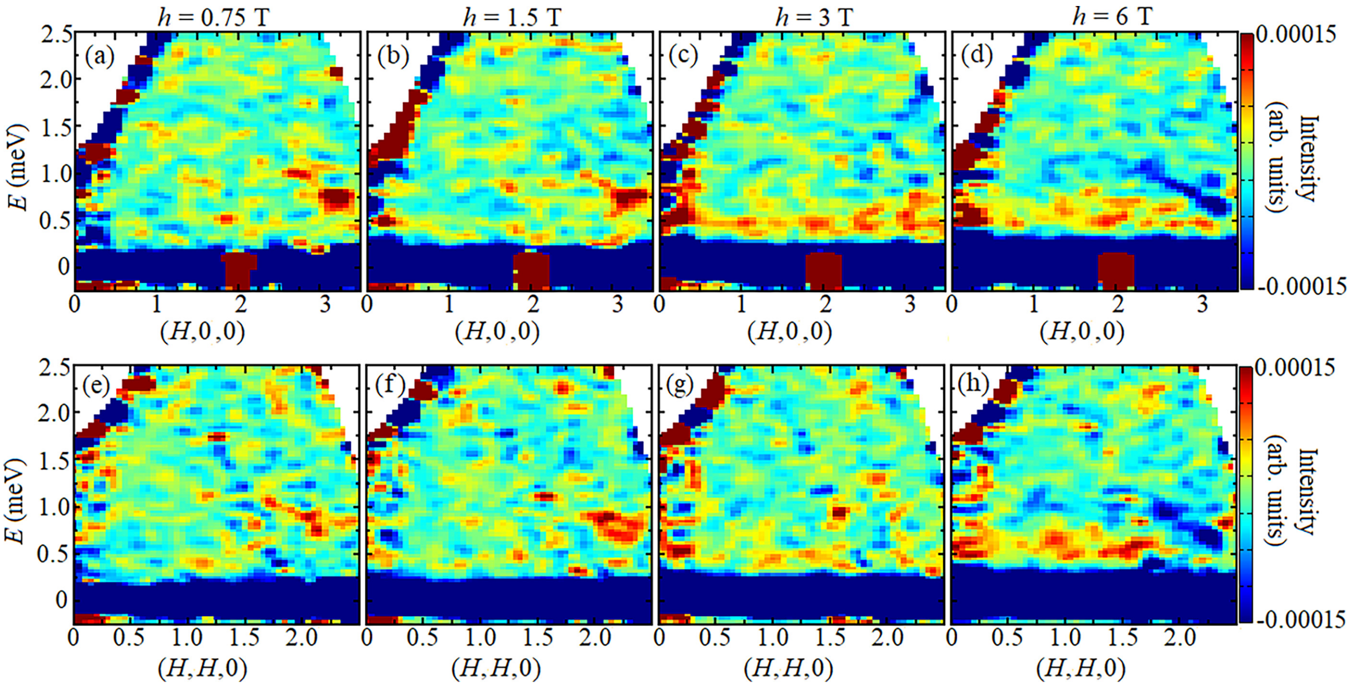

FIG. 22. The symmetrized neutron scattering signal measured at $T = 0.09$ K from a single crystal sample of $Ce_2Zr_2O_7$ aligned in the $(H, K, 0)$ scattering plane in a $[0, 0, 1]$ magnetic field. The energy dependence of the neutron scattering signal along the $(H, 0, 0)$ and $(H, H, 0)$ directions of reciprocal space are shown in (a)–(d) and (e)–(h), respectively, for field strengths of $h = 0.75$ T [(a),(e)], $h = 1.5$ T [(b),(f)], $h = 3$ T [(c),(g)], and $h = 6$ T [(d),(h)]. The $(0, K, 0)$ integration range for (a)–(d) is $K = [-0.5, 0.5]$ and the $(K, \bar{K}, 0)$ integration range for (e)–(h) is $K = [-0.5, 0.5]$. In each case, an integration in the out-of-plane direction, $(0, 0, L)$, from $L = -0.3$ to 0.3 was used and a data set measured at $h = 0$ T has been subtracted.

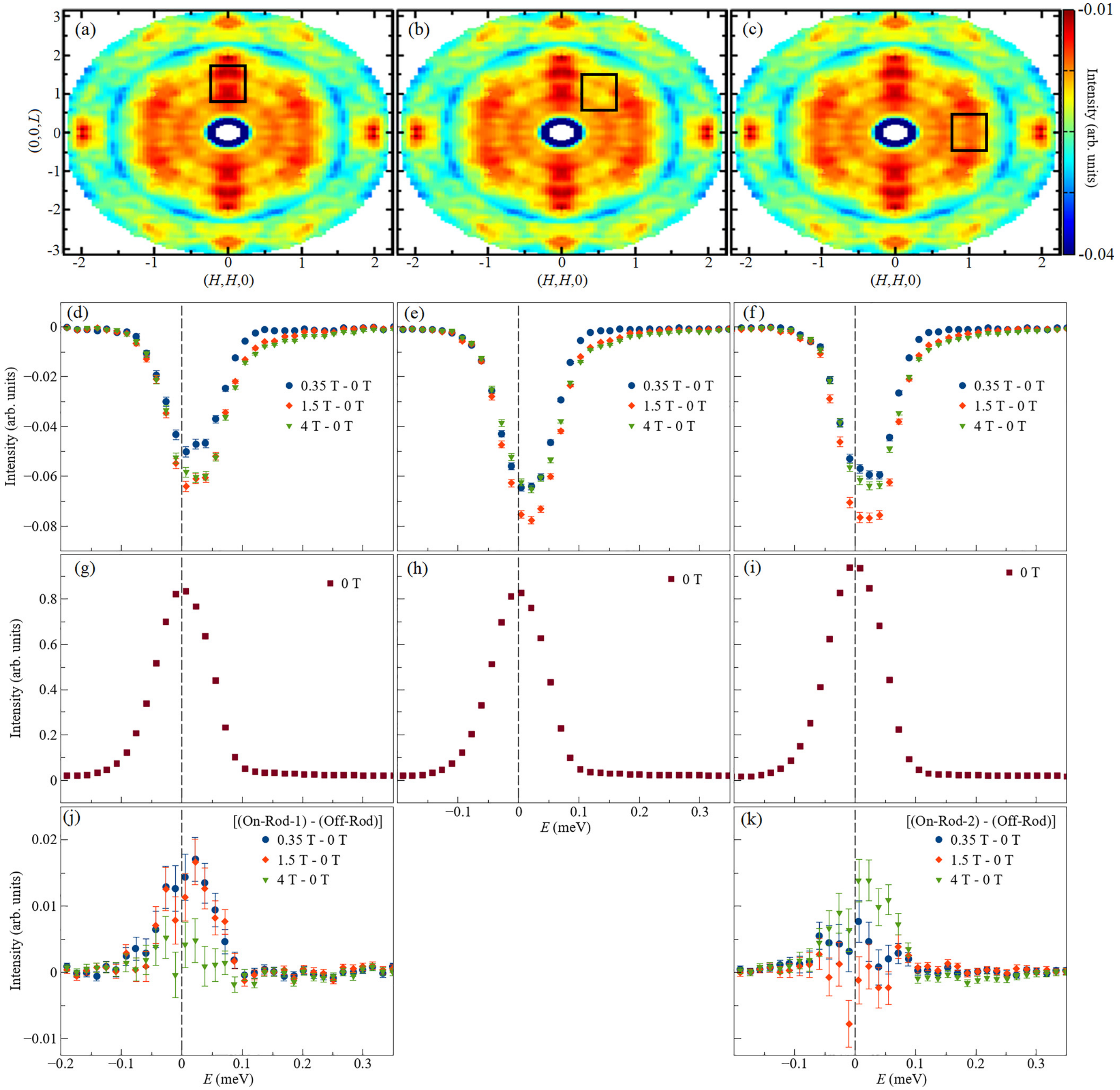

FIG. 23. The neutron scattering signal measured at $T = 0.03$ K from a single crystal sample of $Ce_2Zr_2O_7$ aligned in the (H, H, L) scattering plane in a $[1, \bar{1}, 0]$ magnetic field. (a), (b), and (c) show the quasielastic neutron scattering signal in the (H, H, L) plane for a field strength of $h = 0.35$ T, also shown in Figs. 4(a) and 5(a). The black rectangle in (a) shows the combined integration range for $(0, 0, L)$ and $(H, H, 0)$ defined by $L = [0.75, 1.75]$ and $H = [-0.25, 0.25]$. The black rectangle in (b) shows the combined integration range for $(0, 0, L)$ and $(H, H, 0)$ defined by $L = [0.5, 1.5]$ and $H = [0.25, 0.75]$. The black rectangle in (c) shows the combined integration range for $(0, 0, L)$ and $(H, H, 0)$ defined by $L = [-0.5, 0.5]$ and $H = [0.75, 1.25]$. (d), (e), and (f) show the energy dependence of the integrated neutron scattering intensity within the boxes of reciprocal space depicted in (a), (b), and (c), respectively, for magnetic field strengths of $h = 0.35$ T (blue), $h = 1.5$ T (orange), and $h = 4$ T (green). In each case, a data set measured at $h = 0$ T has been subtracted. (g), (h), and (i) show the energy dependence of the integrated neutron scattering intensity within the boxes of reciprocal space depicted in (a), (b), and (c), respectively, for $h = 0$ T. Integration in $(K, \bar{K}, 0)$ over the range $-0.3 \leqslant K \leqslant 0.3$ was employed for each plot in this figure. (j) shows the subtraction of the energy-cut in (e) centered between the planes, from the energy-cut in (d) centered on the plane at $H = 0$, for each field-subtraction (as labeled). (k) shows the subtraction of the energy-cut in (e) centered between the planes, from the energy-cut in (f) centered on the plane at $H = 1$, for each field-subtraction (as labeled).

gle crystal sample of $Ce_2Zr_2O_7$ for magnetic fields along the $[1, \bar{1}, 0]$ and $[0, 0, 1]$ directions. This compliments the powder-averaged inelastic neutron scattering shown in Fig. 8, which utilizes the entire data set acquired and possesses a better signal-to-noise ratio than the inelastic neutron scattering along specific high-symmetry directions.

Figures 21(a)–21(c) [21(d)–21(f)] show the energy dependence of the measured inelastic neutron scattering signal along the $(H, H, 0)$ $[(0, 0, L)]$ direction of reciprocal space at $T = 0.03$ K for a $[1, \bar{1}, 0]$ magnetic field of strength $h = 0.35$ T, $h = 1.5$ T, and $h = 4$ T. For Figs. 21(a)–21(c) [21(d)–21(f)] we use an integration in $(0, 0, L)$ $[(H, H, 0)]$ from $L = -0.5$ to 0.5 ($H = -0.5$ to 0.5) and in $(K, \bar{K}, 0)$ from $K = -0.3$ to 0.3, with a zero-field data set taken at $T = 0.03$ K subtracted in each case.

Figures 22(a)–22(d) [22(e)–22(h)] shows the energy dependence of the measured inelastic neutron scattering signal along the $(H, 0, 0)$ $[(H, H, 0)]$ direction of reciprocal space at $T = 0.09$ K for a $[0, 0, 1]$ magnetic field of strength $h = 0.75$ T, $h = 1.5$ T, $h = 3$ T, and $h = 6$ T. For Figs. 22(a)–22(d) [22(e)–22(h)] we use an integration in $(0, K, 0)$ $[(K, \bar{K}, 0)]$ from $K = -0.5$ to 0.5 ($K = -0.5$ to 0.5) and in $(0, 0, L)$ from $L = -0.3$ to 0.3, with a zero-field data set taken at $T = 0.09$ K subtracted in each case.

As shown in Fig. 21 (Fig. 22) for the $[1, \bar{1}, 0]$ ($[0, 0, 1]$) field direction, the inelastic scattering along different high-symmetry directions in the scattering plane shows the same general features as the powder-averaged data in Figs. 8(a)–8(c) [8(d)–8(g)]. For both field directions, a continuum of scattering, with no obvious dispersion, separates from the net-negative quasielastic scattering and increases in energy and intensity with increasing field strength. As mentioned in Sec. VI, the lack of sharp spin waves in these measurements is consistent with expectations for a small value of θ (see Appendix D).

APPENDIX G: THE ENERGY-DEPENDENCE OF DIFFUSE SCATTERING IN A $[1, \bar{1}, 0]$ MAGNETIC FIELD

As our time of flight neutron scattering measurements provide energy resolution on a $\sim$0.1 meV scale, it is also possible to examine the energy dependence of the diffuse planes of scattering originating from the β chains. This is particularly interesting and important to examine in this case of $Ce_2Zr_2O_7$ in a $[1, \bar{1}, 0]$ magnetic field, as the planes of diffuse scattering are only evident in subtractions of zero-field data sets from finite-field data sets at $T = 0.03$ K, and this difference is *negative* (as can be seen in Figs. 4–6) meaning that the zero-field quasielastic scattering is more intense than the finite-field quasielastic diffuse scattering (this is clearly not the case for the elastic scattering associated with field-induced magnetic Bragg peaks). This negative quasielastic net scattering that we measure is consistent with the calculations shown in Fig. 9, where the zero-field quasielastic scattering is more intense than the in-field quasielastic scattering everywhere except at magnetic Bragg peak positions.

Figures 23(a), 23(b), and 23(c) show three integration ranges in reciprocal space that we use to examine the energy dependence of the measured diffuse scattering signal: One centered on the plane of β-chain scattering at $H = 0$, which appears as a rod along $(0, 0, L)$ in Fig. 23(a), one between the rods of scattering and centered on $(0.5, 0.5, L)$ in Fig. 23(b), and one centered on the second plane of β-chain scattering at $H = 1$, which appears as a rod along $(1, 1, L)$ in Fig. 23(c). Specifically, the black rectangle of integration in Fig. 23(a) is defined by $L = [0.75, 1.75]$, $H = [-0.25, 0.25]$, the black rectangle of integration in Fig. 23(b) is defined by $L = [0.5, 1.5]$, $H = [0.25, 0.75]$, and the black rectangle of integration in Fig. 23(c) is defined by $L = [-0.5, 0.5]$, $H = [0.75, 1.25]$. Each of these employ the same integration normal to the (H, H, L) plane, which is a $(K, \bar{K}, 0)$ integration from $K = -0.3$ to 0.3. The varying L range employed over the three black rectangles of integration results from avoiding both the oversubtracted (blue intensity) powder ring, and the region near $Q = 0$.

Figures 23(d)–23(f) shows the energy dependence of the measured diffuse scattering for the net data in the integration range in Figs. 23(a)–23(c). Clearly Figs. 23(d)–23(f) show an easily observable decrease in elastic and quasielastic scattering in a magnetic field compared to zero field as previously discussed. The negative net intensities in the field-subtracted data, both centered on the planes of scattering [Figs. 23(d), and 23(f)] and centered between planes [Fig. 23(e)], have energy dependencies that peak at slightly positive energies even though the zero-field data sets themselves are centered on $E = 0$ meV, as shown in Figs. 23(g)–23(i). This is consistent with the fact that the quasielastic scattering from the QSI phase in zero field, that is, the scattering being subtracted and leading to negative net-scattering, is centered at slightly positive energies. Furthermore, as shown in Figs. 23(j) and 23(k), a subtraction of the net intensities centered on a plane of scattering, from that centered between the planes of scattering, shows that the planes of scattering due to the β chains are approximately elastic with center at $E \approx 0$ meV within resolution of the measurements. We refer to this diffuse scattering as quasielastic in the main text as higher-resolution measurements would be needed to definitively determine whether the measured scattering is elastic or inelastic (or more precisely, to decompose any elastic and inelastic portions of the measured quasielastic signal).

Figure 23(j) shows that the elastic intensity associated with the plane of scattering at $H = 0$ is approximately constant in intensity at $h = 0.35$ T and 1.5 T, but then decreases in intensity by a factor of $\sim$3 at $h = 4$ T, in comparison to the intensity of the scattering between the planes of diffuse scattering. On the other hand, Fig. 23(k) shows that the elastic intensity associated with the plane of scattering at $H = 1$ is weaker at $h = 0.35$ T and $h = 1.5$ T than at $h = 4$ T. Comparison of Figs. 23(j) and 23(k) shows that the decrease in scattering at $h = 4$ T, for the plane at $H = 0$ in comparison to the scattering between the diffuse planes, is met with an approximately equal increase in scattering for the plane at $H = 1$ in comparison to the scattering between the diffuse planes. This migration of intensity between the planes at $H = 0$ and $H = 1$ is consistent with conclusions drawn from the $\mathbf{Q}$ dependence of the diffuse scattering shown in Figs. 4(a)–4(c), 5(a)–5(c), and 6(c).

[1] J. S. Gardner, M. J. P. Gingras, and J. E. Greedan, Magnetic pyrochlore oxides, Rev. Mod. Phys. **82**, 53 (2010).
[2] M. J. P. Gingras and P. A. McClarty, Quantum spin ice: A search for gapless quantum spin liquids in pyrochlore magnets, Rep. Prog. Phys. **77**, 056501 (2014).
[3] A. M. Hallas, J. Gaudet, and B. D. Gaulin, Experimental insights into ground-state selection of quantum XY pyrochlores, Annu. Rev. Condens. Matter Phys. **9**, 105 (2018).
[4] J. G. Rau and M. J. Gingras, Frustrated quantum rare-earth pyrochlores, Annu. Rev. Condens. Matter Phys. **10**, 357 (2019).
[5] A. P. Ramirez, Strongly geometrically frustrated magnets, Annu. Rev. Mater. Sci. **24**, 453 (1994).
[6] A. P. Ramirez, Geometrical frustration in magnetism, Czech. J. Phys. **46**, 3247 (1996).
[7] J. E. Greedan, Frustrated rare earth magnetism: Spin glasses, spin liquids and spin ices in pyrochlore oxides, J. Alloys Compd. **408-412**, 444 (2006).
[8] R. Moessner and A. P. Ramirez, Geometrical frustration, Phys. Today **59**, 24 (2006).
[9] S. H. Curnoe, Quantum spin configurations in $Tb_2Ti_2O_7$, Phys. Rev. B **75**, 212404 (2007).
[10] S. Onoda and Y. Tanaka, Quantum fluctuations in the effective pseudospin-$\frac{1}{2}$ model for magnetic pyrochlore oxides, Phys. Rev. B **83**, 094411 (2011).
[11] Y.-P. Huang, G. Chen, and M. Hermele, Quantum Spin Ices and Topological Phases from Dipolar-Octupolar Doublets on the Pyrochlore Lattice, Phys. Rev. Lett. **112**, 167203 (2014).
[12] Y.-D. Li and G. Chen, Symmetry enriched U(1) topological orders for dipole-octupole doublets on a pyrochlore lattice, Phys. Rev. B **95**, 041106(R) (2017).
[13] J. Gaudet, E. M. Smith, J. Dudemaine, J. Beare, C. R. C. Buhariwalla, N. P. Butch, M. B. Stone, A. I. Kolesnikov, G. Xu, D. R. Yahne, K. A. Ross, C. A. Marjerrison, J. D. Garrett, G. M. Luke, A. D. Bianchi, and B. D. Gaulin, Quantum Spin Ice Dynamics in the Dipole-Octupole Pyrochlore Magnet $Ce_2Zr_2O_7$, Phys. Rev. Lett. **122**, 187201 (2019).
[14] B. Gao, T. Chen, D. Tam, C.-L. Huang, K. Sasmal, D. Adroja, F. Ye, H. Cao, G. Sala, M. Stone *et al.*, Experimental signatures of a three-dimensional quantum spin liquid in effective spin-1/2 $Ce_2Zr_2O_7$ pyrochlore, Nat. Phys. **15**, 1052 (2019).
[15] A. S. Patri, M. Hosoi, and Y. B. Kim, Distinguishing dipolar and octupolar quantum spin ices using contrasting magnetostriction signatures, Phys. Rev. Res. **2**, 023253 (2020).
[16] O. Benton, Quantum origins of moment fragmentation in $Nd_2Zr_2O_7$, Phys. Rev. B **94**, 104430 (2016).
[17] O. Benton, Ground-state phase diagram of dipolar-octupolar pyrochlores, Phys. Rev. B **102**, 104408 (2020).
[18] C.-J. Huang, C. Liu, Z. Meng, Y. Yu, Y. Deng, and G. Chen, Extended Coulomb liquid of paired hardcore boson model on a pyrochlore lattice, Phys. Rev. Res. **2**, 042022(R) (2020).
[19] M. Hosoi, E. Z. Zhang, A. S. Patri, and Y. B. Kim, Uncovering Footprints of Dipolar-Octupolar Quantum Spin Ice from Neutron Scattering Signatures, Phys. Rev. Lett. **129**, 097202 (2022).
[20] F. Desrochers, L. E. Chern, and Y. B. Kim, Competing $U(1)$ and $\mathbb{Z}_2$ dipolar-octupolar quantum spin liquids on the pyrochlore lattice: Application to $Ce_2Zr_2O_7$, Phys. Rev. B **105**, 035149 (2022).
[21] A. Banerjee, S. V. Isakov, K. Damle, and Y. B. Kim, Unusual Liquid State of Hard-Core Bosons on the Pyrochlore Lattice, Phys. Rev. Lett. **100**, 047208 (2008).
[22] O. Benton, O. Sikora, and N. Shannon, Seeing the light: Experimental signatures of emergent electromagnetism in a quantum spin ice, Phys. Rev. B **86**, 075154 (2012).
[23] N. Shannon, O. Sikora, F. Pollmann, K. Penc, and P. Fulde, Quantum Ice: A Quantum Monte Carlo Study, Phys. Rev. Lett. **108**, 067204 (2012).
[24] L. Savary and L. Balents, Quantum spin liquids: A review, Rep. Prog. Phys. **80**, 016502 (2017).
[25] E. M. Smith, O. Benton, D. R. Yahne, B. Placke, R. Schäfer, J. Gaudet, J. Dudemaine, A. Fitterman, J. Beare, A. R. Wildes, S. Bhattacharya, T. DeLazzer, C. R. C. Buhariwalla, N. P. Butch, R. Movshovich, J. D. Garrett, C. A. Marjerrison, J. P. Clancy, E. Kermarrec, G. M. Luke, A. D. Bianchi, K. A. Ross, and B. D. Gaulin, Case for a $U(1)_\pi$ Quantum Spin Liquid Ground State in the Dipole-Octupole Pyrochlore $Ce_2Zr_2O_7$, Phys. Rev. X **12**, 021015 (2022).
[26] A. Bhardwaj, S. Zhang, H. Yan, R. Moessner, A. Nevidomskyy, and H. Changlani, Sleuthing out exotic quantum spin liquidity in the pyrochlore magnet $Ce_2Zr_2O_7$, npj Quantum Mater. **7**, 51 (2022).
[27] R. Sibille, E. Lhotel, V. Pomjakushin, C. Baines, T. Fennell, and M. Kenzelmann, Candidate Quantum Spin Liquid in the Ce^{3+} Pyrochlore Stannate $Ce_2Sn_2O_7$, Phys. Rev. Lett. **115**, 097202 (2015).
[28] R. Sibille, N. Gauthier, E. Lhotel, V. Porée, V. Pomjakushin, R. A. Ewings, T. G. Perring, J. Ollivier, A. Wildes, C. Ritter *et al.*, A quantum liquid of magnetic octupoles on the pyrochlore lattice, Nat. Phys. **16**, 546 (2020).
[29] V. Porée, H. Yan, F. Desrochers, S. Petit, E. Lhotel, M. Appel, J. Ollivier, Y. B. Kim, A. H. Nevidomskyy, and R. Sibille, Fractional matter coupled to the emergent gauge field in a quantum spin ice, arXiv:2304.05452.
[30] D. R. Yahne, B. Placke, R. Schäfer, O. Benton, R. Moessner, M. Powell, J. W. Kolis, C. M. Pasco, A. F. May, M. D. Frontzek *et al.*, Dipolar spin ice regime proximate to an all-in-all-out Néel ground state in the dipolar-octupolar pyrochlore $Ce_2Sn_2O_7$, arXiv:2211.15140.
[31] V. Porée, E. Lhotel, S. Petit, A. Krajewska, P. Puphal, A. H. Clark, V. Pomjakushin, H. C. Walker, N. Gauthier, D. J. Gawryluk, and R. Sibille, Crystal-field states and defect levels in candidate quantum spin ice $Ce_2Hf_2O_7$, Phys. Rev. Mater. **6**, 044406 (2022).
[32] V. Porée, A. Bhardwaj, E. Lhotel, S. Petit, N. Gauthier, H. Yan, V. Pomjakushin, J. Ollivier, J. A. Quilliam, A. H. Nevidomskyy, H. J. Changlani, and R. Sibille, Dipolar-octupolar correlations and hierarchy of exchange interactions in $Ce_2Hf_2O_7$, arXiv:2305.08261.
[33] S.-i. Yoshida, K. Nemoto, and K. Wada, Ordered phase of dipolar spin ice under [110] magnetic field, J. Phys. Soc. Jpn. **73**, 1619 (2004).
[34] B. Placke, R. Moessner, and O. Benton, Hierarchy of energy scales and field-tunable order by disorder in dipolar-octupolar pyrochlores, Phys. Rev. B **102**, 245102 (2020).
[35] M. J. Harris, S. T. Bramwell, D. F. McMorrow, T. Zeiske, and K. W. Godfrey, Geometrical Frustration in the Ferromagnetic Pyrochlore $Ho_2Ti_2O_7$, Phys. Rev. Lett. **79**, 2554 (1997).

[36] T. Fennell, O. A. Petrenko, B. Fåk, J. S. Gardner, S. T. Bramwell, and B. Ouladdiaf, Neutron scattering studies of the spin ices $Ho_2Ti_2O_7$ and $Dy_2Ti_2O_7$ in applied magnetic field, Phys. Rev. B **72**, 224411 (2005).

[37] J. P. Clancy, J. P. C. Ruff, S. R. Dunsiger, Y. Zhao, H. A. Dabkowska, J. S. Gardner, Y. Qiu, J. R. D. Copley, T. Jenkins, and B. D. Gaulin, Revisiting static and dynamic spin-ice correlations in $Ho_2Ti_2O_7$ with neutron scattering, Phys. Rev. B **79**, 014408 (2009).

[38] T. Fennell, O. A. Petrenko, G. Balakrishnan, S. T. Bramwell, J. D. M. Champion, B. Fåk, M. J. Harris, and D. M. Paul, Field-induced partial order in the spin ice dysprosium titanate, Appl. Phys. A **74**, s889 (2002).

[39] J. P. C. Ruff, R. G. Melko, and M. J. P. Gingras, Finite-Temperature Transitions in Dipolar Spin Ice in a Large Magnetic Field, Phys. Rev. Lett. **95**, 097202 (2005).

[40] J. Xu, A. T. M. N. Islam, I. N. Glavatskyy, M. Reehuis, J.-U. Hoffmann, and B. Lake, Field-induced quantum spin-$\frac{1}{2}$ chains and disorder in $Nd_2Zr_2O_7$, Phys. Rev. B **98**, 060408(R) (2018).

[41] S. Petit, E. Lhotel, B. Canals, M. Ciomaga Hatnean, J. Ollivier, H. Mutka, E. Ressouche, A. R. Wildes, M. R. Lees, and G. Balakrishnan, Observation of magnetic fragmentation in spin ice, Nat. Phys. **12**, 746 (2016).

[42] E. Lhotel, S. Petit, S. Guitteny, O. Florea, M. Ciomaga Hatnean, C. Colin, E. Ressouche, M. R. Lees, and G. Balakrishnan, Fluctuations and All-In–All-Out Ordering in Dipole-Octupole $Nd_2Zr_2O_7$, Phys. Rev. Lett. **115**, 197202 (2015).

[43] J. Xu, V. K. Anand, A. K. Bera, M. Frontzek, D. L. Abernathy, N. Casati, K. Siemensmeyer, and B. Lake, Magnetic structure and crystal-field states of the pyrochlore antiferromagnet $Nd_2Zr_2O_7$, Phys. Rev. B **92**, 224430 (2015).

[44] J. Xu, C. Balz, C. Baines, H. Luetkens, and B. Lake, Spin dynamics of the ordered dipolar-octupolar pseudospin-$\frac{1}{2}$ pyrochlore $Nd_2Zr_2O_7$ probed by muon spin relaxation, Phys. Rev. B **94**, 064425 (2016).

[45] L. Opherden, J. Hornung, T. Herrmannsdörfer, J. Xu, A. T. M. N. Islam, B. Lake, and J. Wosnitza, Evolution of antiferromagnetic domains in the all-in-all-out ordered pyrochlore $Nd_2Zr_2O_7$, Phys. Rev. B **95**, 184418 (2017).

[46] J. Xu, O. Benton, A. T. M. N. Islam, T. Guidi, G. Ehlers, and B. Lake, Order out of a Coulomb Phase and Higgs Transition: Frustrated Transverse Interactions of $Nd_2Zr_2O_7$, Phys. Rev. Lett. **124**, 097203 (2020).

[47] A. P. Ramirez, A. Hayashi, R. J. Cava, R. Siddharthan, and B. S. Shastry, Zero-point entropy in 'spin ice', Nature (London) **399**, 333 (1999).

[48] S. T. Bramwell, M. J. Harris, B. C. den Hertog, M. J. P. Gingras, J. S. Gardner, D. F. McMorrow, A. R. Wildes, A. Cornelius, J. D. M. Champion, R. G. Melko, and T. Fennell, Spin Correlations in $Ho_2Ti_2O_7$: A Dipolar Spin Ice System, Phys. Rev. Lett. **87**, 047205 (2001).

[49] T. Fennell, P. P. Deen, A. R. Wildes, K. Schmalzl, D. Prabhakaran, A. T. Boothroyd, R. J. Aldus, D. F. McMorrow, and S. T. Bramwell, Magnetic Coulomb phase in the spin ice $Ho_2Ti_2O_7$, Science **326**, 415 (2009).

[50] D. J. P. Morris, D. A. Tennant, S. A. Grigera, B. Klemke, C. Castelnovo, R. Moessner, C. Czternasty, M. Meissner, K. C. Rule, J.-U. Hoffmann *et al.*, Dirac strings and magnetic monopoles in the spin ice $Dy_2Ti_2O_7$, Science **326**, 411 (2009).

[51] S. T. Bramwell and M. J. P. Gingras, Spin ice state in frustrated magnetic pyrochlore materials, Science **294**, 1495 (2001).

[52] J. G. Rau and M. J. P. Gingras, Magnitude of quantum effects in classical spin ices, Phys. Rev. B **92**, 144417 (2015).

[53] R. G. Melko and M. J. P. Gingras, Monte Carlo studies of the dipolar spin ice model, J. Phys.: Condens. Matter **16**, R1277 (2004).

[54] G. Ehlers, A. A. Podlesnyak, J. L. Niedziela, E. B. Iverson, and P. E. Sokol, The new cold neutron chopper spectrometer at the Spallation Neutron Source: Design and performance, Rev. Sci. Instrum. **82**, 085108 (2011).

[55] G. Ehlers, A. A. Podlesnyak, and A. I. Kolesnikov, The Cold Neutron Chopper Spectrometer at the Spallation Neutron Source—A review of the first 8 years of operation, Rev. Sci. Instrum. **87**, 093902 (2016).

[56] R. T. Azuah, L. R. Kneller, Y. Qiu, P. L. W. Tregenna-Piggott, C. M. Brown, J. R. D. Copley, and R. M. Dimeo, DAVE: A comprehensive software suite for the reduction, visualization, and analysis of low energy neutron spectroscopic data, J. Res. Natl. Inst. Stand. Technol. **114**, 341 (2009).

[57] B. Gao, T. Chen, H. Yan, C. Duan, C.-L. Huang, X. P. Yao, F. Ye, C. Balz, J. R. Stewart, K. Nakajima, S. Ohira-Kawamura, G. Xu, X. Xu, S.-W. Cheong, E. Morosan, A. H. Nevidomskyy, G. Chen, and P. Dai, Magnetic field effects in an octupolar quantum spin liquid candidate, Phys. Rev. B **106**, 094425 (2022).

[58] Z. Hiroi, K. Matsuhira, and M. Ogata, Ferromagnetic Ising spin chains emerging from the spin ice under magnetic field, J. Phys. Soc. Jpn. **72**, 3045 (2003).

[59] R. Applegate, N. R. Hayre, R. R. P. Singh, T. Lin, A. G. R. Day, and M. J. P. Gingras, Vindication of $Yb_2Ti_2O_7$ as a Model Exchange Quantum Spin Ice, Phys. Rev. Lett. **109**, 097205 (2012).

[60] B. Tang, E. Khatami, and M. Rigol, A short introduction to numerical linked-cluster expansions, Comput. Phys. Commun. **184**, 557 (2013).

[61] B. Tang, D. Iyer, and M. Rigol, Thermodynamics of two-dimensional spin models with bimodal random-bond disorder, Phys. Rev. B **91**, 174413 (2015).

[62] R. Schäfer, I. Hagymási, R. Moessner, and D. J. Luitz, Pyrochlore $S = \frac{1}{2}$ Heisenberg antiferromagnet at finite temperature, Phys. Rev. B **102**, 054408 (2020).

[63] R. Schäfer, Magnetic frustration in three dimensions, Ph.D. Dissertation, TU Dresden, Dresden, 2022.

[64] E. M. Smith, O. Benton, D. R. Yahne, B. Placke, R. Schäfer, J. Gaudet, J. Dudemaine, A. Fitterman, J. Beare, A. R. Wildes *et al.*, Reply to "Comment on: 'Case for a $U(1)_\pi$ quantum spin liquid ground state in the dipole-octupole pyrochlore $Ce_2Zr_2O_7$' ", arXiv:2209.14956.

[65] S. Rosenkranz, A. P. Ramirez, A. Hayashi, R. J. Cava, R. Siddharthan, and B. S. Shastry, Crystal-field interaction in the pyrochlore magnet $Ho_2Ti_2O_7$, J. Appl. Phys. **87**, 5914 (2000).

[66] M. Ruminy, E. Pomjakushina, K. Iida, K. Kamazawa, D. T. Adroja, U. Stuhr, and T. Fennell, Crystal-field parameters of the rare-earth pyrochlores $R_2Ti_2O_7$ (R = Tb, Dy, and Ho), Phys. Rev. B **94**, 024430 (2016).

[67] J. Gaudet, A. M. Hallas, C. R. C. Buhariwalla, G. Sala, M. B. Stone, M. Tachibana, K. Baroudi, R. J. Cava, and B. D. Gaulin, Magnetoelastically induced vibronic bound state in the spin-ice pyrochlore $Ho_2Ti_2O_7$, Phys. Rev. B **98**, 014419 (2018).

[68] Y. Jana, A. Sengupta, and D. Ghosh, Estimation of single ion anisotropy in pyrochlore $Dy_2Ti_2O_7$, a geometrically frustrated system, using crystal field theory, J. Magn. Magn. Mater. **248**, 7 (2002).

[69] M. Léger, E. Lhotel, M. Ciomaga Hatnean, J. Ollivier, A. R. Wildes, S. Raymond, E. Ressouche, G. Balakrishnan, and S. Petit, Spin Dynamics and Unconventional Coulomb Phase in $Nd_2Zr_2O_7$, Phys. Rev. Lett. **126**, 247201 (2021).

[70] E. Lhotel, S. Petit, M. Ciomaga Hatnean, J. Ollivier, H. Mutka, E. Ressouche, M. R. Lees, and G. Balakrishnan, Evidence for dynamic kagome ice, Nat. Commun. **9**, 3786 (2018).

[71] J. Xu, O. Benton, V. K. Anand, A. T. M. N. Islam, T. Guidi, G. Ehlers, E. Feng, Y. Su, A. Sakai, P. Gegenwart, and B. Lake, Anisotropic exchange Hamiltonian, magnetic phase diagram, and domain inversion of $Nd_2Zr_2O_7$, Phys. Rev. B **99**, 144420 (2019).

[72] E. Lieb, T. Schultz, and D. Mattis, Two soluble models of an antiferromagnetic chain, Ann. Phys. **16**, 407 (1961).

[73] O. Derzhko and T. Krokhmalskii, Numerical approach for the study of the spin-1/2 XY chains dynamic properties, Phys. Stat. Sol. (b) **208**, 221 (1998).

Chapter 4

Summary and Closing Remarks

4.1 Summary, Conclusions, and Closing Discussions

The collection of measurements presented in Publications I, II, and III of this thesis are consistent with a quantum spin ice ground state for the dipole-octupole pyrochlore $Ce_2Zr_2O_7$ in zero-field. The lack of both magnetic order and spin freezing shown in the magnetic susceptibility, zero-field heat capacity, and zero-field elastic neutron scattering measured from $Ce_2Zr_2O_7$, combined with the snowflake pattern of diffuse scattering measured from $Ce_2Zr_2O_7$ in zero field at low temperature, is consistent with expectations for a material with a low-temperature spin ice phase. These results are consistent with a separate study on $Ce_2Zr_2O_7$ in Ref. [22] and together such results form the basis for the general spin ice candidacy of $Ce_2Zr_2O_7$ at a qualitative level. It is worth mentioning that these results on $Ce_2Zr_2O_7$ have since been further corroborated by our new muon spin relaxation measurements on single crystal $Ce_2Zr_2O_7$ in Ref. [132], which also show a lack of both magnetic order and spin freezing, down to the lowest measured temperature of $T = 0.02$ K.

The spin ice candidacy of $Ce_2Zr_2O_7$ is further established and specified by fits of the nearest-neighbor exchange parameters for $Ce_2Zr_2O_7$. These fits use the XYZ Hamiltonian appropriate to the dipole-octupole symmetry of the $|J = 5/2,\ m_J = \pm 3/2\rangle$ CEF ground-state doublet estimated for $Ce_2Zr_2O_7$ in Publication I and Ref. [22]. These exchange-parameter fits also suggest a spin ice phase at low temperature in $Ce_2Zr_2O_7$, but further specify this phase as the low temperate ground state, and as a novel $\mathrm{U}(1)_\pi$ quantum spin ice phase. In further detail, our estimates of the nearest-neighbor exchange parameters for $Ce_2Zr_2O_7$ in Publications II and III of this thesis yield near identical results and in each case point towards a $\mathrm{U}(1)_\pi$ quantum spin ice ground state in zero field with $J_{\tilde{x}}$ and $J_{\tilde{y}}$ approximately equal to one another at $J_{\tilde{x}}, J_{\tilde{y}} \approx 0.063$ meV and much stronger than $J_{\tilde{z}} \approx 0.011$ meV, similar to one of the parameter sets suggested in the separate work on $Ce_2Zr_2O_7$ in Ref. [37]. Each of these studies yield an estimation of $\theta \approx 0$ for the rotation parameter θ, which mixes $\hat{S}^z$-dipoles with $\hat{S}^x$-octupoles and reduces the dipole-octupole Hamiltonian to the XYZ form. In other words, $\{x, y, z\} \approx \{\tilde{x}, \tilde{y}, \tilde{z}\}$ for $Ce_2Zr_2O_7$ such that $\hat{S}^{\tilde{z}}$ carries a significant magnetic dipole moment and insignificant octupole moment, while $\hat{S}^{\tilde{x}}$ and $\hat{S}^{\tilde{y}}$ each carry a significant magnetic octupole moment and insignificant dipole moment. This is particularly intriguing as it means that the proposed quantum spin ice ground state for $Ce_2Zr_2O_7$ is a novel one in which the underlying ice rule is a two-plus, two-minus rule for magnetic octupoles. In terms of pseudospins, this corresponds to a two-plus, two-minus rule for $\hat{S}^{\tilde{x}}$ if $J_{\tilde{x}} > J_{\tilde{y}}$, or a two-plus, two-minus rule for $\hat{S}^{\tilde{y}}$ if $J_{\tilde{y}} > J_{\tilde{x}}$.

Our estimates of the nearest-neighbor exchange parameters for $Ce_2Zr_2O_7$ in Publications II and III of this thesis suggest a quantum spin ice ground state, consistent with the full suite of measurements presented on $Ce_2Zr_2O_7$ in this thesis and in Refs. [22, 37, 132]. In contrast to this, for $Ce_2Sn_2O_7$, a lack of both magnetic order and spin freezing, combined with potential quantum spin ice correlations, has been reported at low temperature *but* experimental estimates of the exchange parameters for $Ce_2Sn_2O_7$ in Ref. [60] point towards a ground state with all-in, all-out order of magnetic dipoles and a long-ranged ordering temperature ($\sim$0.05 K) below the lowest-measured temperature for the vast majority of measurements performed on $Ce_2Sn_2O_7$ [30, 60, 119, 124]. Albeit, a different group has interpreted their measurements on $Ce_2Sn_2O_7$ in terms of an octupolar quantum spin ice ground state (Refs. [30, 124]), and these conflicting interpretations raise further question of the true magnetic ground state in $Ce_2Sn_2O_7$ and elucidate the possibility that the magnetic ground state may vary with how the $Ce_2Sn_2O_7$ samples are synthesized. Nonetheless, this alternative scenario for $Ce_2Sn_2O_7$ highlights the importance of our experimental estimates of the exchange parameters for $Ce_2Zr_2O_7$ in Publications II and III (and those in Ref. [37]), and specifically the fact that the estimates each correspond to a quantum spin ice ground state in the magnetic phase diagrams available in the literature for dipole-octupole pyrochlores [56, 57, 96–98]. Not only is this important due to the possibility of dipole ordering at very low temperature, as the situation for $Ce_2Sn_2O_7$ highlights, but also because octupolar ordering at *any* temperature would be elusive to the vast majority of measurement techniques typically used to investigate magnetic systems, as was discussed in Section 1.5.4 and is elaborated on in the following section.

The fact that our estimates yield $J_{\tilde{x}} \approx J_{\tilde{y}}$ for $Ce_2Zr_2O_7$ is a fortunate convenience that allows for further computation of directional-dependent quantities at finite temperature without knowledge of whether $J_{\tilde{x}}$ or $J_{\tilde{y}}$ is larger; While the magnetic ground state does depends on which one of these exchange parameters is larger, thermal fluctuations lead to near identical calculation results for our $J_{\tilde{x}} \gtrsim J_{\tilde{y}}$ and $J_{\tilde{y}} \lesssim J_{\tilde{x}}$ parameter sets at realistic temperatures, meaning these parameter sets are indistinguishable for almost all practical purposes. The current constraints placed on the nearest-neighbor exchange parameters of $Ce_2Hf_2O_7$ in Ref. [124] are also unable to determine whether $J_{\tilde{x}}$ or $J_{\tilde{y}}$ is larger, but with the constrains also suggesting that one of these exchange parameters is the dominant one by a significant amount for $Ce_2Hf_2O_7$, in contrast to our estimates for $Ce_2Zr_2O_7$. This amounts to multiple, significantly-distinct possibilities for the exchange parameters of $Ce_2Hf_2O_7$ based off the current constraints in Ref. [124]. This alternative scenario for $Ce_2Hf_2O_7$ highlights the convenience of having $J_{\tilde{x}} \approx J_{\tilde{y}}$ for $Ce_2Zr_2O_7$; Otherwise, additional measurements would need to complement those in Publication II, for example, in attempt to further constrain the exchange parameters of $Ce_2Zr_2O_7$, similar to how additional measurements will need to complement those in Ref. [124] for $Ce_2Hf_2O_7$ before estimates are arrived at beyond the level of constraints that leave multiple distinct options.

This fortunate near-equality of $J_{\tilde{x}}$ and $J_{\tilde{y}}$ for $Ce_2Zr_2O_7$ also has some interesting implications for the implied magnetic ground state which are worth highlighting. Along with implying that the quantum spin ice ground state is on the border of dipolar and octupolar character with regard to the symmetry of the emergent electric field, the near-equality of $J_{\tilde{x}}$ and $J_{\tilde{y}}$ for $Ce_2Zr_2O_7$ also leads to relatively large quantum fluctuations. One can see this quickly by examining the ring-exchange term using the same perturbation theory applied in Section 1.5.3, which for the values of $J_{\tilde{x}}$, $J_{\tilde{y}}$, and $J_{\tilde{z}}$ estimated for $Ce_2Zr_2O_7$ in this work, gives $g_{\text{eff}} \sim 12\frac{(0.011+0.062)^3}{64\cdot 0.063^2}$ meV $= 0.018$ meV which is $\sim 30\%$ of the largest exchange parameter. We use this perturbation theory here only to highlight the general size of the quantum fluctuations with a very rough approximation, as in fact, the quantum fluctuations are large enough that such a perturbation theory is not well-justified for actual use. For a magnetic field along the $[1, \bar{1}, 0]$ direction, the constraint $J_{\tilde{x}} \approx J_{\tilde{y}}$ for $Ce_2Zr_2O_7$ dictates that the field-decoupled β chains in $[1, \bar{1}, 0]$ field have nearly gapless excitations, so that the short-ranged ferromagnetic order of these quasi-one-dimensional chains is highly-dynamic.

More generally, the β chains in $Ce_2Zr_2O_7$ in a $[1, \bar{1}, 0]$ magnetic field are intriguing simply due to the fact that they possess the rare combination of quasi-one-dimensionality, field-decoupling, and a high degree of quantum fluctuations. Along with that, and other finer details, our study on $Ce_2Zr_2O_7$ in $[1, \bar{1}, 0]$ magnetic field shows clear evidence for tunability between the zero-field quantum spin ice ground state of two-plus, two-minus octupoles, and the long-ranged magnetic order of dipole moments in the polarized α chains. Similarly, our study on $Ce_2Zr_2O_7$ in $[0, 0, 1]$ magnetic field shows clear evidence for tunability between the zero-field quantum spin ice ground state and the $[0, 0, 1]$-polarized spin ice phase.

4.2 Future Directions

The non-spin-flip channel of our polarized neutron diffraction measurements in Publication II of this thesis, as well as the investigation of the finer features in our unpolarized diffuse scattering signal (Ref. [37]), show the clear need for a further understanding of interactions beyond the nearest-neighbor level in $Ce_2Zr_2O_7$. This is corroborated by our fits to the heat capacity in Publications II and III of this thesis, which show good agreement for all but the lowest measured temperatures, with clear room for improvement at these lowest measured temperatures where weak further-than-nearest neighbor interactions would begin to become significant. In fact, a similar trend is shown in our comparison in Ref. [132], of the Knight shift measured in muon spin rotation measurements on $Ce_2Zr_2O_7$, with the susceptibility calculated using the nearest-neighbor exchange parameters estimated in Publication III. Again, this comparison shows a high-level of agreement for all but the lowest temperatures measured. With all of this in mind, we reiterate that future directions of research on $Ce_2Zr_2O_7$ should include further investigation of interactions beyond nearest neighbors.

In Publication III of this thesis, we estimate a g_z value for $Ce_2Zr_2O_7$ which suggests mixing of the CEF ground state doublet beyond the pure $|J = 5/2,\ m_J = \pm 3/2\rangle$ doublet that was estimated for $Ce_2Zr_2O_7$ in Publication I of this thesis and in Ref. [22] by using the Stevens operator formalism for only the $J = 5/2$ states. References [30, 32] on $Ce_2Sn_2O_7$ and $Ce_2Hf_2O_7$ each include the $J = 7/2$ states in their CEF analysis and show evidence for a CEF ground state doublet that includes mixing of the dominant $|J = 5/2,\ m_J = \pm 3/2\rangle$ states with small amounts of the $|J = 7/2,\ m_J = \pm 3/2\rangle$ states, which also have dipole-octupole symmetry [51, 52]. However, introduction of $|J = 7/2,\ m_J = \pm 3/2\rangle$ states does not affect the value of g_z, and in fact, for an ideal pyrochlore structure, these are the only states that can be mixed with the dominant $|J = 5/2,\ m_J = \pm 3/2\rangle$ states in the approximation that the CEF is a perturbation to the spin-orbit coupling. This is because the action of the CEF Hamiltonian raises or lowers m_J by multiples of 3 for states of constant J and m_J [24], leaving only different $m_J = \pm 3/2$ states mixed with each other in the approximation that CEF states are linear combinations of states with well-define J and m_J, because $|m_J| \leq 7/2$ for Ce^{3+}. Accordingly, the introduction of non-dipole octupole terms comes from beyond the aforementioned approximation. Along with reducing g_z, such terms could be responsible for inducing a small nonzero g_{xy}, and weak non-DO pseudospin-pseudospin interaction terms in the Hamiltonian. In fact, this is particularly important for cerium-pyrochlores due to the relatively small spin orbit gap for the light rare-earth ion, Ce^{3+}, compared to other heavier rare-earth ions [21], and future investigations of $Ce_2Zr_2O_7$ should include studies which focus on estimating the CEF ground state past the aforementioned approximation. Additionally, deviations from perfect three-fold symmetry at the Ce^{3+} sites, due to small amounts of sample oxidation for example, could also introduce terms beyond $m_J = \pm 3/2$ states, as this introduces more terms into the CEF Hamiltonian and loosens the restriction that the CEF Hamiltonian typically raises or lowers m_J by multiples of 3 for pyrochlores [26, 27, 30].

Future investigation of additional terms beyond the XYZ Hamiltonian for $Ce_2Zr_2O_7$, such as any weak further-than-nearest neighbor or non-DO interactions for example, should make an effort to resolve some of the known discrepancies between calculations using the XYZ Hamiltonian and experiment, that have been outlined in Publications II and III of this thesis and in Refs. [37, 132]. This includes the non-spin-flip diffuse scattering and the finer features in the unpolarized diffuse scattering, which are related issues, the low-temperature inaccuracies of the heat capacity calculations, the peculiar field dependence of the inelastic neutron scattering signal in a $[0, 0, 1]$ magnetic field at high fields, and the reorientation of diffuse scattering at $\sim$4 T in a $[1, \bar{1}, 0]$ magnetic field.

Further studies focused solely on sample preparation, characterization, and optimization aspects for both powder and single crystal $Ce_2Zr_2O_7$ would be worthwhile studies given the rare quantum spin liquid phase that seems to exist at low temperature according to the current suite of measurements on $Ce_2Zr_2O_7$, and the corresponding analyses [1–3, 22, 37, 131, 132]. In short, it is known that sample oxidation levels are small but nonzero, as outlined in Publications I, II, and III of this thesis and in Refs. [22, 37, 132], and further efforts to reduce this oxidation level (the value of δ in $Ce^{3+}_{2-2\delta}Ce^{4+}_{2\delta}Zr_2O_{7+\delta}$) should be included in further investigations of this material. Additionally, theoretical investigations into the effect of small amounts of oxidation on the magnetic behavior and phase diagrams for dipole-octupole pyrochlores would be worthwhile; For $Ce_2Zr_2O_7$, this oxidation appears as nonmagnetic dilution in form of nonmagnetic Ce^{4+} ions being in place of the Ce^{3+} ions at random sites affected by the oxidation.

The majority of measurements presented in this thesis have insignificant direct sensitivity to the magnetic octupole moments in $Ce_2Zr_2O_7$, with our heat capacity measurements being a notable exception [3, 103]. For these measurements without direct sensitivity to the octupolar moments, an indirect sensitivity to the octupole moments and their exchange constants, $J_{\tilde{x}}$ and $J_{\tilde{y}}$, can be established in accordance with existing theory and relevant calculations, due to the fact that the behavior of the dipole moment will depend on the magnetic phase of the material and its corresponding behavior at the temperature of interest. This latter point may seem rather obvious taken on its own, but it is important to note that it is this dependence on the magnetic phase of the material and its corresponding behavior at the temperature of interest, which allows for theory to infer the behavior of the octupole moments from the phase implied by the behavior of the dipole moments. Nonetheless, future directions on $Ce_2Zr_2O_7$ should include more measurements with significant direct sensitivity to the octupolar magnetic moments. This could include neutron scattering measurements with a higher incident energy and larger Q range, planned specifically for good coverage over the high Q region around 8 $Å^{-1}$ where scattering from dipoles begins to become insignificant, and scattering from octupoles begins to become significant (due to the different magnetic form factors for dipoles and octupoles) [30, 105].

In Publication I of this thesis we identify a weak dispersionless excitation at $E \sim 100$ meV with intensity that decreases with increasing Q, which we attribute to a possible vibronic bound state between CEF excitation and phonon. This feature is also present at $E \sim 100$ meV in the inelastic neutron scattering data reported for $Ce_2Zr_2O_7$ in Ref. [22], and a similar feature is present in the high-energy inelastic neutron scattering data reported for $Ce_2Hf_2O_7$ in Ref. [32]. In contrast to this, the high-energy inelastic neutron scattering data reported for $Ce_2Sn_2O_7$ in Ref. [30] shows no signs for a potential vibronic bound state near $E \sim 100$ meV. Significant magnetoelastic coupling leading to the formation of a clear vibronic bound state has been reported for other rare-earth pyrochlore materials such as $Ho_2Ti_2O_7$ [72, 133], $Tb_2Ti_2O_7$ [134], and $Pr_2Zr_2O_7$ [135], for example, as well as other cerium-based magnets [136–142]. Interestingly, magnetoelastic coupling can have an effect on the dynamics of monopoles in spin ice materials [133]. Further investigation of the magnetoelastic coupling in cerium-based pyrochlores would be important and beneficial research, especially considering the currently-unknown origin of the feature at $E \sim 100$ meV in the inelastic neutron scattering signals measured from $Ce_2Zr_2O_7$ and $Ce_2Hf_2O_7$, which may be a vibronic bound state in each of these materials.

To end on a positive note, we finish by reiterating that initial studies on $Ce_2Zr_2O_7$, such as those included in this thesis, provide the crucial starting points that lay both the groundwork and motivation for pursing the aforementioned future-directions and beyond.

Bibliography

[1] J. Gaudet, E. M. Smith, J. Dudemaine, J. Beare, C. R. C. Buhariwalla, N. P. Butch, M. B. Stone, A. I. Kolesnikov, G. Xu, D. R. Yahne, K. A. Ross, C. A. Marjerrison, J. D. Garrett, G. M. Luke, A. D. Bianchi, and B. D. Gaulin, *Quantum Spin Ice Dynamics in the Dipole-Octupole Pyrochlore Magnet* $Ce_2Zr_2O_7$, Phys. Rev. Lett. **122**, 187201 (2019).

[2] E. M. Smith, O. Benton, D. R. Yahne, B. Placke, R. Schäfer, J. Gaudet, J. Dudemaine, A. Fitterman, J. Beare, A. R. Wildes, S. Bhattacharya, T. DeLazzer, C. R. C. Buhariwalla, N. P. Butch, R. Movshovich, J. D. Garrett, C. A. Marjerrison, J. P. Clancy, E. Kermarrec, G. M. Luke, A. D. Bianchi, K. A. Ross, and B. D. Gaulin, *Case for a U(1)*$_\pi$ *Quantum Spin Liquid Ground State in the Dipole-Octupole Pyrochlore* $Ce_2Zr_2O_7$, Phys. Rev. X **12**, 021015 (2022).

[3] E. M. Smith, J. Dudemaine, B. Placke, R. Schäfer, D. R. Yahne, T. DeLazzer, A. Fitterman, J. Beare, J. Gaudet, C. R. C. Buhariwalla, A. Podlesnyak, G. Xu, J. P. Clancy, R. Movshovich, G. M. Luke, K. A. Ross, R. Moessner, O. Benton, A. D. Bianchi, and B. D. Gaulin, *Quantum Spin Ice Response to a Magnetic Field in the Dipole-Octupole Pyrochlore* $Ce_2Zr_2O_7$, Phys. Rev. B **108**, 054438 (2023).

[4] K. Momma and F. Izumi, *VESTA3 for Three-Dimensional Visualization of Crystal, Volumetric and Morphology Data*, Journal of Applied Crystallography **44**, 1272–1276 (2011).

[5] A. P. Ramirez, *Strongly Geometrically Frustrated Magnets*, Annual Review of Materials Science **24**, 453–480 (1994).

[6] A. P. Ramirez, *Geometrical Frustration in Magnetism*, Czechoslovak Journal of Physics **46**, 3247–3254 (1996).

[7] J. E. Greedan, *Frustrated Rare Earth Magnetism: Spin Glasses, Spin Liquids and Spin Ices in Pyrochlore Oxides*, Journal of Alloys and Compounds **408-412**, 444–455 (2006).

[8] R. Moessner and A. P. Ramirez, *Geometrical Frustration*, Physics Today **59**, 24–29 (2006).

[9] J. S. Gardner, M. J. P. Gingras, and J. E. Greedan, *Magnetic Pyrochlore Oxides*, Rev. Mod. Phys. **82**, 53–107 (2010).

[10] M. J. P. Gingras and P. A. McClarty, *Quantum Spin Ice: A Search for Gapless Quantum Spin Liquids in Pyrochlore Magnets*, Rep. Prog. Phys **77**, 056501 (2014).

[11] A. M. Hallas, J. Gaudet, and B. D. Gaulin, *Experimental Insights into Ground-State Selection of Quantum XY Pyrochlores*, Annu. Rev. Condens. Matter Phys **9**, 105–124 (2018).

[12] J. G. Rau and M. J. Gingras, *Frustrated Quantum Rare-Earth Pyrochlores*, Annu. Rev. Condens. Matter Phys **10**, 357–386 (2019).

[13] N. W. Ashcroft and N. D. Mermin, *Solid State Physics* (Saunders College Publishing, 1976).

[14] S. J. Blundell, *Magnetism in Condensed Matter* (Oxford University Press, 2001).

[15] J. J. Sakurai and J. Napolitano, *Modern Quantum Mechanics, Second Edition* (Pearson, 2010).

[16] S. Rosenkranz, A. P. Ramirez, A. Hayashi, R. J. Cava, R. Siddharthan, and B. S. Shastry, *Crystal-Field Interaction in the Pyrochlore Magnet* $Ho_2Ti_2O_7$, Journal of Applied Physics **87**, 5914–5916 (2000).

[17] J. Gaudet, D. D. Maharaj, G. Sala, E. Kermarrec, K. A. Ross, H. A. Dabkowska, A. I. Kolesnikov, G. E. Granroth, and B. D. Gaulin, *Neutron Spectroscopic Study of Crystalline Electric Field Excitations in Stoichiometric and Lightly Stuffed* $Yb_2Ti_2O_7$, Phys. Rev. B **92**, 134420 (2015).

[18] M. Ruminy, E. Pomjakushina, K. Iida, K. Kamazawa, D. T. Adroja, U. Stuhr, and T. Fennell, *Crystal-Field Parameters of the Rare-Earth Pyrochlores* $R_2Ti_2O_7$ ($R =$ Tb, Dy, *and* Ho), Phys. Rev. B **94**, 024430 (2016).

[19] A. M. Hallas, J. Gaudet, M. N. Wilson, T. J. Munsie, A. A. Aczel, M. B. Stone, R. S. Freitas, A. M. Arevalo-Lopez, J. P. Attfield, M. Tachibana, C. R. Wiebe, G. M. Luke, and B. D. Gaulin, *XY Antiferromagnetic Ground State in the Effective* $S = \frac{1}{2}$ *Pyrochlore* $Yb_2Ge_2O_7$, Phys. Rev. B **93**, 104405 (2016).

[20] J. Gaudet, A. M. Hallas, A. I. Kolesnikov, and B. D. Gaulin, *Effect of Chemical Pressure on the Crystal Electric Field States of Erbium Pyrochlore Magnets*, Phys. Rev. B **97**, 024415 (2018).

[21] A. J. Freeman and R. E. Watson, *Theoretical Investigation of Some Magnetic and Spectroscopic Properties of Rare-Earth Ions*, Phys. Rev. **127**, 2058–2075 (1962).

[22] B. Gao, T. Chen, D. Tam, C.-L. Huang, K. Sasmal, D. Adroja, F. Ye, H. Cao, G. Sala, M. Stone, C. Baines, J. Barker, H. Hu, J.-H. Chung, X. Xu, S.-W. Cheong, M. Nallaiyan, S. Spagna, M. Maple, and P. Dai, *Experimental Signatures of a Three-Dimensional Quantum Spin Liquid in Effective Spin*-1/2 $Ce_2Zr_2O_7$ *Pyrochlore*, Nat. Phys. **15**, 1052–1057 (2019).

[23] J. Xu, C. Balz, C. Baines, H. Luetkens, and B. Lake, *Spin Dynamics of the Ordered Dipolar-Octupolar Pseudospin-*$\frac{1}{2}$ *Pyrochlore* $Nd_2Zr_2O_7$ *Probed by Muon Spin Relaxation*, Phys. Rev. B **94**, 064425 (2016).

[24] A. Bertin, Y. Chapuis, P. D. de Réotier, and A. Yaouanc, *Crystal Electric Field in the* $R_2Ti_2O_7$ *Pyrochlore Compounds*, Journal of Physics: Condensed Matter **24**, 256003 (2012).

[25] K. W. H. Stevens, *Matrix Elements and Operator Equivalents Connected with the Magnetic Properties of Rare Earth Ions*, Proceedings of the Physical Society. Section A **65**, 209 (1952).

[26] M. Hutchings, *Point-Charge Calculations of Energy Levels of Magnetic Ions in Crystalline Electric Fields*, Solid State Physics **16**, 227–273 (1964).

[27] J. L. Prather, *Atomic Energy Levels in Crystals*, National Institute of Standards and Technology, Gaithersburg, MD, NBS MONO 19 (1961).

[28] B. Z. Malkin, A. R. Zakirov, M. N. Popova, S. A. Klimin, E. P. Chukalina, E. Antic-Fidancev, P. Goldner, P. Aschehoug, and G. Dhalenne, *Optical Spectroscopy of* $Yb_2Ti_2O_7$ *and* $Y_2Ti_2O_7$*:* Yb^{3+} *and Crystal-Field Parameters in Rare-Earth Titanate Pyrochlores*, Phys. Rev. B **70**, 075112 (2004).

[29] Z. Dun, X. Bai, M. B. Stone, H. Zhou, and M. Mourigal, *Effective Point-Charge Analysis of Crystal Fields: Application to Rare-Earth Pyrochlores and Tripod Kagome Magnets* $R_3Mg_2Sb_3O_{14}$, Phys. Rev. Res. **3**, 023012 (2021).

[30] R. Sibille, N. Gauthier, E. Lhotel, V. Porée, V. Pomjakushin, R. Ewings, T. Perring, J. Ollivier, A. Wildes, C. Ritter, T. Hansen, D. Keen, G. Nilsen, L. Keller, S. Petit, and T. Fennell, *A Quantum Liquid of Magnetic Octupoles on the Pyrochlore Lattice*, Nat. Phys. **16**, 546–552 (2020).

[31] N. Kabeya, S. Takahara, T. Arisumi, S. Kimura, K. Araki, K. Katoh, and A. Ochiai, *Eigenstate Analysis of the Crystal Electric Field at Low-Symmetry Sites: Application for an Orthogonal Site in the Tetragonal Crystal* Ce_2Pd_2Pb, Phys. Rev. B **105**, 014419 (2022).

[32] V. Porée, E. Lhotel, S. Petit, A. Krajewska, P. Puphal, A. H. Clark, V. Pomjakushin, H. C. Walker, N. Gauthier, D. J. Gawryluk, and R. Sibille, *Crystal-Field States and Defect Levels in Candidate Quantum Spin Ice* $Ce_2Hf_2O_7$, Phys. Rev. Materials **6**, 044406 (2022).

[33] J. Xu, V. K. Anand, A. K. Bera, M. Frontzek, D. L. Abernathy, N. Casati, K. Siemensmeyer, and B. Lake, *Magnetic Structure and Crystal-Field States of the Pyrochlore Antiferromagnet* $Nd_2Zr_2O_7$, Phys. Rev. B **92**, 224430 (2015).

[34] C. Mauws, A. M. Hallas, G. Sala, A. A. Aczel, P. M. Sarte, J. Gaudet, D. Ziat, J. A. Quilliam, J. A. Lussier, M. Bieringer, H. D. Zhou, A. Wildes, M. B. Stone, D. Abernathy, G. M. Luke, B. D. Gaulin, and C. R. Wiebe, *Dipolar-Octupolar Ising Antiferromagnetism in* $Sm_2Ti_2O_7$*: A Moment Fragmentation Candidate*, Phys. Rev. B **98**, 100401 (2018).

[35] K. A. Ross, L. Savary, B. D. Gaulin, and L. Balents, *Quantum Excitations in Quantum Spin Ice*, Phys. Rev. X **1**, 021002 (2011).

[36] Z. Dun, X. Bai, J. A. M. Paddison, E. Hollingworth, N. P. Butch, C. D. Cruz, M. B. Stone, T. Hong, F. Demmel, M. Mourigal, and H. Zhou, *Quantum Versus Classical Spin Fragmentation in Dipolar Kagome Ice* $Ho_3Mg_2Sb_3O_{14}$, Phys. Rev. X **10**, 031069 (2020).

[37] A. Bhardwaj, S. Zhang, H. Yan, R. Moessner, A. H. Nevidomskyy, and H. J. Changlani, *Sleuthing out Exotic Quantum Spin Liquidity in the Pyrochlore Magnet* $Ce_2Zr_2O_7$, npj Quantum Materials **7**, 51 (2022).

[38] L. Savary, K. A. Ross, B. D. Gaulin, J. P. C. Ruff, and L. Balents, *Order by Quantum Disorder in* $Er_2Ti_2O_7$, Phys. Rev. Lett. **109**, 167201 (2012).

[39] J. G. Rau and M. J. P. Gingras, *Magnitude of Quantum Effects in Classical Spin Ices*, Phys. Rev. B **92**, 144417 (2015).

[40] Y. Li, G. Chen, W. Tong, L. Pi, J. Liu, Z. Yang, X. Wang, and Q. Zhang, *Rare-Earth Triangular Lattice Spin Liquid: A Single-Crystal Study of* $YbMgGaO_4$, Phys. Rev. Lett. **115**, 167203 (2015).

[41] J. G. Rau, L. S. Wu, A. F. May, L. Poudel, B. Winn, V. O. Garlea, A. Huq, P. Whitfield, A. E. Taylor, M. D. Lumsden, M. J. P. Gingras, and A. D. Christianson, *Anisotropic Exchange within Decoupled Tetrahedra in the Quantum Breathing Pyrochlore* $Ba_3Yb_2Zn_5O_{11}$, Phys. Rev. Lett. **116**, 257204 (2016).

[42] O. Benton, *Quantum Origins of Moment Fragmentation in* $Nd_2Zr_2O_7$, Phys. Rev. B **94**, 104430 (2016).

[43] J.-J. Wen, S. M. Koohpayeh, K. A. Ross, B. A. Trump, T. M. McQueen, K. Kimura, S. Nakatsuji, Y. Qiu, D. M. Pajerowski, J. R. D. Copley, and C. L. Broholm, *Disordered Route to the Coulomb Quantum Spin Liquid: Random Transverse Fields on Spin Ice in* $Pr_2Zr_2O_7$, Phys. Rev. Lett. **118**, 107206 (2017).

[44] S. Lee, S. Onoda, and L. Balents, *Generic Quantum Spin Ice*, Phys. Rev. B **86**, 104412 (2012).

[45] A. M. Hallas, *The Effect of Chemical Pressure on the Magnetic Ground States of Rare Earth Pyrochlores*, PhD Thesis, McMaster University (2017).

[46] J. Gaudet, *Fragile Magnetism in Rare Earth XY Pyrochlores*, PhD Thesis, McMaster University (2018).

[47] A. Banerjee, S. V. Isakov, K. Damle, and Y. B. Kim, *Unusual Liquid State of Hard-Core Bosons on the Pyrochlore Lattice*, Phys. Rev. Lett. **100**, 047208 (2008).

[48] Y. Jana, A. Sengupta, and D. Ghosh, *Estimation of Single Ion Anisotropy in Pyrochlore* $Dy_2Ti_2O_7$*, a Geometrically Frustrated System, Using Crystal Field Theory*, Journal of Magnetism and Magnetic Materials **248**, 7–18 (2002).

[49] S. H. Curnoe, *Quantum Spin Configurations in* $Tb_2Ti_2O_7$, Phys. Rev. B **75**, 212404 (2007).

[50] S. Onoda and Y. Tanaka, *Quantum Fluctuations in the Effective Pseudospin-*$\frac{1}{2}$ *Model for Magnetic Pyrochlore Oxides*, Phys. Rev. B **83**, 094411 (2011).

[51] Y.-P. Huang, G. Chen, and M. Hermele, *Quantum Spin Ices and Topological Phases from Dipolar-Octupolar Doublets on the Pyrochlore Lattice*, Phys. Rev. Lett. **112**, 167203 (2014).

[52] Y.-D. Li and G. Chen, *Symmetry Enriched U(1) Topological Orders for Dipole-Octupole Doublets on a Pyrochlore Lattice*, Phys. Rev. B **95**, 041106(R) (2017).

[53] S. Simon, A. S. Patri, and Y. B. Kim, *Ultrasound Detection of Emergent Photons in Generic Quantum Spin Ice*, Phys. Rev. B **106**, 064427 (2022).

[54] P. A. McClarty, S. H. Curnoe, and M. J. P. Gingras, *Energetic Selection of Ordered States in a Model of the* $Er_2Ti_2O_7$ *Frustrated Pyrochlore XY Antiferromagnet*, Journal of Physics: Conference Series **145**, 012032 (2009).

[55] H. Yan, O. Benton, L. Jaubert, and N. Shannon, *Theory of Multiple-Phase Competition in Pyrochlore Magnets with Anisotropic Exchange with Application to* $Yb_2Ti_2O_7, Er_2Ti_2O_7$*, and* $Er_2Sn_2O_7$, Phys. Rev. B **95**, 094422 (2017).

[56] O. Benton, *Ground-state Phase Diagram of Dipolar-Octupolar Pyrochlores*, Phys. Rev. B **102**, 104408 (2020).

[57] M. Hosoi, E. Z. Zhang, A. S. Patri, and Y. B. Kim, *Uncovering Footprints of Dipolar-Octupolar Quantum Spin Ice from Neutron Scattering Signatures*, Phys. Rev. Lett. **129**, 097202 (2022).

[58] B. C. den Hertog and M. J. P. Gingras, *Dipolar Interactions and Origin of Spin Ice in Ising Pyrochlore Magnets*, Phys. Rev. Lett. **84**, 3430–3433 (2000).

[59] A. Scheie, J. Kindervater, S. Zhang, H. Changlani, G. Sala, G. Ehlers, A. Heinemann, G. Tucker, S. Koohpayeh, and C. Broholm, *Multiphase Magnetism in* $Yb_2Ti_2O_7$, Proc. Natl. Acad. Sci. U.S.A. **117**, 27245–27254 (2020).

[60] D. R. Yahne, B. Placke, R. Schäfer, O. Benton, R. Moessner, M. Powell, J. W. Kolis, C. M. Pasco, A. F. May, M. D. Frontzek, E. M. Smith, B. D. Gaulin, S. Calder, and K. A. Ross, *Dipolar Spin Ice Regime Proximate to an All-In-All-Out Néel Ground State in the Dipolar-Octupolar Pyrochlore* $Ce_2Sn_2O_7$, arXiv: 2211.15140 [cond-mat.str–el] (2022).

[61] V. Porée, A. Bhardwaj, E. Lhotel, S. Petit, N. Gauthier, H. Yan, V. Pomjakushin, J. Ollivier, J. A. Quilliam, A. H. Nevidomskyy, H. J. Changlani, and R. Sibille, *Dipolar-Octupolar Correlations and Hierarchy of Exchange Interactions in* $Ce_2Hf_2O_7$, arXiv: 2305.08261 [cond-mat.str–el] (2023).

[62] K. A. Ross, Y. Qiu, J. R. D. Copley, H. A. Dabkowska, and B. D. Gaulin, *Order by Disorder Spin Wave Gap in the XY Pyrochlore Magnet* $Er_2Ti_2O_7$, Phys. Rev. Lett. **112**, 057201 (2014).

[63] J. Robert, E. Lhotel, G. Remenyi, S. Sahling, I. Mirebeau, C. Decorse, B. Canals, and S. Petit, *Spin Dynamics in the Presence of Competing Ferromagnetic and Antiferromagnetic Correlations in* $Yb_2Ti_2O_7$, Phys. Rev. B **92**, 064425 (2015).

[64] J. D. Thompson, P. A. McClarty, D. Prabhakaran, I. Cabrera, T. Guidi, and R. Coldea, *Quasiparticle Breakdown and Spin Hamiltonian of the Frustrated Quantum Pyrochlore* $Yb_2Ti_2O_7$ *in a Magnetic Field*, Phys. Rev. Lett. **119**, 057203 (2017).

[65] A. M. Hallas, J. Gaudet, N. P. Butch, G. Xu, M. Tachibana, C. R. Wiebe, G. M. Luke, and B. D. Gaulin, *Phase Competition in the Palmer-Chalker XY Pyrochlore* $Er_2Pt_2O_7$, Phys. Rev. Lett. **119**, 187201 (2017).

[66] R. Sibille, N. Gauthier, H. Yan, M. Hatnean, J. Ollivier, B. Winn, U. Filges, G. Balakrishnan, M. Kenzelmann, N. Shannon, and T. Fennell, *Experimental Signatures of Emergent Quantum Electrodynamics in* $Pr_2Hf_2O_7$, Nature Physics **14**, 711–715 (2018).

[67] J. Xu, O. Benton, V. K. Anand, A. T. M. N. Islam, T. Guidi, G. Ehlers, E. Feng, Y. Su, A. Sakai, P. Gegenwart, and B. Lake, *Anisotropic Exchange Hamiltonian, Magnetic Phase Diagram, and Domain Inversion of* $Nd_2Zr_2O_7$, Phys. Rev. B **99**, 144420 (2019).

[68] J. A. Hodges, P. Bonville, A. Forget, M. Rams, K. Królas, and G. Dhalennem, *The Crystal Field and Exchange Interactions in* $Yb_2Ti_2O_7$, Journal of Physics: Condensed Matter **13**, 9301 (2001).

[69] S. T. Bramwell, M. J. Harris, B. C. den Hertog, M. J. P. Gingras, J. S. Gardner, D. F. McMorrow, A. R. Wildes, A. L. Cornelius, J. D. M. Champion, R. G. Melko, and T. Fennell, *Spin Correlations in* $Ho_2Ti_2O_7$*: A Dipolar Spin Ice System*, Phys. Rev. Lett. **87**, 047205 (2001).

[70] S. T. Bramwell and M. J. P. Gingras, *Spin Ice State in Frustrated Magnetic Pyrochlore Materials*, Science **294**, 1495–1501 (2001).

[71] S. T. Bramwell and M. J. Harris, *The History of Spin Ice*, Journal of Physics: Condensed Matter **32**, 374010 (2020).

[72] J. Gaudet, A. M. Hallas, C. R. C. Buhariwalla, G. Sala, M. B. Stone, M. Tachibana, K. Baroudi, R. J. Cava, and B. D. Gaulin, *Magnetoelastically Induced Vibronic Bound State in the Spin-Ice Pyrochlore* $Ho_2Ti_2O_7$, Phys. Rev. B **98**, 014419 (2018).

[73] T. Yavors'kii, T. Fennell, M. J. P. Gingras, and S. T. Bramwell, $Dy_2Ti_2O_7$ *Spin Ice: A Test Case for Emergent Clusters in a Frustrated Magnet*, Phys. Rev. Lett. **101**, 037204 (2008).

[74] A. W. C. Wong, Z. Hao, and M. J. P. Gingras, *Ground State Phase Diagram of Generic XY Pyrochlore Magnets with Quantum Fluctuations*, Phys. Rev. B **88**, 144402 (2013).

[75] H. Fukazawa, R. G. Melko, R. Higashinaka, Y. Maeno, and M. J. P. Gingras, *Magnetic Anisotropy of the Spin-Ice Compound* $Dy_2Ti_2O_7$, Phys. Rev. B **65**, 054410 (2002).

[76] J. M. Farmer, L. A. Boatner, B. C. Chakoumakos, M.-H. Du, M. J. Lance, C. J. Rawn, and J. C. Bryan, *Structural and Crystal Chemical Properties of Rare-Earth Titanate Pyrochlores*, Journal of Alloys and Compounds **605**, 63–70 (2014).

[77] E. Lhotel, S. Petit, M. Ciomaga Hatnean, J. Ollivier, H. Mutka, E. Ressouche, M. R. Lees, and G. Balakrishnan, *Evidence for Dynamic Kagome Ice*, Nature Communications **9**, 3786 (2018).

[78] P. W. Anderson, *Ordering and Antiferromagnetism in Ferrites*, Phys. Rev. **102**, 1008–1013 (1956).

[79] M. J. Harris, S. T. Bramwell, D. F. McMorrow, T. Zeiske, and K. W. Godfrey, *Geometrical Frustration in the Ferromagnetic Pyrochlore* $Ho_2Ti_2O_7$, Phys. Rev. Lett. **79**, 2554–2557 (1997).

[80] E. Lhotel, S. Petit, S. Guitteny, O. Florea, M. Ciomaga Hatnean, C. Colin, E. Ressouche, M. R. Lees, and G. Balakrishnan, *Fluctuations and All-In–All-Out Ordering in Dipole-Octupole* $Nd_2Zr_2O_7$, Phys. Rev. Lett. **115**, 197202 (2015).

[81] V. K. Anand, D. L. Abernathy, D. T. Adroja, A. D. Hillier, P. K. Biswas, and B. Lake, *Muon Spin Relaxation and Inelastic Neutron Scattering Investigations of the All-In, All-Out Antiferromagnet* $Nd_2Hf_2O_7$, Phys. Rev. B **95**, 224420 (2017).

[82] L. Opherden, J. Hornung, T. Herrmannsdörfer, J. Xu, A. T. M. N. Islam, B. Lake, and J. Wosnitza, *Evolution of Antiferromagnetic Domains in the All-In-All-Out Ordered Pyrochlore* $Nd_2Zr_2O_7$, Phys. Rev. B **95**, 184418 (2017).

[83] J. Xu, A. T. M. N. Islam, I. N. Glavatskyy, M. Reehuis, J.-U. Hoffmann, and B. Lake, *Field-Induced Quantum Spin-$\frac{1}{2}$ Chains and Disorder in* $Nd_2Zr_2O_7$, Phys. Rev. B **98**, 060408 (2018).

[84] J. Xu, O. Benton, A. T. M. N. Islam, T. Guidi, G. Ehlers, and B. Lake, *Order out of a Coulomb Phase and Higgs Transition: Frustrated Transverse Interactions of* $Nd_2Zr_2O_7$, Phys. Rev. Lett. **124**, 097203 (2020).

[85] A. P. Ramirez, A. Hayashi, R. J. Cava, R. Siddharthan, and B. S. Shastry, *Zero-Point Entropy in 'Spin Ice'*, Nature **399**, 333–335 (1999).

[86] L. Pauling, *The Structure and Entropy of Ice and of Other Crystals with Some Randomness of Atomic Arrangement*, Journal of the American Chemical Society **57**, 2680–2684 (1935).

[87] J. D. Bernal and R. H. Fowler, *A Theory of Water and Ionic Solution, with Particular Reference to Hydrogen and Hydroxyl Ions*, The Journal of Chemical Physics **1**, 515–548 (1933).

[88] T. Fennell, P. P. Deen, A. R. Wildes, K. Schmalzl, D. Prabhakaran, A. T. Boothroyd, R. J. Aldus, D. F. McMorrow, and S. T. Bramwell, *Magnetic Coulomb Phase in the Spin Ice* $Ho_2Ti_2O_7$, Science **326**, 415–417 (2009).

[89] D. J. P. Morris, D. A. Tennant, S. A. Grigera, B. Klemke, C. Castelnovo, R. Moessner, C. Czternasty, M. Meissner, K. C. Rule, J.-U. Hoffmann, K. Kiefer, S. Gerischer, D. Slobinsky, and R. S. Perry, *Dirac Strings and Magnetic Monopoles in the Spin Ice* $Dy_2Ti_2O_7$, Science **326**, 411–414 (2009).

[90] G. C. Lau, R. S. Freitas, B. G. Ueland, B. D. Muegge, E. L. Duncan, P. Schiffer, and R. J. Cava, *Zero-Point Entropy in Stuffed Spin-Ice*, Nature Physics **2**, 249–253 (2006).

[91] C. Castelnovo, R. Moessner, and S. L. Sondhi, *Magnetic Monopoles in Spin Ice*, Nature **451**, 42–45 (2008).

[92] L. D. C. Jaubert and P. C. W. Holdsworth, *Signature of Magnetic Monopole and Dirac string Dynamics in Spin Ice*, Nature Physics **5**, 258–261 (2009).

[93] O. Benton, O. Sikora, and N. Shannon, *Seeing the Light: Experimental Signatures of Emergent Electromagnetism in a Quantum Spin Ice*, Phys. Rev. B **86**, 075154 (2012).

[94] N. Shannon, O. Sikora, F. Pollmann, K. Penc, and P. Fulde, *Quantum Ice: A Quantum Monte Carlo Study*, Phys. Rev. Lett. **108**, 067204 (2012).

[95] L. Savary and L. Balents, *Quantum Spin Liquids: A Review*, Reports on Progress in Physics **80**, 016502 (2016).

[96] A. S. Patri, M. Hosoi, and Y. B. Kim, *Distinguishing Dipolar and Octupolar Quantum Spin Ices using Contrasting Magnetostriction Signatures*, Phys. Rev. Research **2**, 023253 (2020).

[97] F. Desrochers, L. E. Chern, and Y. B. Kim, *Competing U(1) and $\mathbb{Z}_2$ Dipolar-Octupolar Quantum Spin Liquids on the Pyrochlore Lattice: Application to* $Ce_2Zr_2O_7$, Phys. Rev. B **105**, 035149 (2022).

[98] C.-J. Huang, C. Liu, Z. Meng, Y. Yu, Y. Deng, and G. Chen, *Extended Coulomb Liquid of Paired Hardcore Boson Model on a Pyrochlore Lattice*, Phys. Rev. Research **2**, 042022(R) (2020).

[99] B. Placke, R. Moessner, and O. Benton, *Hierarchy of Energy Scales and Field-Tunable Order by Disorder in Dipolar-Octupolar Pyrochlores*, Phys. Rev. B **102**, 245102 (2020).

[100] M. Hermele, M. P. A. Fisher, and L. Balents, *Pyrochlore Photons: The U(1) Spin Liquid in a* $S = \frac{1}{2}$ *Three-Dimensional Frustrated Magnet*, Phys. Rev. B **69**, 064404 (2004).

[101] C.-J. Huang, Y. Deng, Y. Wan, and Z. Y. Meng, *Dynamics of Topological Excitations in a Model Quantum Spin Ice*, Phys. Rev. Lett. **120**, 167202 (2018).

[102] G. Chen, *Spectral Periodicity of the Spinon Continuum in Quantum Spin Ice*, Phys. Rev. B **96**, 085136 (2017).

[103] G. Chen, *Distinguishing Thermodynamics and Spectroscopy for Octupolar U(1) Spin Liquid of Ce-Pyrochlores*, arXiv: 2304.01892 [cond-mat.str–el] (2023).

[104] D. J. Griffiths, *Introduction to Electrodynamics*, 3rd ed. (Prentice Hall, 1999).

[105] E. M. Smith, O. Benton, D. R. Yahne, B. Placke, R. Schäfer, J. Gaudet, J. Dudemaine, A. Fitterman, J. Beare, A. R. Wildes, S. Bhattacharya, T. DeLazzer, C. R. C. Buhariwalla, N. P. Butch, R. Movshovich, J. D. Garrett, C. A. Marjerrison, J. P. Clancy, E. Kermarrec, G. M. Luke, A. D. Bianchi, K. A. Ross, and B. D. Gaulin, *Reply to "Comment on: 'Case for a $U(1)_\pi$ Quantum Spin Liquid Ground State in the Dipole-Octupole Pyrochlore* $Ce_2Zr_2O_7$*' "*, arXiv: 2209.14956 [cond-mat.str–el] (2022).

[106] K. Skold and D. Price, *Neutron Scattering, Volume 23A, First Edition* (Academic Press, 1986).

[107] G. Shirane, S. M. Shapiro, and J. M. Tranquada, *Neutron Scattering with a Triple-Axis Spectrometer: Basic Techniques* (Cambridge University Press, 2002).

[108] A. Garcia and E. M. Henley, *Subatomic Physics, Third Edition* (World Scientific Publishing, 2007).

[109] G. L. Squires, *Introduction to the Theory of Thermal Neutron Scattering* (Cambridge University Press, 2012).

[110] J. E. Sherwood, T. E. Stephenson, and S. Bernstein, *Stern-Gerlach Experiment on Polarized Neutrons*, Phys. Rev. **96**, 1546–1548 (1954).

[111] V. F. Sears, *Neutron Scattering Lengths and Cross Sections*, Neutron News **3**, 26–37 (1992).

[112] M. Schowalter, A. Rosenauer, J. T. Titantah, and D. Lamoen, *Temperature-Dependent Debye-Waller Factors for Semiconductors with the Wurtzite-Type Structure*, Acta Crystallogr A **65**, 227–231 (2009).

[113] J. F. Vetelino, S. P. Gaur, and S. S. Mitra, *Debye-Waller Factor for Zinc-Blende-Type Crystals*, Phys. Rev. B **5**, 2360–2366 (1972).

[114] L.-M. Peng, G. Ren, S. L. Dudarev, and M. J. Whelan, *Debye-Waller Factors and Absorptive Scattering Factors of Elemental Crystals*, Acta Crystallographica Section A **52**, 456–470 (1996).

[115] F. D. Vila, J. J. Rehr, H. H. Rossner, and H. J. Krappe, *Theoretical X-ray Absorption Debye-Waller Factors*, Phys. Rev. B **76**, 014301 (2007).

[116] E. J. Lisher and J. B. Forsyth, *Analytic Approximations to Form Factors*, Acta Crystallographica Section A **27**, 545–549 (1971).

[117] W. E. Grummit and G. Wilkinson, *Fission Products of* U235, Nature **158**, 163 (1946).

[118] J. Copley and J. Cook, *The Disk Chopper Spectrometer at NIST: A New Instrument for Quasielastic Neutron Scattering Studies*, Chemical Physics **292**, 477–485 (2003).

[119] R. Sibille, E. Lhotel, V. Pomjakushin, C. Baines, T. Fennell, and M. Kenzelmann, *Candidate Quantum Spin Liquid in the* Ce^{3+} *Pyrochlore Stannate* $Ce_2Sn_2O_7$, Phys. Rev. Lett. **115**, 097202 (2015).

[120] T. Fennell, O. A. Petrenko, B. Fåk, S. T. Bramwell, M. Enjalran, T. Yavors'kii, M. J. P. Gingras, R. G. Melko, and G. Balakrishnan, *Neutron Scattering Investigation of the Spin Ice State in* $Dy_2Ti_2O_7$, Phys. Rev. B **70**, 134408 (2004).

[121] A. M. Samarakoon, K. Barros, Y. W. Li, M. Eisenbach, Q. Zhang, F. Ye, V. Sharma, Z. L. Dun, H. Zhou, S. A. Grigera, C. D. Batista, and D. A. Tennant, *Machine-Learning-Assisted Insight into Spin Ice* $Dy_2Ti_2O_7$, Nature Communications **11**, 892 (2020).

[122] K. Kimura, S. Nakatsuji, J.-J. Wen, C. Broholm, M. B. Stone, E. Nishibori, and H. Sawa, *Quantum Fluctuations in Spin-Ice-Like* $Pr_2Zr_2O_7$, Nature Communications **4**, 1934 (2013).

[123] S. Petit, E. Lhotel, S. Guitteny, O. Florea, J. Robert, P. Bonville, I. Mirebeau, J. Ollivier, H. Mutka, E. Ressouche, C. Decorse, M. Ciomaga Hatnean, and G. Balakrishnan, *Antiferroquadrupolar Correlations in the Quantum Spin Ice Candidate* $Pr_2Zr_2O_7$, Phys. Rev. B **94**, 165153 (2016).

[124] V. Porée, H. Yan, F. Desrochers, S. Petit, E. Lhotel, M. Appel, J. Ollivier, Y. B. Kim, A. H. Nevidomskyy, and R. Sibille, *Fractional Matter Coupled to the Emergent Gauge Field in a Quantum Spin Ice*, arXiv: 2304.05452 [cond-mat.str–el] (2023).

[125] Y. Kato and S. Onoda, *Numerical Evidence of Quantum Melting of Spin Ice: Quantum-to-Classical Crossover*, Phys. Rev. Lett. **115**, 077202 (2015).

[126] M. P. Kwasigroch, *Vison-Generated Photon Mass in Quantum Spin Ice: A Theoretical Framework*, Phys. Rev. B **102**, 125113 (2020).

[127] T. Fennell, O. A. Petrenko, G. Balakrishnan, S. T. Bramwell, J. D. M. Champion, B. Fåk, M. J. Harris, and D. M. Paul, *Field-Induced Partial Order in the Spin Ice Dysprosium Titanate*, Applied Physics A **74**, s889–s891 (2002).

[128] T. Fennell, O. A. Petrenko, B. Fåk, J. S. Gardner, S. T. Bramwell, and B. Ouladdiaf, *Neutron Scattering Studies of the Spin Ices* $Ho_2Ti_2O_7$ *and* $Dy_2Ti_2O_7$ *in Applied Magnetic Field*, Phys. Rev. B **72**, 224411 (2005).

[129] J. P. C. Ruff, R. G. Melko, and M. J. P. Gingras, *Finite-Temperature Transitions in Dipolar Spin Ice in a Large Magnetic Field*, Phys. Rev. Lett. **95**, 097202 (2005).

[130] J. P. Clancy, J. P. C. Ruff, S. R. Dunsiger, Y. Zhao, H. A. Dabkowska, J. S. Gardner, Y. Qiu, J. R. D. Copley, T. Jenkins, and B. D. Gaulin, *Revisiting Static and Dynamic Spin-Ice Correlations in* $Ho_2Ti_2O_7$ *with Neutron Scattering*, Phys. Rev. B **79**, 014408 (2009).

[131] B. Gao, T. Chen, H. Yan, C. Duan, C.-L. Huang, X. P. Yao, F. Ye, C. Balz, J. R. Stewart, K. Nakajima, S. Ohira-Kawamura, G. Xu, X. Xu, S.-W. Cheong, E. Morosan, A. H. Nevidomskyy, G. Chen, and P. Dai, *Magnetic Field Effects in an Octupolar Quantum Spin Liquid Candidate*, Phys. Rev. B **106**, 094425 (2022).

[132] J. Beare, E. M. Smith, J. Dudemaine, R. Schäfer, M. R. Rutherford, S. Sharma, A. Fitterman, C. A. Marjerrison, T. J. Williams, A. A. Aczel, S. R. Dunsiger, A. D. Bianchi, B. D. Gaulin, and G. M. Luke, *μSR Study of the Dipole-Octupole Quantum Spin Ice Candidate* $Ce_2Zr_2O_7$, arXiv: 2308.02800 [cond-mat.str–el] (2023).

[133] M. Ruminy, S. Chi, S. Calder, and T. Fennell, *Phonon-Mediated Spin-Flipping Mechanism in the Spin Ices* $Dy_2Ti_2O_7$ *and* $Ho_2Ti_2O_7$, Phys. Rev. B **95**, 060414 (2017).

[134] T. Fennell, M. Kenzelmann, B. Roessli, H. Mutka, J. Ollivier, M. Ruminy, U. Stuhr, O. Zaharko, L. Bovo, A. Cervellino, M. K. Haas, and R. J. Cava, *Magnetoelastic Excitations in the Pyrochlore Spin Liquid* $Tb_2Ti_2O_7$, Phys. Rev. Lett. **112**, 017203 (2014).

[135] Y. Xu, H. Man, N. Tang, S. Baidya, H. Zhang, S. Nakatsuji, D. Vanderbilt, and N. Drichko, *Importance of Dynamic Lattice Effects for Crystal Field Excitations in the Quantum Spin Ice Candidate* $Pr_2Zr_2O_7$, Phys. Rev. B **104**, 075125 (2021).

[136] P. Thalmeier and P. Fulde, *Bound State between a Crystal-Field Excitation and a Phonon in* $CeAl_2$, Phys. Rev. Lett. **49**, 1588–1591 (1982).

[137] P. Thalmeier, *Theory of the Bound State Between Phonons and a CEF Excitation in* $CeAl_2$, Journal of Physics C: Solid State Physics **17**, 4153 (1984).

[138] R. Schedler, U. Witte, M. Loewenhaupt, and J. Kulda, *Coupling Between Crystal Field Transitions and Phonons in the 4f-Electron System* $CeCu_2$, Physica B: Condensed Matter **335**, Proceedings of the Fourth International Workshop on Polarised Neutrons for Condensed Matter Investigations, 41–43 (2003).

[139] M. Loewenhaupt and U. Witte, *Coupling Between Electronic and Lattice Degrees of Freedom in 4f-Electron Systems Investigated by Inelastic Neutron Scattering*, Journal of Physics: Condensed Matter **15**, S519 (2003).

[140] L. Chapon, E. Goremychkin, R. Osborn, B. Rainford, and S. Short, *Magnetic and Structural Instabilities in* $CePd_2Al_2$ *and* $LaPd_2Al_2$, Physica B: Condensed Matter **378-380**, Proceedings of the International Conference on Strongly Correlated Electron Systems, 819–820 (2006).

[141] D. T. Adroja, A. del Moral, C. de la Fuente, A. Fraile, E. A. Goremychkin, J. W. Taylor, A. D. Hillier, and F. Fernandez-Alonso, *Vibron Quasibound State in the Noncentrosymmetric Tetragonal Heavy-Fermion Compound* $\mathrm{CeCuAl_3}$, Phys. Rev. Lett. **108**, 216402 (2012).

[142] V. K. Anand, A. Fraile, D. T. Adroja, S. Sharma, R. Tripathi, C. Ritter, C. de la Fuente, P. K. Biswas, V. G. Sakai, A. del Moral, and A. M. Strydom, *Crystal Electric Field and Possible Coupling with Phonons in Kondo Lattice* $\mathrm{CeCuGa_3}$, Phys. Rev. B **104**, 174438 (2021).